Final Technical Report – Executive Summary

Project Title: Microscale Enhancement of Heat and Mass Transfer for Hydrogen Energy Storage (Hydrogen Storage Engineering Center of Excellence (HSECoE)

Project Period: February 1st, 2009 to June 30th 2015
Date of Report: September 30th 2015

Recipient: Oregon State University
Award Number: DE-FC36-09GO19005

Working Partners: Oregon State University is a member of the HSECoE
Cost-Sharing Partners: Oregon Nanoscience and Microtechnology Institute (ONAMI)

Contact: Principle Investigator - Kevin Drost
Phone - 541-713-1344
Email- kevin.drost@oregonstate.edu

DOE Managers: Ned Stetson, DOE Hydrogen Storage Program Manager; Jesse Adams, DOE Technology Manager

Project Objective: Our objective is to optimize the performance characteristics and reduce the size, weight, and cost of adsorption hydrogen storage systems through 1) thermal integration and 2) The application of microscale enhancements of heat and mass transfer.

EXECUTIVE SUMMARY

Hydrogen storage involves coupled heat and mass transfer processes that are significantly impacted the by size, weight, cost, and performance of system components. Micro-technology devices that contain channels of 10-500 microns in characteristic length offer substantial heat and mass transfer enhancements by greatly increasing the surface-to-volume ratio and by reducing the distance that heat or molecules must traverse. These enhancements often result in a reduction in the size of energy and chemical systems by a factor of 5 to10 over conventional designs, while attaining substantially higher heat and mass transfer efficiency. We are developing micro-technology based advanced adsorption tank inserts (MATI) for high media utilization and enhanced heat and mass transfer during charge and discharge of adsorbent hydrogen storage systems.

The objective of this study was to Use microchannel processing techniques to:

- Demonstrate reduction in size and weight of hydrogen storage systems
- Improve charge/and discharge rates of hydrogen storage systems

- Reduce size and weight and increase performance of thermal balance of plant components

By meeting these objectives we have addressed the following technical barriers from the Technical Challenges section (3.3.4) of the Hydrogen, Fuel Cells and Infrastructure Technologies Program Multi-Year Research, Development and Demonstration Plan:

- System Weight and Volume
- Charging/Discharging Rates
- Balance of Plant (BOP) Components

Our technical approach was to identify high priority compoents that could benefit from process intensification and for each high-priority component, use microchannel technology to reduce the relevant barriers to heat and mass transfer. Our approach involved: 1) Optimizing the performance of a single unit cell (i.e., an individual microchannel) and then "Numbering Up" using appropriate simulation tools that we then validate by experimental investigation; and 2) Developing microlamination methods as a path to "numbering up" by low-cost high-volume manufacturing.

PROJECT ORGANIZATION – The OSU involvement in the HSECoE was organized into three Phases.

- **PHASE 1** - In Phase 1, OSU identified two micro channel components which could significantly benefit hydrogen storage. The first involved the use of a micro channel combustor/heat exchanger for providing thermal energy to desorb hydrogen from a metal hydride system. The second application was for cryogenic adsorption hydrogen storage and involved the use of micro channel cooling plates to allow the use of a cooling fluid other than hydrogen. This approach was designated as the Modular Adsorption Task Insert (MATI) and the concept is described in more detail below. The MATI has the advantages of maintaining good thermal performance and an extremely high packing factor for the media (in excess of 95% for a tank with flat end caps) and allows the use of fuel cell waste heat for the hydrogen desorption process significantly improving the on-board efficiency of the adsorption hydrogen storage system.

- **PHASE 2** - During Phase 2, OSU conducted laboratory testing and model validation relative to the both the microcombustor and the MATI. The microcombustor was focused on providing supplemental heating during the discharge of an adsorption hydrogen storage system. The MATI was designed to provide thermal management of the adsorption hydrogen storage system during both charging and discharging. Based on these results and systems modeling conducted by SNRL, DOE decided to fund the fabrication and testing of a 2 liter MATI test article in Phase 3.

- **PHASE 3** – In Phase 3 OSU designed and fabricated four 2 liter MATI test articles and provided two of these to SRNL for testing. OSU modified our existing

test facility to accommodate the 2 liter MATI and used the facility to demonstration the impact of conduction enhancement options. Finally during Phase 3, OSU upgraded our simulation of the MATI integrated with MOF-5 densified pucks and validated the simulation with experimental data produced by SRNL.

A summary of key results for each phase is presented below.

PHASE 1 – Key results and conclusions from the Phase 1 research are summarized below.

- **The Microchannel combustor/heat exchanger is a significant improvement when compared to existing combustion systems** –The microchannel combustor represents a factor of 10 reduction in volume when compared to a state of the art heat exchanger developed by Sandia National Laboratory for automotive hydrogen storage applications. The volume reduction was primarily due to the ability of a microchannel combustor to prevent gas phase combustion. Both simulation and experimental results confirmed the high performance predicted for this device. As part of assembling the test articles, we successfully demonstrated all of the fabrication processes needs for high volume production.

- **Experimental Capabilities –** OSU successfully established the capability to experimentally investigate room temperature charging and discharging for both metal hydride and adsorption systems using densified media. Several issues associated with the experimental technique were identified and were subsequently resolved in Phase 2. In Phase 2 the test apparatus was modified to allow testing at cryogenic temperature.

- **Simulation** – Simulation capability were established and preliminary comparisons with experimental data demonstrated several areas where the modeling needed additional detail. These were addressed in Phase 2

- **The MATI has important impacts on the Adsorption System Design** – The use of the MATI has several important system impacts including 1) the MATI allows the use of densified media with a very high packing factor. The MATI allows up to 95% of the volume of the adsorption pressure vessel to be media and 2) since the cooling fluid and hydrogen are separate; the MATI allows the use of fuel cell waste heat for discharge though a small amount of supplemental heating from hydrogen combustion is required.

Based on these results the decision was made to further develop the MATI and the microchannel combustor/heat exchanger in Phase 2.

PHASE 2 – Key results and conclusions from the Phase 2 research are summarized below.

- **The microchannel Combustor/Heat exchanger Technology is an extremely attractive approach to providing combustion heat for discharging a hydrogen storage system**. – Simulation and experimental results confirmed that microchannel technology can result in an extremely compact device for providing thermal energy to a hydrogen storage system.

- **Based on Simulation the MATI concept is Technically Feasible** – Modeling and experimental results demonstrated that the MATI thermal and chemical performance is well understood and performs as expected.

- **The MATI concept is Manufacturable** – Fabrication studies demonstrated that the MATI could be fabricated out of aluminum 6061 using proven industrial processes amenable to high volume production.

- **The MATI concept can meet mass and weight goals for Adsorption Storage with a reasonable production cost** – The results of Phase two demonstrate that the MATI could meet the DOE Smart Goals for the device. To meet the smart goals, a number of important design modifications were required. These included the 1)The location of the hydrogen distribution plate needs to be in the middle of the puck to allow the hydrogen to provide cooling where it is most needed, 2) use aluminum 6061 in place of stainless steel, 3) use aluminum pins to enhance conduction in the pucks and 4) use microscale pyramidal truss networks for hydrogen distribution and for the internals of the cooling plates.

Based on these results the decision was made to further develop the MATI in Phase 3.

PHASE 3 – Key results and conclusions from the Phase 3 research are summarized below.

- **When We Are Addressing a Diffusion Limited Process Microchannel Technology Can Have a Dramatic Impact** – The microchannel combustor/heat exchanger is a classic application of microchannel technology because the performance of this device is limited by diffusion of mass and heat. Using microchannel dimensions can significantly improve the performance of this class of device. The OSU microchannel combustor/heat exchanger was a small fraction of the size of a state of the art conventional combustor/heat exchanger developed by Sandia National Laboratory. Clearly whenever a hydrogen storage system needs a device which is limited by diffusion, microchannel technology should be considered.

- **The MATI Highlights Other Advantages of Microchannel Technology** – Heating and cooling the media is a diffusion limited process due to the low thermal conductivity of many storage materials but the use of microchannels only improves the performance of a the cooling device and does not address the primary resistance to heat transfer which is the media itself. However the use of microchannels in the form of the MATI has other advantages including

maximizing the fraction of the tank volume which is media and the use of a second fluid for heating and cooling. This is particularly important for the heating case where the MATI allows the use of fuel cell waste heat rather then electricity.

- **The MATI is Technically Feasible and Has the Potential For Low Cost** – Design, testing and simulation at OSU did not identify any issues related to the feasibility of the concept and extensive manufacturing and cost studies confirmed that the MATI could be fabricated in high volumes using standard industrial practices and at an attractive cost.

- **Microengineering the Densified Media Pucks Offers a Solution to Low Conductivity Materials** – The use of microengineered conduction enhancements in the densified media pucks appear to offer an attractive option for improving heat transfer in a low conductivity densified media. Simulation and preliminary experimental results suggest this approach is attractive but more detailed experimental investigations are required to optimize the conduction enhancements

Final Technical Report

Project Title: Microscale Enhancement of Heat and Mass Transfer for Hydrogen Energy Storage (Hydrogen Storage Engineering Center of Excellence (HSECoE)

Project Period: February 1st, 2009 to June 30th 2015
Date of Report: September 30th 2015

Recipient: Oregon State University
Award Number: DE-FC36-09GO19005

Working Partners: Oregon State University is a member of the HSECoE
Cost-Sharing Partners: Oregon Nanoscience and Microtechnology Institute (ONAMI)

Contact: Principle Investigator - Kevin Drost
Phone - 541-713-1344
Email- kevin.drost@oregonstate.edu

DOE Managers: Ned Stetson, DOE Hydrogen Storage Program Manager; Jesse Adams, DOE Technology Manager

Project Objective: Our objective is to optimize the performance characteristics and reduce the size, weight, and cost of adsorption hydrogen storage systems through 1) thermal integration and 2) The application of microscale enhancements of heat and mass transfer.

1.0 BACKGROUND: Hydrogen storage involves coupled heat and mass transfer processes that are significantly determined by size, weight, cost, and performance. As part of the Hydrogen Storage Engineering Center of Excellence (HSECoE), Oregon State University (OSU) applied advanced heat and mass transfer enhancement techniques, based on the use of microscale features and phenomena with a characteristic length scale of 10 to 500 microns, to improve the heat and mass transfer efficiency and reduce the size, weight, and cost of automotive hydrogen storage systems. OSU participated in two technology areas: Subscale Prototype Construction, Testing and Evaluation (T. Semelsberger, Los Alamos National Laboratory [LANL]) and Engineering Design, Modeling and Validation (B. Hardy, Savannah River National Laboratory [SRNL]). OSU developed microchannel-based components integral to the storage system and balance of plant components necessary for the efficient use of waste heat for adsorption hydrogen storage systems while Pacific Northwest National Laboratory (PNNL) developed microchannel components integral to chemical hydride storage. The project was conducted at Microproducts Breakthrough Institute (MBI), a joint research institute operated by OSU and PNNL and focused on the development and commercialization of microchannel-based technology.

Fundamentally, microchannel technology reduces barriers to heat and mass transfer by reducing characteristic diffusion lengths. Any diffusion-limited process can be improved by reducing the characteristic diffusion length associated with that process. As an example, consider a cool fluid flowing in a channel with hot walls. For a diffusion-limited process (laminar flow), the residence time necessary for the fluid to come to the temperature of the walls is a function of channel D^2 where D is the width of the channel. A similar effect is encountered in any other diffusion-limited process. The residence time can be reduced without increasing the pressure drop by adding more channels. If the total flow area is kept constant as the channel dimensions are reduced, moving to a larger number of smaller channels increases heat (or mass) transfer, which in turn allows the channels to be shorter. For laminar flow, the increase in pressure drop caused by reduced channel size is just offset by the impact of the shorter channel on pressure drop. A significant reduction in barriers to heat and mass transfer will improve the heat and mass transfer efficiency and reduce the size, weight, and cost of automotive hydrogen storage systems.

The positive impact of using microscale channels (10 to 500 microns) for heat transfer was reported in the 1980s with an emphasis on cooling electronic components. Starting in the early 1990s, research at PNNL and OSU focused on the application of microchannel technology to energy and chemical systems applications. Examples of where OSU has applied microchannel technology to reduce heat and mass transfer barriers include: microscale combustion systems, high flux microscale heat exchangers and recuperators, microtechnology-based heat-actuated heat pumps, microchannel thermal management systems for fuel cells, microscale absorption and adsorption systems, microchannel catalytic reactors for hydrogen production, microchannel biodiesel reactors, microchannel hemodialysis systems, microscale separations systems, and microreactors for the production of nanoparticles. Applying microchannel heat and mass transfer enhancement to energy and chemical systems has often resulted in a reduction factor of 5 to 10 in the size of the device while attaining high thermal and mass transfer efficiency. Currently, four companies are commercializing microtechnology-based energy and chemical systems developed at OSU and PNNL. The status of microscale enhancement of heat transfer and mass transfer is discussed below relative to applications in both the storage unit and in balance of plant components.

Microscale enhancement of heat and mass transfer can be applied to two classes of problems related to hydrogen storage. First, the microscale enhancement can be used in the actual automotive hydrogen storage component to enhance heat and mass transfer allowing rapid charging of the storage system, rapid startup, and quick response to changing driving conditions. This application led to the development of the Modular Adsorbing Tank Insert (MATI) which is described below and is included in Phase 3. In addition, the overall efficiency of the hydrogen storage system can depend on how efficiently the system can use the available waste heat from the fuel cell. This is particularly true for hydrogen storage systems where material characteristics require temperatures above that available from the fuel cell, mandating the use of hydrogen combustion. The performance of the balance of plant components, needed for utilization

of fuel cell waste heat or combustion of hydrogen, will to a great extent determine the round trip efficiency of the system. The use of microscale components for balance of plant applications has the potential to allow efficient use of fuel cell waste heat and efficient combustion of hydrogen for discharging storage. Microtechnology-based balance of plant components such as microscale heat exchangers, recuperators, and combustors have been demonstrated for similar applications. This application led to the development of the micro channel integrated combustor/heat exchanger which demonstrated a significant improvement over other combustion schemes for metal hydride storage. With the center focusing on adsorption based cooling, the micro channel combustor/heat exchanger was not included in Phase 3.

2.0 PROJECT ORGANIZATION – The OSU involvement in the HSECoE was organized into three Phases.

PHASE 1 - In Phase 1, OSU identified two micro channel components which could significantly benefit hydrogen storage. The first involved the use of a micro channel combustor/heat exchanger for providing thermal energy to desorb hydrogen from a metal hydride system. The second application was for cryogenic adsorption hydrogen storage and involved the use of micro channel cooling plates to allow the use of a cooling fluid other than hydrogen. This approach was designated as the Modular Adsorption Task Insert (MATI) and the concept is described in more detail below. The MATI has the advantages of maintaining good thermal performance and an extremely high packing factor for the media (in excess of 95% for a tank with flat end caps) and allows the use of fuel cell waste heat for the hydrogen desorption process significantly improving the on-board efficiency of the adsorption hydrogen storage system.

PHASE 2 - During Phase 2, OSU conducted laboratory testing and model validation relative to the both the microcombustor and the MATI. The microcombustor was focused on providing supplemental heating during the discharge of an adsorption hydrogen storage system. The MATI was designed to provide thermal management of the adsorption hydrogen storage system during both charging and discharging. Based on these results and systems modeling conducted by SNRL, DOE decided to fund the fabrication and testing of a 2 liter MATI test article in Phase 3. This progress report is focused on describing progress on our Phase 3 scope of work.

PHASE 3 – In Phase 3 OSU designed and fabricated four 2 liter MATI test articles and provided two of these to SRNL for testing. OSU modified our existing test facility to accommodate the 2 liter MATI and used the facility to demonstration the impact of conduction enhancement options. Finally during Phase 3, OSU upgraded our simulation of the MATI integrated with MOF-5 densified pucks and validated the simulation with experimental data produced by SRNL.

The balance of the report is organized by Phase with the objectives, task structure, technical results and conclusions being presented for each Phase.

3.0 PHASE 1 ORGANIZATION AND RESULTS

This section presents and overview of Phase 1. Section 3.1 discusses the objectives of OSU's Phase 1 activities while Section 3.2 discusses the Phase 1 scope of work while Section 3.3 presents the technical results by task.

3.1 PHASE 1 OBJECTIVES - Microscale enhancement of heat and mass transfer can be applied to two classes of problems related to hydrogen storage. First, the microscale enhancement can be used in the actual automotive hydrogen storage component to enhance heat and mass transfer allowing rapid charging of the storage system, rapid startup, and quick response to changing driving conditions. In addition, for hydrogen storage systems that require heat to discharge storage, the overall efficiency of the hydrogen storage system will depend on how efficiently the system can use the available waste heat from the fuel cell. This is particularly true for hydrogen storage systems where material characteristics require temperatures above that available from the fuel cell, mandating the use of hydrogen combustion. The performance of the balance of plant components, needed for utilization of fuel cell waste heat or combustion of hydrogen, will to a great extent determine the round trip efficiency of the system. The use of microscale components for balance of plant applications has the potential to allow efficient use of fuel cell waste heat and efficient combustion of hydrogen for discharging storage. Microtechnology-based balance of plant components such as microscale heat exchangers, recuperators, and combustors have been demonstrated for similar applications. Based on OSU's experience in developing other microtechnology-based systems, when compared to conventional components we expect an increase in heat and mass transfer efficiency, and a significant reduction in size and weight.

In Phase 1, the OSU research objectives were:

1) Identification of at least one option for using microchannel technology as a thermal management option within the storage system. Initially we focused on metal hydride applications but ultimately changed our focus to cryogenic adsorption storage systems. In both cases we developed experimentally validated model of the process.
2) Identification of at least one option for using microchannel technology to reduce the size and cost and improve the performance of a balance of plant component. Initially we focused on a combustion system for metal hydride applications but ultimately changed our focus to a smaller combustion system for cryogenic adsorption storage systems. In both cases we developed experimentally validated model of the process.

3.2 PHASE 1 TASK STRUCTURE – The Phase 1 research was organized into five tasks. Each is discussed below.

Task 1.1 Enabling Technologies – The Phase 1 focus of this task was on the development of a hydrogen combustion driven heating system for a metal hydride hydrogen storage system. The task included the design, fabrication, modeling and experimental validation for an integrated microchannel combustor and heat exchanger that would heat oil for discharging a metal hydride storage system. The task included one special study conducted on a concept for in-tank combustion heating proposed by General Motors.

Task 1.2 Experimental Validation (In-Tank Thermal Management) – The focus of this task was on the design, assembly and start-up of a test apparatus capable of testing adsorption in densified pucks of adsorbing media. This task also developed experimental data that was used to validate the simulation developed in Task 1.3.

Task 1.3 Simulation of Adsorption (In-Tank Thermal Management) – Task 1.3 involved the development of a adsorption simulation tool capable of modeling heat and mass transfer and the adsorption process.

Task 1.4 Modular Adsorption Tank Insert (MATI) Concept Development – This task included the development of the MATI concept and one special study requested by UTRC on an ammonia decomposition microchannel reactor

Task 1.5 Fabrication Research – Task 1.5 focused on the development of fabrication schemes necessary for high volume manufacturing of the MATI and on the development of a manufacturing plan.

3.3 PHASE 1 RESULTS; Progress on each of the five task described above is described in the following sections.

Task 1.1 Enabling Technologies: OSU activities related to enabling technologies were focused on the development of thermal devices for balance of plant applications. As part of this effort it was decided that OSU would initiate experimental and simulation based characterization of an integrated microchannel hydrogen combustor/oil heater/ recouperator. Based on past experience, OSU was confident that the application of microchannel technology to this application would result in a dramatic reduction in size and weight of the combustion system need to product heat for discharging a metal hydride storage system. The goal in phase 1 was to develop a relatively simple, validated model that can predict the performance of a combustor to be used to desorb hydrogen from the hydride bed. This section first describes the large-array CHX preliminary design, followed by the approach to be undertaken in phase 1 of the project in order to arrive at the final design. In addition we also discuss a special study OSU conducted at the request of General Motors on the feasibility of desorbing a metal hydride storage tank with a combustion system located within the tank.

Large Array Combustor/heat exchanger (CHX): A preliminary estimate of the requirements of the CHX was undertaken based on a limited survey of literature. The goal was to determine the amount of hydrogen per unit time that needed to be

combusted for desorption of hydrogen from sodium alanate so that the DOE technical target for minimum discharge rate is satisfied. For a 35 kW fuel cell (typical of the Mercedes class B 2010 model) the DOE target of minimum full flow rate translated to a supply of ~0.7 g/s of hydrogen to the fuel cell. For sodium alanate, this corresponded to a heat transfer rate of 14 kW at a temperature of ~150 to 200 ^{o}C. Based on stoichiometric combustion, 0.12 g/s of hydrogen needed to be combusted to provide this heat load to the hydride bed. In order to desorb a total of 5 kg of H2 from the hydride bed, an additional 0.8 kg of H2 was required for the combustor.

As a first step in the sizing of the large-array CHX, calculations of pressure drop and heat transfer were performed on varying sizes of combustion, exhaust gas and oil channels. The calculations were based on several variable geometric and fluidic parameters as well as constraints. For this preliminary analysis, the heat exchange was limited to that between the exhaust gas channels and the oil channels. Based on expected combustion temperature from Norton et al. [2] of 600 ^{o}C, a counter-flow HX analysis revealed that the heat transfer rate would be, as should be anticipated, limited by the gas side heat transfer coefficient. A spreadsheet was created to help determine the pressure drop and heat transfer rate for various parametric variations and constraints. A typical size for a 4 kW combustor, based on this approximate analysis, would be 15 cm x 12 cm x 4 cm (LxWxH). The CHX would have 400 combustion channels, each 150 microns x 2 mm in cross section. There would be 800 corresponding exhaust gas channels, 400 on each side of the combustion channels, in two arrays. These two arrays of exhaust gas channels would exchange heat with two arrays of oil channels. Each array of oil channels would consist of 200 channels of 300 micron x 2 mm in cross section. The pressure drop in the combustion gas channels (not including manifold and minor losses) would be 80 kPa (11.6 psi) and the oil side pressure drop would be 1.39 kPa (0.2 psi).

In order to arrive at the above design several key assumptions were made, which needed to be tested using a smaller array CHX. Some of these assumptions were:

1. The exhaust gas inlet temperature was based on a study in literature and needed to be verified by global measurements of temperature
2. The heat transfer coefficients in the exhaust gas and oil channels are based on laminar flow, constant heat flux condition. The pressure drop was also based on laminar flow. Both pressure drop and heat transfer data needed to verify these assumptions
3. Alignment and bonding of the device was feasible with the assumed spacing of 250 microns between channels.
4. The film temperature of oil should not exceed the maximum specified film temperature by the manufacturer.
5. Extraneous heat losses were not taken into account; these needed to be held to a minimum

In addition, several other aspects needed to be verified with the smaller array CHX. These include

1. Catalyst deposition and amount of catalyst to be used needed to be studied
2. The percentage of heat distribution between oil and combustion channels from the exhaust gas channels needed to be identified. This would provide an indication of the amount of energy going into preheating the incoming reactant gases in the combustion channel.
3. Design of inlet and exit manifolds needed careful attention in the design so that bonding on the manifolds to the channel stack could be achieved without leaks.

***Approach**:* The approach was to develop initially a small-scale combustor/HX with a single central combustion channel, two exhaust gas channels and two oil HX channels as shown in Fig. 1.

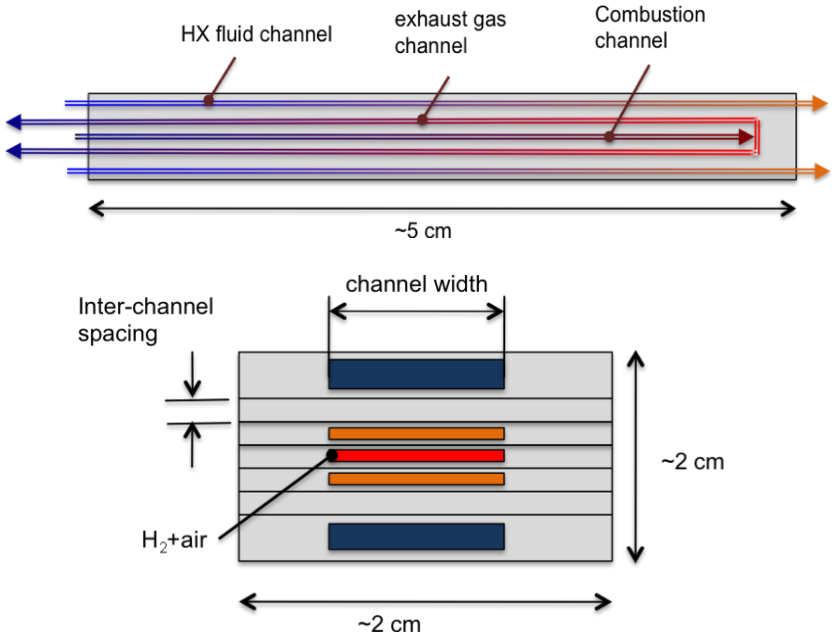

Figure 1 – Single array small-scale CHX schematic

Experimental Facility Design:, A schematic of the experimental facility for the small-scale CHX testing is provided in Fig. 2. The equipment and instrumentation were chosen based on minimizing the uncertainty in estimating the heat transfer rate to less than two percent.

Temperatures from calibrated thermocouples were read using a National Instruments USB thermocouple module with a 24-bit, in-built cold-junction compensator. A National Instruments USB-6009 data acquisition board was used to acquire voltage signals from the pressure transducers and oil flowmeter and to send digital out signals to the proportional valve amplifier. A LabVIEW program was used to collect data from the thermocouples, pressure transducers, and flowmeters. The same program was used to control the two mass flow controllers as well as obtain flow rate readings from these flow controllers.

During the start-up process the μ-CHX body was preheated using a thick film heater. This was used to bring the gases up to the temperature required for combustion. Once these heated gases reached the catalyst, they combusted and heated the incoming gases. At this point the preheater was turned off. The gases exiting the combustor were collected and analyzed using a gas chromatograph to determine their composition. This was used to validate the analytical model and determine the extent of combustion. The oil flow loop was controlled with a proportional valve and a flow meter. The oil was heated by the μ-CHX and cooled with city water in a plate-type heat exchanger. Thermocouples and pressure sensors were attached to the oil and gas inlets and exits in order to measure the temperature rises and pressure drops across the μ-CHX.

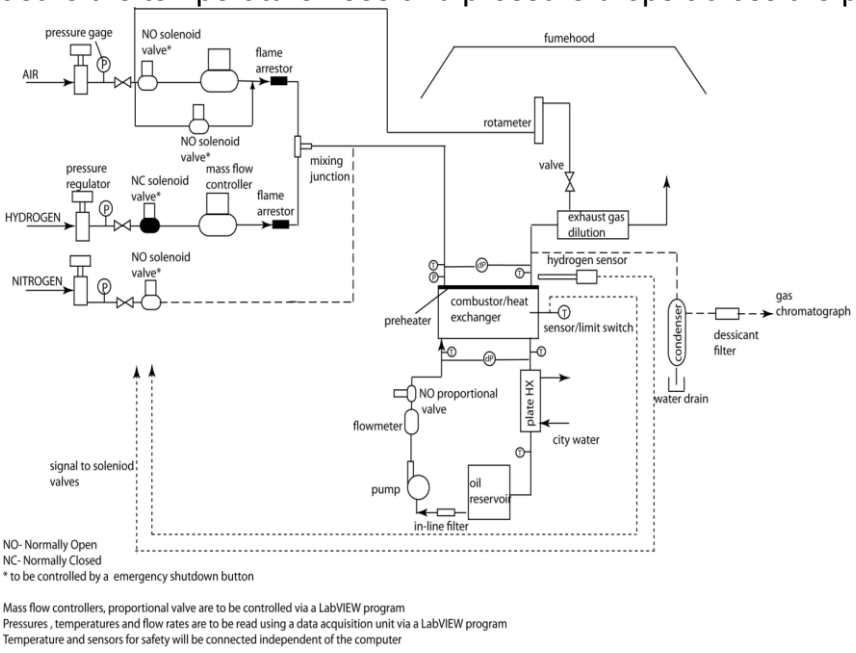

Figure 2. Proposed experimental facility schematic

The experiments were performed in a vent hood supplied with H_2 gas, clean and dry compressed air, N_2, vacuum and process cooling water. The vent hood was large enough for the entire flow loop to be contained within it. The 100 psi absolute pressure transducers were calibrated to within 0.25 psi (0.25% Full Scale). The 5 psi differential pressure transducer were calibrated to 0.068 psi (1.4% Full Scale). The T-type thermocouples were calibrated to within 0.36 °C over a range of 15 to 180 °C. This is the entire temperature range that is anticipated for the oil loop and the gas inlet.

First Generation μ-CHX Test Article Design: A small-scale combustor (a single unit cell) was designed and was used to quantify the performance of the microscale combustor and validate the numerical model. A schematic is shown in Fig. 3. This design had a single combustor channel, recuperator channel and oil channel. The combustor channel was insulated with a high temperature ceramic. The oil side was insulated with PEEK, a high temperature plastic with a low coefficient of thermal conductivity. These insulating materials reduced the temperature of large surfaces on the top and bottom of the combustor, reducing heat losses.

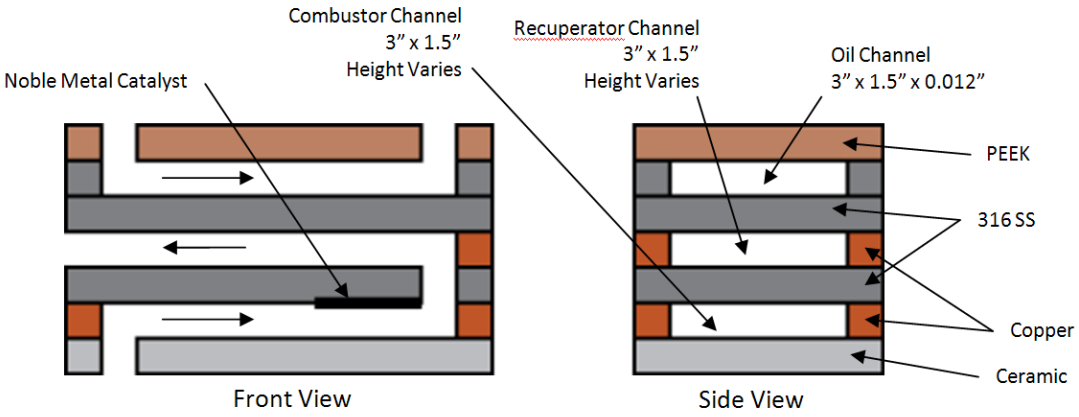

Figure 3: Cross-sectional schematic of the μ-CHX (not to scale)

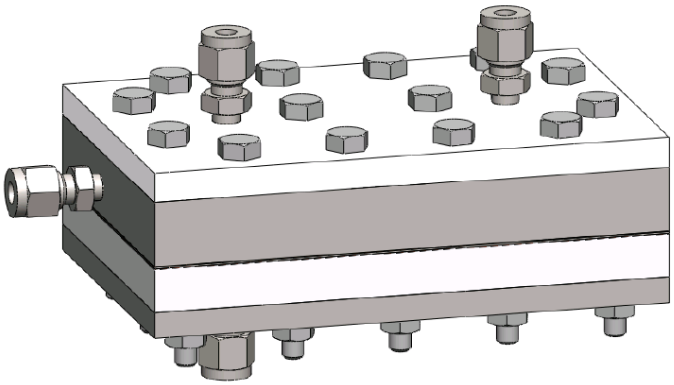

Figure 4: Assembled μ-CHX

The assembled combustor is shown in Fig. 4 and an exploded view is shown in Figure 5. Headers were ¼" Swagelok tube fittings and will have plastic tubing attached directly after the header to reduce conductive heat losses. Combustion gases were supplied via the header on the bottom of the combustor and exhaust gases were removed through the side header. The oil headers were located on the top of the combustor.

The channels for the combustor and recuperator were formed by thin copper shims. These compressed under pressure, sealing the channels. The bottom plate and the oil part were machined out of stainless steel and will evenly distribute the pressure from the bolts. The combustor was designed for easy disassembly, allowing different combustor configurations to be tested.

The first μ-CHX design was manufactured and was leak tested. Despite efforts to maintain uniform bolt pressure, the ceramic plate cracked. A new bottom plate was then designed and manufactured out of stainless steel. However, the μ-CHX leaked when pressurized. Extensive leak testing was performed on this design in order to determine the sources of leaks. The leakage rate of air at 1 bar (gage) was found to be 0.83 kPa/min (0.12 psi/min). Helium was also tested, but there was no significant difference

in leakage rates between the two gases. It was determined that there were two factors that caused the leaks. First, the bolt holes used for sealing the oil side extended to the copper shim, causing leakage from the bolt holes. Secondly, pressure testing revealed that air leaked through the shims on the short sides of the combustor. The leaks were located in the middle of the gaps between those bolts. No leakage was observed between the bolts on the long side of the µ-CHX.

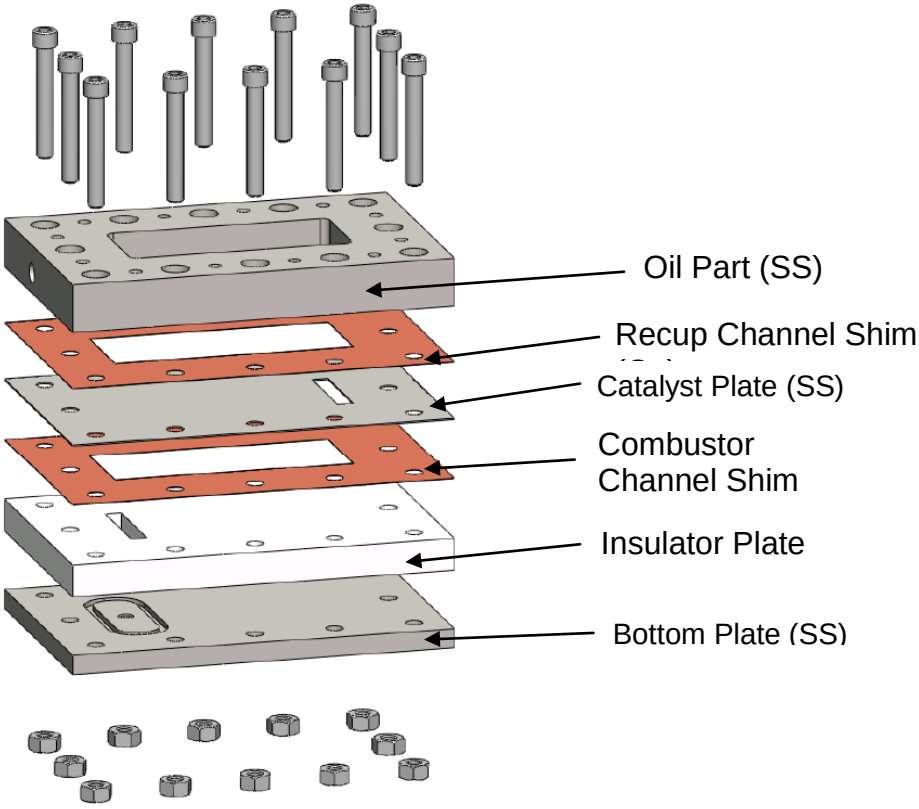

Figure 5: Exploded µ-CHX

In order to further analyze the cause of the leak, a finite element analysis (FEA) was performed on the combustor. The FEA model correctly identified the location of the leaks to be on the shorter sides of the combustor. The bolt spacing was too large to provide enough pressure to seal the copper gasket. The combustor design was modified in order to address the leakage problem.

The modified design retained the channel dimensions and header system of the µ-CHX discussed above. thermocouple ports in the base of the µ-CHX were also added. There was a 3x6 array of thermocouple ports with 12.7 mm (0.5”) spacing, located 0.5mm (0.020”) below the combustion channel. These allowed for temperature profile measurements both along the length of the combustor and the width of the channel. This provided insight into the temperature variations caused by catalytic combustion and aided in validating the numerical model and helped confirm that there is uniform heating across the width of the channel. There was also a thermocouple port on the side of the µ-CHX to obtain temperature measurements of the combustor body. Another

modification involved adding the holes for the cartridge heaters in the base. This helped bring the combustor up to the temperature required to initiate combustion more quickly.

The revised µ-CHX design was manufactured and was leak tested. Some minor leakage was still observed, but at 2 bars of pressure it was less than 0.1% of the minimum flow rate possible with the mass flow controllers in the experimental facility (50 ml/min). Therefore, this leakage rate was considered to be negligible for the combustion experiments. Table 1 shows the results of the pressure test. The successful completion of this test demonstrated that the µ-CHX was ready for experimentation.

Table 1. µ-CHX Leak Test Results

Pressure (bar)	Pressure Loss (Pa/s)	Helium Leakage Rate (g/s)	Helium Leakage Rate (ml/min)
1	4.42	6.51E-08	0.0235
2	9.93	1.46E-07	0.0527

A 2-inch palladium target was purchased for use in the AJA Orion sputter tool. A survey of literature on this process indicated that palladium has a greater cohesive force than adhesive force. This generally results in thickly deposited layers not adhering to the substrate while thinner layers adhere better. This fit our observations while performing the “Scotch Tape Test” on various deposition thicknesses. Thinner depositions were not removed by Scotch Tape applied to the film. Using a scanning electron microscope (SEM), palladium deposits were investigated using x-ray dispersion analysis. X-ray dispersion analysis of this process before and after the tape test indicated similar amounts of palladium, demonstrating that the palladium has good adherence to the substrate. However, The sputter deposited palladium catalyst was tested with limited success. While combustion was achieved, the reactivity was very low and seemed to deactivate as time progressed. There was not enough heat generated to run oil through the combustor to obtain performance data. Due to this poor initial performance, alternative catalyst deposition methods were considered.

The revised catalyst support method involved using an etched stainless steel shims. The 316 stainless steel shims were electrochemically etched, to increase the surface roughness prior to the catalyst deposition. The shim was masked with polyester tape prior to etching for 60 minutes in a 0.5 M solution of oxalic acid at room temperature. The masking tape was necessary to confine the etching to the deposition region. The shim was etched at a potential of 15 V and drew about 7 A. This resulted in a current density of approximately 0.28 A/cm^2. This current density was sufficient to increase the surface roughness by a factor of 2. A sample image of an electrochemically etched stainless steel surface is shown in Figure 6.

Once etched, a platinum catalyst was wet deposited onto the shim. The polyester masking tape used during etching was left on the shim to contain the catalyst to the desired area. Chloroplatinic acid hexahydrate ($H_2PtCl_6 \bullet 6H_2O$), obtained from Sigma Aldrich, was used as the catalyst precursor. A 0.007 M solution was dripped onto the

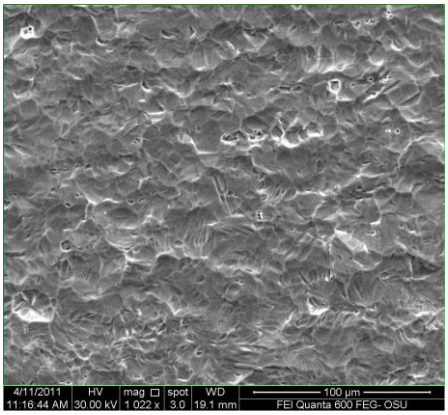

Figure 6. Etched Stainless Steel Prior to Catalyst Deposition

shim from a pipette until the surface was fully covered, then placed in an oven at 80 deg C. The shim was left at this temperature until the liquid fully evaporated. This process was repeated three times before the masking tape was removed. At this point, the deposition region was black from the platinum acid deposit. The surface was fully covered, but not entirely uniform due to the tendency of the liquid to form into drops as the liquid evaporated. The shim was then calcined in air at ~570 C for 3 hours, and then reduced it in a 10:1 N2:H2 mixture for 4 hours at the same temperature.

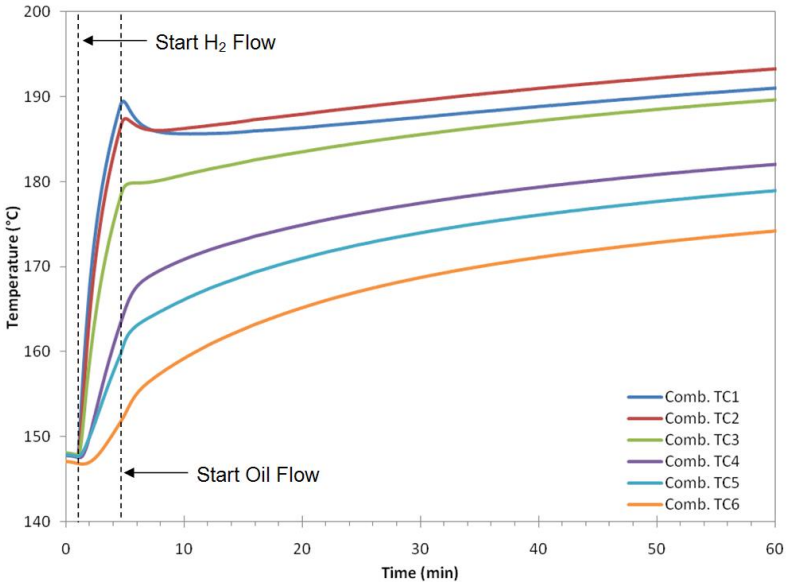

Figure 7. Transient Combustion Response (ϕ=1)

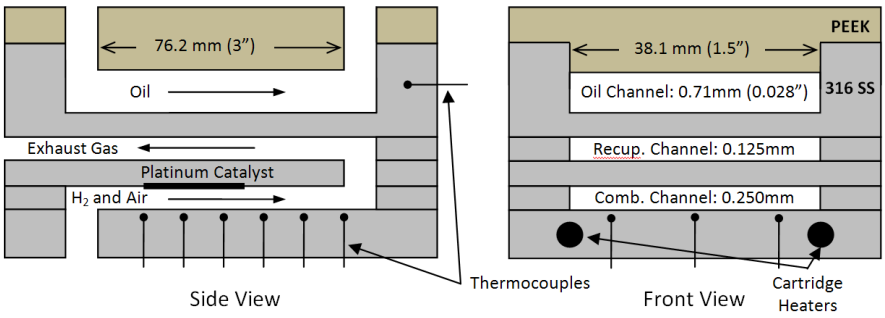

Figure 8. Cross Sectional View of Combustor

This catalyst was much more reactive than the sputtered palladium. A time series plot of the combustion process is shown in Figure 7. Steady state operation was eventually reached after an extended period of time. The large thermal mass of the µ-CHX limited the transient response of the system and increased the amount of time required to reach steady state operation. The temperatures were measured by the thermocouples below the combustion channel. The schematic of the µ-CHX is shown in Figure 8, with TC1 located near the gas inlet and TC6 located at the end of the combustion channel.

Simulation of a Unit cell of the Microscale Combustor Heat Exchanger: A two-dimensional model of a unit cell of the microscale combustor-recuperator-heat exchanger (m-CRHX) is illustrated in Fig. 9. The hydrogen and air (approximated as a 21 percent by volume oxygen and 79 percent by volume nitrogen mixture) mixture enters the combustion channel at inlet velocity and temperature of 4m/s and 300K, respectively. The mass fraction of species at the inlet was defined by the equivalence ratio, which is unity in these cases. The equivalence ratio, f, was defined as the ratio of the molar fuel-to-air ratio at the test conditions to that at stoichiometric conditions. Thus, an f value of less than unity denotes a lean mixture and that greater than unity denotes a rich mixture.

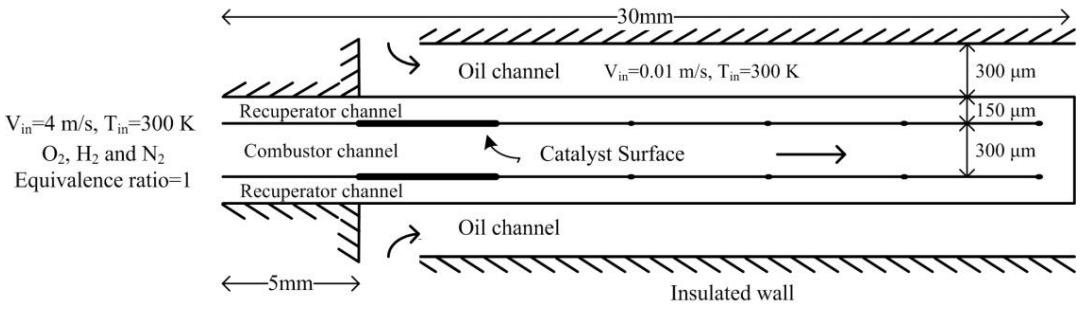

Figure 9. Schematic view of the device

The combustor channel walls were assumed to be coated with platinum catalyst to facilitate the heterogeneous combustion reaction. Only heterogeneous reactions were modeled in this study based on the literature results that found that flame combustion (homogeneous combustion) did not occur in microchannels with dimensions of 250 microns or less. In Fig. 9, 5mm of the wall is shown as coated with Platinum. The exit boundary conditions for the recuperator and oil channels were chosen to have desired

outlet conditions, which were: 1) an outlet oil temperature of more than 170^{o}C (443 K), 2) an oil film temperature lower than 316^{o}C (583 K) and 3) the recuperator exhaust gas temperature of at least 100^{o}C (373 K) to avoid condensation of water vapor within the channels.

In the simulations, the channel wall was assumed thermally thin so that the axial heat conduction along the wall was neglected. Moreover, because of the very small size of the combustion channel, no gas phase reaction was assumed and only surface reactions were considered where five gas species (O_2 H_2 N_2 OH and H_2O) and five surface species (Pt(s), H(s), O(s), OH(s) and H_2O(s)) participated in the 14 simultaneous reactions. Paratherm MG oil was assumed to be the heat transfer fluid used in these simulations because of the appropriate working temperature range and properties. Because of the large temperature variation in the device, all properties are imported to FLUENT as a function of temperature, while mixture viscosity, specific heat and thermal conductivity were calculated from a mass average of species properties. A flat profile was assumed for both gas mixture and oil inlet velocities with no slip boundary conditions near the walls, and atmospheric pressure was assumed at the outlet. A premixed hydrogen and dry air (approximated as a 21 percent by volume oxygen and 79 percent by volume nitrogen mixture) mixture enters the combustion channel. The mass fraction of species at the inlet is defined by the equivalence ratio, ε, which is defined as the ratio of the molar fuel-to-air ratio at the test conditions to that at stoichiometric conditions. Thermal diffusion and mass diffusion at the inlet was also considered.

Non-uniform mesh was used to refine the near-wall regions. The total number of grids was 51000 for the whole model which consists of 606×30 grids combustion channel, 506×20 for each oil channel and 606×10 grids for each recuperator channel. The simulation convergence was decided when the residuals approaches steady values asymptotically and when the relative residuals were smaller than 10^{-3} in all cases.

Simulation Results - The performance of the μ-CHX was characterized through a range of geometrical and thermo-fluidic parameters. The varied parameters investigated included the catalyst location, catalyst length, oil speed and inlet temperature, and channel length. In addition we investigated the effect of different catalysts, equivalence ratios, and channel heights are presented. In order to quantify the performance of each configuration, an efficiency index was defined as the ratio of amount of heat transferred to oil to the chemical energy of input hydrogen, Eq 1.

$$\varepsilon = \frac{\dot{m}_{oil}(h_{out} - h_{in})_{oil}}{\dot{m}_{H_2}\Delta h_{reaction} / M_{H_2}} \qquad (1)$$

where M_{H_2} is the molar mass of hydrogen, $\Delta h_{reaction}$ reaction is the molar enthalpy of reaction , and $\dot{m}_{H_2}$ is the inlet hydrogen mass flow rate. Enthalpy of reaction was calculated at the average temperature of the combustion gases.

***Effect of length of catalyst region**:* Figure 10 shows the efficiency index as a function of length of the catalyst bed. All catalyst beds in this study began at 5 mm from the combustor inlet. An increase in efficiency was observed with increasing catalyst length. This trend was attributed to the fact that for shorter catalyst bed lengths, not all the hydrogen was consumed and exits the recuperator channel uncombusted. However, for catalyst lengths beyond 15 mm, almost all of the hydrogen was consumed and consequently the efficiency index varied only slightly due to changes in recuperator exhaust gas temperature.

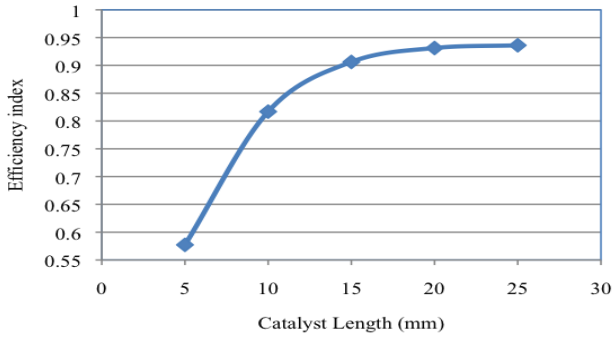

Figure 10. Efficiency index as a function of catalyst length

Figure 11 depicts the oil and exhaust outlet temperatures as a function of catalyst length. The oil exit temperatures were above 440 K, which was the desired minimum oil temperature, for all catalyst lengths. The recuperator exit gas temperature for all cases was also above 373 K thereby ensuring that condensation of water vapor did not occur. The results shown in Fig. 10 and 11 suggest that the amount of catalyst would be minimized using a catalyst bed length of 15 mm. Therefore, 15mm catalyst bed length was the basis for the following parametric studies.

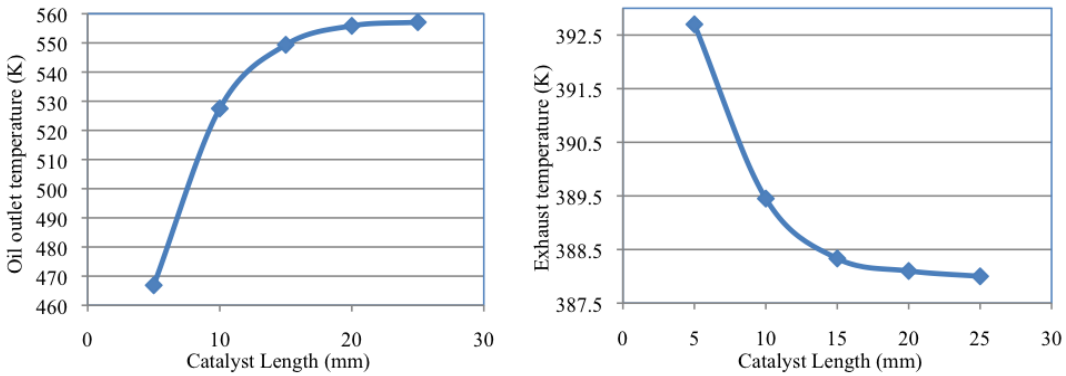

Figure 11. Oil and exhaust outlet temperatures versus catalyst length

Temperature, H_2 and H_2O mass fraction contours for catalyst bed length of 15mm are shown in Figs. 12, 13 and 14 respectively.

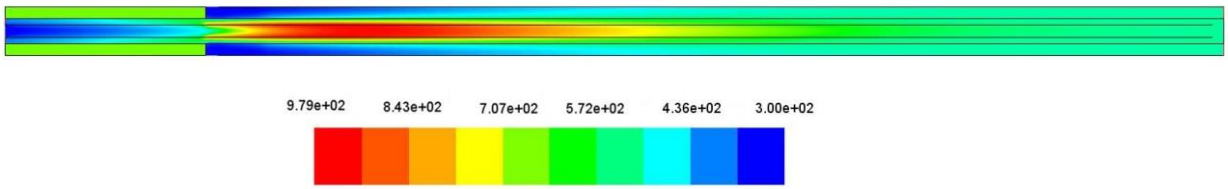

Figure 12. Temperature (K) contour along the device for catalyst length of 15mm

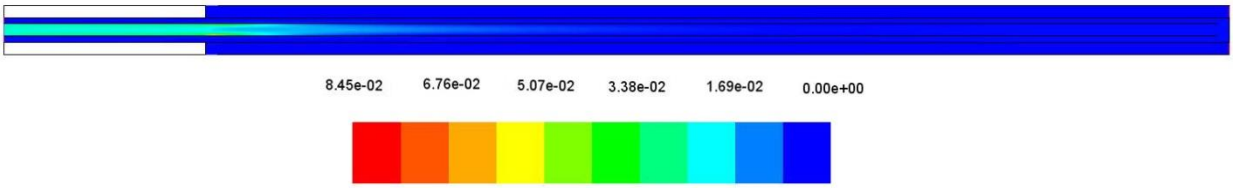

Figure 13. H_2 mass fraction contour along the device for catalyst length of 15mm

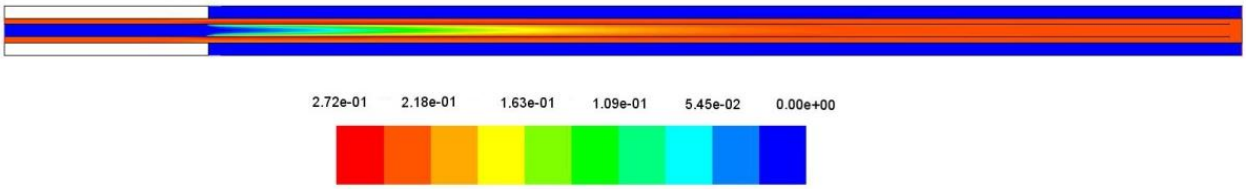

Figure 14. H_2O mass fraction contour along the device for catalyst length of 15mm

***Effect of catalyst location*:** In order to study the effect of catalyst location on the device efficiency, and desired oil and recuperator gas outlet temperatures, three different locations (beginning, middle and end of the 30 mm combustor channel) were considered with catalyst length of 15mm. As Fig. 15 indicates, when the catalyst was shifted to the end of the channel, the efficiency index is increased. For the downstream locations of catalyst bed, a larger fraction of heat was transferred to the oil relative to the heat transferred to preheating the incoming gas mixture. If hydrogen consumption was identical for all three cases, larger oil heat transfer rate implies that that the numerator in Eq. 1 increased for the downstream-located catalysts beds resulting in the observed trend In Fig. 7.

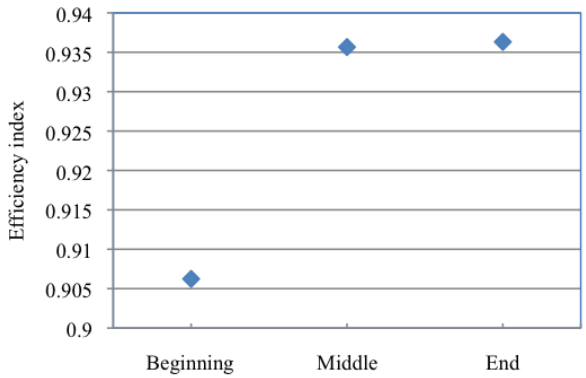

Figure 15. Efficiency index in different catalyst locations

In Fig. 16, the oil and exhaust outlet temperatures are shown as a function of catalyst location. Although efficiency index was higher for catalyst at the end of the channel, the exhaust gases temperature was not what was desired. So there seems to be a balance between the efficiency index and desired outlet oil and exhaust temperatures. In these cases, only catalyst at the beginning of the channel met the requirements of high efficiency and desired exit temperatures of fluid streams.

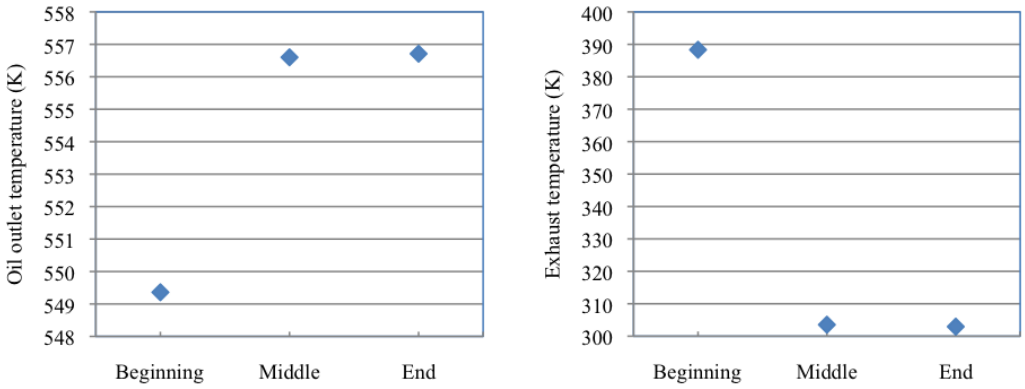

Figure 16. Oil and exhaust outlet temperatures versus catalyst location

***Effect of oil velocity*:** Variation of efficiency index with inlet oil velocity is plotted in Fig. 17. The index decreased with increasing the oil velocity and that was because of a decrease in outlet oil temperature. Although a decrease in oil temperature was accompanied with an increase in oil mass flow rate, variation in temperature with mass flow rate was non-linear (see Fig. 18a) resulting in the noted change in efficiency index. Two catalyst lengths are shown in these figures (15mm and 20mm). As mentioned before, the efficiency index for the larger length was more than the shorter one; however, the difference between the outlet temperatures of oil as well as the exhaust was small.

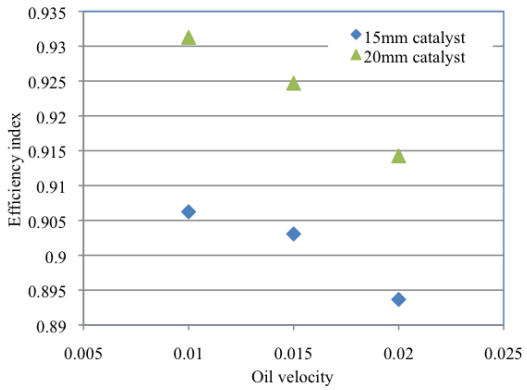

Figure 17. Efficiency index in different inlet oil velocities

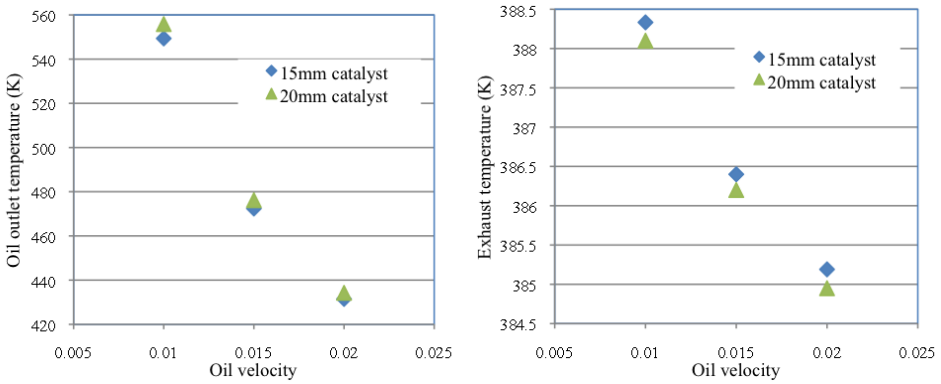

Figure 18. Variation of oil and exhaust outlet temperatures with inlet oil velocity

***Effect of channel size*:** In this parametric study, the catalyst length was kept constant (15mm) and the length of the channels (combustion, recuperator and oil channels) was varied. The oil flow rate was the same for all the following cases (0.01 m/s) and all other boundary conditions were identical to those in previous parametric studies. Efficiency index as a function of channel length is plotted in Fig. 19. A slight increase in the index of about 2 percent is observed for increasing the channel length.

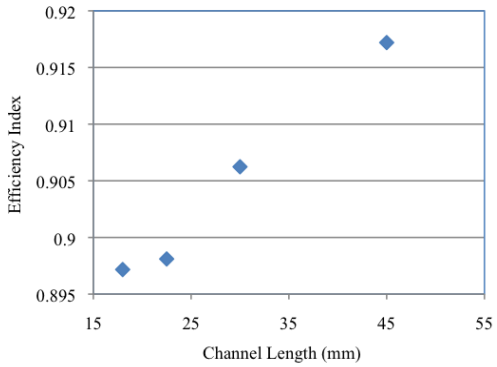

Figure 19. Efficiency index in different channel lengths

Exhaust gas and oil outlet temperatures are presented in Fig. 20. By increasing the length of the channel, there is more surface available to transfer heat from the combustion and recuperator channels to the oil channel so outlet oil temperature (and as a result efficiency) will be higher. On the other hand, more heat is going to be absorbed from the exhaust gases by the inlet gas mixture, therefore exhaust gas temperature will decrease by increasing the channel length. For the set of fixed parameters in this study, the 30 mm long channel meets the requirements of high efficiency combined with the desired outlet temperatures.

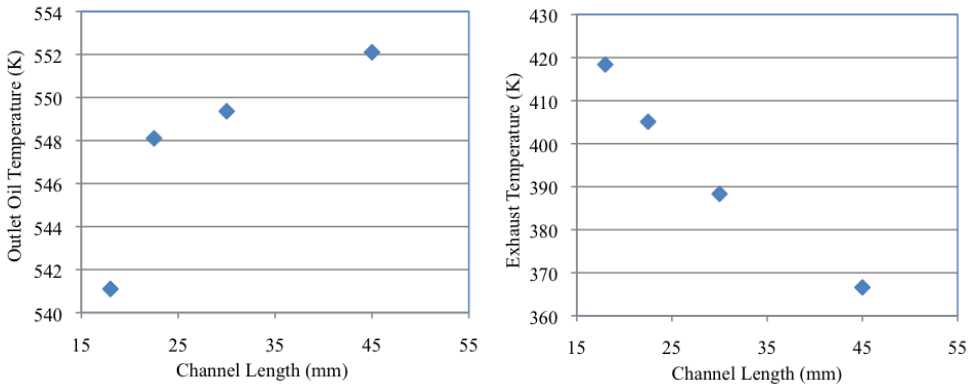

Figure 20. Variation of oil and exhaust outlet temperatures with channel length

***Effect of oil inlet temperature*:** This was a fluid parameter of relevance for the automotive hydrogen storage application. The combustor heat exchanger was used to heat the oil that was then used to desorb hydrogen from the metal hydride in the tank. Desorption is most effective over a narrow range of temperatures. For the case of a sodium alanate, this temperature range was approximately between 160 ^{o}C and 180 ^{o}C. Fig. 21 illustrates the variation of efficiency index with varying oil inlet temperature. In these cases, the oil and gas mixture inlet velocities were 0.01 m/s and 4 m/s, respectively. The figure shows that efficiency does not change appreciably with oil inlet temperature for the fixed parameters of this study.

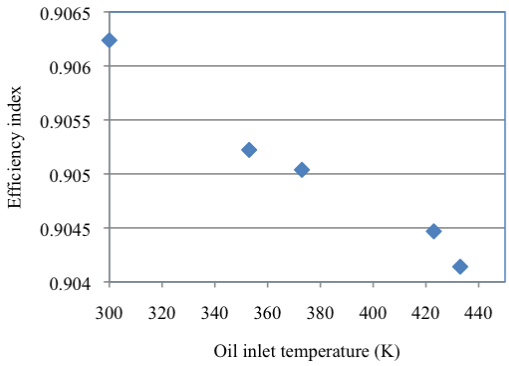

Figure 21. Efficiency index in different oil inlet temperatures

Oil outlet and exhaust gas temperatures are depicted in Fig. 22. An increase in oil outlet temperature with an increase in oil inlet temperature was to be expected since the rate of combusted hydrogen and the mass flow rate of oil remain the same for all oil inlet temperature studies. Note that the film temperature of oil placed a restriction on the higher value of oil exit temperatures. The increase in recuperator exhaust gas temperature with oil inlet temperature as seen in Fig. 22 was related to the decrease in efficiency index with increase in oil inlet temperature, see Fig. 21.

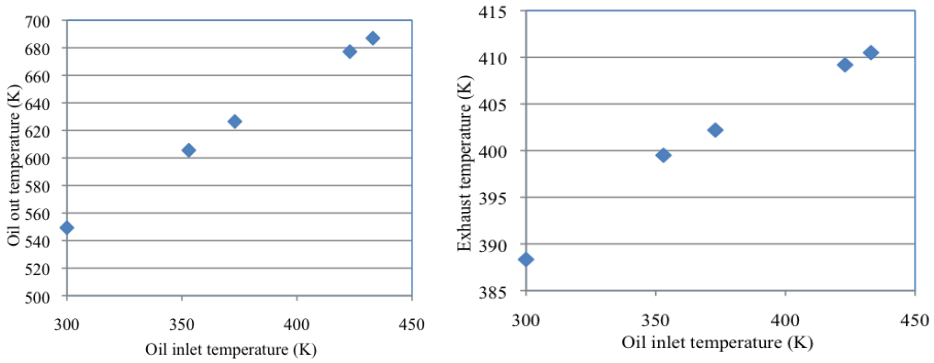

Figure 22. Variation of oil and exhaust outlet temperatures with inlet oil temperature

***Effect of Equivalence Ratio*.** The equivalence ratio, ε, is defined as the ratio of the molar fuel-to-air ratio at the test conditions to that at stoichiometric conditions and it can play an important role in the combustion and performance of a μCHX. Figure 23 shows how efficiency index changes by equivalence ratio.

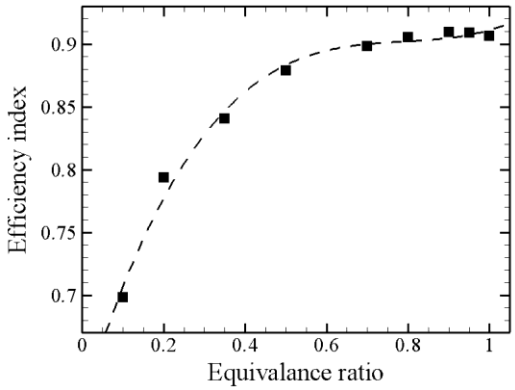

Figure 23. Efficiency index versus equivalence ratio

Parameters held constant for this study are summarized in Table 2. At very lean mixtures, efficiency was low and increased by increasing the equivalence ratio and the change was small for equivalence ratios near one. By increasing the equivalence ratio, more heat was generated and as a result, the oil temperature was higher at higher equivalence ratios. This fact is implied in Figure 24.

Table 2. Test conditions for different equivalence ratios

Parameter	Value
Channel length (mm)	30
Gas mixture inlet velocity (m/s)	4
Oil inlet temperature (K)	300
Oil inlet velocity (m/s)	0.01

Catalyst length (mm)	15
Catalyst location	Beginning
Catalyst	Platinum

In Figure 25, the exhaust temperature is plotted as a function of equivalence ratio. It went up to reach its highest value at equivalence ratios of about 0.4 and came down again. When the exhaust gas temperature was higher, it meant that more heat was lost therefore, efficiency index was lower. But in this case efficiency index was not following the exhaust gas temperature and acted normally. On the other hand, the lower the unconsumed hydrogen, the higher was the efficiency. The ratio of unconsumed hydrogen over total hydrogen input for different equivalence ratios is plotted in the same figure for better understanding. It can be seen that the area with lowest ratio was approximately the same as the area with higher exhaust temperature. Thus these two parameters neutralize their effect on the efficiency index.

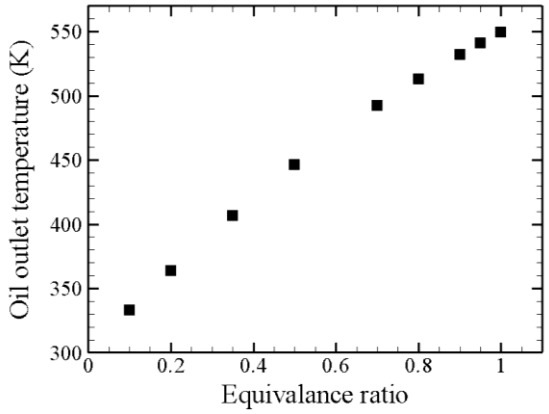

Figure 24. Oil outlet temperature as a function of equivalence ratio.

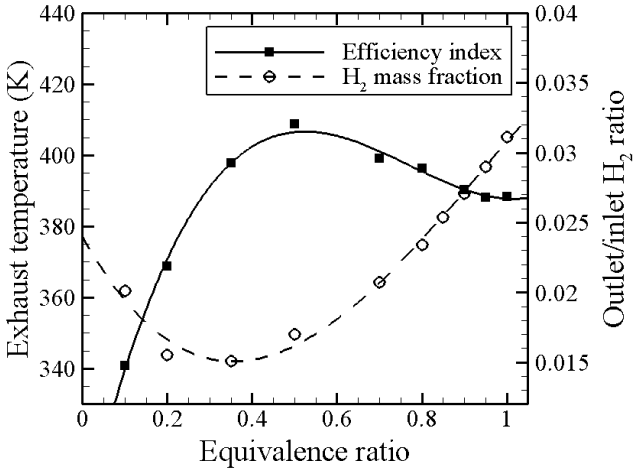

Figure 25. Exhaust temperature and hydrogen outlet/inlet ratio

***Effect of Combustion Channel Height*.** Changing the combustion channel height influences the results both chemically and physically. For larger channel heights, physical diffusion of species to channel walls could result in a lower completion rate of the reaction. However, as shown in Figure 26, pressure drop was lower in wider channels. Table 3 shows the test conditions of this section where the mass rate of hydrogen flowing into the channel was the same for all different channel heights. It can be seen that by decreasing the channel height, the efficiency index increased which is a result of both better heat transfer and greater conversion rate. Considering efficiency index and pressure drop simultaneously, it can be concluded that channel with the height of 200 µm is the most appropriate channel.

Table 3. Test conditions for different combustion channel heights

Parameter	Value
Oil inlet velocity (m/s)	0.01
Channel length (mm)	30
Equivalence ratio	1
Oil inlet temperature (K)	300
Catalyst length (mm)	15
Catalyst location	Beginning
Catalyst	Platinum

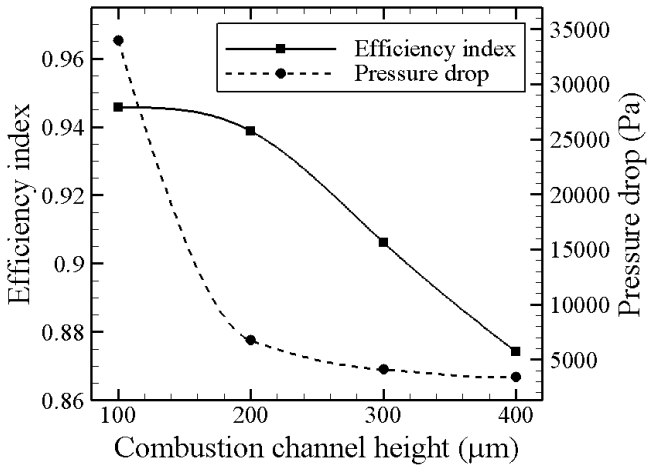

Figure 26. Efficiency index and Pressure drop at different channel heights

As shown on Figure 27, because of higher heat transfer rate, oil outlet temperature was higher for smaller channels. It can be seen that for the case of 100 µm, exhaust temperature decreased to 372K which was below the condensation temperature of water vapor; this temperature was not desired for the system and water should come out of the system in vapor.

***Catalyst effects*.** In all of the previous results shown, platinum was used as the catalyst. Here the performance of palladium was compared to platinum. The mechanism files of hydrogen combustion on palladium were imported to Fluent in Chemkin format. The same model with the catalyst surface length of 15mm (test conditions are shown in Table 4) was modeled and the results are shown and compared in Table 5 for both platinum and palladium catalysts. It can be seen that combustion proceeds to a greater degree of completion with platinum as compared with palladium with an increase in efficiency index of about 3 percent. Whereas platinum is a more active catalyst, the increase in the efficiency index as compared with the significant increased cost of Pt should be considered in choosing a the catalyst for practical applications.

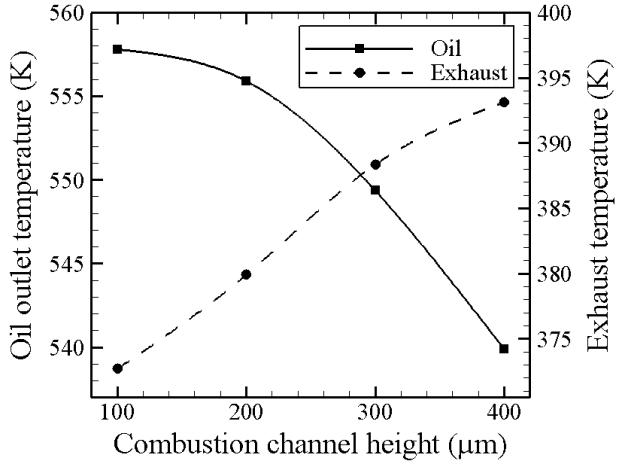

Figure 27. Variation of Exhaust and oil outlet temperature by channel heights

Table 4. Test conditions for different catalysts

Parameter	Value
L (mm)	30
Gas mixture inlet velocity (m/s)	4
Inlet oil velocity (m/s)	0.01
Equivalence ratio (ϕ)	1
Oil inlet temperature (K)	300
Catalyst length (mm)	15
Catalyst location	Beginning

Table 5. Comparison between platinum and palladium performance

catalyst	Oil outlet temperature (K)	Exhaust temperature (K)	Uncombusted H_2 (mass fraction)	Efficiency index
Platinum	559.8	464.2	4.00E-06	0.906
Palladium	550.9	394.7	6.30E-04	0.874

***Wall conduction effects*:** When the wall is thermally thin, there is no axial conduction along the wall. The heat that is produced in the upstream section of the catalyst increases the bulk temperature of combustion gases; as a result, the reaction rate increases thereby producing more heat. Therefore the temperature keeps rising until the mole fraction of hydrogen decreases. When wall thickness is considered, conduction through the wall transfers heat from the hot region and provides a more uniform temperature distribution.

Results from simulations for two similar cases, with and without consideration for wall conduction, are summarized in Figure 28 and Table 6. In both cases, 15 mm of the combustor wall was coated with platinum catalyst. It should be noted that although wall conduction provided better temperature distribution along the channel, the efficiency was lower for the case with wall thicknesses.

Table 6. Summary of the results for cases with and without considering wall thickness

	inlet gas velocity (m/s)	inlet oil velocity (m/s)	inlet gas and oil temperature (K)	catalyst length (mm)	outlet oil temperature (K)	Exhaust temperature (K)	hydrogen mass fraction at the outlet	Efficiency
No wall thickness	4	0.01	300	15	551.6	390.6	0.0006	93.7%
With wall thickness	4	0.01	300	15	548.1	382.9	0.0012	91.2%

Axial conduction along the wall distributes heat over a larger area, causing a decrease in temperature at the catalyst. A decrease in temperature at the catalyst site resulted in a decrease in reaction rates. The highest catalyst wall temperature was 820 K for the case with wall conduction while it was 1018 K for the other one. The lower catalyst temperature was manifested as a decrease in the amount of hydrogen combusted.

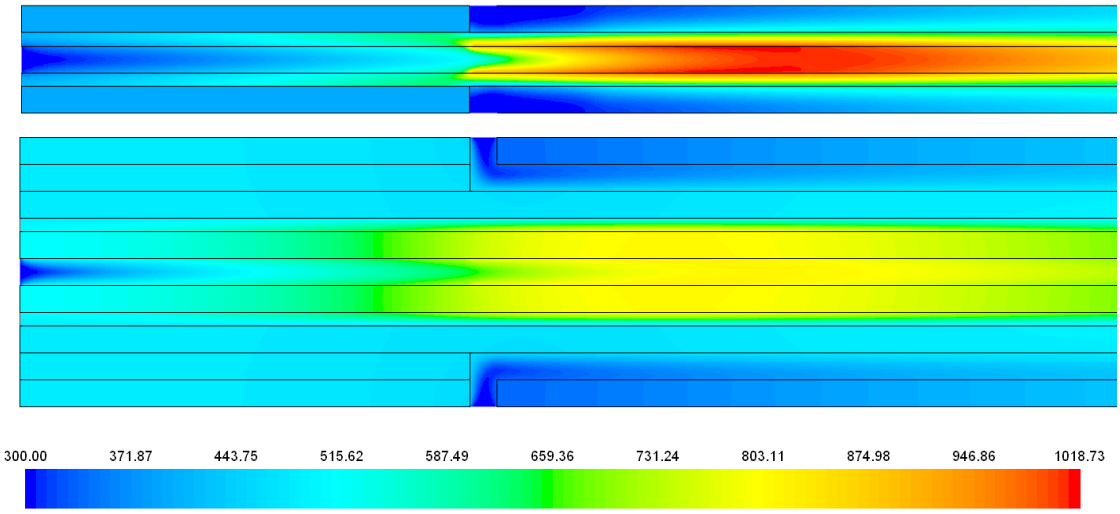

Figure 28. Temperature contours for two cases, without wall (top) and with wall thickness (down)

***Potential to use Aluminum as opposed to stainless steel for the μ-CHX*:** All simulations performed up to this point were based on stainless steel as the material for the μ-CHX. High weight of steel led to investigating the possibility of using a lighter material. Aluminum is a great choice because of its light weight (~1/3 weight of steel) and high thermal conductivity (5 times higher than steel) as well as good fabrication conditions. The main problem was low melting point of aluminum compared to steel. In the simulations with stainless steel, wall temperatures of up to 800 ^{o}C were observed, Aluminum (series 3000) should operate below 500 ^{o}C. A comparative study between the performance of a stainless steel and an aluminum μ-CHX for the working conditions presented in Table 7 was undertaken. For this comparison, the catalyst was distributed in segments along the combustor channel to prevent the wall temperatures from getting above 500 ^{o}C for the aluminum combustor. The distribution and segment lengths are provided in Table 8. Both stainless steel and aluminum combustors have the same distribution of catalyst.

Results of the comparison are shown in Fig. 29, which shows the axial variation in combustion gas temperatures at the centerline of the channel. Since the channel was of microscale dimensions, this temperature was indicative of the axial wall temperature variation as well. Spikes in temperature, corresponding to locations of catalyst on the wall, can be observed for both aluminum and stainless steel combustors. It was seen that the maximum temperature reached in the steel combustor was greater than that in the aluminum combustor. Also, the temperature profile for the aluminum combustor was relatively flat compared to the stainless steel combustor profile. Both these observations may be attributed to larger axial wall conduction in aluminum. While the lower temperature was desirable from a functional standpoint of use of aluminum, the lower temperature causes lower reaction rates; therefore less hydrogen combusts in the channel that made the aluminum device less efficient. For example in these cases, the efficiency of steel μ-CHX is 93.4 percent and the efficiency of aluminum μ-CHX is 89.3 percent. However, the reduction in efficiency is quite insignificant and well justifies use

of aluminum as the material for the combustor. By properly tuning the spacing of the catalyst segments, higher efficiencies can be attained.

Table 7. Test conditions for steel and aluminum μ-CHX

Parameter	Value
L (mm)	30
$H_{Cumbustor,\ Oil}$ (μm)	300
H_{Walls} (μm)	300
Oil inlet velocity (m/s)	0.22
Gas mixture inlet velocity (m/s)	3
Equivalence ratio	1
Catalyst length (mm)	14.9
Oil inlet temperature (K)	300
Catalyst	Pt

Table 8. Distribution and length of catalyst segments

C=catalyst, N=no catalyst	N	C	N	C	N	C	N	C	N	C	N	C	N	C
length (mm)	6	0.2	0.9	0.2	0.9	0.2	0.9	0.2	0.9	0.5	2	1	1	15

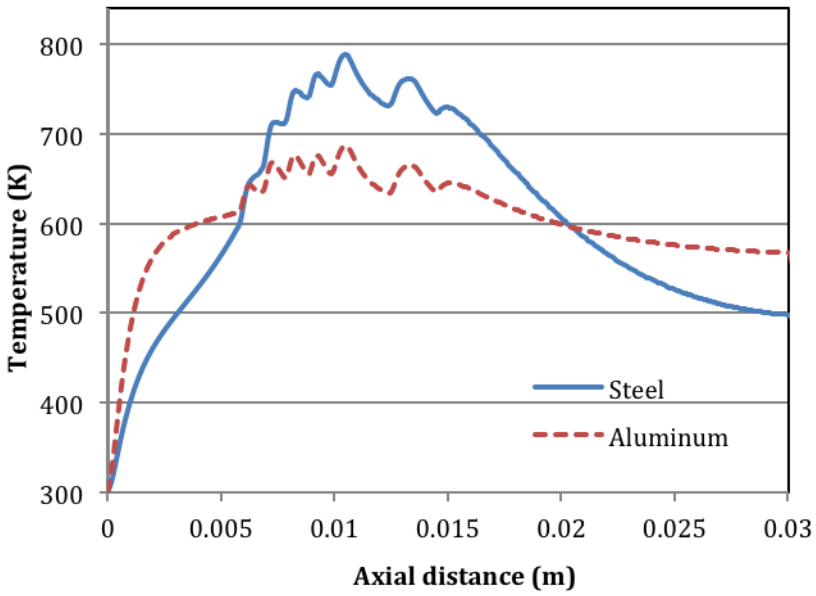

Figure 29. Temperature of the combustion gasses along the channel for both steel and aluminum

***Effect of variations in catalyst distribution on combustor walls*:** Segmented catalyst plays two important roles: First, one can control the temperatures inside the combustion chamber by properly selecting the number of segments, size of segments and spacing between segments. Second, reduction in catalyst usage can be realized.

Figure 30 illustrates the temperature contours in a µ-CHX with catalyst segments. In this case, the gas and oil inlet temperature is 300 K. The inlet velocity of gas and oil was 4 m/s and 0.01 m/s, respectively.

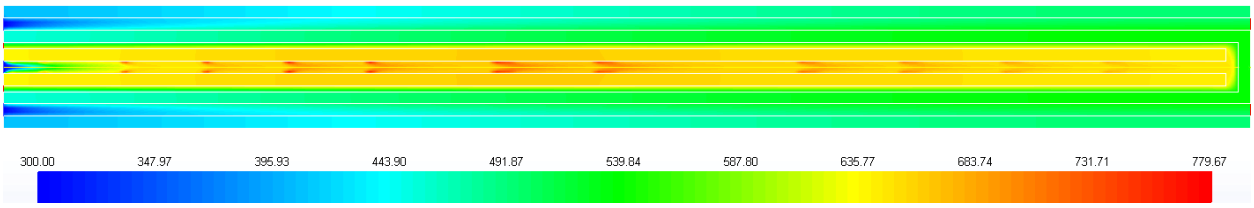

Figure 30. Temperature distribution of the aluminum µ-CHX

A wide range of segment lengths (from 0.1 mm to 10 mm) as well as segment locations were investigated. Different catalyst configurations were considered here and are summarized in Table 9. Centerline temperature of combustion gases as well as hydrogen mass fraction is plotted in Figs. 31 and 32.

Table 9. Summary of geometrical and thermo-fluidic parameters of three different cases

	Total catalyst length (mm)	Inlet oil velocity (m/s)	Inlet gas velocity (m/s)	Inlet oil temperature (K)	Outlet oil temperature (K)	Outlet hydrogen mass fraction	Efficiency	Highest temperature (K)
Case 1	17.3	0.22	3	438	448.1	0.0013	89.30%	733
Case 2	14.9	0.22	3	438	447.3	0.0011	89.30%	760
Case 3	13.2	0.22	3	438	447.3	0.0011	89.10%	768

The efficiencies for all these cases were about the same while their total catalyst lengths were different. Case 1 had a lower and more uniform temperature distribution. Although the total catalyst coated length was higher in case 1, less hydrogen was combusted. To avoid this, in two other cases the segments were placed closer together allowing the combustor to reach higher temperatures. For example case 3 had a total catalyst length of 13.2 mm and combusted the same amount of hydrogen while keeping the temperature below 500 ^{o}C. Steeper drop in hydrogen mass fraction was a sign of higher reaction rates and therefore higher temperatures. Thus, there needs to be a compromise between maintaining higher temperatures in order to increase combusted hydrogen, and maintaining temperatures within material operability limits.

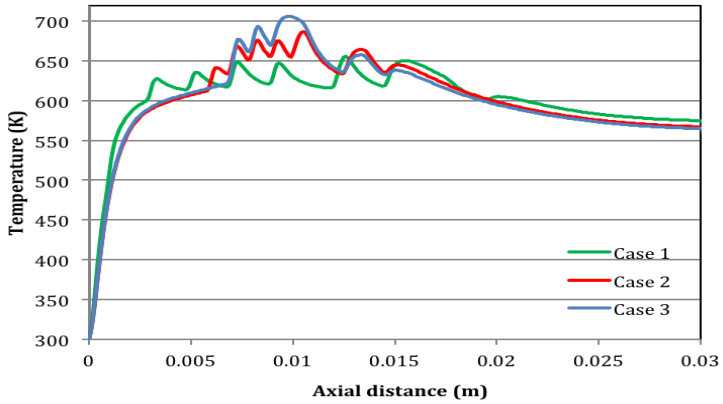

Figure 31. Combustion channel's centerline temperature along the channel

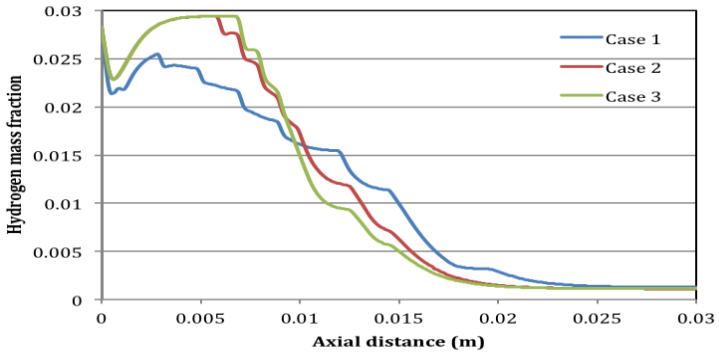

Figure 32. Combustion channel's centerline hydrogen mass fraction along the channel

Full Size Combustor Design: A full scale designs of the μ-CHX was developed based on the results of the FLUENT model. A 12 kW combustor and a 30 kW combustor have been designed in order to determine the size, weight and cost of full size combustors. The 12 kW combustor is shown in Fig. 33. The combustor designs shown are only of the parts that are to be diffusion bonded together..

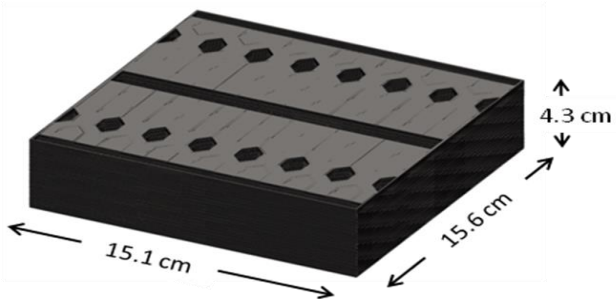

Figure 33. 12 kW Combustor Preliminary Design

The primary challenge that arose in the development of this design was in distribution of the fluid streams to the individual unit cells. A complex fluid header system was required. The headers were designed while seeking to minimize pressure losses. As a preliminary approach, the design sought to maintain constant fluid velocity through all

the headers. In effect, they were designed to maintain a constant flow area. For example, if a single header is feeding 10 channels, then the cross-sectional area of the header was designed to be 10 times greater than the cross-sectional area of the channel. Multiple headers designs were considered in order to select a design that minimized the volume and weight of the combustor. An Excel worksheet was developed in which the number of unit cells in width, length and height could be varied in order to determine the overall size of the combustor. Circular, oval, rectangular and triangular header shapes were considered before arriving at the selected design. Hexagonal headers were used for the combustion gases and pentagonal headers are used for the exhaust gases. The oil inlets and outlets were rectangular in shape. The cooler oil flowed in from the outside of the combustor while the hot oil flowed up and out through a central, rectangular header to minimize heat losses. This design best balanced the size of the combustor with manufacturability and flow distribution. An exploded view of a single “stack” of shims is shown in Fig. 34. A “stack” refers to a set of shims that is one unit cell in height. The 12 kW combustor design is 2 unit cells in length, 14 units in width and 20 units in height for a total of 560 unit cells.

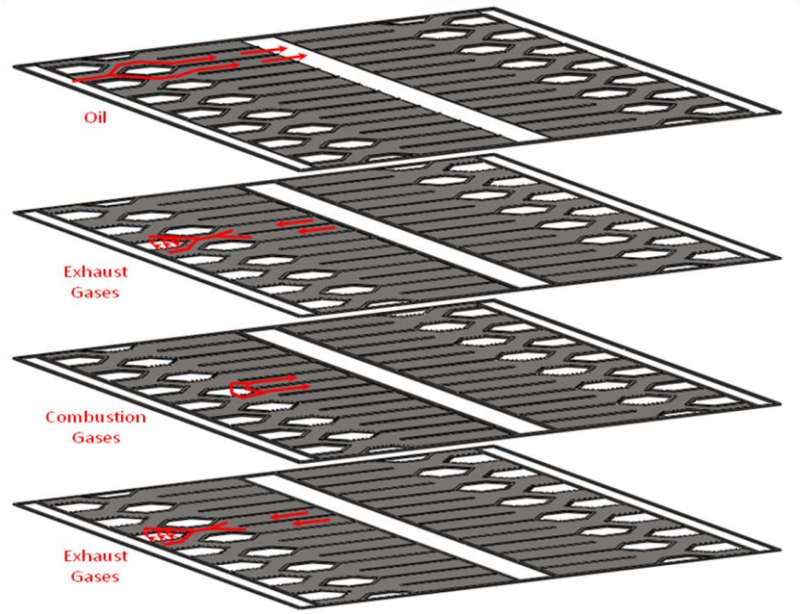

Figure 34. Exploded View of a Single Stack of Shims

The 30 kW combustor was designed in the same manner as the 12 kW combustor with the difference being that the overall size of the device was larger due to the increased number of unit cells. It was assumed that 316 stainless steel would be the material for both devices and the weight was calculated accordingly. A comparison between the 12 kW and 30 kW described is shown in Table 10, along with the 30 kW Sandia combustor design. Using aluminum instead of the stainless steel was explored in to reduce the weight of the device further. Aluminum has a density of 2.7 g/cc compared to 8 g/cc for the stainless steel. Implementing this change was expected to significantly reduce the weight of the combustor. However, aluminum has a lower melting point than the steel, so further investigation was required in order to confirm the material compatibility.

Preliminary results from detailed modeling presented above indicated that that by suitably locating segmented catalysts along the combustor walls, the temperature within the combustor can be kept within the operability limits for aluminum.

Table 10. Full Size Combustor Comparison

	12 kW OSU	30 kW OSU	30 kW Sandia
Width (cm)	15.1	22.2	32.0
Length (cm)	15.6	21.1	38.1
Height (cm)	4.3	7.9	29.7
Volume (L)	1.0	3.7	36.2
316 SS Weight (kg)	3.76	11.74	Unknown

First Generation μ-CHX Experiments: Using the test apparatus and test articles described above data was collected during the entire course of each trial in order to determine when steady state operation was reached. For the first trial, steady state data was collected for almost 60 minutes to demonstrate stability. Some of the most important measurements for the efficiency calculation and energy balance were the oil outlet temperature, oil flow rate and gas outlet temperatures. These are shown in Figure 35.

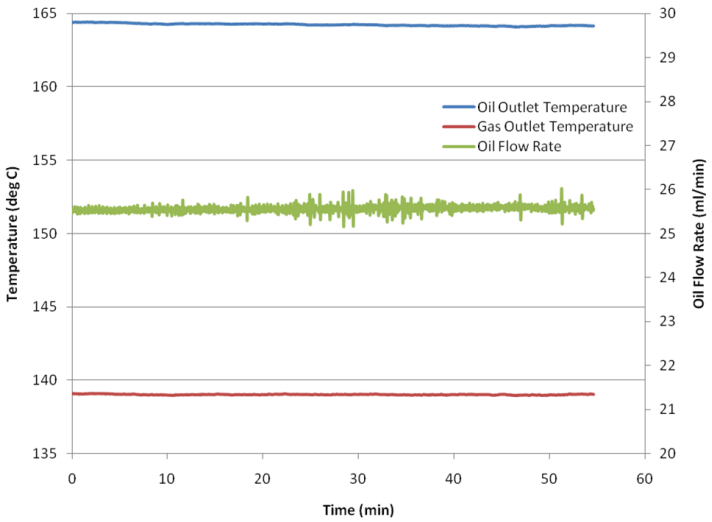

Figure 35 Key temperatures as a function of Time

The temperature profile along the combustion channel was obtained at steady state. The results from two trials at the same operating conditions are shown in Figure3 6, demonstrating the repeatability of the experiment. The higher temperatures near the beginning of the channel indicated that the combustion reaction may be greater there than at the end of channel. If this is the case, then the catalyst near the end of the

channel is not needed.

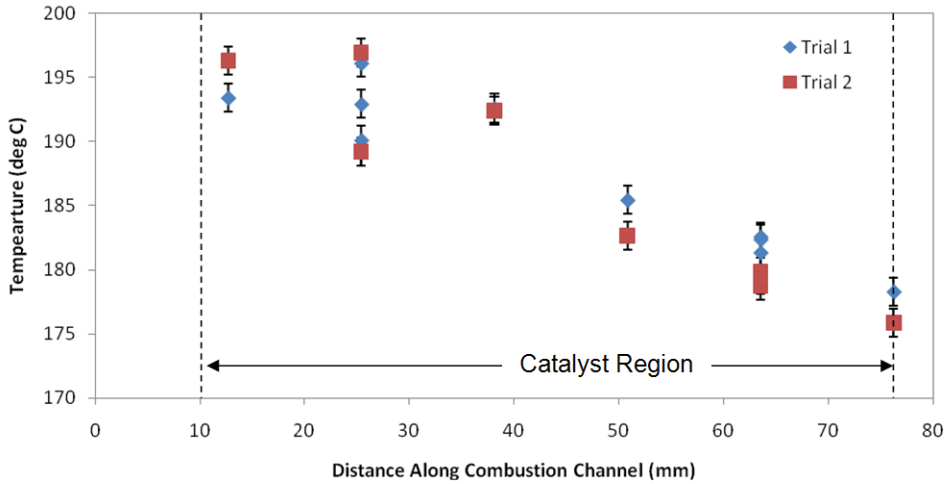

Figure 36. Steady State Combustion Channel Temperature Profiles

The geometric and fluidic parameters of the combustor for these trials are shown in Tables 11 and 12, respectively. The uncertainty for most of the parameters was quantified for a complete uncertainty analysis. The design and manufacturing of the μ-CHX and experimental facility resulted in low uncertainties for the majority of the parameters. Only the oil channel height could not be accurately measured because it was an indirect measurement based on multiple stacked components. However, this inaccuracy only impacts the uncertainty of the oil velocity, not any of the performance parameters. The uncertainties of calculated parameters were determined by following the Kline & McClintock method.

Table 11. Geometric Parameters of the μ-CHX for Trials 1 and 2

	Size (mm)	Uncertainty (mm)	% Uncertainty
Catalyst Length	66.040		
Combustion Channel Height	0.250	0.005	2.0%
Channel Width	38.100		
Comb/Recup SS Thickness	0.255	0.005	1.8%
Recup. Channel Height	0.128	0.004	3.0%
Recup/Oil SS Thickness	1.859	0.039	2.1%
Oil Channel Height	0.707	0.157	22.2%

Table 12. Fluidic Parameters of the μ-CHX for Trials 1 and 2

	Parameter	Uncertainty	% Uncertainty
Total Gas Flow Rate (sccm)	2704.03	20.71	0.8%
Equivalence Ratio	1.00	0.01	1.4%
Comb. Gas Velocity (m/s)	4.73	0.10	2.2%
Recup. Gas Velocity (m/s)	9.21	0.29	3.1%
Inlet Oil Velocity (mm/s)	15.8	3.5	22.3%
Residence Time over Pt (ms)	14.0	0.3	2.2%

The μ-CHX performance for Trials 1 and 2 are shown in Table 13. Efficiencies around 93% were obtained for both trials with low uncertainty. The efficiency was defined here as the ratio of heat gained by the oil, relative to the amount of heat rate available from combustion,

$$\varepsilon = \frac{Q_{oil}}{Q_{H_2}} \tag{2}$$

where the heat transferred to oil was determined using the sensible energy transfer rate equation,

$$\dot{Q}_{oil} = \dot{m}_{oil}\left(T_{oil,e}c_p\big|_{T_{oil,e}} - T_{oil,i}c_p\big|_{T_{oil,i}}\right) \tag{3}$$

and the available heat rate from combustion was determined using the lower heating value,

$$\dot{Q}_{H_2} = \rho_{H_2}\big|_{0°C,1atm}\dot{V}_{H_2}q_{H_2,LHV} \tag{4}$$

An energy balance performed on the gas stream indicated the change of energy between the inlet and outlet of the gas stream,

$$\dot{Q}_{Gas} = \left(\dot{n}_{H_2}\bar{h}_{H_2} + \dot{n}_{air}\bar{h}_{air}\right)_{inlet} - \left(\dot{n}_{H_2O}\bar{h}_{H_2O} + \dot{n}_{H_2}\bar{h}_{H_2} + \dot{n}_{O_2}\bar{h}_{O_2} + \dot{n}_{N_2}\bar{h}_{N_2}\right)_{outlet} \tag{5}$$

This balance was determined only using inlet gas composition, the gas inlet temperature and the gas outlet temperature. The major assumption in this calculation was that the hydrogen was fully combusted and that the air consisted of 79% N_2 and 21% O_2. The assumption of completely combusted hydrogen was reasonable, both because hydrogen was not detected with the gas leak detector and because the energy balance quantity was reasonable. If there was any uncombusted hydrogen, it was probably a small amount. Based on these calculations, estimations of the heat losses can be obtained. The difference between the H_2 energy input and the gas energy balance indicated the amount of energy lost to the exhaust gas. In essence, this was the heat carried away in the hot exhaust gas. The difference between the gas energy balance and the energy gained by the oil indicated the conduction heat losses through the insulation and fittings on the μ-CHX. Both of these heat loss terms were minor, as was expected due to the high efficiency of these trials.

A parametric study on the μ-CHX was then performed. For all experiments presented herein, the catalyst shim was covered by platinum using a wet deposition method. In this method, the desired surface area of the shim was electrochemically etched and then a platinum compound is deposited, finally by calcining at high temperatures the platinum surface sites were activated. The method was described above.

Table 13. Performance Results

	Trial 1		Trial 2		
	Value	**Uncertainty**	**Value**	**Uncertainty**	**Average**
Gas Side Pressure Drop (kPa)	37.56	0.15	37.56	0.15	37.56
Oil Side Pressure Drop (Pa)	355.42	20.8	365.35	21.0	360.39
H2 Energy Input (W)	143.8	1.4	143.8	1.4	143.8
Gas Energy Balance (W)	137.4	1.4	137.7	1.4	137.6
Oil Energy Gained (W)	133.5	1.0	134.7	1.2	134.1
Energy Lost to Exhaust (W)	6.3	2.0	6.0	2.0	6.2
Energy Lost to Environment (W)	4.0	1.8	3.0	1.8	3.5
Efficiency Index	**92.8%**	**1.3%**	**93.7%**	**1.3%**	**93.3%**

The performance of the µ-CHX was characterized for variations in equivalence ratio, residence time and oil flow rate. The above parametric variations were performed using catalyst shim A, which had a larger length (surface area) covered with catalyst. Residence time experiments were also performed on shim B. The 77 percent shorter catalyst length of shim B (15.2 mm for shim B compared to 66.0 mm for shim A) allowed for shorter residence times to be obtained with shim B than with shim A. However, varying the catalyst length not only changed the residence time, but also the heat generation rate per unit residence time. A comparison of similar residence times between catalyst shims A and B, indicative of the effect of variation in catalyst length, on the efficiency of the µCHX is also provided.

The stability of catalyst shims A and B were demonstrated by initial tests and tests after approximately 80 and 40 hours of operation, respectively. The efficiency of the device using shim A was essentially identical after 80 hours of testing, while the efficiency of shim B was reduced by 0.8 percent, which was well within the uncertainty of efficiency measurements of 3.2 percent.

Residence time effect: The performance of the µCHX with catalyst shim A was investigated for various residence times. The typical outlet oil temperature for these experiments was 150 °C, resulting in an average oil temperature of 85 °C. The equivalence ratio was kept constant at unity. The performance is characterized based on efficiency and on hydrogen conversion, the latter helping to indicate a source of the reduced efficiency. The efficiency of the µCHX was found to decrease linearly as the residence time increased, as shown in Fig. 37. The available heat from combustion also

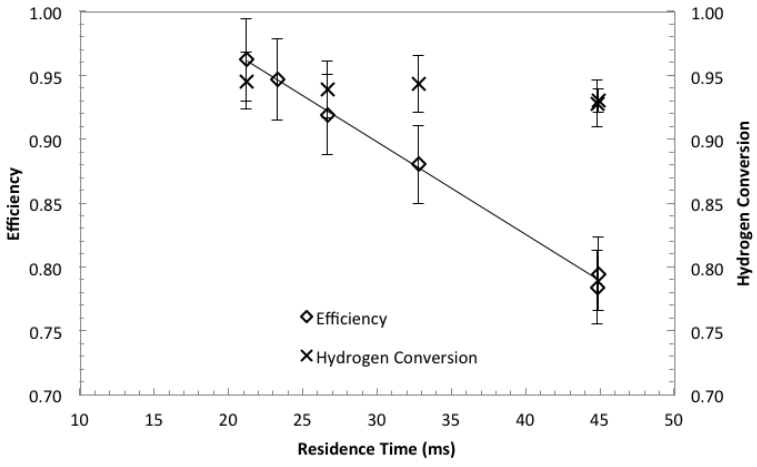

Fig. 37. µCHX performance for residence time variation experiments with catalyst shim A

decreased with residence time because the total gas flow rate had to be reduced, causing a correspondingly lower H_2 flow rate, in order to obtain higher residence times. The hydrogen conversion efficiency was measured to be 93 – 96%, with no significant variation with residence time. Higher residence times provided more time for the gases to react on the catalyst. The high hydrogen conversion rates indicate that the combustion reaction was not residence time limited over the range of residence times tested.

The centerline combustor temperature profiles measured along the combustion channel are shown in Fig. 38a, along with a schematic of the µCHX with catalyst shim A in Fig. 38b for reference. The temperatures shown were obtained from the thermocouples along the centerline of the combustion channel. These temperatures were measured in the stainless steel base about 1 mm below the combustion channel and are therefore only indicative combustion temperatures.

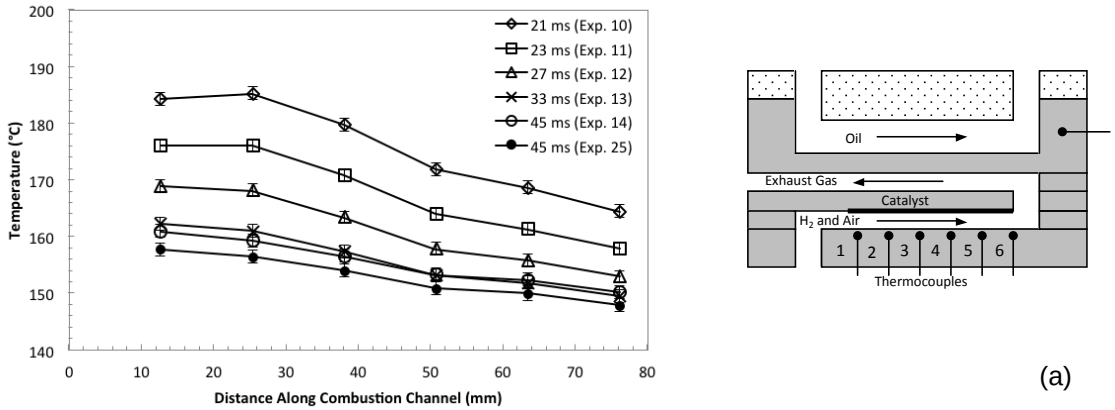

Fig. 38. Centerline combustor channel wall temperatures for combustor with shim A (a) temperature profiles, (b) schematic indicating location of thermocouples.

Higher temperatures along the combustor length were measured for the experiments that operated at lower residence times. Greater heat release rates occur at the lower residence times due to the higher H_2 flow rate, causing higher temperatures in the combustion channel. The higher efficiencies obtained correspond to the higher measured temperatures along the combustion channel, for which there is a larger driving potential for heat transfer to oil. A simplified one-dimensional resistance model with parallel paths for heat to flow from the combustor to the oil and heat loss through the insulation was developed. This model indicated that higher temperatures in the combustion channel resulted in a greater portion of the generated heat being transferred to the oil than being lost through the insulation. In essence, the µCHX is heat transfer limited at longer residence times.

Performance tests were conducted on the µCHX with catalyst shim B while varying the residence time of the gases over the catalyst. The shorter catalyst length of shim B allowed for shorter residence times to be tested than with shim B. These experiments

were all conducted at an average oil temperature of 85 °C and at an equivalence ratio of unity. The sole exception was the experiment at 20 ms, which operated at 83.5 °C due to difficulty achieving a high enough outlet oil temperature. Longer residence times were found to lead to increased efficiencies until about 7 ms. Lower efficiencies were obtained for residence times longer than around 7 ms. The highest efficiencies around 75 percent were obtained at residence times between 6 and 11 milliseconds. Hydrogen conversion tended to increase with longer residence times, with a maximum hydrogen conversion of 92.4 percent at a residence time of 13.9 ms.

The increase in efficiencies and hydrogen conversion for increased residence times indicated that the reaction was residence time limited until about 14 ms. The decreasing efficiencies at residence times longer than 7 ms suggest that heat transfer limitations reduced the performance beyond 7 ms. In the same manner as the residence time experiments with shim A, longer residence times were obtained by reducing the flow rate of H_2 and air. Reduction in heat generation rate also reduced the temperatures along the combustor channel, thereby reducing the driving potential for heat to the oil.

Catalyst length effect: Examining performance impact for varied catalyst lengths is important in order to minimize the amount of catalyst required. The performance of the µCHX was investigated for shims A and B. Three experiments were conducted that compare the effects of varying catalyst length and are listed in Table 14. Experiments 1 and 2 are compared on the basis of similar hydrogen heat input while experiments 1 and 3 are compared on the basis of similar residence time.

Table 14. Performance comparison for varying catalyst length

Exp.	Shim	l_{cat} (mm)	$\frac{l_{cat}}{L_{chan}}$	Φ	H_2 Heat Input (W)	t_{res}	Avg. T_{oil} (°C)	H_2 Conversion (%)	□ (%)
1	A	66.0	0.87	1	144	21	85.9	96.2	96.2
2	B	15.2	0.20	1	144	4.9	85.3	87.6	67.8
3	B	15.2	0.20	1	24	20	83.5	91.2	45.9

First, the variation of catalyst length were considered for constant H_2 heat input. Efficiency and H_2 conversion were both higher for the longer catalyst length of exp. 1, compared to exp. 2. The residence time was also higher for experiment 1, allowing more time for the combustion reaction to occur and resulting in higher H_2 conversion, which in turn contributes to the observed increase in efficiency of experiment 1. Also, the temperature profile of exp. 1 is 11 °C higher over the whole channel than the temperature profile of exp. 2, which increased the driving potential for heat transfer to oil, which contributed to a higher efficiency.

Experiments 1 and 3 in Table 14 were compared on the basis of similar residence time. Both experiments operated with high H_2 conversions of 96.2 and 91.2 percent, respectively. However, the combustion channel temperatures were much lower for exp. 3 due to the smaller H_2 heat input. The substantially lower combustion channel

temperatures contributed to decreased efficiency due to a decreased driving potential for heat transfer to oil, causing a greater portion of the heat released from combustion to be lost through the insulation. Further investigation is needed with additional catalyst lengths in order to better characterize the effects of catalyst length on the performance of the combustor.

Equivalence ratio effect: The performance of the µCHX with catalyst shim A was tested for equivalence ratios between 0.3 and 1. The performance results are shown in Fig. 39. For these tests the combined flow rate of air and H_2 was maintained at 2700 sccm, resulting in residence times between 19 and 22 ms. The slight variation in residence time was due to the differences in pressure and temperature at the inlet between experiments. The average temperature of the oil was maintained around 85 °C for the variation of equivalence ratio tests.

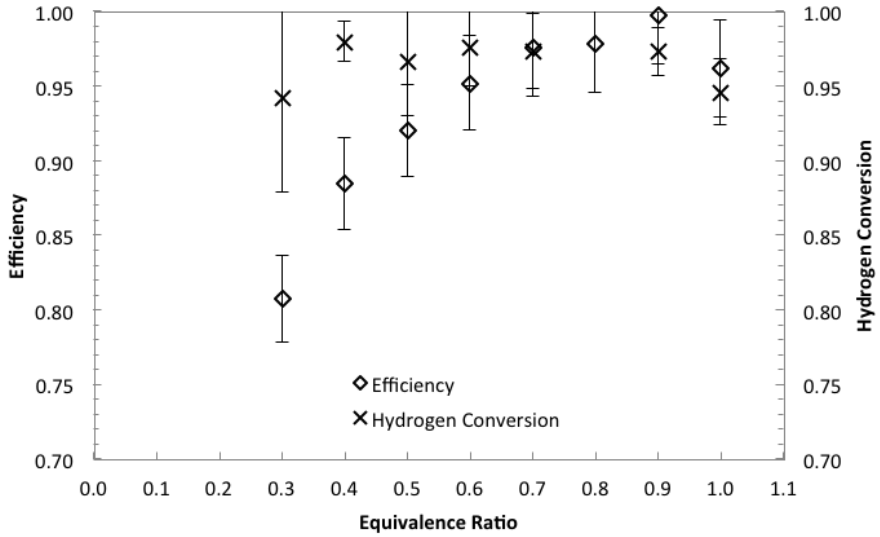

Fig. 39. µCHX performance for equivalence ratio variation experiments with catalyst shim A

Increasing efficiencies were obtained for increasing equivalence ratios and the highest efficiencies were obtained for equivalence ratios between 0.7 and 0.9. Both efficiency and hydrogen conversion were lower at the stoichiometric equivalence ratio, indicating that a slightly lean mixture facilitates maximum conversion of H_2. While the 99.7 percent efficiency obtained with an equivalence ratio of 0.9 is unreasonably high, the uncertainty range of ±3.2% accounts for a lower, more reasonable performance. Hydrogen conversion from the 0.8 equivalence ratio test was not determined because the GC was not available in the timeframe required for analyzing that particular exhaust gas sample. The hydrogen conversion for all other equivalence ratios was measured to be around 95 percent, supporting the conclusion that the performance of the µCHX is not residence time limited at residence times around 20 ms. While there appears to be a slight reduction in hydrogen conversion at leaner equivalence ratios, the variation is well within the uncertainty.

Temperature profiles for the variation of equivalence ratio tests are shown in Fig. 40; as a reference. The outlet oil temperature was maintained near 150 °C for all these tests in order to obtain the desired 85 °C average oil temperature. The magnitude of the temperature profiles tended to decrease with lower equivalence ratios. This was expected due to the lower hydrogen heat input at the lower equivalence ratios. However, different behavior occurred at equivalence ratios near unity; the temperature profiles were nearly identical, despite the different H_2 flow rates and equivalence ratios. The lower H_2 conversion at the stoichiometric equivalence ratio caused the actual heat release rate to be more similar to the 0.9 equivalence ratio experiment, resulting in similar combustion channel temperature profiles. The trend of decreasing efficiency with lean equivalence ratio of Fig. 6 was attributed to the lower driving potential for heat transfer to oil as well as to the increased amount of energy carried away by excess air.

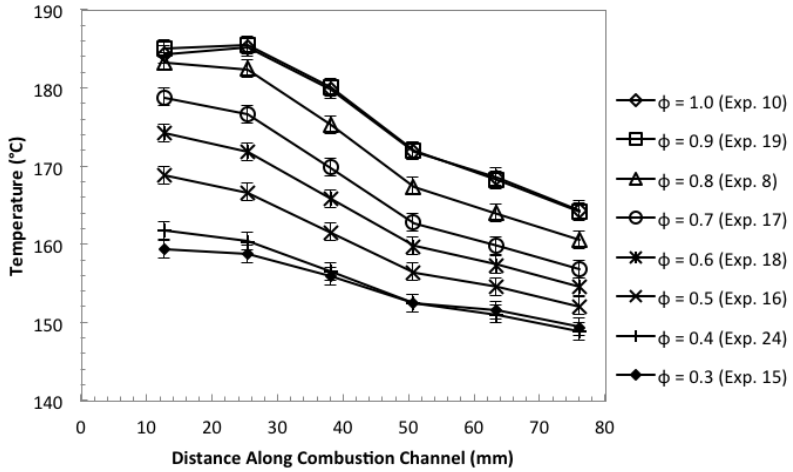

Fig. 40. Axial combustor temperature profiles for equivalence ratio variation experiments with catalyst shim A

Average oil temperature effect: The performance of the µCHX with shim A was investigated at various average oil temperatures. Residence time and equivalence ratio were fixed around 21 ms and 1, respectively. The efficiency results with varying average oil temperatures from these tests are shown in Fig.41, following page. For these experiments, the oil flow rate was adjusted until the desired average oil temperature was achieved. The full temperature range possible with the current experimental setup was investigated. For the fixed oil inlet temperature around 20 °C that was tested, average oil temperatures less than about 63 °C were found to result in exhaust gas temperatures below 100 °C. This was considered undesirable because it would allow the water vapor in the exhaust to condense inside the µCHX. Oil temperatures above 105 °C would cause the outlet oil temperature to exceed the 204 °C temperature limit of the PFA tubing.

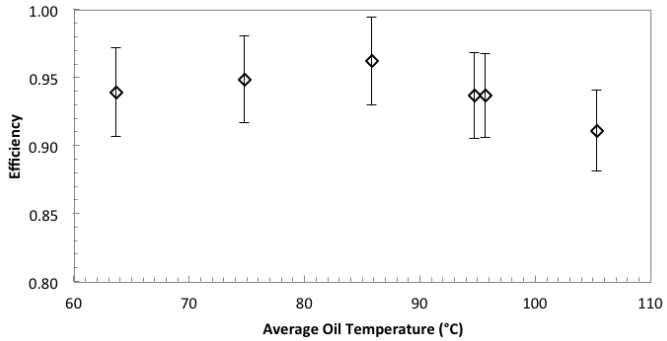

Fig. 41. Effect of average oil temperature variation with catalyst shim A

Efficiencies in excess of 90 percent were obtained for all average oil temperatures tested. Variation in the average oil temperature was found to have a minimal effect on the efficiency of heat transfer to the oil. While the trend was mostly within the uncertainty bands, the peak efficiency of 96.2% was obtained at an average oil temperature of 85 °C and indicates reduced efficiencies for either higher or lower average oil temperatures. A slight decrease in efficiency for higher oil temperatures was reasonable because one would expect higher heat losses for higher oil temperatures.

***Summary of 1st Generation Test Article Experimental Results*:** Changes in efficiency with residence time, equivalence ratio, and oil average temperature were studied. Device performance with catalyst shim lengths, one covering 87 percent of the channel length (shim A) and a second covering 20 percent of the channel length (shim B) were contrasted. Salient conclusions are noted below:

1. Efficiencies in excess of 95 percent were obtained for residence times greater than 20 ms with catalyst shim A. Efficiency decreased with increased residence time due to heat transfer limitations
2. Efficiency trends for shim B with residence time were initially limited by the hydrogen conversion rate at low residence times followed by heat transfer limitations at larger residence times
3. The larger catalyst length tested resulted in higher efficiencies. However, further investigation is needed to identify the optimal catalyst length.
4. Efficiency increased with equivalence ratio and reached a plateau for ratios in the range of 0.7 – 0.9 before decreasing slightly.
5. Average oil temperature variation in the range tested had little effect on device efficiency.

Special Study; A Preliminary Feasibility Study of an In-tank Combustor: Based on a suggestion from General Motors, OSU evaluated the technical feasibility of combusting hydrogen in an array of microchannels to provide the thermal energy in side of the metal hydride storage tank to desorb hydrogen from metal hydride. This approach had the advantage of eliminating the external combustion system and the heat transfer loop needed to transfer thermal energy from the external combustion to the metal hydride material in the storage tanks. Depending on the allowable temperature drop in the heat transfer fluid the mass flow rate of the heat transfer fluid can be high, requiring

a large inventory of heat transfer fluid and a large pump. OSU has conducted preliminary calculations to assess the feasibility of the concept.

Figure 42 depicts a schematic of the proposed concept of directly heating the hydride using an array of combustor/recuperator microchannels. Each array consisted of a central combustor channel, with two sets of recuperator channels surrounding it on each side. A noble metal catalyst will be deposited along the walls of the combustor channels. The combusted products (anticipated to be around 600 degrees C) then flows through the recuperator channels. The design shown in Figure 42 has a two pass recouperator. The number of recuperator passes need to be selected to insure that the external temperature in the outer row of channels does not exceed 200 ^{o}C which is the maximum allowable temperature for the metal hydride. Based on a 26 kW combustion load and stoichiometric combustion, 13 g/min of hydrogen needed to be combusted. The amount of air needed for stoichiometric combustion was 461.3 g/min. If this total flow rate was spread across 1000 combustor channels of 2 mm x 0.3 mm cross sectional area each (correspondingly 4000 recuperator channels), the total pressure drop (based on laminar flow) would be ~40 kPa (6 psi).

A simple heat exchanger analysis was performed to determine the surface area needed to transfer 24 kW to the hydride. The analysis included only the outer recuperator channel row exchanging heat with the surrounding metal hydride bed. It was assumed that the inlet temperature at this outer row of recuperator channels was 200 ^{o}C. With an exit temperature of 180 ^{o}C, and a constant hydride bed temperature of 170 ^{o}C, a surface area of 1.6 m^2 was needed to transfer 26 kW of thermal energy into the metal hydride. With a combustor recuperator of microchannel length of 0.3 m, the width of the heat transfer surface is approximately 2.7 m. Pressure drop constraints forced us to slightly increase the width of the heat transfer surface to 3 m. This results in a total volume for the 24 kW combustion system of 4500 cm^3 (3 m x 0.3 m x 5 mm = 0.0045 m^3 or 4500 cm^3). This represents a 16.5-cm-side cube which will need to be included in the tank.

While we have described the combustion system as being a 16.5-cm-side cube it is likely that the combustion system will be separated into a number of combustors distributed around the tank (see Fig. 1) but the total volume of the distributed combustors would still be approximately 4500 cm^3.The system described about would have the combustion products leaving the bed at approximately 180 C. Efficient operation of the combustion system would probably require an second microchannel recouperator external to the tank that would reduce the temperature of the combustion products from 180 C to on the order of 120 C while preheating the incoming combustion air and hydrogen.

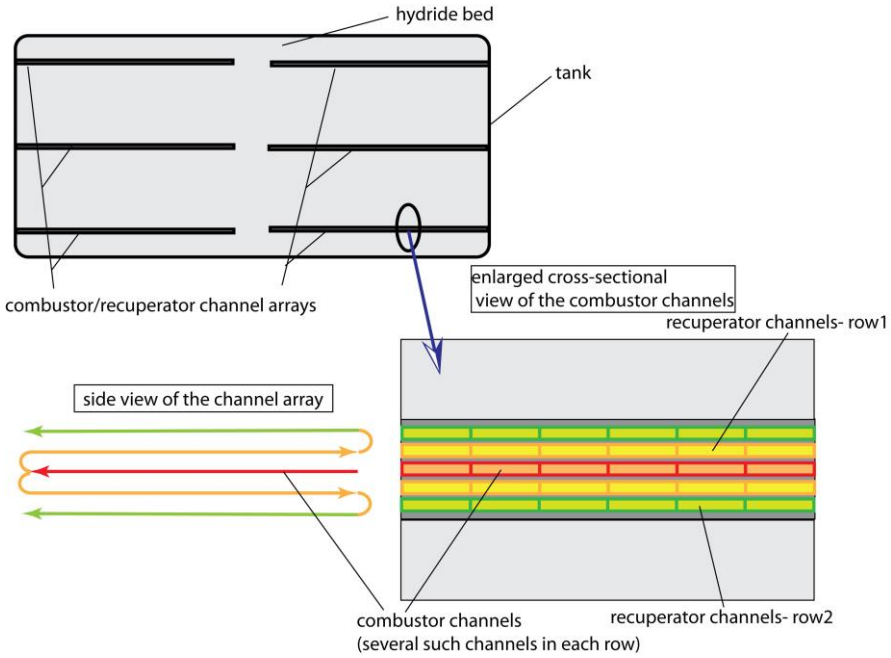

Fig. 42. In-Tank Combustion Concept

There are a number of issues associated with this concept that needed to be considered

Safety – The combustion of hydrogen inherently produces water vapor. Our assumption was that having the water vapor contact the metal hydride would result in a significant safety issue. While the water vapor was contained within the microchannels of the combustion system we do not know what would be required to design a system that was sufficiently safe for use in a commercial product. Several observations relative to the safety issue include:

- Pressure Difference – The interior of the tank will be at perhaps 50 bars while the interior of the combustion system will be at less than one bar. If a leak occurred it is likely that hydrogen will enter the combustion system rather than water vapor enter the storage tank. Combustion in the combustion system will be limited by the oxygen present so having hydrogen enter the combustion system should not increase the heat generation rate in the system.

- Inventory of Water Vapor – The inventory of water vapor will be very small. It is the volume of the exhaust channels where approximately 80% of the volume is nitrogen. Given that the pressure in the exhaust channels will be around ambient, the density of the water vapor will be low.

- Highly Parallel Architecture – There will be on the order of 2000 exhaust microchannels. Any single channel will contain 1/2000 of the already very

small inventory of water vapor. We would need to hypothesize the simultaneous failure of all the channels to release already small inventory of water vapor.

Tank Volume – The volume of the bed would increase by 4500 cm^3. This would increase the size and cost of the tank though it would eliminate the need for an external combustor and the heat transfer loop from the external combustor to the tank.

Temperature Limits on metal hydride – Catalytic combustion of hydrogen occurs and approximately 600 C and the metal hydride can't exceed 200 C. However, by using locating the recouperator between the combustion zone and the metal hydride we can prevent the temperature of the metal hydride exceeding its 200 C limit though this may require a multiple pass recouperator design.

To summarize, an in-bed combustion is technically feasible and would eliminate the need for an external combustor and heat transfer fluid. However these advantages needed to be compared with the increased cost of the tank and safety issues associate with having water vapor in the exhaust microchannel from the combustion system. Based on safety concerns, the Center decided to not pursue the development of the in-tank combustion system.

Key Findings From Task 1.1 – *The key findings from task 1.1 are summarized below.*

- ***The Microchannel combustor/heat exchanger is a significant improvement when compared to existing combustion systems*** – *As shown in table 13, the microchannel combustor represents a factor of 10 reduction in volume when compared to a state of the art heat exchanger developed by Sandia National Laboratory for automotive hydrogen storage applications. The volume reduction was primarily due to the ability of a microchannel combustor to prevent gas phase combustion. The Sandia design required a large amount of excess air to prevent gas phase combustion. This amount of excess air also effected the system efficiency.*

- ***The concept has significant optimization potential particularly in catalyst selection and deposition and material selection*** – *Further optimization has the potential to reduce cost and weight particularly the use of aluminum as the material of construction*

- ***Simulation and Experimental Results both validate Performance Predictions*** – *Both simulation and experimental results confirmed the high performance predicted for this device.*

- ***Fabrication has been successfully demonstrated*** – *As part of assembling the test articles, we successfully demonstrated all of the fabrication processes needs for high volume production.*

Task 1.2 Experimental Validation (In-Tank Thermal Management) OSU activities related to engineering concept design, modeling and validation where focused on an evaluation of a structured bed geometry (using densified pucks of storage materials). Initially our activities were focused on development of a microtechnology-based approach to metal hydride hydrogen storage bed thermal management. When the center eliminated metal hydrides as a candidate storage media, this activity was redirected to investigate structured beds for adsorption hydrogen storage systems. This change was made before we had an operational test unit so no experimental data on metal hydride hydrogen storage was obtained. Therefore we will focus our discussion on adsorption testing at room temperature with activated carbon as the adsorbing material. In phase 2 we developed a cryogenic test apparatus and switched to experimental investigations of adsorption in MOF-5. The major focus in the development of the hydrogen storage apparatus enhanced with microtechnology elements was the development of *the basic storage unit element or Unit Cell* whose characteristics were complete and amenable to numbering-up approach in manufacturing a unit of nominal storage capacity. The optimization (with respect to weight, volume, cost, etc.) of *the unit cell*, then, provided a realistic opportunity to achieve the overall program goals. The design of *the unit cell* consisted of:

- The layer of densified adsorbent material whose dimensions are subject to optimization process;

- The microchannel-based cooling plate that will also contain openings for hydrogen feed streams and openings for six thermocouples.

- the microchannel-based hydrogen distribution plate;

- the bank of six thermocouples that will be permanently fixed with respect to the cooling and the hydrogen distribution plates

The entire storage element will be encased in a reinforced polymer container with sufficient insulation value that will permit adiabatic wall approximation. Figure 43 is schematic representation of the Test Loop that contains the experimental apparatus. Figure 44 shows the composite view of the structured bed of metal hydride.

The main part of the experimental apparatus, consists of three main subunits: i) a high pressure rated steel shell, ii) a glass filled PTFE tube that will serve as the reactor, and iii) a combined heat exchange and feed gas distribution system.

As hydrogen enters the reaction volume and begins to react with the adsorbing media, a temperature wave is expected to propagate axially as the reaction progresses. To provide improved temperature control of the reaction volume it is preferred to feed the hydrogen gas into the reaction volume through the heat exchanger plate. This integrated Heat Exchanger and Distributor Plate subsystem was constructed out of stainless steel and consists of three separate parts, which were diffusion bonded. The

three parts of the integrated subsystem were: 1) Hydrogen distribution plate, 2) Heat transfer fluid distribution plate and 3) Heat transfer plate

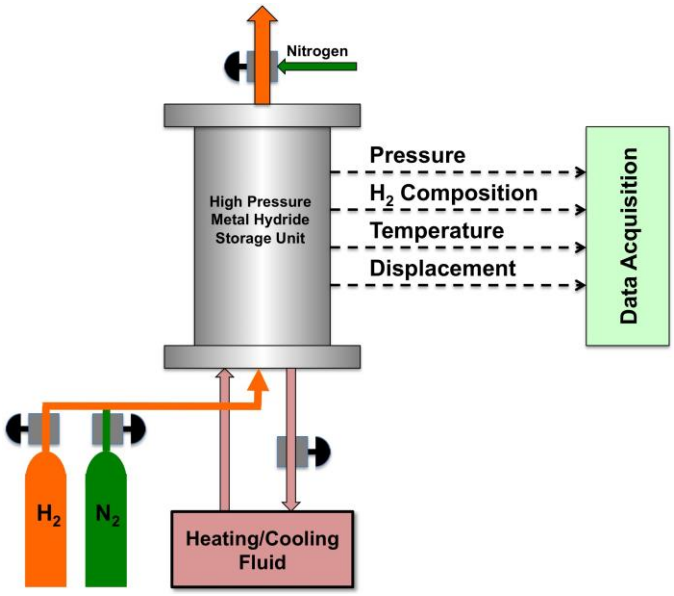

Figure 43.: Schematic representation of the Test Loop.

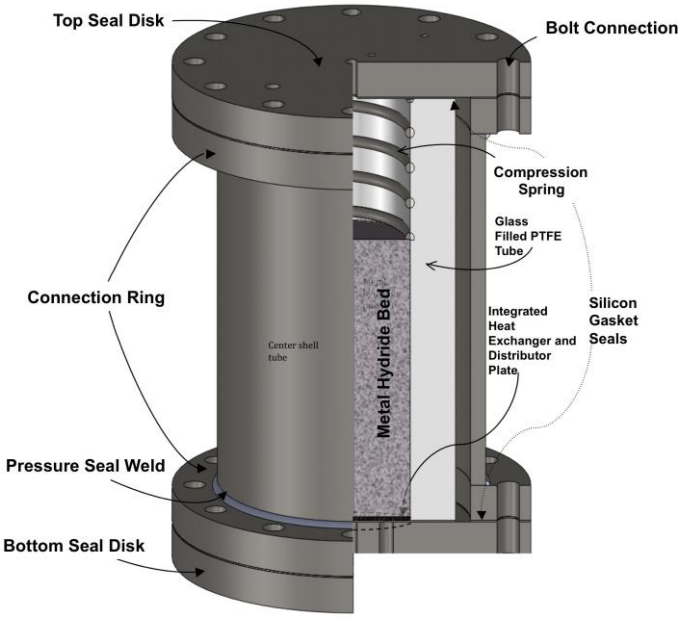

Figure 44 .: Composite view of the *High Pressure Metal Hydride Storage Unit*.

The hydrogen distribution and heat transfer fluid plates were initially 500 µm thick and were chemically etched to create a 250 µm plate containing large number of 250 µm tall cylindrical pillars. The pillars were designed to provide structural support to solid plate area during bonding. The added support ensures a flat surface by preventing the

warping of metal during the high pressure and temperature bonding process. In addition to structural support the pillars provided uniform distribution of cooling/heating fluid throughout the plate.

Hydrogen is fed into the reactor volume by flowing through approximately 90 pre-drilled holes in the heat exchanger plate and the nine thermocouple locations. The hydrogen distribution plate is shown in Figure 45**.**

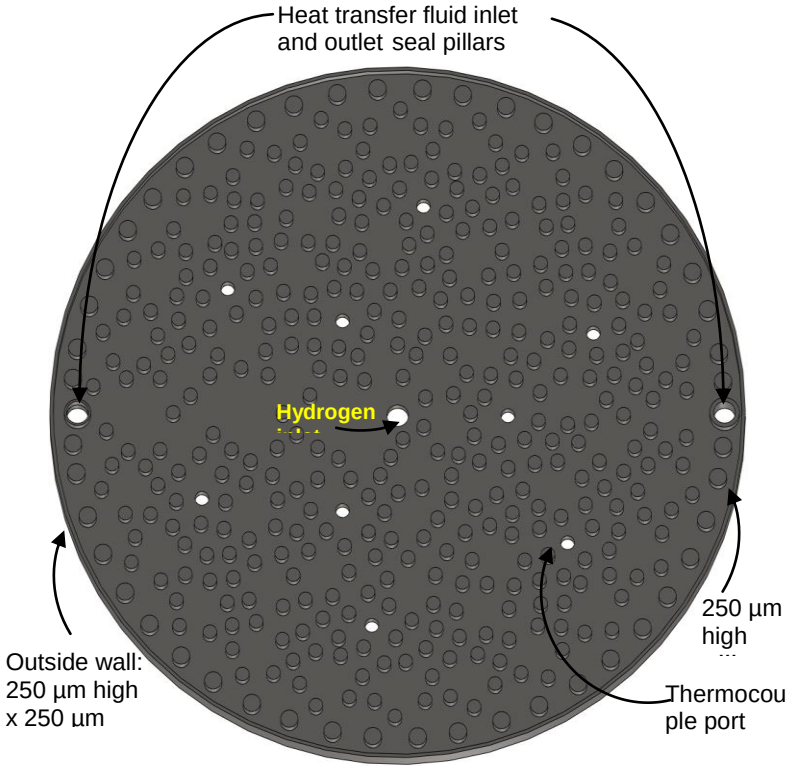

Figure 45.: Design of the Hydrogen distributor plate.

A similar process was followed with the heat transfer fluid distribution plate, however, there were two additional sealing bosses 250 µm thick x 250 µm high etched into the surface in addition to outer perimeter sealing boss and cylindrical pillars. These features are shown in Figure 46.

The second sealing boss acted as a channel for the incoming heat transfer fluid. It guided the fluid to the center of plate where it was subsequently distributed and contacted the third wall containing small, equally spaced, slits along its circumference creating a second channel to allow the fluid to collect and exit the system.

The Heat Exchanger and Distributor Plate integrated subsystem was placed in the bottom of the glass-filled PTFE tube and was not physically secured to either the bottom

of the shell or the PTFE tube. There was a silicon seal placed between the integrated subsystem and the bottom of the steel shell.

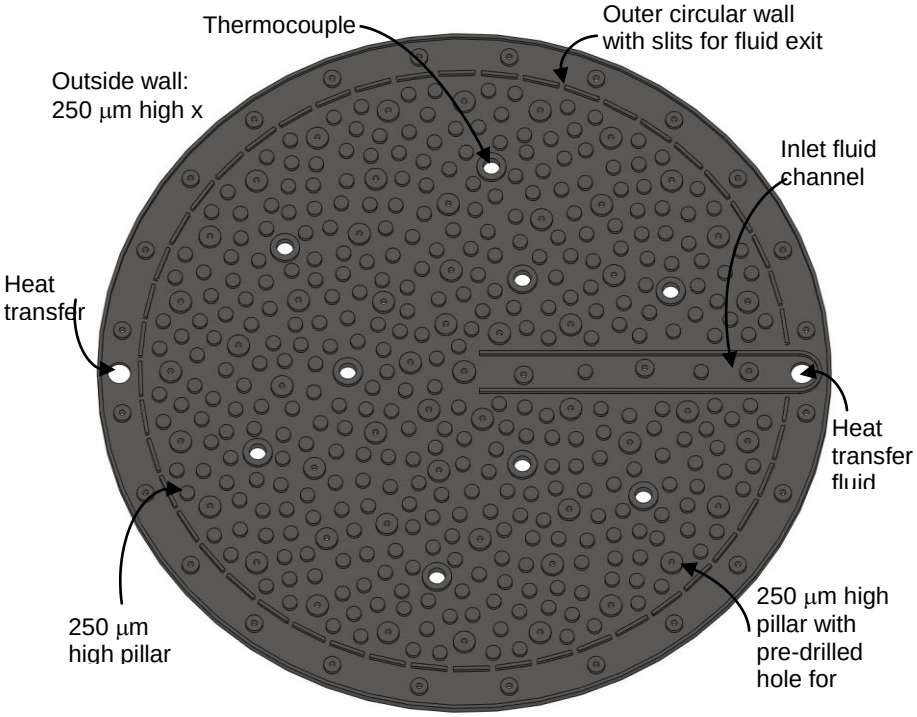

Figure 46: Design of the Heat transfer & Fluid distributor plate.

Preliminary experiments were performed with nitrogen as adsorbing gas, the cooling plates were not used. The carbon bed was a cylinder 1.3 (in) high and 2.0 (in) in diameter made of granulated activated carbon with binder, which was obtained from the University of Quebec. Figure 47 shows the carbon bed used in these experiments.

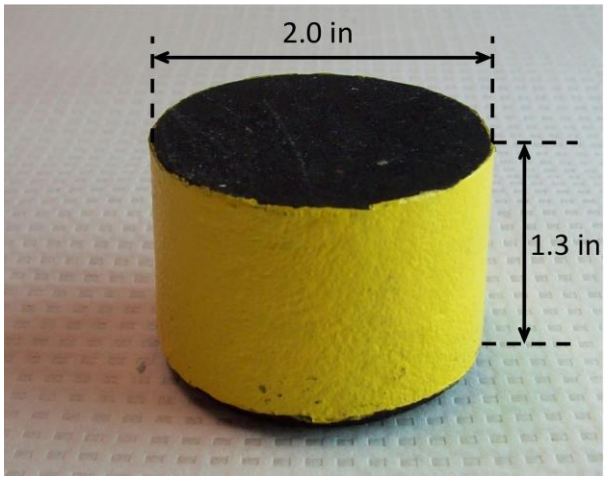

Figure 47.: Adsorption Carbon Bed made of granulated carbon with binder.

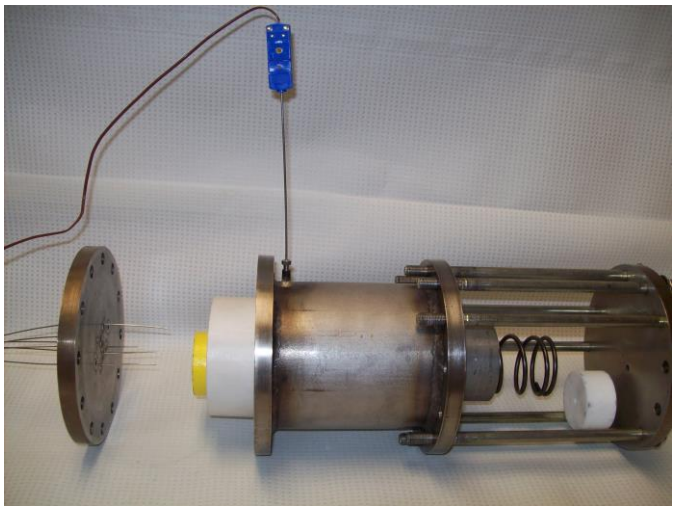

Figure 48**.:** Exploded view the experimental pressure vessel with Carbon Bed.

Figure 48 shows exploded view of the experimental pressure vessel with carbon bed. Protruding from the bottom plate are the thermocouples which will be imbedded into carbon bed. In Figure 49 we show how the carbon bed was positioned into the stainless steel cylinder, and into a cylinder made of PTFE® polymer, which both fit into experimental pressure vessel as indicated in Figure 48.

Figure 49**.:** Exploded view of the Carbon Bed placed into SS cylinder and PTFE cylinder.

Preliminary experimental data suggested several modifications of the elements of the test loop. These included:

- Modifications in the test-loop have to facilitate faster pressurization (N_2 or H_2 inlet) of the pressure vessel. Currently, the nitrogen inlet line is 1/16 (in) OD, which somewhat impedes and prolongs gas-charging process.

- Modifications in the test-loop to facilitate “control” experiments; i.e. experiments without adsorption Carbon bed, and experiments with control heat “losses” through SS and PTFE cylinders.

- Modifications in the test-loop to facilitate faster pressure measurements in the three compartment of the pressure vessel.

- Modifications in the test-loop to facilitate charging of activated carbon in powder form into the pressure vessel.

The photograph of the fully operational vessel, including the modifications described above is shown in Figure 50 below.

The overall experimental effort began by observing pressure and temperature changes inside of an empty pressure vessel (no adsorbing material present) during pressurization from atmospheric to approximately 50 bars of nitrogen gas at ambient temperature. The delivery pressure was set to 50 bars and the inlet valve to the vessel were manually operated (opened) for a period of 10 seconds, allowing the vessel to fill with nitrogen gas. The locations of the thermocouples and pressure transducers inside of the pressure vessel are shown in ***Figure 55***.

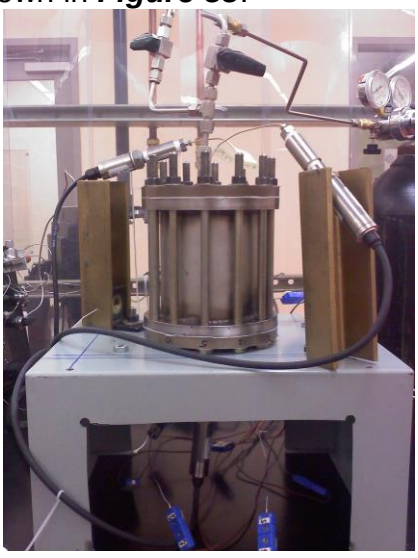

Figure 50: Fully constructed pressure vessel and instrumentation in OSU Hydrogen Lab at Microproducts Breakthrough Institute (MBI) facility.

Figure 51 shows a typical pressure change in the vessel during gas charging process into the vessel. From this figure one can conclude that the vessel quickly fills with gas and once the valve is closed, a slight decay in pressure is observed before the nitrogen gas equilibrates inside of the vessel. The pressure decay is a consequence of temperature decay inside the vessel, due to heat loss. Figure 53 shows how pressure and temperature of the gas inside the vessel are changing during a charging.

All pressure transducers are in agreement with one another i.e. they essentially read identical pressure. Figure 52 shows that the vessel is filled in roughly five seconds at a linear rate of 10 [bar/s]; and, then remains constant until the valve is closed and finally begins a slight decay in pressure due to heat loss from the vessel.

Due to the short filling time this process is representative of an adiabatic comperssion, as indicated from the temperature increase shown in Figure 53. As the inlet valve is opened the temperature begins to increases sharply, a maximum temperature increase of approximately 45^{o}C was recorded inside the vessel.

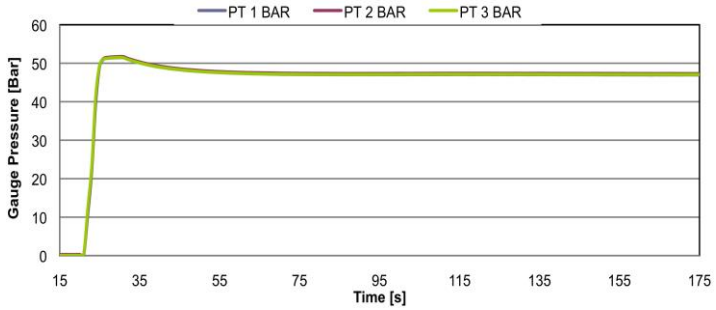

Figure 51.: Pressure change in the vessel (without adsorbent) during nitrogen charging process.

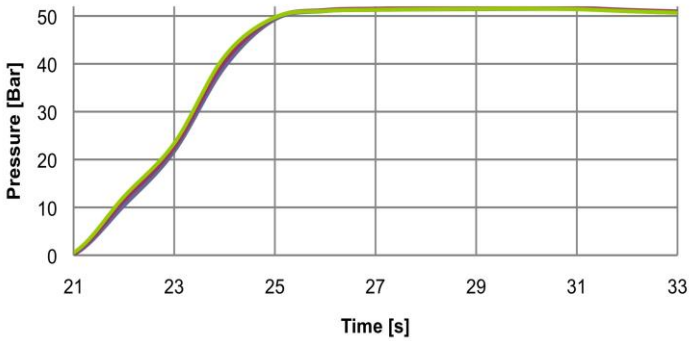

Figure 52: Pressure response in the vessel (without adsorbing material) during charging cycle.

The peak temperature increase coincides with reaching the delivery pressure inside the vessel. Once the nitrogen inlet valve is closed the system begins to cool to ambient temperature; thus, the pressure starts decreasing until the temperature equilibrates and pressure stabilizes. For the vessel without adsorbent, the time required for the compressed gas to reach ambient temperature was on the order of 100 seconds.

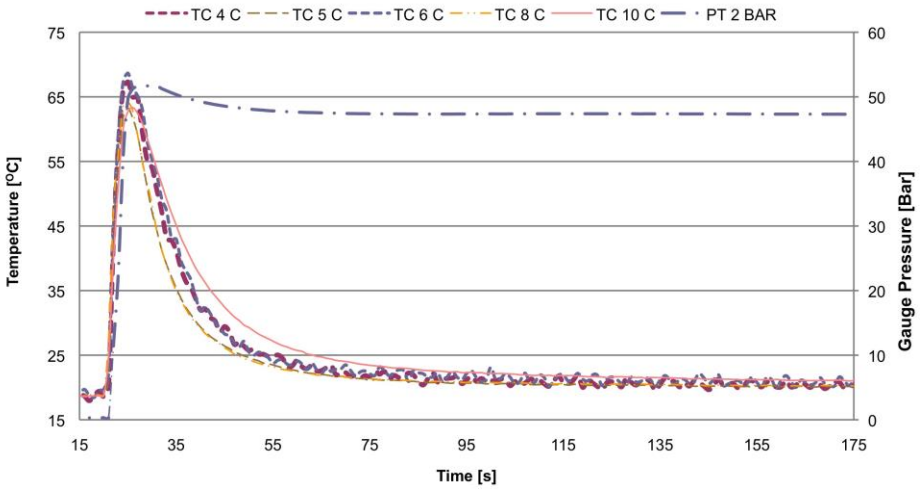

Figure 53.: Temperature and pressure response during vessel pressurization with nitrogen.

The second stage of experimentation includesd the addition of activated carbon bed storage material (2 inch diameter by 1.33 inch tall cylinder) into of the pressure vessel. All of the thermocouples were used in this experiment and the experimental set-up is schematically represented in Figure 54 below. The carbon bed cylider was suspended inside of the pressure vessel by resting on six thermocouples. Holes were drilled into the carbon bed to predetermined depths. Thermocouples fit tightly inside the holes and a sealing polymer material was positioned along the length of a thermocouple (except for the tip of the thermocouple) to prevents gas from creeping into the carbon bed along thermocouples. The last thermocouple was positioned below the carbon bed and was located near the center of the tank; ¾" above the tanks base. This thermocouple recorded the temperature inside of the tank while the other six probes recorded temperature inside the carbon bed. The circumference of the carbon bed was painted with standard latex paint to eliminate nitrogen gas from entering the carbon bed on the side and to force the gas to enter from either the top or the bottom of the bed.

The pressure response curve of the carbon-filled vessel was similar to that of the empty vessel. A quick filling time was followed by a sudden decay that leveled off; see Figure 55. Figure 56 is the pressure response curve during the filling of the vessel. It resembles the filling cycle of the empty vessel. Figure 56 is the pressure response in a carbon-filled vessel during N_2 charging process.

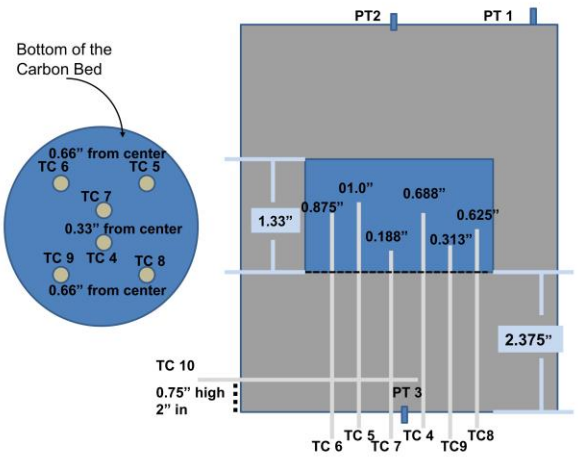

Figure 54.: Locations of thermocouples and pressure transducers inside the pressure vessel with carbon bed adsorbent.

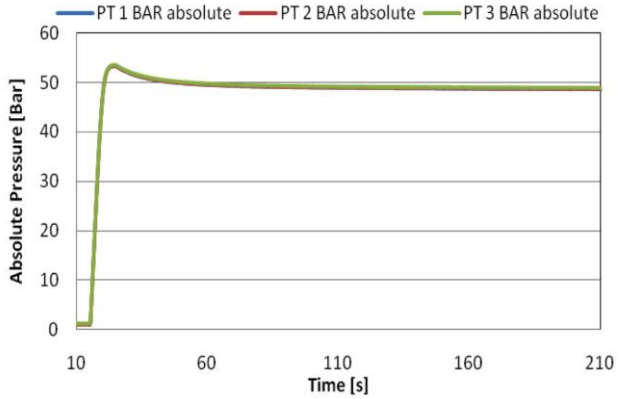

Figure 55.**:** Pressure response in carbon-filled vessel during N_2 gas filling process.

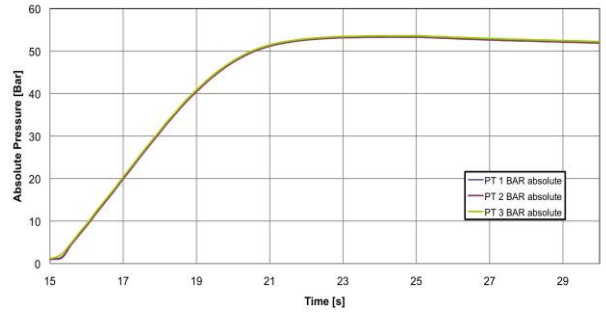

Figure 56.: Pressure response in a carbon-filled vessel during N_2 charging process

The temperature response curves recorded in the vessel with adsorbing material differ substantially from temperature response curves obtained in the empty vessel operation. The temperature profiles of the seven thermocouples are shown in Figure 57. As expected the six thermocouple probes located inside of the carbon bed have a much different response compared to the thermocouple that is located below the carbon bed, thus recording the temperature of gas inside the vessel.

The thermcouple in the vessel, TC 10, displayed a similar response to the empty vessel, however, has a maximum temperature reading that is approximately 10 [^{o}C] lower than that experienced in the empty vessel experiment. In the adsorbing system, TC 10, appears to experience a slightly longer temperature decay but follows a similar overall trend as it cools to ambient temperature.

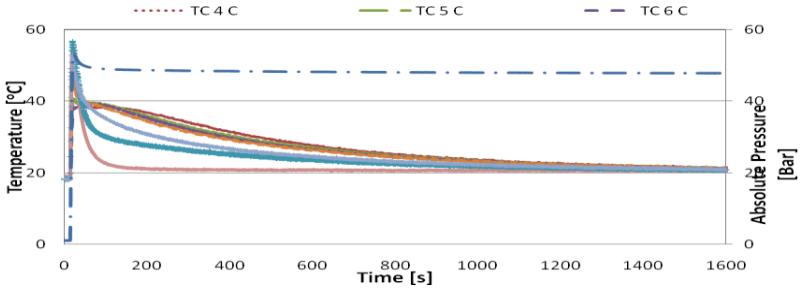

Figure 57.: Temperature and pressure response in a carbon-filled vessel.

The thermocouples nearest to bottom of the carbon bed, TC 7 (nearest to bottom) and TC 9, displayed the most similar response to that of TC 10, reaching similar maximum temperatures. The greatest difference is in the time required to return to ambient temperature, nearly 1200 seconds for the two probes in the bed compared to 140 seconds for the probe below the carbon bed. TC 8, located just under halfway into the carbon bed, produced a lower maximum temperature than TC 7, 9, and 10, and displayed a much slower temperature decay, requiring almost 1500 seconds to return to ambient tempearture.

The three thermocouples, TC 4, TC 5, and TC 6, located in the upper half of the carbon bed experienced a substantially different response during the filling process compared to the other thermocouples. Whereas the temperature response of the probes in the vessel and the lower half of the bed represented skewed Gaussian curves, the upper half probes reach their maximum temperatures, approximately 15 [^{o}C] lower than the vessel maximum, flatten out, and begin a slow gradual cooling. Figure 58 shows more detailed temperature and pressure responses in the carbon-filled vessel.

Using the ideal gas law, the moles of nitrogen present in the system was assumed to be a function of the vessel temperature (TC 10) and pressure (PT 2). The moles of nitrogen present in the vessel at any time during the filling cycle was calculated and is shown in Figure 59. One can notice a sharp increase in the number of moles during initial stage of the filling process and then leveling off. However, in the carbon-filled vessel a slight decrease in nitrogen is initially noticed, and then the system begins to recover. In Figure 60 a closer look at the “dip” which systematically showed in all experiments in carbon-filled vessel. The sudden decrease in nitrogen followed by the slow recovery to its final value was evidence of nitrogen gas adsorbing into the actived carbon bed suspended in the vessel.

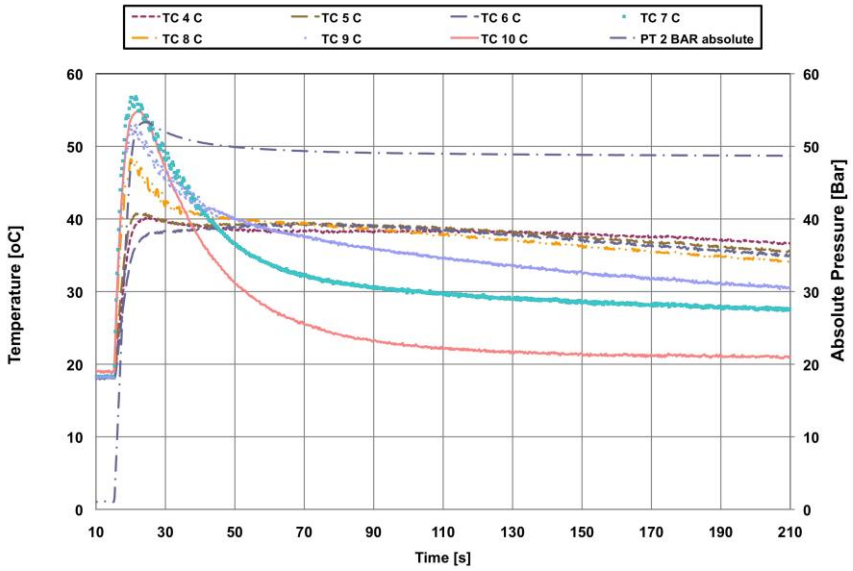

Figure 58.: Carbon-filled vessel temperature response during charging

From the initial series of experiments it was evidentthat that a large increase in temperature due to adiabatic compression was taking place during pressurization of the vessel. In an empty vessel, with no adsorbing material, pressure equilibrates quickly while the temperature takes longer to return to ambient. With an adsorbing material present in the system, the cooling time in the vessel was slightly longer but the cooling of the adsorbing carbon bed takes aproximately 15 times longer to return to ambient conditions. Comparing the moles of nitrogen present in both situations, a sharp dip was observed in the presence of the adsorbing material, indicating the adsorption of nitrogen during the experiment.

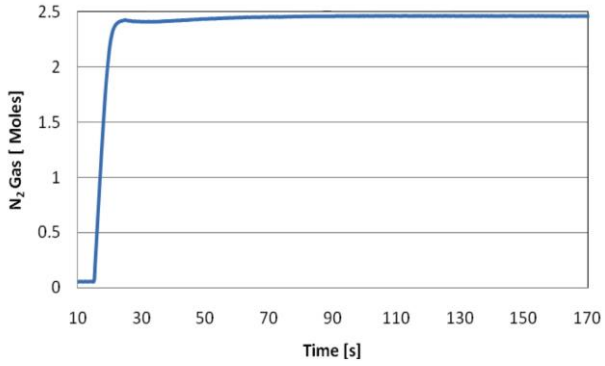

Figure 59.: Moles of nitrogen gas present in the carbon-filled vessel.

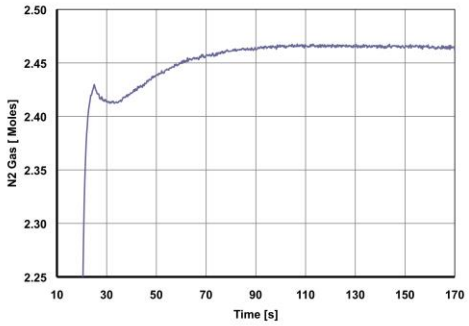

Figure 60.: Moles of nitrogen gas present in the carbon-filled vessel during initial time of the filling process.

Pressure drop through the microchannel heat exchanger & H_2 distribution plates.

One of the major challenges identified during the development of the microchannel heat exchanger for the cooling of the storage media was the anticipation of high pressure drop through the device. The microchannel heat exchanger & distributor has an important role in providing cooling and even distribution of hydrogen throughout the bed of storage material. Several important concepts hinge on its proper performance.

Water at room temperature is used in the pressure drop experiments. To accurately determine the pressure drop through the micro-channel heat exchanger, Figure 61, it was necessary to determine the pressure drop associated with the experimental setup outside of the *microchannel heat exchanger & H_2 distribution plates*.

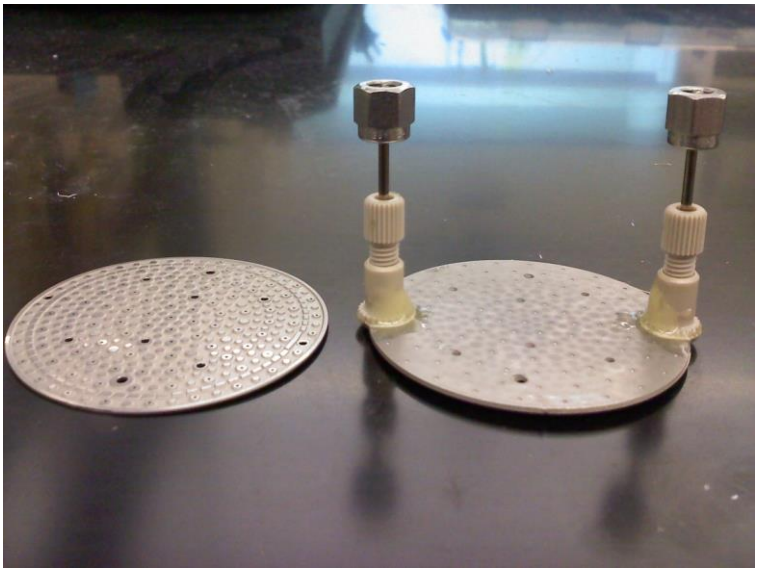

Figure 61: Close up of internal structure of the heat exchange device and heat exchanger with fluidic connectors.

For this reason an experimental apparatus was constructed to facilitate independent measurements of the pressure drop through the rest of the system and connectors (background pressure). We utilized 1/16” outer diameter and 3.5” long tubing to replace the *microchannel heat exchanger & H_2 distribution plates*. The pressure drop through the tubing was calculated based on the flow rate and Reynolds number and was subsequently subtracted from the pressure drop data of the entire system. The experimental subsystem with 3.5” long tubing in place, for “background” pressure measurement is shown in Figure 62.

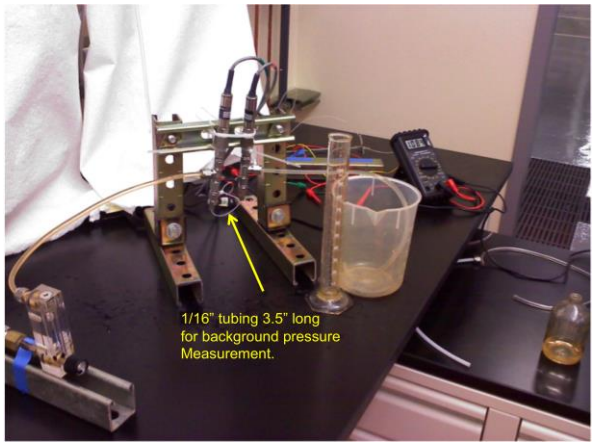

Figure 62: Experimental setup for the pressure drop measurement in *the microchannel heat exchanger & H_2 distributor* with 1/16" OD tube in place for “background” pressure drop measurement.

The pressure drop experiments (through the apparatus and tubing) were performed by regulating the water flow rate with a rotameter. Flow rates were determined by timing the collection of 10 or 20 [mL] samples, and the voltage output at pressure transducers were recorded (range 1-100 [psi]). Three complete trials, water collection, timing, and voltage monitoring, were taken at each flow rate; each experiment tested 18 flow rates. Four experiments were conducted, which exhibited high repeatability; see Figure 63.

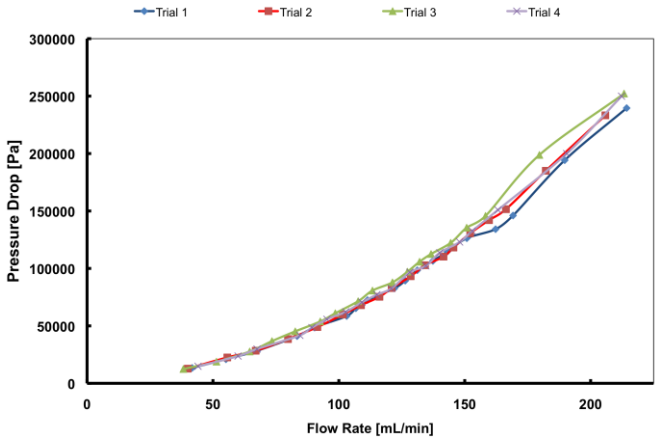

Figure 63.: Pressure drop versus flow rate using 1/16" diameter 3.5” long tubing.

It was assumed that the pressure drop through the bulk of the experimental apparatus, excluding tube length, would remain constant after the heat exchanger is inserted in place of the tube length. Therefore, the pressure drop associated with the bulk of the experimental apparatus was the pressure drop through the complete setup less the pressure drop through the tube length. The pressure drop through the tube length was estimated via,

$$\Delta P_{Tube} = \frac{2\rho_w f \acute{Z} L_{Tube} u_{ave}^2}{D} \tag{6}$$

The friction factor in Equation 1 for laminar flow was;

$$f = \frac{16}{\mathrm{Re}} \quad \text{for Re} < 2200 \tag{7}$$

And for turbulent flow (Levenspiel 1986):

$$f = 0.079\,\mathrm{Re}^{-1/4} \quad \text{for Re} > 2200 \tag{8}$$

Where:

$$u_{ave} = \frac{4F}{\pi D^2} \tag{9}$$

and *F* is the volumetric fluid flow measured during the experimental trial. The pressure drop through the 1/16" OD and 3.5" long tube was plotted versus flow rate in Figure 64.

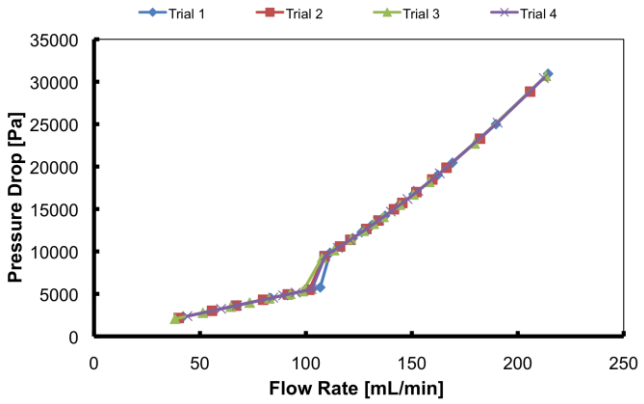

Figure 64: Pressure drop through tube length versus flow rate.

Therefore, the pressure drop through the bulk of the apparatus is:

$$\Delta P_{Apparatus} = \Delta P_{ExperimentalData} - \Delta P_{Tube} \tag{10}$$

The resulting pressure drop through the apparatus ("background pressure drop) for all four experiments is plotted as one data series to create a correlation for pressure drop versus water flow rate. These results are shown in Figure 65.

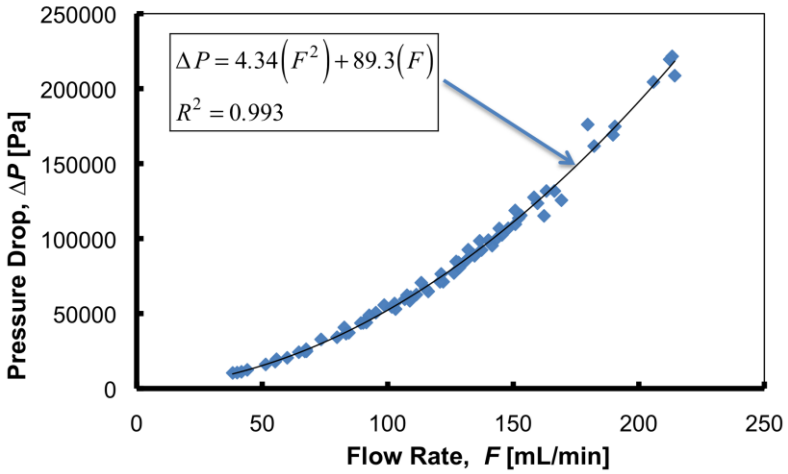

Figure 65: Correlation for pressure drop through the apparatus as a function of water flow rate.

The resulting second order polynomial was used to determine the pressure drop through the microchannel heat exchanger using the same experimental setup.

A 2" diameter *microchannel heat exchanger & H2 distributor plate,* with 250 [μm] high fluid channels, was inserted into the experimental apparatus and the experimental procedure was repeated. The heat exchanger was connected to the apparatus by two 1.5" long, 1/16" OD SS-316, tubes, as shown in Figure 66.

Figure 9 is also a close up of the micro-channel heat exchanger with fluidic connections, right, and the internal pattern that defines the fluid channel, left.

Four highly repeatable pressure drop experiments were conducted with the micro-channel heat exchanger, as is shown in Figure 67.

The same procedure for determining the pressure drop through the plastic tube was used to determine the pressure drop through the heat exchanger's inlet and outlet fluidic connections, yielding the final equation for determining the pressure drop through the heat exchanger.

$$\Delta P_{HEX} = \Delta P_{ExperimentalData} - \Delta P_{Apparatus} - \Delta P_{EntranceTube} - \Delta P_{ExitTube} \qquad (11)$$

The calculated pressure drop data through the heat exchanger is plotted in Figure 68 as a single data set. The maximum calculated pressure drop across the heat exchanger is 5.12 [psi] at a water flow rate of 215. [mL/min].

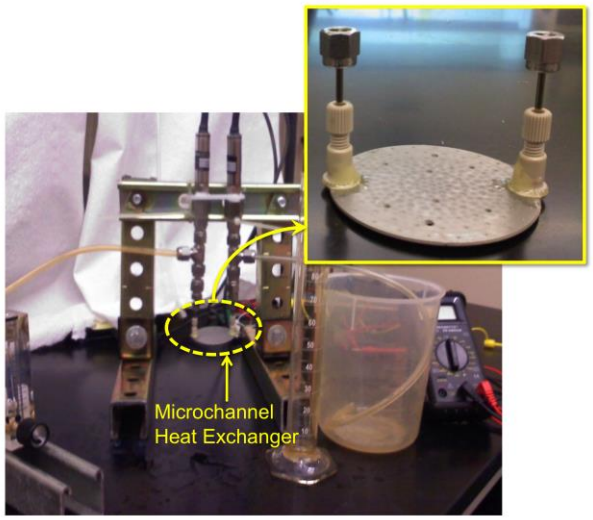

Figure 66: Experimental apparatus with micro-channel heat exchanger in place.

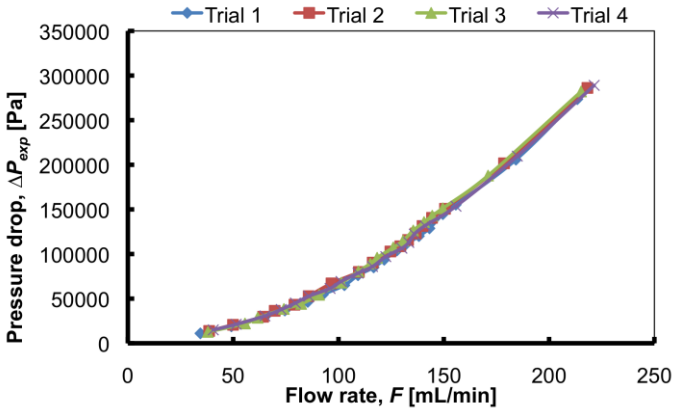

Figure 67: Total apparatus pressure drop versus flow rate with heat exchanger**.**

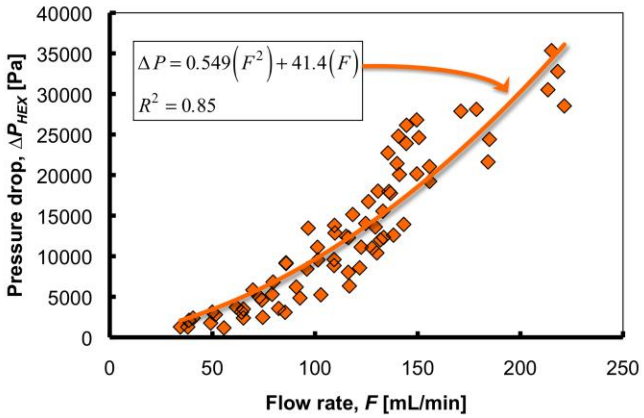

Figure 68: Pressure drop versus water flow rate correlation for micro-channel heat exchange device alone.

The overall conclusion from these experiments is that the pressure drop through the microchannel heat exchanger & H_2 distributor plates is reasonably small. In addition, one can conclude that in the design of a scaled-up microchannel *heat exchanger & H_2 distributor plates* (30 [cm] in diameter) laminar flow should be preserved to limit the growth of the pressure drop through the heat exchanger, ΔP_{HEX}. Furthermore the above experiments indicate that the major pressure drop in the cooling subsystem will be located in the coolant feed and exit lines.

Key Findings From Task 1.2 – *The key findings from task 1.2 are summarized below.*

- ***OSU successfully established the capability to conduct charging and discharging tests on a densified media. –*** *This capability was used extensively in Phase 2 to investigate adsorption based cooling.*

- ***Results were consistent with expectations and allowed preliminary model validation described below.***

1.3 Simulation of Carbon Bed Adsorption: Although the initial focus of at OSU was on the collection of experimental data, some of the effort in this reporting period was spent on representation/articulation of experimental data, collected in the pressure vessel with carbon bed (schematically shown in Figure 54), with the COMSOL numerical model which was originally developed by SRNL.

After initial difficulties in running the COMSOL numerical model, which was caused by different software versions available, the mathematical model was running smoothly.

To make our experimental data fully comparable with numerical simulations, we have changed some architectural features/dimensions in the program as well as some boundary conditions. SRNL program was written with this flexibility embedded into the code.

In this section we present both experimental and simulation results. The overall plan of our work reflects the need to, first, 'train' the numerical model to fairly represent the set of experimental data obtained at room temperature with adsorption of N_2 into carbon bed. Only then did we undertake more complex simulations that would attempt to model experiments performed at cryogenic temperatures.

System geometry; Our numerical simulation model reflected the actual architecture of the experimental apparatus through three simulation domains: carbon bed (domain 1), vessel (domain 2) and inlet tube (domain 3). Coordinate system used is cylindrical. System is depicted in Figure 69.

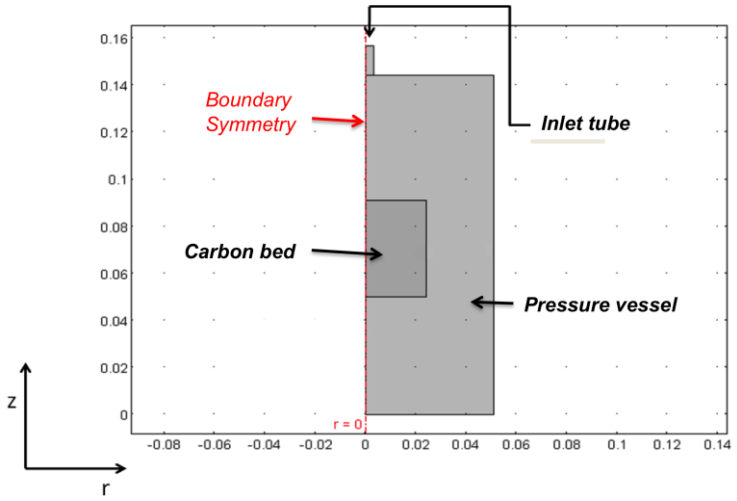

Figure 69: Domain definitions and boundaries.

Domain dimensions closely resembled the experimental setup and its sizes are listed in Table 15.

Table 15.

	Carbon bed	Pressure vessel	Inlet tube
Radius, m	0.024	0.51	0.0032
Height (length), m	0.041	0.144	0.0127

Gas enters the vessel through the tube; it expands into the vessel, and penetrates the carbon (porous) bed where it is adsorbed. There are three different physic modes /interfaces used in the model: “Non-Isothermal Flow” for domains 2 and 3, “Brinkman Equations” for domain 1 and “Heat Transfer” for all three domains. The “Free and Porous Media Flow” which combines the two domains could alternatively, replaced the separate representation for the open space in the vessel, and for the porous bed. In the combined representation of the porous media and open vessel flow, only weakly compressible flows were used with Mach numbers less than 0.3. It can be easily shown that during initial gas charge into the vessel the flow is highly compressible, and it needs to be modeled with a Mach number close to 1. Thus using the improper interface easily yields to numerical instabilities.

To maintain proper coupling between the two momentum transfer interfaces, pressure and velocity fields were established as common variables for all three domains. Temperature is a common variable by default as “Heat Transfer” interface includes the whole system. This model represents a modification of the original SRNL model. We produced numerical simulation of the experiments previously performed in our experimental apparatus. Then, we determined how well the numerical simulation compared to the corresponding experimental data.

Figures 70 and 71 clearly showed that results of numerical simulations were not reflecting experimental data. We have identified several potential reasons for this discrepancy. The most obvious cause of the observed discrepancies between numerical simulation and experimental data was probably inadequate modeling of heat losses in the vessel. Other possible causes for the observed discrepancies may arise from numerical instabilities, which were clearly displayed in Figure 72. These, and perhaps other sources of inconsistencies may become evident from more detailed numerical modeling planned for the future.

REFERENCES

Levenspiel, O., Engineering Fluid Flow and Heat Exchange, Plenum Press, New York, NY (1986)

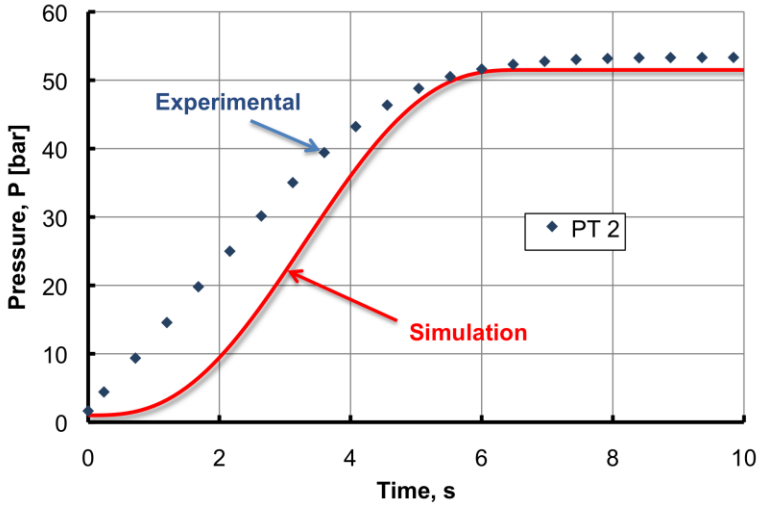

Figure 70: Pressure in the vessel.

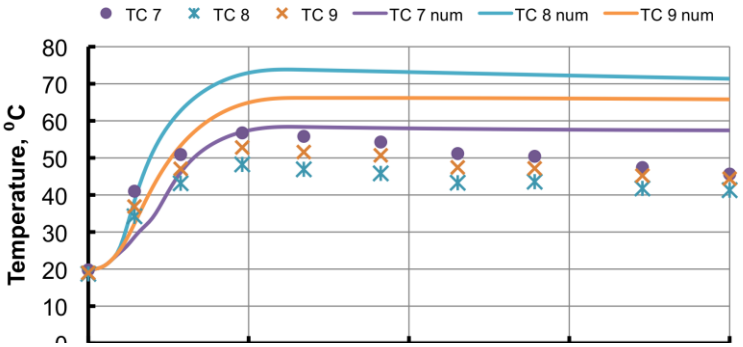

Figure 71: Temperatures near the edge of the carbon bed.

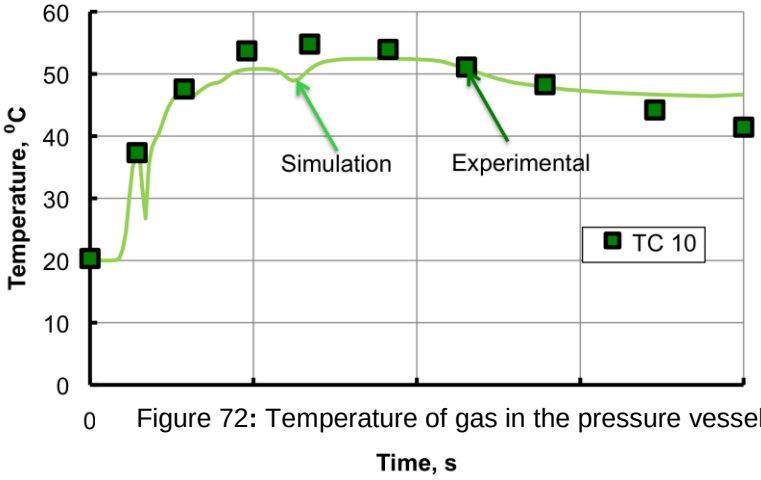

Figure 72: Temperature of gas in the pressure vessel.

Carbon Adsorption Modeling: Following the fluid and heat transfer modeling, we added adsorption to our simulation. Most of the key parameters were calculated on the basis of literature data and variety of assumptions. Several important parameters related to the nature of the carbon material, the binder, carbon-to-binder ratio, bed porosity and adsorption kinetics were estimated. Results of these estimates were built into a simplified mass, and energy transfer model (in COMSOL 4.0) and the results of the simulations were compared to the experimental results, obtained from the first set of experiments with a longer vessel filling time.

System dimensions

Key system dimensions for the test apparatus carbon bed and the vessel without carbon are given below.

Carbon bed:

D_b	0.0483	m
H_b	0.0413	m
V_b	7.55E-5	m^3

Vessel (without carbon):

D	0.102	m
H	0.144	m
V	0.00117	m^3

Equilibrium

Based on the heat generated during adsorption of nitrogen on activated carbon, we conclude that the adsorption process could be represented by physisorption model, Chorkendorff (2007); i.e. the associative adsorption model could be used:

$$N_2 + * \underset{k_A^-}{\overset{k_A^+}{\rightleftarrows}} N_2^* \qquad (12)$$

where (*) represents the empty site or an adsorbed molecule. It is further assumed that all adsorbed species were distributed randomly over the surface and there were no interactions between them. If the amount of nitrogen adsorbed under operating conditions was not too high, i.e. the surface of carbon was not densely populated with adsorbate the above assumption was acceptable and Langmuir adsorption kinetic model was be used. Rate equation for nitrogen coverage of carbon surface which is defined as θ_A was then:

$$\frac{d\theta_A}{dt} = p_A k_A^+ (1-\theta_A) - k_A^- \theta_A \quad \left[\frac{\text{Occupied sites}}{\text{Total number of sites} \times \text{s}}\right] \qquad (13)$$

Here the total number of sites was not known but the article by Chorkendorff (2007) provides comparison with data for CO_2 adsorption, which adsorbs more readily than nitrogen. Thus the maximum number of sites was estimated to 9 [mmol/g_{carbon}]. Equilibrium constant, K_A,MPa^{-1} was derived from equation (2) assuming equilibrium conditions:

$$p_A k_A^+ \left(1-\theta_A\right) - k_A^- \theta_A = 0$$

$$p_A k_A^+ \left(1-\theta_A\right) = k_A^- \theta_A$$

$$K_A = \frac{k_A^+}{k_A^-} \quad \left[MPa^{-1}\right]$$

$$\theta_A = \frac{K_A p_A}{1+K_A p_A} \;\; where: \;\; \theta_A = \frac{n_{A,\max}(p_A)}{9}$$

where ***n*** represents number of occupied sites.

Transforming the equation for coverage we could finally obtain:

$$\frac{1}{\theta_A} = \frac{1}{K_A} \times \frac{1}{p_A} + 1 \qquad (14)$$

which yields a linear relationship between partial pressure of nitrogen and the maximum nitrogen coverage with slope equal to reverse value of the equilibrium constant. Results are shown below (Figure 73).

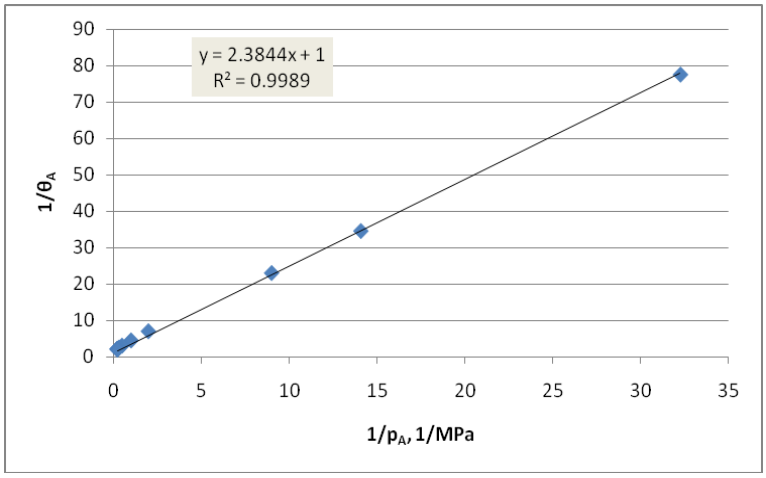

Figure 73:. Partial Pressure of Nitrogen vs Max Nitrogen Coverage

This results in a value of K_A given by, K_A = 0.419 Mpa^{-1}.

Estimates of Adsorption Rates:

Adsorption rate i.e. constants k^+ (kinetic parameter for adsorption) and k^- (kinetic parameter for desorption) were calculated under assumption that initially the adsorption dominates the process thus desorption term can be (initially) neglected:

$$\frac{d\theta_A}{dt} = p_A k_A^+ \left(1-\theta_A\right) - k_A^- \theta_A$$

$$p_A k_A^+ \left(1-\theta_A\right) \square \quad k_A^- \theta_A$$

$$\frac{d\theta_A}{dt} = p_A k_A^+ \left(1-\theta_A\right) \Rightarrow \ln\left(1-\theta_A\right) = -p_A k_A^+ \times t \qquad (15)$$

$$k_A^+ = \frac{slope}{p_A} \quad \left[MPa^{-1}\right]$$

$$K_A = \frac{k_A^+}{k_A^-} \Rightarrow k_A^- = \frac{k_A^+}{K_A}$$

Equation (4) was used to estimate adsorption rate constant from the slope of initial adsorption data. Pressure was fixed at 50 bar which was the nominal pressure for our longest experimental run. From this analysis and assumptions we obtained that:

$$k_A^+ = 0.00145 \quad \left[MPa^{-1}\right] \text{and} \; k_A^- = 0.00346 \left[MPa^{-1}\right]$$

There is no adequate data available to estimate a temperature dependence of constants. However, the temperature interval is not very broad (between 10 and 30°C) and for a first order of magnitude estimate it gave satisfactory accuracy. Thus the final equation used in simulations was:

$$\frac{d\theta_A}{dt} = p_A k_A^+ \left(1-\theta_A\right) - k_A^- \theta_A$$

$$p_A = 50 \; bar = const.$$

$$n_{tot} = 9\times10^{-3} \left[\frac{mol}{g_{carbon}}\right] \times 36.28 \quad \left[g_{carbon}\right]$$

$$\frac{1}{n_{tot}}\frac{dn}{dt} = p_A k_A^+ \left(1-\frac{n}{n_{tot}}\right) - k_A^- \frac{n}{n_{tot}} \qquad (16)$$

$$\frac{1}{V_b}\frac{dn}{dt} = p_A k_A^+ n_{tot} \left(\frac{1}{V_b} - \frac{n}{V_b \times n_{tot}}\right) - k_A^- \frac{n}{V \times n_{tot}}$$

$$\frac{dc}{dt} = p_A k_A^+ n_{tot} \left(\frac{1}{V_b} - \frac{c}{n_{tot}}\right) - k_A^- \frac{c}{n_{tot}}$$

Kinetics verification

Equation (5) was solved in MATLAB using a 4th order Runge-Kutta scheme. Initial values were take for a pressure of 50 bar, and average temperature of 300 [K]:

$$c_i = \frac{n(50\_bar)}{V_{vessel}}$$

$$n(50\ \ bar) = \frac{p_{nominal} \times V_{vessel}}{RT} \frac{50\times10^5\left[Pa\right]\times\left(0.00117-7.55\times10^{-5}\right)\ \left[m^3\right]}{8.314\left[\frac{J}{mol\times K}\right]\times300\ \left[K\right]}$$

$$n(50\ \ bar) = 2.188\ \ \left[mol\right]$$

$$c_i = \frac{2.188\ \ \left[mol\right]}{\left(0.00117-7.55\times10^{-5}\right)\ \left[m^3\right]} = 2004.7\ \ \left[\frac{mol}{m^3}\right] \qquad (17)$$

Comparison was made between calculated and experimental values obtained for the equilibrium concentration of adsorbed nitrogen, and the time needed to reach that concentration. Equilibrium concentration of nitrogen for run 6 was obtained from eqn 17:

$$c_f = \frac{n(50\ \ bar)-n_f}{V} = \frac{2.1882-0.098256}{0.00117} = 1924.5\ \ \left[\frac{mol}{m^3}\right]$$

Kinetic model yields a final concentration of about 1779 [mol/m^3], which was close to experimental value of 1924.5 [mol/m^3].

Comparison of times needed to reach equilibrium concentration:

Experimental data for nitrogen pressure change in the experimental vessel as a function of time for run 6 is shown in Figure 74:

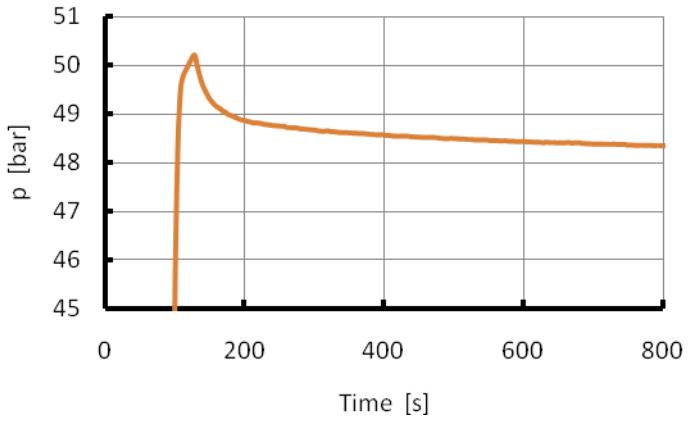

Figure 74: Test Vessel Nitrogen Pressure as a function of time

From this figure we see that equilibrium in the experiment is reached after fairly long time; more than 800 [s]. According to our kinetic model this time should be approximately 350 [s]. However, MATLAB solution assumes uniform initial concentration of nitrogen throughout the vessel (including carbon bed), whereas in the real system the adsorption process concentration of nitrogen in the carbon bed is a much smaller and it increases as the gas enters the bed by diffusion. In addition, the computed results do not take into account any mass transfer resistance between the gas in the vessel and carbon bed. Thus, this result could be still acceptable as the most intense change nitrogen pressure occurs within 400 [s].

Effective Diffusion Coefficient

Diffusion coefficient was calculated from random pore model:

$$D_e = D_M \varepsilon_M^2 + \frac{\varepsilon_\mu^2 \left(1+3\varepsilon_M\right)}{1-\varepsilon_M} D_\mu \qquad (18)$$

The amount of nitrogen that is adsorbed is not very high so there will be many empty sites available in macropores (index M).Therefore adsorption in micropores (index μ) can be neglected:

$$D_{1\text{–}1^*} = \frac{2}{3}\left(\frac{k_B}{\pi}\right)^{3/2} \bar{N}^{1/2} \frac{T^{3/2}\left(\frac{1}{M_1}\right)^{1/2}}{P\sigma_1^2}$$

$$D_e = D_M \varepsilon_M^2 \qquad (19)$$

ε is than the total porosity of the bed and D_e is the effective diffusion coefficient. Evaluating D_M:

$$\frac{1}{D_M} = \frac{\left(1-\alpha y_1\right)}{D_{1\text{–}1}} + \frac{1}{D_{KM,1}}$$

First term reflects self diffusion of nitrogen and the second term is Knudsen diffusion in the bed. We do not know the pore size in the bed, but since Knudsen diffusion contribution is inversely proportional to nominal pressure, which is high, this term can be neglected. Thus this model reduces to a self-diffusion case:

$$\alpha = 1 + \frac{n_2}{n_1} = 1 + \left(-1\right) = 0$$

$$D_M = D_{1\text{–}2}$$

For self-diffusion the following relation holds:

$$D_{1-1^*} = \frac{2}{3}\left(\frac{k_B}{\pi}\right)^{3/2} \bar{N}^{1/2} \frac{T^{3/2}\left(\frac{1}{M_1}\right)^{1/2}}{P\sigma_1^2}$$

Currently we are assuming that the process of model development, $D_{1\text{-}1^*}$ will be a constant. In the mathematical model, we focused on modeling mass and energy balances. Experiments in which the filling time was fast (approximately 10 [s]) required the inclusion of the momentum balance equations. We will now compare the results of the model with experimental results. In all figures, the dashed lines represent numerical solutions, and the solid lines stand for the corresponding experimental data.

Compression of Gas in the Experimental Vessel

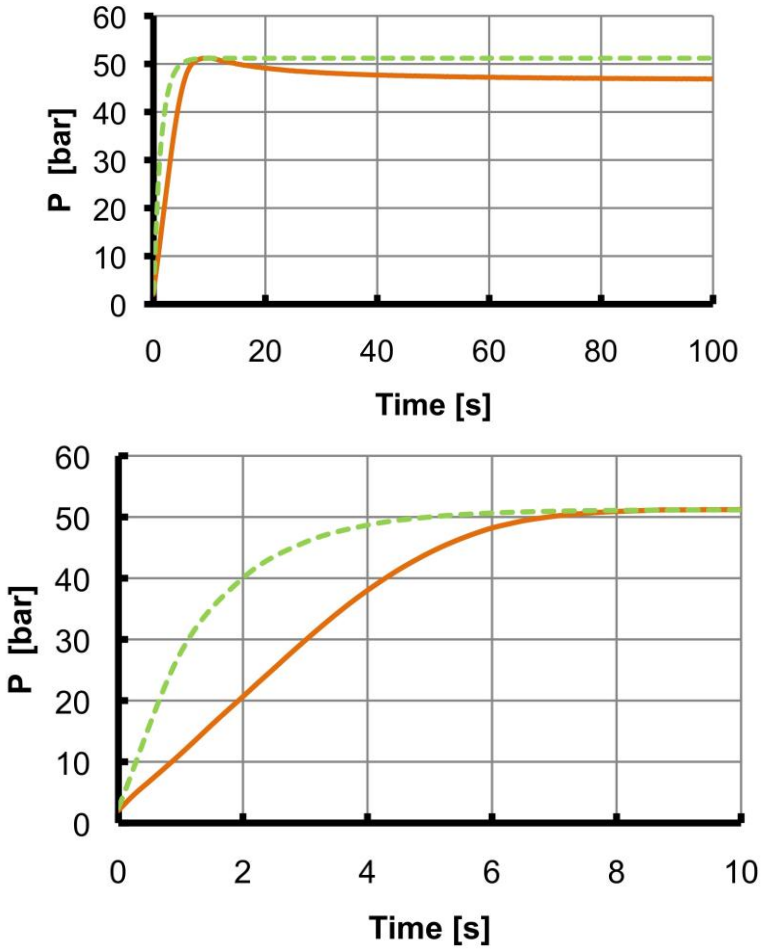

Figures 75 and 76. Comparison between numerical simulation and experimental data during initial compression of gas into the vessel that contains adsorption material.

The numerical simulation of the initial compression process does not take into account adsorption of nitrogen into carbon bed, which takes place within first few seconds of the

experiments. Thus the experimental values shown in Figures 75 and 76 are somewhat lower predicted by the model. Otherwise data and simulations are show similar trends.

Adsorption Process

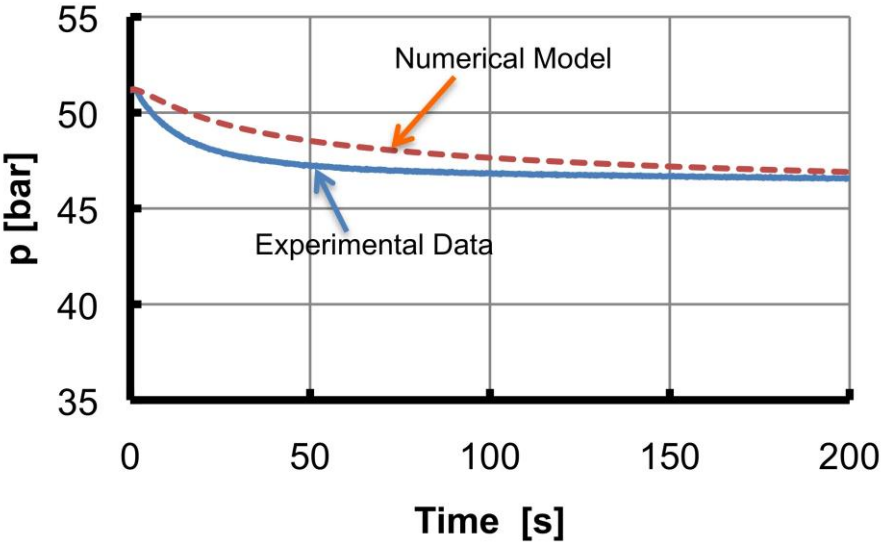

Figure 77.: Comparison of numerical simulation and experimental data for the pressure response in the vessel during adsorption process into carbon bed.

Pressure response due to adsorption recorded outside of the carbon bed is shown in *Figure 77*. After 200 [s] the results are almost identical. This indicates that the initial numerical model underestimates the amount of nitrogen that could be loaded per unit of carbon bed. Results obtained via numerical simulation indicate that there is a need for a proper momentum balance of gas outside the carbon bed to provide more realistic gas mixing and convective heat transfer.

Temperature Change

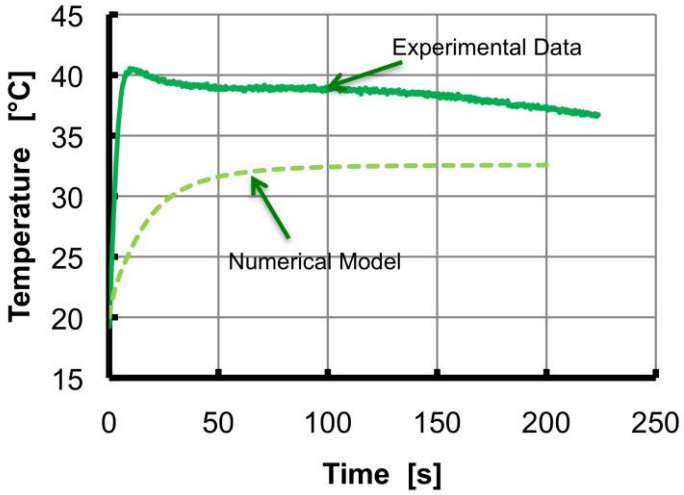

Figure 78.: Temperature change in the carbon bed and numerical simulation of the same change at the identical position in the bed.

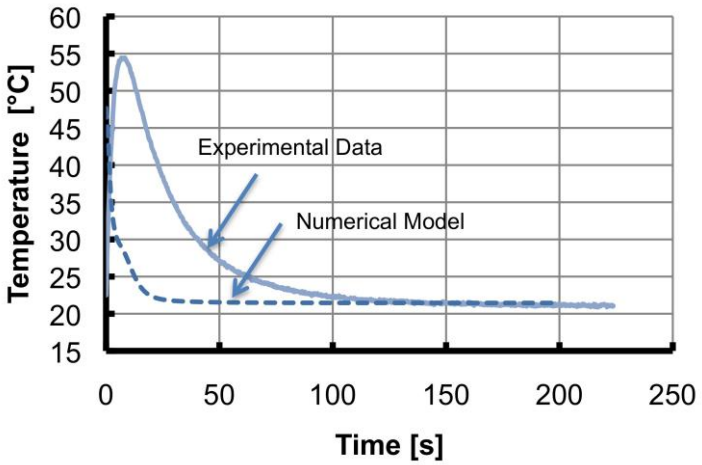

Figure 79.: Temperature change of the gas outside of the carbon bed, near the wall of the vessel.

Figures 78 and 79 show substantial differences between the experimental and simulation results for the temperature in the carbon bed, and the temperature of the gas surrounding the carbon bed near the wall of the vessel.

In both cases numerical predictions underestimates experimental results, which indicates a systematic error in the kinetic model. It is interesting to note that the equilibrium temperatures are almost identical in both cases indicating that the numerical model has correctly models the fundamental processes in the energy balance equation.

Key Findings From Task 1.3 – *The key findings from task 1.3 are summarized below.*

- ***OSU successfully established the capability to model adsorption charging and discharging in a densified media. –*** *This capability was used extensively in Phase 2 to investigate adsorption based cooling.*

- ***The comparison with experimental results indicated that further model development was necessary in Phase 2 -*** Observed discrepancies were remedied in Phase 2 by increasing the complexity of the model and improving accuracy of estimated parameters; especially properties of the carbon/MOF-5 bed.

Task 1.4: Modular Adsorption Tank Insert (MATI) Concept Development – During Phase 1, OSU working with other center members develop a concept for applying the adsorption unit cell described above to thermal management of a complete automotive adsorption hydrogen storage system. The MATI consists of a pressure vessel that is filled with a number of individual unit cells were each unit cell includes a disk or “puck” of densified storage material, a hydrogen distribution and cooling plates. Multiple unit cells are connected with a cooling fluid header and a method of providing hydrogen to each unit cell (either a header or an annular region between the unit cell and the pressure vessel wall). A schematic of the MATI system is show below (Figure 80).

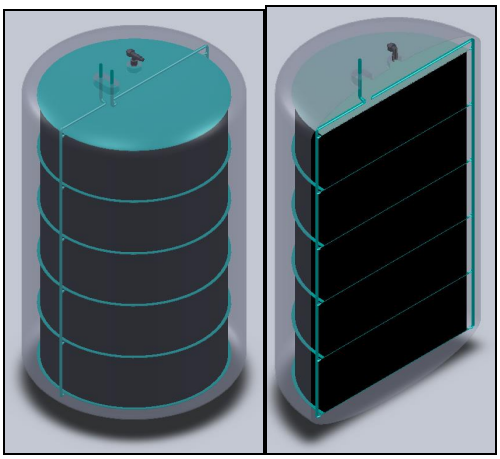

Figure 80 : Phase 1 MATI Concept

During the last few quarters of Phase 1, OSU research activities associated with thermal management of the storage system were focused on the MATI. This includes the experimental and modeling work described above and the fabrication research described below.

Special Study - Simulation of Ammonia Decomposition Reactor – During Phase 1, OSU was requested to investigate the feasibility of using a microchannel reactor to destroy ammonia. Ammonia is a poison for most fuel cells and was being produced as a byproduct of one of the hydrogen storage options being investigated in Phase 1. Ammonia could be removed from the hydrogen stream either be adsorption in a bed of adsorbing material or decomposed in a chemical reactor. The objective of this activity was to determine the technical feasibility of using a microchannel catalytic reactor to decompose ammonia in the hydrogen stream. Some types of metal and chemical hydride hydrogen storage systems produce significant amounts of ammonia during discharge of the storage system and the ammonia concentration must be reduced to 10 ppm before it can be used in a PEM fuel cell.

We used simulation to predict the performance of the ammonia decomposition reactor. Typical results are shown in Figure 81. These results were for a microchannel catalytic reactor that operates at 900 K and 5 bar pressure. The reactor used channels with a channel height of 500 microns and 30 cm long. The incoming hydrogen stream was assumed to have a velocity of 2 m/s with inlet concentrations or 500, 1000 and 2000 ppm. The results showed the following.

- Equilibrium sets a lower limit on the attainable reduction in ammonia concentration. At this concentration, ammonia is being produced by hydrogen reacting with nitrogen at the same rate it is being decomposed at the catalyst

sites. The equilibrium concentration is high because of the high pressure and the large amount of hydrogen available to react with any nitrogen.

- Given the constrain set by equilibrium, the reactor can reduce the concentration of ammonia by a factor of 2.5 to 4 depending on inlet concentration. If this were combined with an adsorption system, this would allow the adsorption system to be reduced in weight by approximately a factor of 2.5 to 4.

- The microchannel reactors reach equilibrium after traveling about 5 cm in the 30 cm long reactor. This means that the microchannel reactor only needs to have a length of 5 cm.

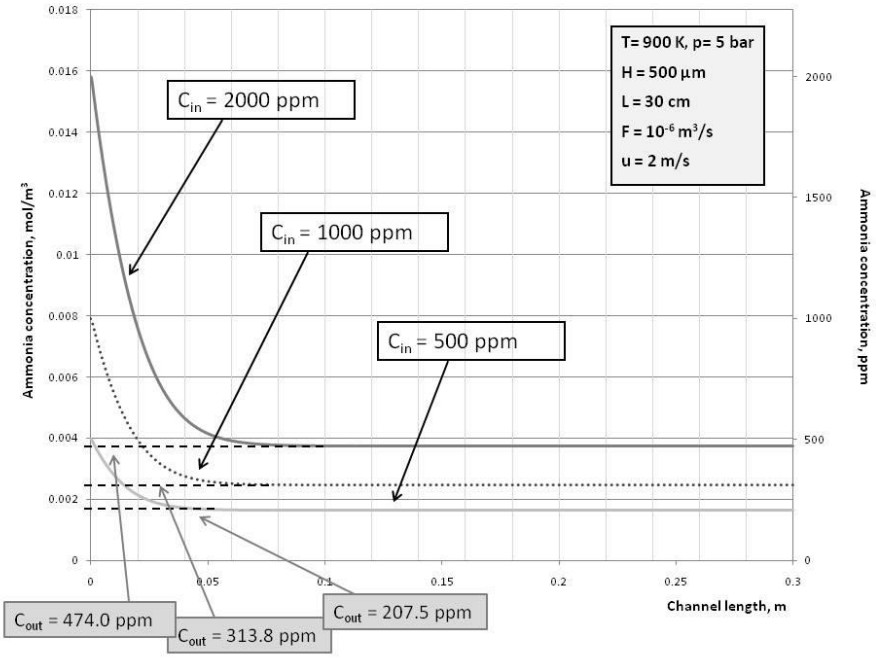

Figure 81; Ammonia concentration as a function of reactor location

Given the constraints set by equilibrium, the microchannel ammonia decomposition reactor can't reach the desired ammonia concentration (10 ppm). However, when coupled with an adsorption system the reactor may be able to reduce the weight of the overall hydrogen clean up system.

The microchannel ammonia decomposition reactor can also be used to decompose ammonia in the exhaust stream from a temperature swing ammonia adsorption system. In this case, during the discharge cycle, a nearly pure stream of ammonia is produced at near atmospheric pressure. The reactor, operating at atmospheric pressure and decomposing pure ammonia stream, would be more productive and would minimize the impact of equilibrium conditions. Figure 82 shows the results for a reactor operating at 1

bar with pure ammonia feed. The results show a factor 40 reduction in ammonia concentration in a reactor that would be about 5 cm long.

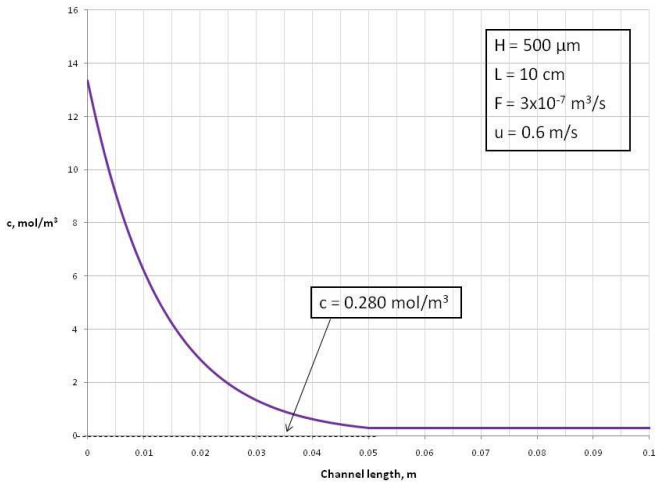

Figure 82, Ammonia Concentration as a function of reactor location for 1 bar pure ammonia feed

Key Findings From Task 1.4 – *The key findings from task 1.4 are summarized below.*

- ***Working with other center members OSU developed a thermal management concept that relies that consists of a large number of identical unit cells with each unit cell contains a puck of densified adsorption media, a cooling/heating plate and a hydrogen distribution system. The cooling/heating plates are connected by an inlet and outlet header which provided cooling/heating fluid to remove/add heat during charge and discharge. -*** *The Modular Adsorbing Tank Insert (MATI) became the focus of our Phase 2 and 3 center activities*

- ***OSU investigated the theoretical feasibility of using an ammonia microchannel reactor to remove ammonia from a hydrogen stream –*** *Given the constraints set by equilibrium, the microchannel ammonia decomposition reactor couldn't reach the desired ammonia concentration (10 ppm) and was not pursued father.*

Task 1.5 Fabrication Research – The objective of this task is to develop a preliminary design of a modular adsorbing tank insert (MATI) for adsorbing materials along with a reasonable fabrication approach and production cost estimate. The current concept involves a modular system that stores an adsorbing material. Our Phase 1 designs were based on using activated carbon as the adsorbing material. In Phase 2 we switched our focus to MOF-5. This task is focused on the development of a manufacturable concept

which successfully meets the most critical DOE goals and on the development of a cost model to evaluate the manufacturing cost of the insert.

The adsorbent tank insert is a modular design containing a heat exchanger. During charging (when hydrogen adsorbs to the carbon), heat is generated and will be removed using microchannel heat exchanging plates. The optimal distance between cooling plates (heat exchangers) was determined in Phase 2 and was selected to ensure the insert can remove enough heat to keep the hydrogen at cryogenic temperatures (77 K, hydrogen adsorbs best at this temperature). For our analyses, we have assumed a distance of 5 cm between cooling plates. The required distance between plates will then determine how many adsorbent modules are required to store a given amount of material. Initially we planned to integrate the cooling plates with microchannel hydrogen distribution plates to providing accelerated radial transport of the hydrogen into the packed bed. The thermal management system will be combined with the adsorbent modules which have been compressed to increase density. Combined, the thermal management system and carbon modules will occupy the inside of a cylindrical pressure vessel.

There are five key requirements that we are focused on for the design of the Phase 1 thermal management system: 1) Remove the heat of adsorption to store 5.6 kg of hydrogen in an adsorbent bed; 2) Minimize mass and cost; 3) Withstand 50 atm differential pressure; 4) Maintain an LN2 pressure drop of less than 4 atm through a cooling fin; and 5) Hermetically seal LN2 circuit from the 50 bar hydrogen atmosphere. A decision was made to make the thermal management system from 3003 aluminum due to its reduced mass and cost versus stainless steel and its resistance to hydrogen permeability.

Tank Insert Concepts: Initially, there were two design concepts that were explored for manufacturability. In both concepts, assumptions include that the adsorbent bed will be provided in a densified state. The first concept uses welding techniques to isolate the coolant whereas the second concept uses compression seals or brazing methods. Potential materials of fabrication were 316 stainless steel and 3003 or 6061 aluminum due to their general weldability and resistance to hydrogen embrittlement.

The concept, shown in the figure below (Figure 83), is a stack of compacted, modular adsorbent beds with a liquid nitrogen cooling plate between each module. Hydrogen is pressurized within the tank and the adsorbent is exposed to the hydrogen atmosphere. The liquid nitrogen is manifolded into each cooling plate using header tubes.

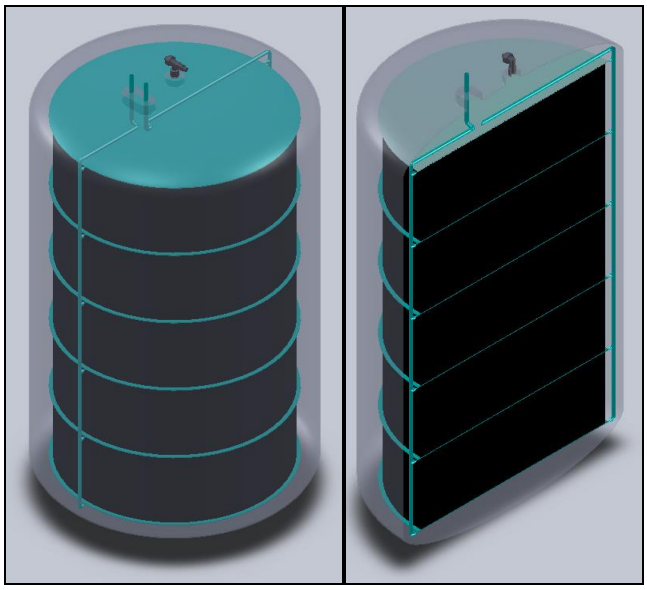

Figure 83: MATI Concept - Isometric view and isometric section view

Cooling Plate Design: The design of the individual cooling plates was a major focus on Phase 1. A CFD simulation of flow and heat transfer in the cooling plate was performed to analyze cooling performance. Liquid nitrogen (LN2) was used as the cooling fluid. The mesh was generated for both fluid and solid regions in the cooling plate. Figure 84 shows the cooling plate geometry and computational mesh. A symmetry boundary was used to reduce computer memory requirements. A two-dimensional hybrid mesh was created to discretize a plane of the model. Four layers of structured cells covered all walls while fluid and solid regions were filled with an unstructured quad-pave mesh. The two-dimensional mesh was then extruded to create the three-dimensional geometry. A summary of boundary conditions and material properties is presented on Tables 16 and 17.

Microchannel flows are typically laminar due to small dimensions but, because the viscosity of LN2 is relatively low, the Reynolds number is much greater than 2,300 and the flow must be considered as turbulent. At the estimated required flow rate for this device the Reynolds number is 54,000 based on inlet diameter (9.6 mm). It is unclear if currently available commercial turbulence models are able to handle micro-scale phenomena. The renormalization group (RNG) k-epsilon turbulence model was selected because it is the preferred option for modeling swirl and low-Reynolds number effects. Flow velocity on the downstream side of pillars is low and modeling in this region may be more accurately achieved using this turbulence option. Enhanced wall treatment was used instead of wall functions to capture near-wall effects. The mesh must be refined in regions of high wall shear stress, therefore solution-adaptive mesh refinement was used to tailor the original mesh to the flow phenomena within the geometry at the given flow rate. A first-order flow solution was attained, then the mesh was adapted based on turbulence parameter (y+) values (see Figure 85). Another first order solution was computed, then the mesh was refined again and the process repeated until

physical parameters (ie: inlet pressure) became steady. The energy equation was then solved.

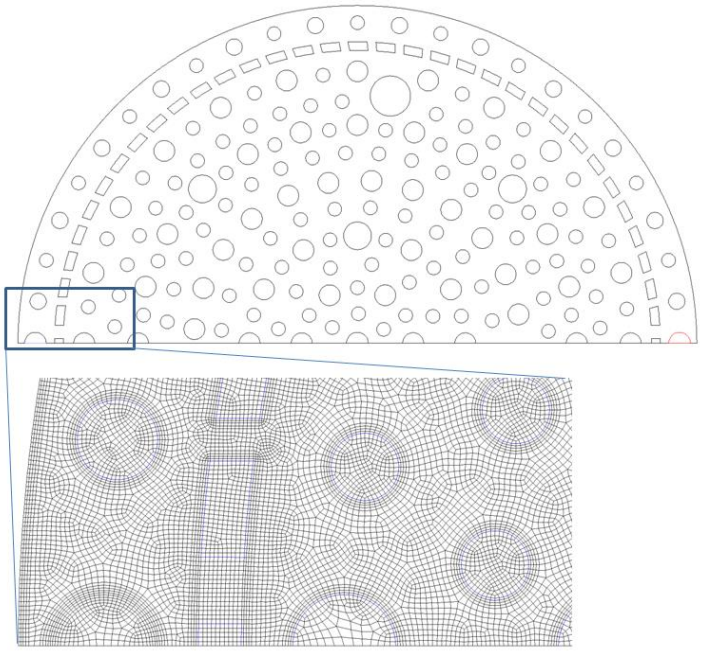

Figure 84. The cooling plate is 30 cm in diameter, one mm thick, and is populated with cylindrical and rectangular pillars to help distribute the flow. The geometry is symmetric. A close up of the unrefined mesh shows a 4-layer structured grid attached to the pillar walls, with fluid and solid regions filled using the quad-pave algorithm.

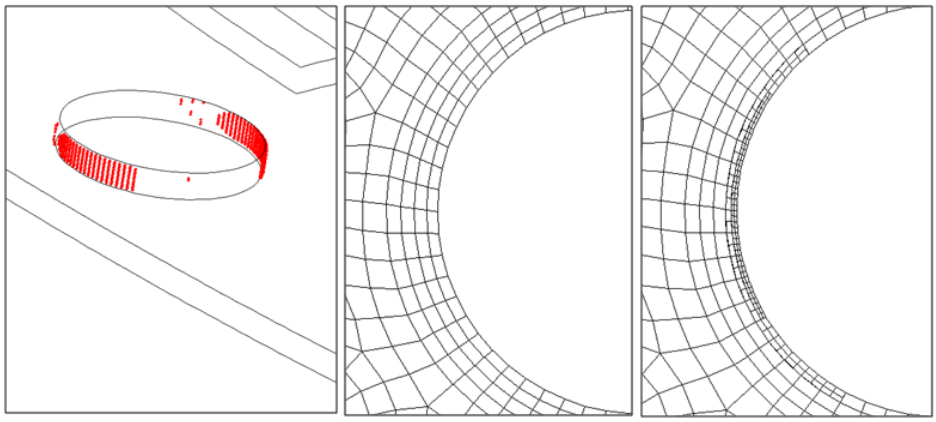

Figure 85. Solution adaptive mesh refinement. Cells are marked in red for refinement based on wall turbulence parameter y+. The center image shows the original mesh and the right shows the mesh after the second adaption. For clarity, the mesh in the solid regions is not shown. Original grid: 2,569,488 cells; Adapted grid: 3,226,557 cells.

Figure 86 shows temperature contours on the bottom (heated) surface of the cooling plate, pillar walls, top of pillars, and flow path lines colored by temperature. The LN2 enters the header at 70K, flows throughout the cooling plate and exits at 77K. Larger diameter pillars conduct heat directly from the adsorbent bed leading to hot spots. Fluid temperature is above 77K in some regions, indicating that localized boiling is likely in an atmospheric pressure environment. Temperature contours on the top wall are shown in Figure 87.

Pressure drop from header inlet to header outlet is 16.4 kPa (about 2.37 psi). As shown in Figure 86, the LN2 is subject to a 90 degree turn when entering and exiting the plate. A re-designed header that introduces LN2 parallel to the plate could reduce pressure drop by approximately 50%.

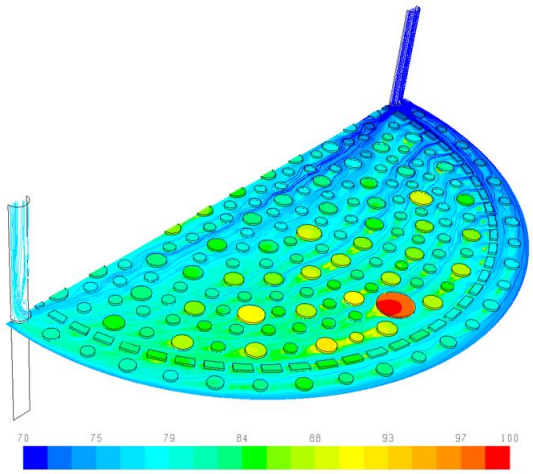

Figure 86. Temperature contours (K) along bottom wall, pillar walls and top of pillars. Flow streamlines released from the inlet are colored by temperature.

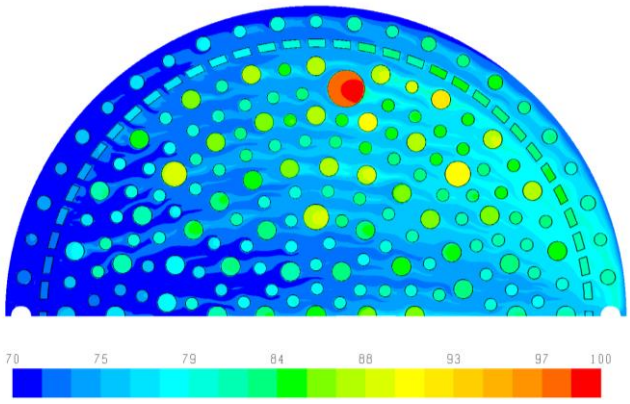

Figure 87. Temperature contours on the top wall of the cooling plate. This wall is in direct contact with the hydrogen distribution plate.

Inlet	Liquid N_2 Velocity = 1.1 m/s, Re = 54,000, turbulence intensity = 4.1% (calculated using $TI = 0.16(Re)^{-1/8}$), turbulent length scale = 0.07 mm (calculated using $L_T = 0.07L$ where L is a characteristic dimension), Temperature = 70K
Outlet	Gage Pressure = 0, backflow temperature 77K
Top Wall	Adiabatic (contacts hydrogen distribution plate)
Bottom Wall	Heat Flux = 12,956 W/m^2 (contacts adsorbent bed)
Symmetry	-----

Table 16. Summary of Boundary Conditions

	LN2	SS316
Density (kg/m^3)	807	8030
Viscosity (kg/m-s)	1.58E-04	-----
Thermal Conductivity (W/m-K)	0.14	16.3
Specific Heat (J/kg-K)	2042	500

Table 17. Properties of liquid nitrogen and stainless steel.

Liquid Nitrogen Header Design: Following the preliminary design of the cooling, we then focused on the LN_2 distribution system. The key requirement that were evaluated was the ability to hermetically seal the liquid nitrogen in the thermal management system from the adsorbed hydrogen bed. Three design concepts were explored for manufacturability. In each concept it was assumed that the adsorbent bed will be provided in a densified state. The three concepts for making hermetic joints were: laser welding; compression seals; and braze bath.

The MATI concept, shown in the figure below, was a stack of compacted, modular adsorbent beds with liquid nitrogen cooling plates and hydrogen distributors between each module. A cooling plate contacted each top and bottom edge of an adsorbent bed so there are two cooling plates to each adsorbent bed. The hydrogen distributors were in between cooling plates to ensure that hydrogen is introduced axially in each bed. Hydrogen was pressurized within the tank so the adsorbent was also exposed to the hydrogen atmosphere where it was introduced radially. The liquid nitrogen was fed into each distributor using header tubes. Manufacturing of the joint required that a laser welding tool access the joint as shown by the red circle in the figure(s) below (See Figures 88-90).

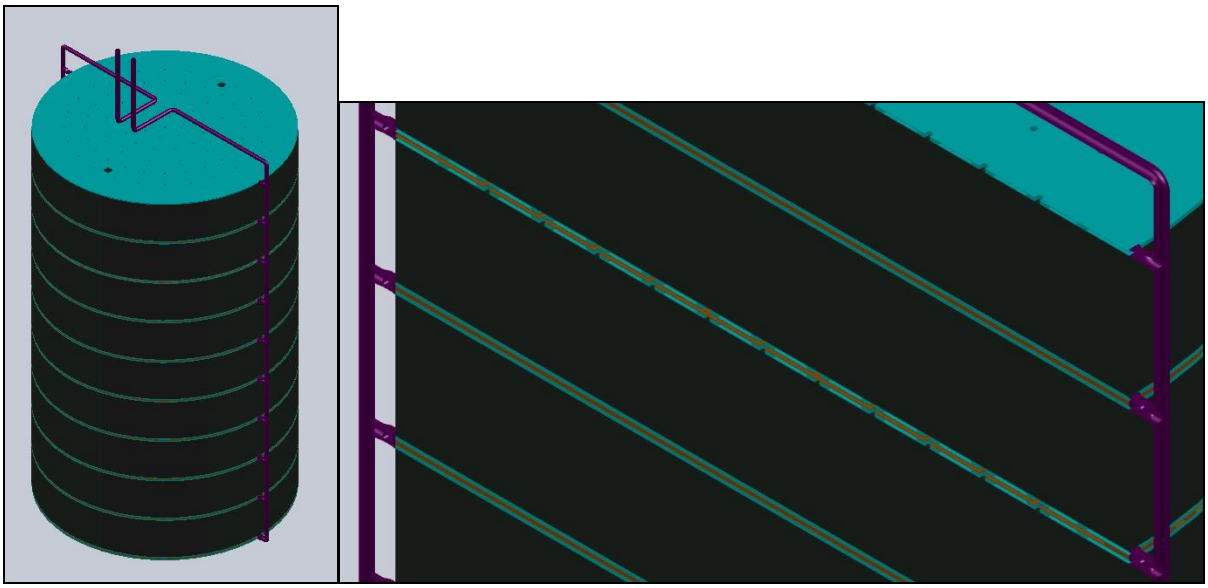

Figure 88: Close-up section view of cooling plates (blue) and distributors (orange)

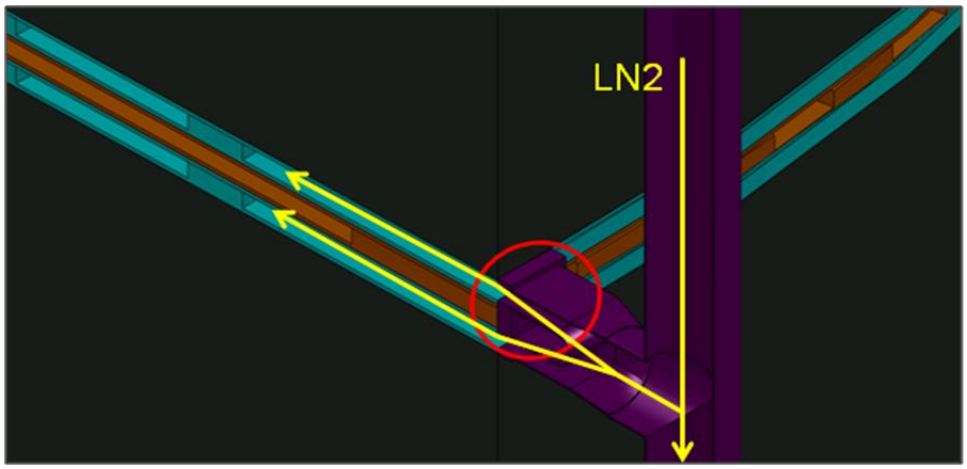

Figure 89: Section view of welded joint (red circle) and LN_2 flow path (yellow)

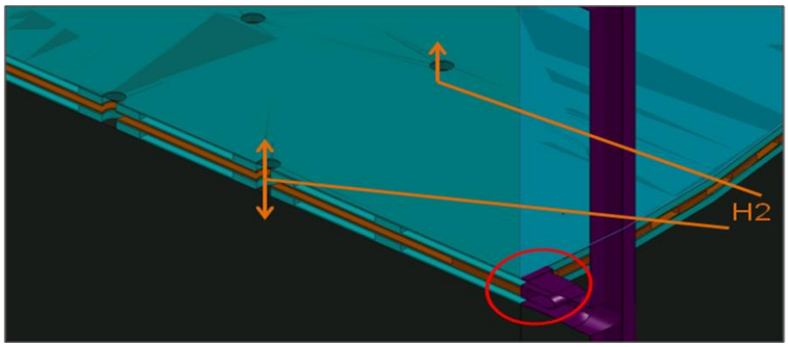

Figure 90: – Section view of welded joint (red circle) and H_2 flow path (orange)

Concept II enclosed each adsorbent bed module within an extruded tube having integral features (headers) for distributing liquid nitrogen between distributor plates. As shown, compressible gaskets were compressed to seal the coolant as it transitions between the modular tubes and cooling plates. The stack was held in compression within an outer shell having top and bottom end caps which were mechanically fastened. Liquid nitrogen was distributed into and out of the top cap which had embedded distribution channels. Distributor plates allowed for flow of hydrogen to the interior of the adsorption module (See Figures 91 to 93).

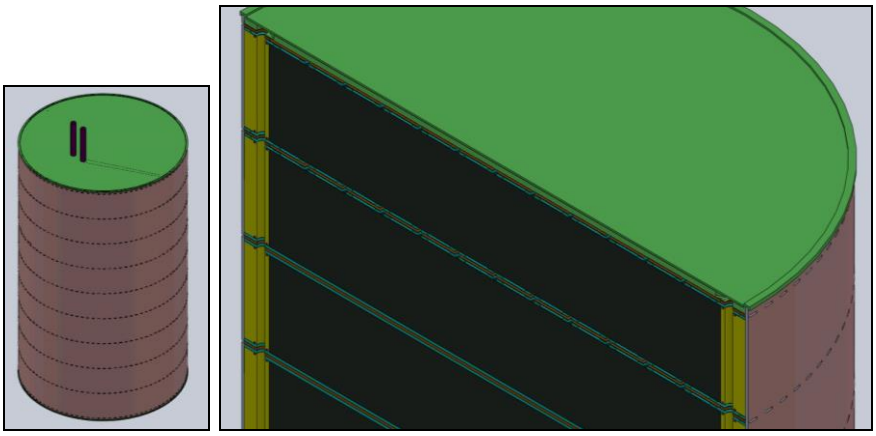

Figure 91: Concept II - Isometric view; isometric section view of cooling plates (blue), distributors (orange)

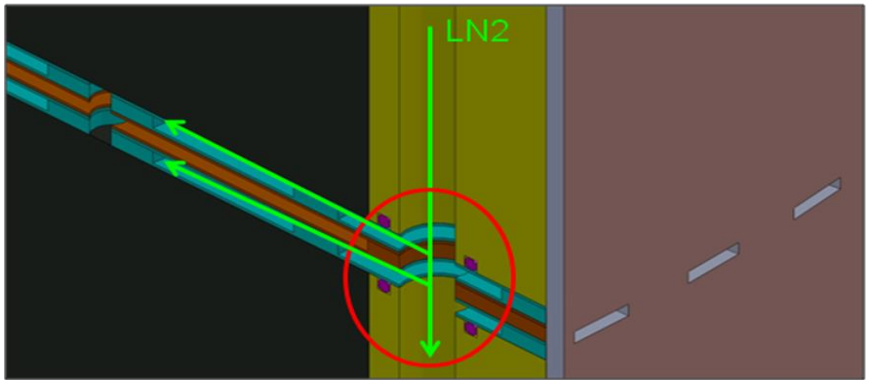

Figure 92: Concept II - Section view of compressed gaskets (pink), extruded tube (yellow), outer shell (light brown), hermetic joint (red) and LN_2 flow path (green)

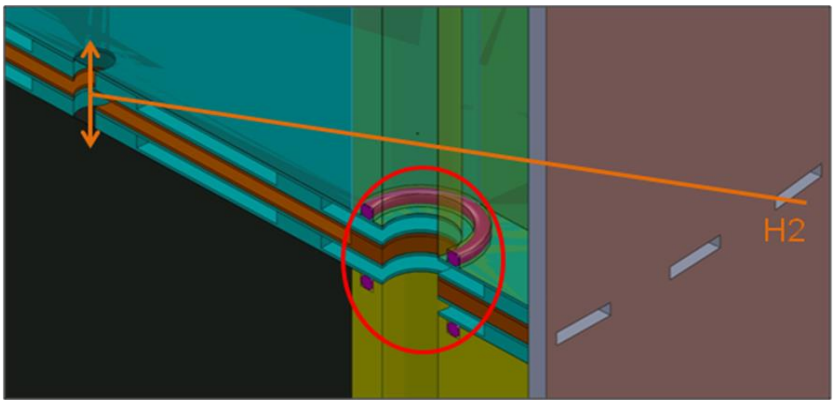

Figure 93: Concept II - Section view of hermetic joint (red) and H_2 flow path (orange)

Concept III was similar in form and function to the initial concept described above. This concept used a braze bath to join the headers to each cooling plate similar to header to fin joining techniques used to fabricate automotive radiators (See Figures 94-96).

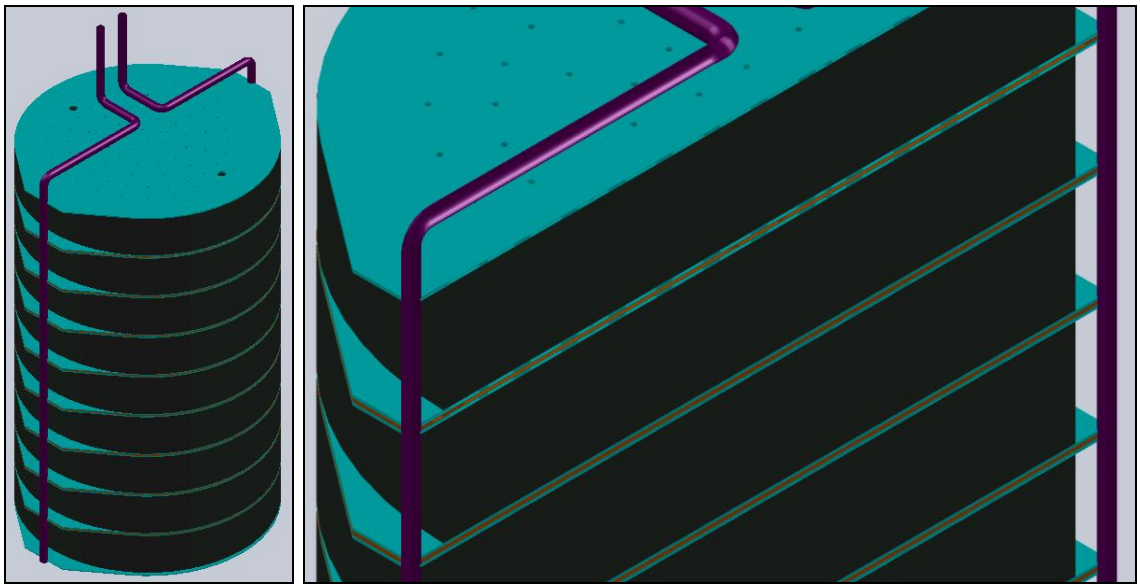

Figure 94: Concept III - Isometric view; close-up section view of cooling plates (blue) and distributors (orange)

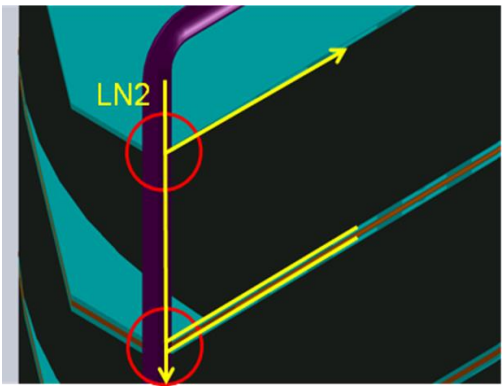

Figure 95: Concept III – Section view of welded joint (red circles) and LN_2 flow path (yellow)

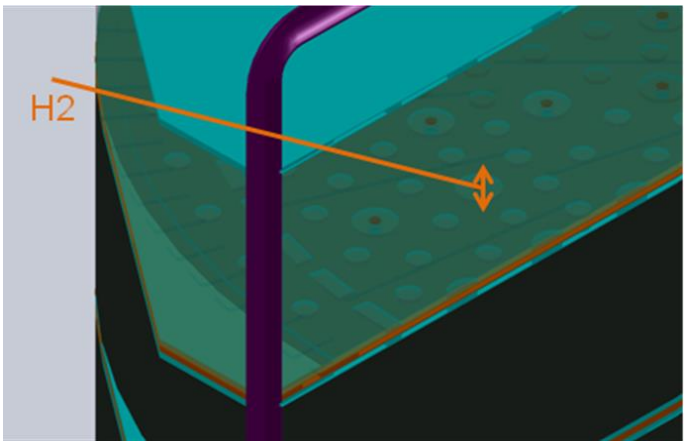

Figure 96: Concept III – Section view of welded joint (red circle) and H_2 flow path (orange)

Manufacturability was assessed through the use of a Pugh analysis developed in concert with Ford Motor Company. Based on the Pugh analysis (Table 18, below), the most manufacturable concept was determined to be Concept III involving the use of a solder bath join cooling/H_2 distribution plates with headers. These manufacturing techniques are similar to those used for automotive radiators.

Pugh Analysis			Concept			
Alternatives	Weight	Baseline	I	II	III	
Criteria						Definition
Quality	1	0	0	0	0	Based on the relative level of quality of the finished concept.
Cost	1	0	1	0	1	Based on the relative cost of each concept based on number of parts and processes required to build the concept.
Reliability	1	0	1	0	-1	Based time to failure due to failure modes of erosion and fatigue.
Manufacturability	2	0	1	0	1	Based on the relative availability of commonly used manufacturing techniques, number of parts and processes and geometry required to build the concept.
Ease of Assembly	2	0	-1	-1	1	Based on the relative number of steps and techniques required to build the concept.
Insert Mass	1	0	1	-1	1	Based on the relative mass of each concept by number of parts, types of parts and materials used to build the concept.
Insert Volume	2	0	1	-1	1	Based on the relative amount of volume each concept will consume due to the size of the insert.
Internal Stresses	1	0	0	-1	0	Based on the relative stresses on the concept that are independent of the stresses encountered due to temperature and pressure gradients of charging and discharging H2 and LN2 flows.
Fluid Separation	1	0	0	-1	0	Based on the ability to achieve and maintain separation between LN2 and H2 and the relative number of processes required to achieve and maintain separation in the concept.
	Total	**0**	**4**	**-7**	**8**	

Key	
Concept I	Laser Welding
Concept II	Compression Seal
Concept III	Braze/Solder Bath

Figure 18: Pugh analysis for assessing the manufacturability of concepts.

Our first iteration of a design using the solder bath joining technique featured flanged ends on opposite sides of the cooling/distributor plates consisting of a bonded stack of two liquid nitrogen cooling plates on either side of a hydrogen distribution plate. This permits the plates to be soldered onto the headers using a solder bath. Solder baths are commonly used in the automotive industry to manufacture radiators. The technique uses low temperature solders that flow over a submerged header-fin joint. For the thermal management system, aluminum solders with melting temperatures below 400°F (204°C), such as Zn-Sn, are being investigated for cost and capability. It is envisioned that the cooling/H2 distribution plates will be fabricated separately and then aligned and soldered onto the headers. Adsorbent packs will be inserted after soldering. This design assumes that the adsorbent will be provided in a compressed state with binder.

The final Phase 1 design of the thermal management system is shown below in Figures 97-98. Inlets and exits were brought into the cooling plates so the headers would be able to fit within a 30 cm inner diameter pressure vessel. Plate thicknesses were reduced to microchannel dimensions to reduce mass and optimize heat transfer. Pillars have been reduced to sub-millimeter diameter in size and increased in number to reduce the span between pillars (less than 3.9 mm).

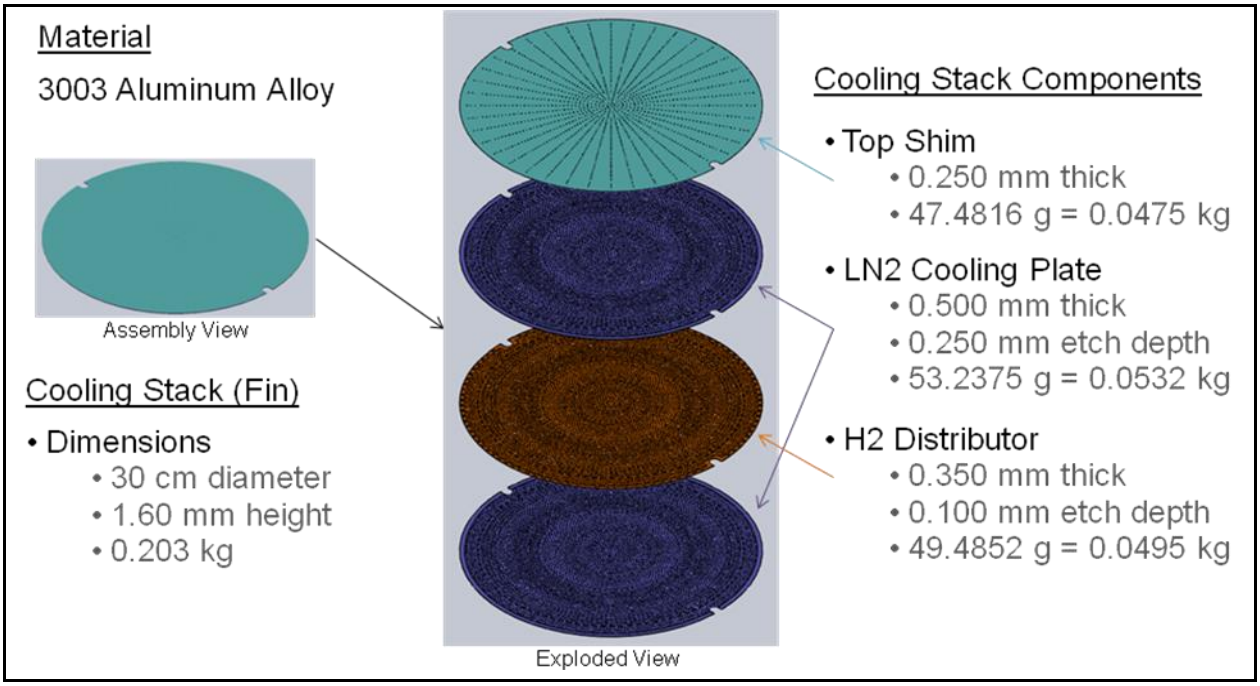

Figure 97: Exploded view of current cooling/H_2 distributor plate with dimensions and mass.

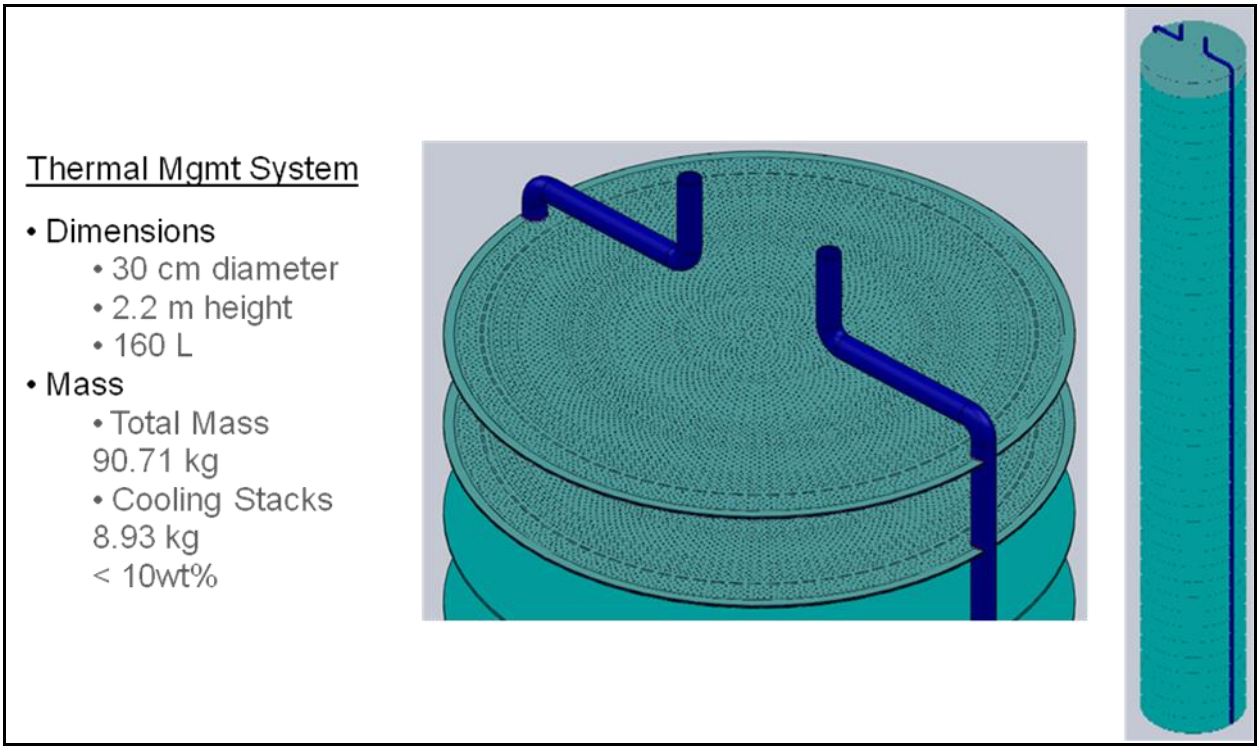

Figure 97: Phase 1 MATI system concept with dimensions and mass.

From a system design standpoint, a series of analyses have been performed to better understand the form and function of the thermal management system. An Excel workbook has been developed based on various assumptions for the thermal management system as well as DOE and HSECoE storage goals. Assumptions included a 5 cm adsorbent bed height and a 30 cm diameter of the cooling/distribution plates. Using a hydrogen storage requirement of 5.6 kg, a storage density of 0.067 kg H_2/kg adsorbent and a heat of adsorption of 4000 J/mol, our calculations showed the need for a volumetric flow rate of 45 cc/s of LN_2 at 70K through each cooling channel. The average velocity entering the LN_2 cooling plates was calculated to be approximately 0.59 m/s leading to a Reynold's number of 29,521, suggesting turbulent flow. At the required flow rates, the pressure drop through the tubular header was estimated to be 0.26 psi (0.02 atm) which is about $1/10^{th}$ of the pressure drop in the cooling plates based on previous CFD analyses. This suggested that the current design should be able to manage proper flow distribution through cooling plates.

To reduce the mass and volume of the cooling thermal management system, fin thickness and LN_2 channel height were reduced to 0.250 mm and the height of the H_2 distribution channel was reduced to 0.1 mm. These changes required refinements to the distance between support pillars to minimize microfin deflection under an H_2 pressure of 50 atm. After deflection analysis, the pillar arrangement were evaluated based on LN_2 pressure drop through the cooling stack.

By reducing the fin thickness to 250 microns, deflection calculations were used to find the span between pillars that would allow for less than a 5% max channel deviation. Plate mechanic calculations for a simply-supported circular disk with constant thickness and a uniformly distributed pressure across one surface showed that a distance of 3.9 mm between pillar centers was acceptable. In addition, improvements in the inlet and exit LN_2 plate headers have reduced pressure drops through the plates.

To verify the plate deflection calculations, a finite element model was developed in Abaqus to better account for the specific geometries within the cooling plate. A mesh of the cooling plate is shown in Figure 99.

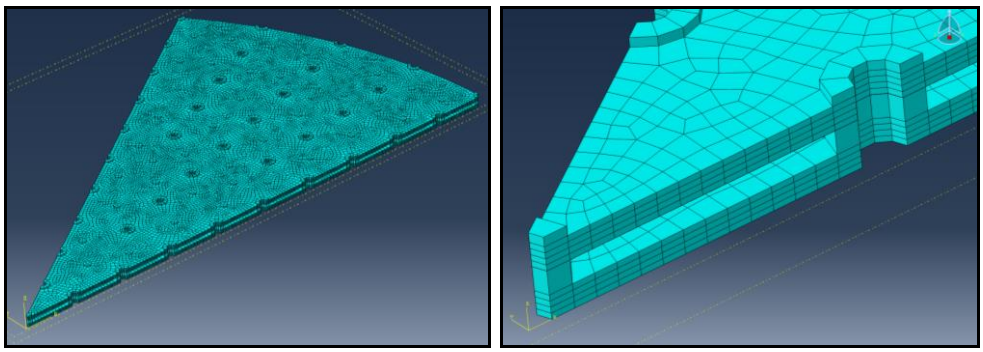

Figure 99: Mesh of radial slice of the LN_2 cooling channel.

System volume calculations showed that the system will be around 0.159 m^3 = 160 L and the mass of the adsorbent bed with the thermal management system will be just over 90 kg. By itself, the thermal management system will have a mass of only 8.93 kg, approximately 10% of the adsorbent bed. Within a 30 cm diameter, the inside of the adsorbent tank would need to be approximately 2.17 m long.

A manufacturing plan was used to develop of a cost model. A process flowchart is shown below (Figure 100) which outlines methods for manufacturing the thermal management system using techniques common within the automotive industry.

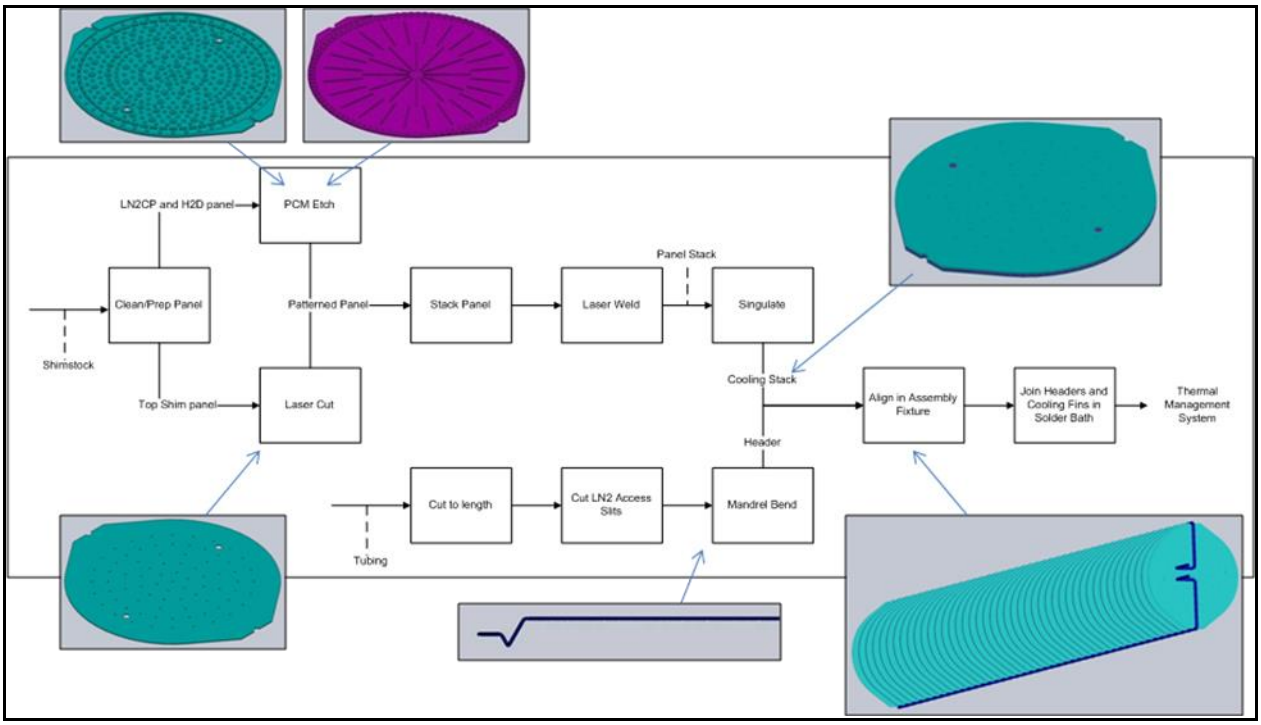

Figure 100: Process flow chart to manufacture a thermal management system

A bottom-up cost model was developed using this process flow chart. The cost model produced a cost of goods sold at a given production volume.

Key Findings From Task 1.5 – *The key findings from task 1.5 are summarized below.*

- *Brazing was identified as the preferred approach to attaching the cooling plates to the headers*

- *Based on thermal and mechanical simulation we developed a theoretical Phase 1 design for the cooling plates. These plated combined cooling and heating with hydrogen distribution. Ultimately in Phase 2 we separated these functions into two different plates.*

4.4 PHASE 1 CONCLUSIONS – Conclusions from the Phase 1 research are summarized below.

- **The Microchannel combustor/heat exchanger is a significant improvement when compared to existing combustion systems** –The microchannel combustor represents a factor of 10 reduction in volume when compared to a state of the art heat exchanger developed by Sandia National Laboratory for automotive hydrogen storage applications. The volume reduction was primarily due to the ability of a microchannel combustor to prevent gas phase combustion. Both simulation and experimental results confirmed the high performance predicted for this device. As part of assembling the test articles, we successfully demonstrated all of the fabrication processes needs for high volume production.

- **Experimental Capabilities –** OSU successfully established the capability to experimentally investigate room temperature charging and discharging for both metal hydride and adsorption systems using densified media. Several issues associated with the experimental technique were identified and were subsequently resolved in Phase 2. In Phase 2 the test apparatus was modified to allow testing at cryogenic temperature.

- **Simulation** – Simulation capability were established and preliminary comparisons with experimental data demonstrated several areas where the modeling needed additional detail. These were addressed in Phase 2

- **The MATI has important impacts on the Adsorption System Design** – The use of the MATI has several important system impacts including 1) the MATI allows the use of densified media with a very high packing factor. The MATI allows up to 95% of the volume of the adsorption pressure vessel to be media and 2) since the cooling fluid and hydrogen are separate; the MATI allows the use of fuel cell waste heat for discharge though a small amount of supplemental heating from hydrogen combustion is required.

- **The MATI concept is Manufacturable** – Fabrication studies demonstrated that the MATI could be fabricated out using brazing to attach the headers to microchannel cooling plates and a preliminary manufacturing plan has been developed.

- **Results of special studies** – The in-Tank combustion heater study showed that the concept was technically feasible but safety concerns were sufficiently great to prevent further investigation of the concept. The ammonia decomposition reactor could be very small but equilibrium conditions prevented the reactor from reaching the required reduction in ammonia concentration in the fuel cell hydrogen feed.

Based on these results the decision was made to further develop the MATI and the microchannel combustor/heat exchanger in Phase 2.

4.0 PHASE 2 ORGANIZATION AND RESULTS

This section presents and overview of Phase 2. Section 4.1 discusses the objectives of OSU's Phase 2 activities while Section 4.2 discusses the Phase 2 scope of work while Section 4.3 presents the technical results by task. Section 4.4 presents a summary of conclusions from the Phase 2 research activities

4.1 PHASE 2 OBJECTIVES – During Phase 1 of the center, OSU identified two applications of microchannel technology that had the potential to significantly improve the performance of an adsorption hydrogen storage system. These technologies include

- **Microchannel Combustor/Heat Exchanger** (Enabling Technology) – In Phase 1 we demonstrated the impact of using microchannel technology for providing combustion heat to drive the desorption of a metal hydride system. In Phase 2 we switched to adsorption hydrogen storage and modified the microchannel combustor/heat exchanger technology to provide supplemental heating for the discharge of and adsorption system. In this application most of the thermal energy used for discharging the adsorption system comes from the fuel cell waste heat but some supplemental heating is required to meet DOE's performance requirements for storage discharge. The microchannel combustor/heat exchanger provides this waste heat in an extremely compact device.

- **Modular Adsorption Tank Insert** (Adsorption Storage Technology) - . In this design, the tank is filled with densified adsorption media in the form of 1.5 to 2.5 cm thick disks (pucks) which have a diameter slightly less than the internal diameter of the tank. A standard unit cell consists of a stack of a cooling plate, a media puck, a hydrogen distribution plate, a second media puck and then a second cooling plate.

  During charging, hydrogen is introduced into the hydrogen distribution plate and diffuses through the puck. As the hydrogen diffuses, it is adsorbed by the media producing heat that must be removed. Simultaneously, liquid nitrogen is passing through the cooling plates. As the heat of adsorption is produced, it is conducted through the media to a cooling plate where it is transferred to the liquid nitrogen which leaves the cooling plate at a slightly elevated temperature (90K) and is returned to the forecourt .The heat of adsorption is removed by two processes. First, the low temperature hydrogen being used for adsorption is at a temperature lower than the bed temperature and will remove some of the heat of adsorption as the hydrogen increases in temperature to the temperature of the bed. The balance of the heat of adsorption is removed by having the heat conduct through the bed to the cooling plates.

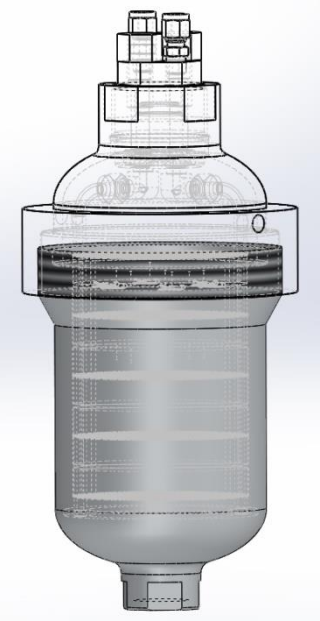

Figure 1: MATI prototype assembly inside of 2 L aluminum tank

The complete MATI consists of a number of cells (typically between 10 and 50) which are connected by headers to provide liquid nitrogen to the cooling plates and collect it so that it can be returned to the forecourt. In our current embodiment, the MATI has a diameter slightly smaller than the inside diameter of the tank, forming an annular region between the outside of the MATI and the inside wall of the tank. This allows hydrogen to flow in the annual region to the hydrogen distribution plates. An alternative configuration would eliminate the annual region and utilize distribution headers to deliver and collect the hydrogen. Use of distribution headers allows an increase in the diameter (approximately 2 mm or larger) and an improvement in the overall volumetric and gravimetric efficiency of the device.

In phase 2 OSU focused on model development, experimental model validation and fabrication studies to determine the technical and economic feasibility of these two technologies. Task 2.1 was focused on the development of the microchannel combustor/heat exchanger for adsorption applications while tasks 2.2 through 2.7 were focused on the development of the MATI.

4.2 PHASE 2 TASK STRUCTURE – The Phase 2 research activities were organized into seven tasks. Each is described below.

Task 2.1 Enabling Technologies – In Phase 2, OSU activities related to Enabling Technologies was focused on conducting an experimental and simulation based characterization of an integrated microchannel hydrogen combustor-heat exchanger (μ-CHX) which can be used to provide supplemental heating for discharging an adsorption storage system.

Task 2.2 Cryogenic Test Apparatus Development: This activity involves the development of two cryogenic test apparatus, one for separate effects testing and one for integrated testing with a media. The separate effects test apparatus focused on heat transfer and pressure drop testing of MATI cooling plates in cryogenic conditions. The integrated test involved testing of a MATI unit cell including a cooling plate, hydrogen distribution, and a puck of densified MOF-5. The integrated test apparatus was used for model validation during charge and discharge cycles.

Task 2.3 Test Article Design and Fabrication: This task is focused on the design and fabrication of test articles which were used in the experimental investigations documented below. Test articles developing during this task include: 1) single cooling plates for separate effects testing, 2) multi cooling plate 5 cm dia. stainless steel test articles with three cooling plates and LN_2 headers and 3) Densified pucks with embedded conduction enhancement.

Task 2.4 Experimental Investigations: Experimental investigations include: 1) separate effects tests (cooling plate heat transfer coefficient, pressure drop etc.), multi-plate test article thermal and mechanical testing and 3) integrated testing where a cooling plate is integrated with media.

Task 2.5 Model Development and Validation: This task focused on the validation of the integrated simulation model used to model the phenomena occurring in the integrated test facility and the development and application of an integrated model (including heat and mass transfer and adsorption reactions) which could be used for design studies. This task also included the application of the design model to two problems: 1) the impact of conduction enhancement on adsorption and 2) desorption.

Task 2.6 Fabrication Investigations: This task consisted of number of studies focused on fabrication issues that helped establish the technical feasibility of large scale manufacturing of a MATI. The focus was on establishing the feasibility of using aluminum as a material of fabrication. The use of aluminum in a MATI required the demonstration of 1) the ability to bond aluminum lamina to form cooling plates (Welding Studies), 2) the ability to pattern aluminum lamina to form cooling (Stamping studies), and 3) the ability to attach the cooling plates to the headers (brazing studies).

Task 2.7 System Studies: This task involves system design studies focused on assessing the impact of design changes to the modular adsorption tank insert on the performance, size, weight and cost of a commercial storage system in large scale production. This activity included production cost modeling using a “Bottom up” manufacturing cost model.

4.3 TECHNICAL RESULTS: The technical results of the seven tasks discussed above are discussed by task in the sections below.

Task 2.1 Enabling Technologies: OSU Phase 2 activities related to enabling technologies are focused on the development of thermal devices for balance of plant

applications. OSU is conducting an experimental and simulation based characterization of an integrated microchannel hydrogen combustor-heat exchanger (μ-CHX) which can be used to provide supplemental heating for discharging an adsorption storage system. This builds on our Phase 1 investigation of a combustion system for applications in a metal hydride storage system. **The objective of this task is to complete the design and experimental validation of the adsorption system supplemental heater.**

A microscale combustor heat exchanger (μCHX) is being considered to increase the temperature of hydrogen upstream to the fuel cell in cold start conditions. The goal defined for this μCHX is to increase the temperature a hydrogen flow from 200 K to 233K or higher. The hydrogen flow rate may vary from 0.5 g/s to 2 g/s. Based on safety and availability considerations in the use of hydrogen gas, for this stage of the project nitrogen will be used in the μCHX as the working fluid.

Microscale Combustor Time Scale Analysis - As reported in our Phase 1 results, several phenomena related to combustion, flow and heat transfer are contributing to the observed efficiency trends in the system. A more in-depth analysis was conducted on the unit cell geometry shown in Fig. 2. To better understand these effects. The simulation method was validated with available experimental data. The simulation convergence was decided when the residuals approaches steady values asymptotically and when the relative residuals were smaller than 10^{-3} in all cases (less than 10^{-7} for continuity, momentum, energy and major species). In these simulations, the dilute approximation has been considered for diffusion of different species, which is more accurate than using constant diffusion coefficients in prior simulations.

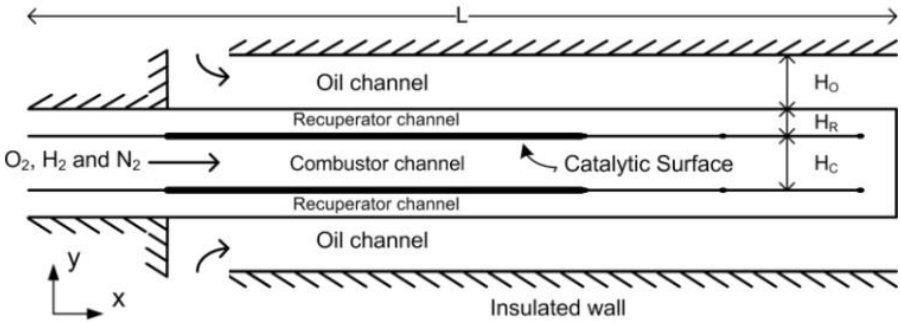

Fig. 2: Schematic geometry of the μCHX

Parametric trends observed while changing the inlet gas velocity were investigated. Increasing the inlet gas mixture velocity increases the amount of chemical energy input by hydrogen because the equivalence ratio is kept the same. The effect of increasing inlet velocity on efficiency depends on the length of the catalyst and can be significant for small catalyst lengths. There are three different time scales that are important for catalytic combustion in a combustion system, namely the residence time, diffusion time, and reaction time. Residence time refers to the time that the flow has before it leaves the desired section (in this case the catalytic surface), and is therefore defined as

$$t_r = L_{Cat} / \overline{V}$$

where L_{Cat} is the length of the catalyst and $\overline{V}$ is the averaged velocity at a cross section of the combustion channel.

The second time scale characterizes the time it takes for reactants to reach the surface, where the heterogeneous catalytic chemical reaction occurs. In flows with low Reynolds numbers (laminar flows) the turbulent mixing is very small; therefore the species mixing will be by diffusion. The diffusion time scale is defined as

$$t_d = R^2 / D_k$$

where R is the cross- stream distance and D_k is the diffusivity of kth species.
The third time scale is known as the reaction time and is the time to have a complete reaction and is defined as the initial value of the fuel over the rate of fuel consumption. In a chemically reacting flow it can be calculated based on the mass flux of incoming fuel

$$t_c = \frac{\frac{r_{H_2,in}}{M_{H_2}}}{\frac{\dot{m}_{mix}}{M_{H_2}} \frac{dY_{H_2}}{dx}}$$

Figure 3 shows the three time scales estimated based on local values along the channel for inlet gas mixture velocity of 4 m/s. The residence time is calculated by dividing the remaining length of the catalyst to the local velocity of each cross section.

For a completed reaction, the reaction time should be smaller than residence time. In addition, the diffusion time should be less than both reaction and residence times to make sure that the fuel molecules reach to the catalyst surface before they leave the catalyst section. To make the comparisons simpler and easier to understand, two dimensionless numbers are used which are Damkohler numbers (Da_1 and Da_2) where

$$Da_1 = \frac{t_r}{t_c}, Da_2 = \frac{t_d}{t_c}$$

$Da_1 > 1$ and $Da_2 < 1$ imply that in that specific geometry and flow characteristics, the reaction time is small enough compared with the residence and diffusion times for the reaction to be complete. It should be noted that Da_2 is calculated based on the diffusion time of oxygen instead of hydrogen because as it can be seen in Fig. 3, diffusion times for oxygen is larger than that of hydrogen and hence oxygen diffusion presents the limiting value.

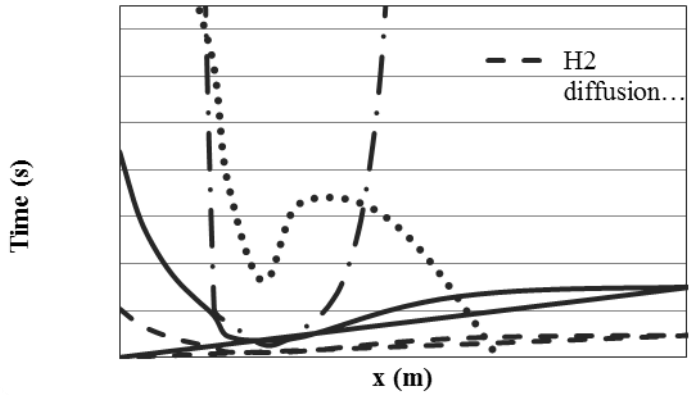

Figure 3. Different time scales along the length of the combustion channel

A parametric study of residence time effects for the case with the geometry shown in Fig. 1 and fluidic parameters (Table.1) was undertaken. The residence times varied (based on the inlet velocity) from 1.5 ms (Re=122.5) to 7.5 ms (Re=24.6). The effect of changing residence time can be seen from Fig. 4 where efficiency index and hydrogen conversion are shown. The efficiency increases by increasing the residence time, however the hydrogen conversion doesn't follow a specific trend. Therefore, the change in residence time cannot alone describe the conversion trends. In Fig. 5 the averaged reaction times for different residence times are plotted and it can be seen that the three cases with the lowest reaction times have the highest hydrogen conversions.

Table 1. Summary of geometrical and thermo-fluidic parameters

Parameter	**Value**
L (mm)	30
H_C (μm)	300
H_O (μm)	300
Oil inlet velocity (m/s)	0.01
Gas mixture inlet velocity (m/s)	2-10
Equivalence ratio (ϕ)	1
Catalyst length (mm)	15
Oil inlet temperature (K)	300

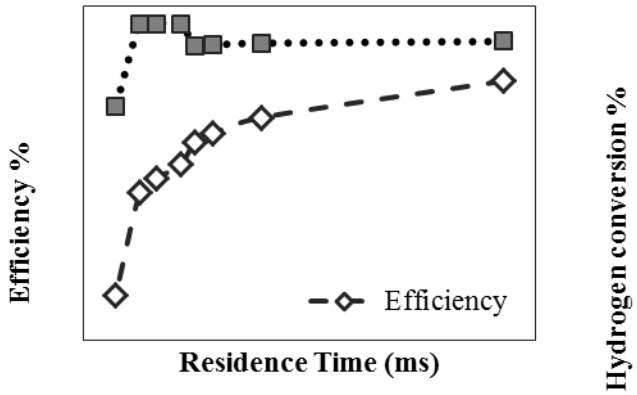

Figure 4. Efficiency index and hydrogen conversion at different residence times.

The variation of local Da_1 along the channel is shown in Fig. 6 for three different residence times. The peaks show locations of high conversion rates. When the residence time is higher, almost all of hydrogen combusts at the beginning portion of the catalyst, corresponding to the location where the conversion rate is the highest and a peak can be observed in the Da_1 plot. With decreasing the residence time, the plot tends to flatten because hydrogen exists until the end of the catalyst area.

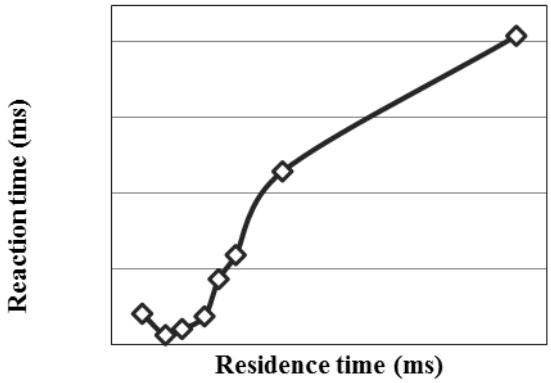

Figure 5 Averaged reaction times at different residence times.

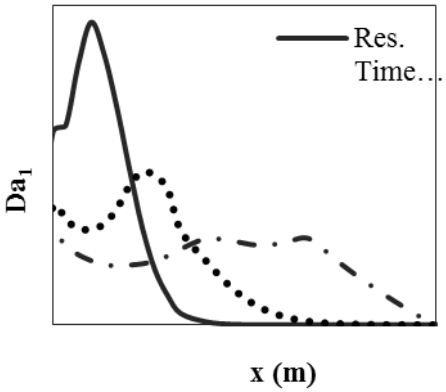

Figure 6. First Damkohler number along the channel for different residence times

Close Out of Metal Hydride Storage System Combustor Development: The design of the microscale integrated combustor heat exchanger with recuperation (μCHX) for the purposes of desorption of hydrogen from a metal hydride bed has been described in Phase 1. In this section we will describe the effect of variation of different geometrical and thermo-fluidic parameters on the efficiency of the device. The parameters investigated included catalyst surface length, catalyst location, gas and oil inlet velocity, oil inlet temperature, channel length and height, and equivalence ratio and are summarized in Table 2. The effect of these parameters was captured non-dimensionally using Da_1, Da_2 and Pe which are defined above.

Table 2. Fixed parameters for each parametric variation

	Varied Parameter						
Parameter	Catalyst length	Channel length	Channel Height	Gas inlet velocity	Equivalence ratio (f)	Oil inlet velocity	Oil inlet temperature
Catalyst bed length (mm)	5-25	10	10	10	10	10	10
L (mm)	30	15-60	30	30	30	30	30
H_C (μm)	300	300	300-700	300	300	300	300
Gas inlet velocity (m/s)	4	4	4	3-7	4	4	4
Equivalence ratio (f)	1	1	1	1	0.3-1	1	1
Oil inlet velocity (m/s)	0.01	0.01	0.01	0.01	0.01	0.01-0.03	0.01
Oil inlet temperature (K)	300	300	300	300	300	300	300-370

For the parameter space considered, a catalyst surface length of 15 mm presents a compromise between high efficiency and increased cost of the noble metal catalyst. It was found that higher hydrogen conversion resulted from higher residence time, which means that a longer catalyst bed and lower velocities increase the total efficiency. In addition, the simulation results showed that although hydrogen conversion decreases by increasing the equivalence ratio, the efficiency does not change much, owing to an increase in effectiveness with equivalence ratio. Furthermore, changing oil inlet velocity or temperature does not have a significant effect on hydrogen conversion. However, higher oil inlet temperatures result in lower efficiencies.

As described above, three different dimensionless numbers (Da_1, Da_2 and Pe) were used to explain the effects of different geometrical and fluidic parameters. First Damkohler number has the most effect on hydrogen conversion and efficiency; however, Da_2 as well as Pe are the dominant players where the reaction rate is limited by diffusion, for example in combustors with larger channel heights.

Based on the estimates of efficiency index from simulations, a predictive correlation for efficiency (η) was developed,

$$\eta = 0.93\exp\left(-0.17 Da_1^{-1.5} Da_2^{0.5}\right) \quad (1)$$

which can also be written as

$$\eta = 0.93\exp\left(-0.17 Da_1^{-1} Pe^{0.5}\right) \quad (2)$$

The correlation is valid for the μCHX geometry studied and over the range of parameters for which it was developed, as summarized in Table 2. Figure 7 compares predicted efficiencies to the efficiencies found by simulations. Equation 1 can predict 95% of the numerical results within ±10% error and 70% of the numerical results within ±5% error.

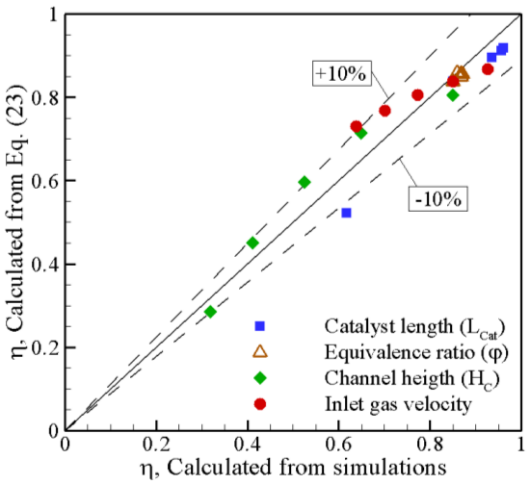

Figure 7. Calculated efficiencies versus efficiencies predicted by Equation 1

As suggested by Eq. 1, a high efficiency index can be achieved by increasing Da_1 and decreasing Da_2. A more visual indication of the regions of high efficiency is provided by a contour map of efficiency in a Da number space as shown in Fig. 8. It can be seen from Fig. 8 that both Da_1 and Da_2 have significant effect on η and one should try to operate the μCHX in the upper right corner of the plot (high Da_1 and low Da_2) for high efficiency. Da_1 has stronger effect on η when Da_1 is less than 0.5 and Da_2 is greater than 0.2. In this region, η becomes nearly independent of Da_2 when it reaches the value of 0.3. This region, wherein efficiency is limited by Da_1, has low efficiency and must be avoided in operation of the μCHX. On the other hand, for Da_1>0.5 and Da_2<0.3, the μCHX operates in a region of the parameter space which is sensitive to Da_2. In the rest of the parametric space, both Da_1 and Da_2 are important in determining the efficiency of the μCHX.

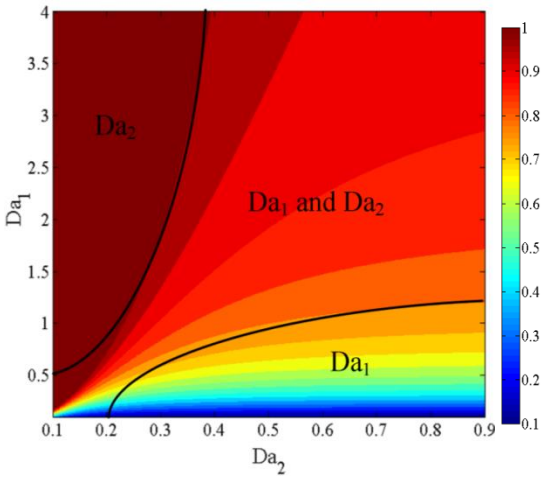

Figure 8. Contours of η at different Damkohler numbers

Pressure drop is also important when designing a heat exchanger and should be considered along with efficiency. A contour map of pressure drop of the simulated cases in the Da_1-Da_2 space is plotted in Fig. 9. It can be seen that lower Da_2 and Da_1 have highest pressure drops. A low Da_2 corresponds to smaller channel cross-section while a lower Da_1 corresponds to a higher inlet velocity, both of which increase pressure drop through the device.

Based on the efficiency map, it can be concluded that lower channel heights (lower Da_2), lower inlet velocities and longer catalyst beds (higher Da_1) lead to higher efficiencies; however, depending on the systems application and limitations, pressure drop may place a constraint on the operating space.

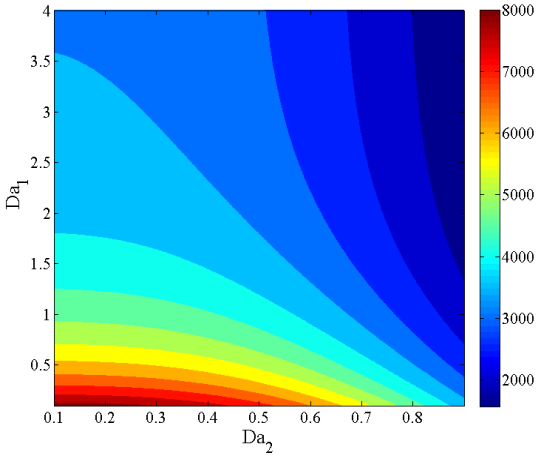

Figure 9. Contours of Pressure drop (in Pa) at different Damkohler numbers

Considering both contours of efficiency and pressure drop, the Da_1-Da_2 space for the µCHX operation can be divided into four regions as shown in Fig. 10.

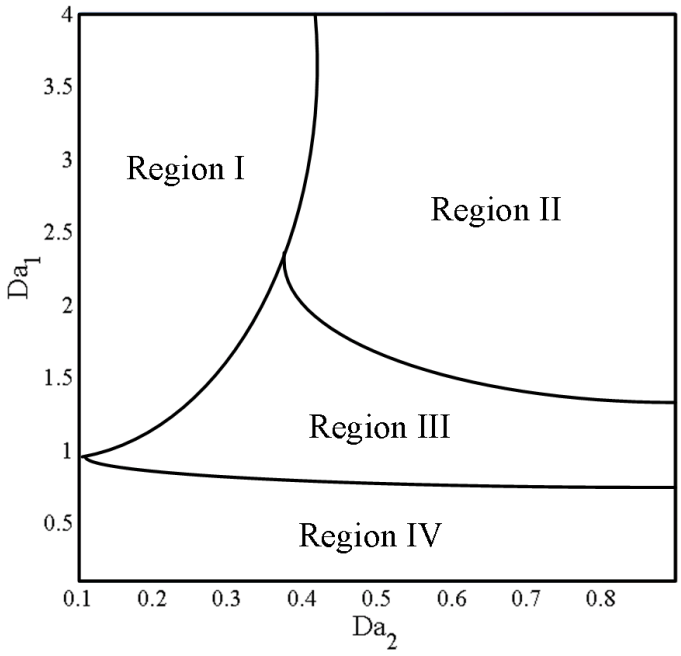

Figure 10. Diagram of different regions based on η and ΔP- The regions are described in Table 2.

Table 3 summarizes the description of these regions and gives examples of physical parameters that one can use to attain the performance characteristics indicated by that region.

Table 3. Different regions (Fig. 10) and their performance ranges

Region	Range of η	Range of ΔP (Pa)	Example of physical variable combinations
I	$\eta > 90\%$	$3000 < \Delta P < 4500$	$3 \text{ (m/s)} < V_g < 4 \text{ (m/s)}$, $300 \text{ (μm)} < H_C < 400 \text{ (μm)}$, $L_{Cat} > 10 \text{ (mm)}$
II	$75\% < \eta < 90\%$	$2000 < \Delta P < 3000$	$V_g < 3 \text{ (m/s)}$, $500 \text{ (μm)} < H_C < 700 \text{ (μm)}$, $L_{Cat} > 15 \text{ (mm)}$
III	$50\% < \eta < 75\%$	$4500 < \Delta P < 5500$	$5 \text{ (m/s)} < V_g < 10 \text{ (m/s)}$, $300 \text{ (μm)} < H_C < 700 \text{ (μm)}$, $L_{Cat} < 10 \text{ (mm)}$
IV	$\eta < 50\%$	$5500 < \Delta P$	

In cases where very high efficiencies are necessary and pressure drop is of secondary importance, region I is the best choice. If both high efficiencies and low pressure drop is considered, region II satisfies the needs. Region III has moderate efficiencies and pressure drop and Region IV has either poor efficiencies or high pressure drops, and one should avoid using the µCHX in this region.

Microscale Combustor Development for Adsorption Systems: Early in Phase 2 OSU evaluated four different locations for a microscale combustor and heat exchanger where this device would assist in discharging an adsorption hydrogen storage system. Given the MATI's ability to use a heat transfer fluid different than hydrogen, it was decided to focus on a system where hydrogen discharged from the storage system would be headed by fuel cell waste heat to approximately 40C. The microscale combustion system would then burn a small amount of hydrogen to raise the temperature of the discharged hydrogen to approximately 120 C. The hot hydrogen would then pass through the MATI providing heat for discharging more hydrogen. The now cold hydrogen would leave the MATI and go to the fuel cell where it would be used for the production of electricity. This scheme is shown in Fig. 11.

Table 4 summarizes the design consideration for this option. The design for this microscale combustor heat exchanger (µCHX) has been changed from the Metal Hydride design so that it would be more compact. The air channels in the previous design were eliminated and the combustor and heat exchanger sections were integrated. The role of air channels was to provide a thermal buffer between the combustor and hydrogen channels so that the very cold hydrogen stream would not have direct contact to the combustor channel, a direct contact can extinguish combustion. In the new design, recuperator channels acted as thermal buffer as well as providing for preheating of the entering combustion gas mixture. Figure 2 shows a schematic of the new design. The combustor and hydrogen channel heights are 300 µm and recuperator channel heights are 150 µm, the width is assumed to be 1 mm.

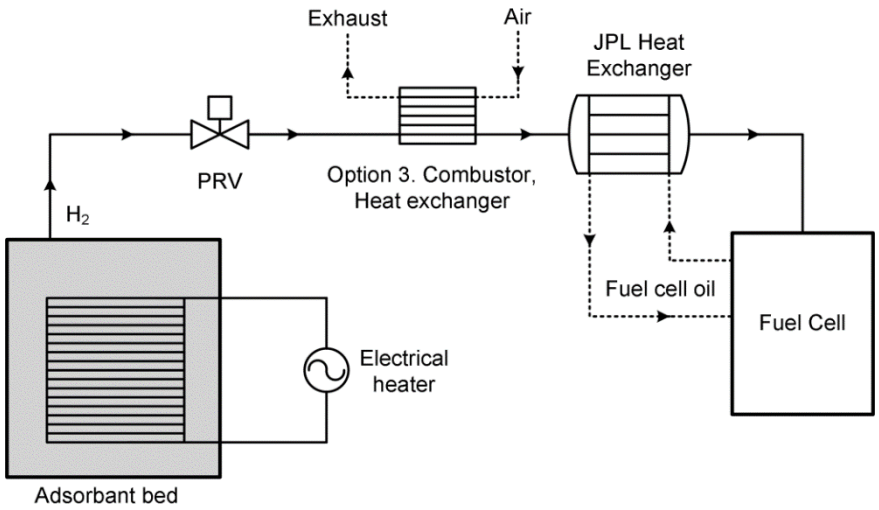

Figure 11.. Schematic view of option 3 heat exchanger in the system

Table 4. Option 3 heat exchanger placement and operating conditions

Location	Secondary system attached to or downstream from a traditional heat exchanger
Purpose	Heat the H_2 stream to the acceptable fuel cell temperature ranges when the ambient temperature is below -30 ^oC and/or the fuel cell coolant is at ambient temperature
Pressure range	Inlet pressure of 5 to 20 bar; outlet pressure greater than or equal to 5 bar
Temperature range	Inlet temperature of ~200 K
Target Heating	Increase temperature to a minimum of -40 ^oC
Fluid flow rate	Maximum 2 g/s

A key innovation was made in the catalyst arrangement to permit high efficiency combustion at these low temperatures. Previously the entire catalyst bed was located in the combustor channel. In this arrangement, since the inlet hydrogen stream temperature is very low, the gas temperature at the end of the combustion channel was so low that complete combustion was not attained. Simulations indicated that although there was still around 15% of the initial hydrogen content in the channel, having catalyst at the end of the channel did not cause completion of the reaction due to the low temperatures of the inlet hydrogen stream. So in order to achieve conversions higher than 85%, the catalyst location was shifted from the end of the to the recuperator channel on the other side of the wall were the first patch of catalyst was located (Figure 2). The new place of catalyst had high temperatures and, as a result, higher conversion. With this new arrangement of catalyst bed, simulations predict that hydrogen conversion of higher than 99% were achieved with the catalyst length of 12.5 mm. That reduced the total size of the µCHX to 15 mm

Figure 12 shows temperature contours for the above-mentioned design with hydrogen stream pressure of 5 bar. The hot area clearly shows the locations of the heterogeneous reaction. Table 5 summarizes the achieved conditions for the range of the desired pressures and hydrogen mass flow rates. The maximum hydrogen mass flow rate was assumed to be 2 g/s whereas 0.5 g/s is a normal operating condition flow rate. Efficiencies higher than 92% were achieved in all cases.

As mentioned before, a small portion of the hydrogen stream is taken to combust and heat the main hydrogen stream. These simulations showed that in all cases about 0.5% of the main hydrogen mass flow rate was needed to heat up the stream. An estimate of the size of the combustor was determined based on simulation results. Dividing the maximum to the mass flow rate in each unit cell gives the total number of unit cell needed. For this case, a total number of 330 unit cells would be enough to provide heat to 2 g/s hydrogen mass flow rate. For lower mass flow rate of hydrogen (say 0.5 g/s), the same number of unit cells will do the job but with lower flow rates in each of them. For example, for the hydrogen stream pressure of 20 bar, for 2 g/s total mass flow rate,

each of the 330 unit cells carries 6.1 mg/s while for 0.5 g/s total mass flow rate, each unit cell carries 1.5 mg/s of hydrogen in the hydrogen streams.

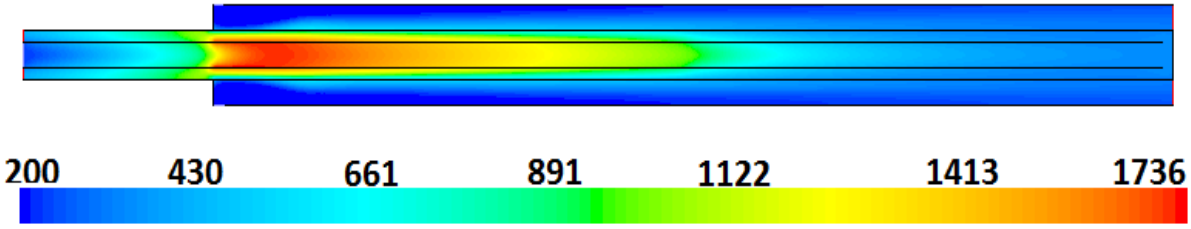

Figure 12. Temperature contours for option 3 geometry (K)

Table 5. Simulation results for the desired pressure and hydrogen mass flow rate ranges

H_2 mass flow rate (g/s)	H_2 pressure (bar)	H_2 outlet temperature (K)	H_2 conversion (in combustor) (%)	Efficiency (%)
2	5	235.7	99.8	93.3
	20	236.1	99.5	92.9
0.5	5	237.7	99.8	92.4
	20	243.8	99.4	92.1

The metal hydride header scheme was used to provide air and hydrogen to the combustion process and hydrogen to be heated (Fig. 13). Based on this header design, the size of the system with 330 unit cells would be 30 mm × 75.6 mm × 35.7 mm. This consists of 2 unit cells in length, 15 unit cells in width and 11 unit cells in height plus two caps on top and bottom.

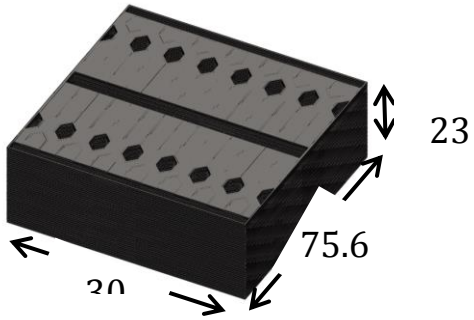

Figure 13. System with 330 unit cells and headering

To have a better estimate of the size and weight, 15 mm of insulation was added all around the system. The insulation was assumed to be Pyrogel XT. This gave a final size and weight estimate (assuming stainless steel as the metal) as 406 g and 0.416 l, respectively. The final dimensions are 60 mm × 105.6 mm × 65.7 mm.

A prototype of the microchannel combustion system for adsorption system supplemental heating was then designed and fabricated. Hydrogen and air flow rates in a single unit cell were very small and the existing mass flow controllers cannot be used for testing a single unit cell. If multiple unit cells were considered for testing, current mass flow controllers could then be used for flow rate measurements of air and hydrogen streams. A flow measurement device is necessary for nitrogen stream. In order to reduce the heat loss and provide an accurate estimate of heat transfer rate, a multi-unit cell combustor was designed. This multiple unit cell approach also helped to hone the fabrication procedures and to characterize the flow distribution within the headers. The multi-unit cell combustor was to be fabricated by diffusion bonding. The limit of the channel aspect ratio for this method is 1:7 (channel height to width) and since the channel height is 300 μm, the width of the channel should not be larger than 2 mm. Therefore 2 mm was chosen for the width of the channel. Unit cell positioning was designed in a way that several of them were placed in one plate (shim) and shims were stacked up on each other to make blocks of unit cells A combustor channel shim is shown in Fig. 14. Four channels are located on each side and combustion gas flow toward the center. Locations of different headers are also shown in Fig. 41. Figure 15 shows the flow direction of each of the streams. These five layers of shims build a block of 8 unit cells.

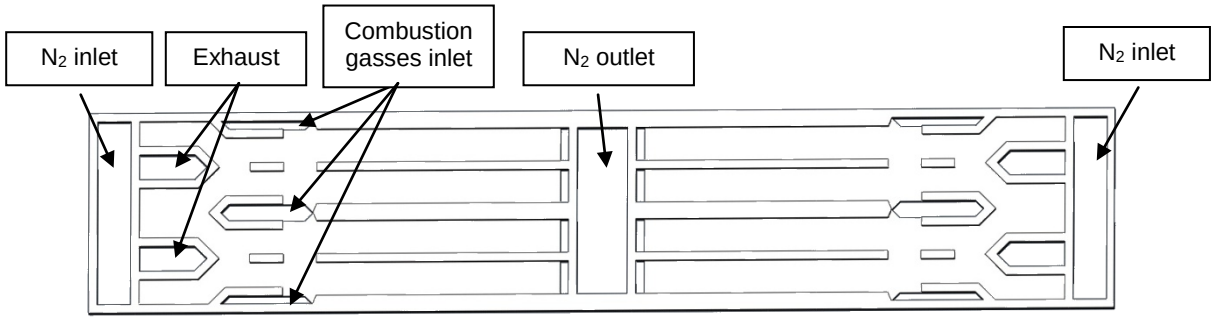

Figure 14. Combustor channel shim consisting 8 channels and headers

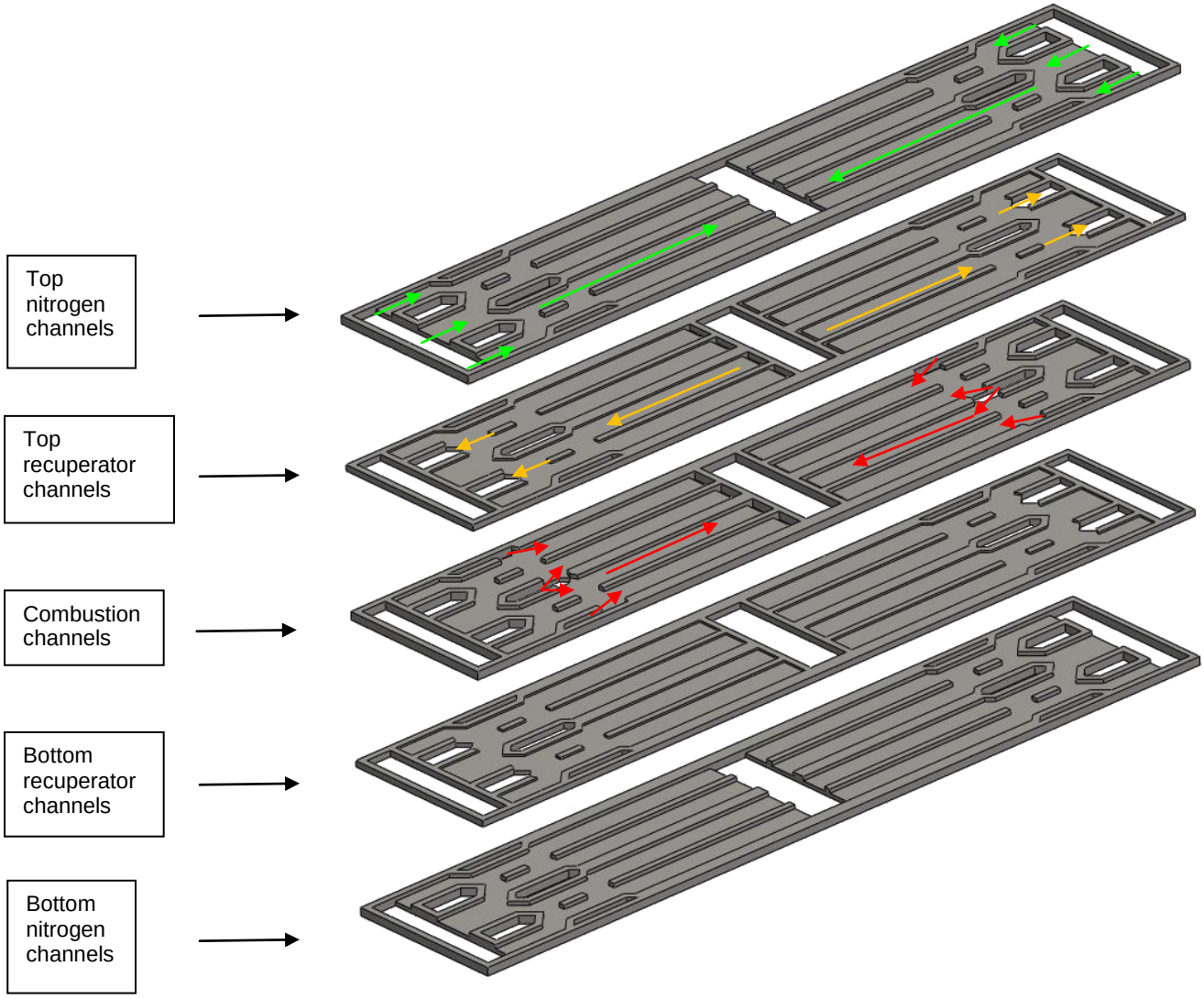

Figure 15. Different channel shims and flow directions

Three such blocks were stacked along with a top and a bottom header caps to form a 24 unit cell microscale combustor heat exchanger. A collapsed view of the combustor is shown in Fig. 16. The total size of a 24 unit cell combustor heat exchanger based on this design is 61 mm × 12 mm × 7.5 mm.

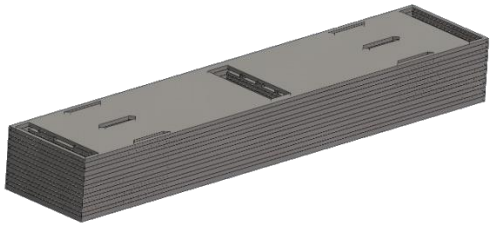

Figure 16. Collapsed view of the 24 unit cell microscale combustor

In the present design, several unit cells were placed in one plate (shim) and shims were stacked up on each other to make blocks of unit cells. The multi-unit cell combustor was fabricated by diffusion bonding. In a parallel effort thermal effects tests were carried out on a set of layers with 16 unit cells that were bolted together.

For the thermal effects tests the layers were held together by bolts. Two PEEK headers on the top and bottom sides of the layers provided insulation as well as fluidic headers. In order to prevent damage to PEEK headers, two aluminum caps were included on top and bottom to bear the bolt pressure. Figure 17 shows the assembled device.

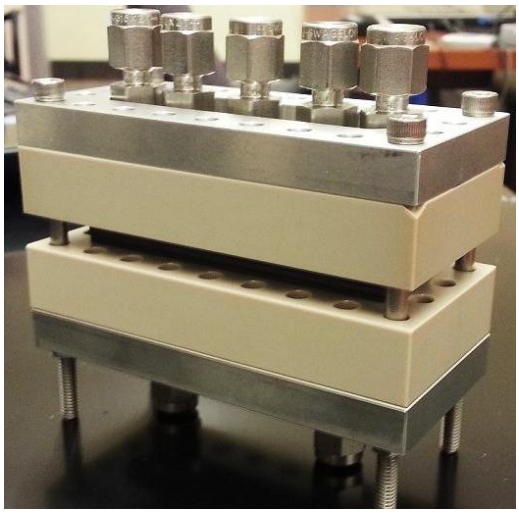

Figure 17. Assembled configuration of the µCHX

Catalyst bed preparation: In the case of an adsorption heating system, the combustor will be used to heat hydrogen at cryogenic temperatures. When a very cold fluid is flowing close to the combustor and recuperator channels, the reaction rate decreases and condensation of water vapor in the channels is very probable. To avoid is, catalyst beds are located on both sides of the combustor channel and one side of the recuperator channels. Figure 2 shows the location of catalyst beds with heavy lines. In each unit cell, two of the layers had catalyst deposited on both sides of the layer. For the shim (combustor layer) shown in Fig. 18, the front side deposition was done inside the etched channels. The other side of this shim, was a flat surface and deposition of the catalyst added an extra thickness to the layer and reduces the channel height of the below channels. Moreover, a rough surface provides for better attachment of the catalyst material on the surface via wet deposition.

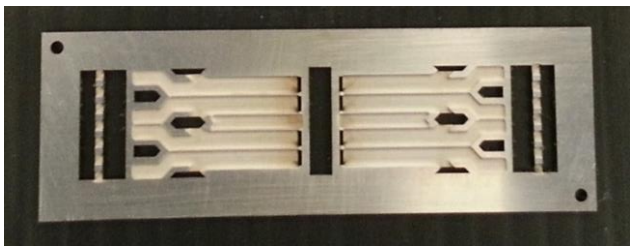

Figure 18. Top view of a combustor layer

Etching the back side of the shims: To provide the desired rough surface and room for the catalyst bed, the back side of the combustor and recuperator channels were etched using 0.5 Molar Oxalic acid solution and masks laser-cut from a Kapton tape (Figure 19).

Figure 19. A combustor shim covered with mask for etching.

One important factor during the etching process was to ensure that the space between two channels should be at least 500 µm to make sure that enough contact exists with the bottom layer walls for bonding. Therefore the mask shown in Fig. 4 was cut in such a way that the back side channels have smaller length and width compared to the actual channels. Based on the previous experience an etch depth of 30 µm was chosen for the catalyst bed. A sample of the etched layer is shown in Fig. 20.

Figure 20. Etched channels on the back side of a channel.

Figure 21a shows results from profilometery of the etched channels with the etched parts shown in blue. Figure 21b shows the depth of the etched channels along the black line shown in Fig. 21a. It can be seen that the depth of the etched area is about 35 µm. The top flat surface in Fig. 21b is the wall between the two channels and is 1500 µm, which is sufficient for bonding purposes.

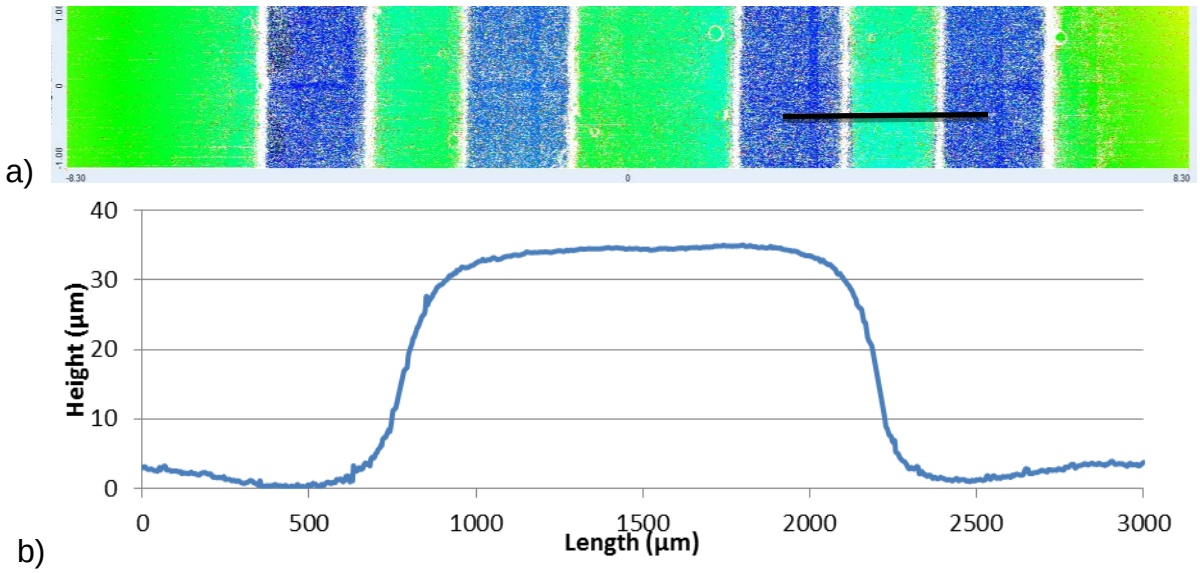

Figure 21. a) Profile of a section of the channels, b) Plot of the height of the area shown with a dark line

Catalyst deposition: After the back sides were etched, the shims were ready for catalyst deposition. Kapton tape masks were laser-cut again and were attached on top of the sides. Pins were used to align the tape and the shim. 0.007 Molar solution of chloroplatinic acid hexahydrate were deposited with the density of 0.529 ml/cm^2. Eight 1 ml syringes were used to deposit the desired amount of the catalyst solution on each of the eight channels on each layer. After each deposition, the shim was put aside to dry and then the next round of injection was performed. Upon drying of the catalyst precursor, the mask was removed, and catalyst was deposited on the back side of the shim (i.e. recuperator wall- see Fig. 22).

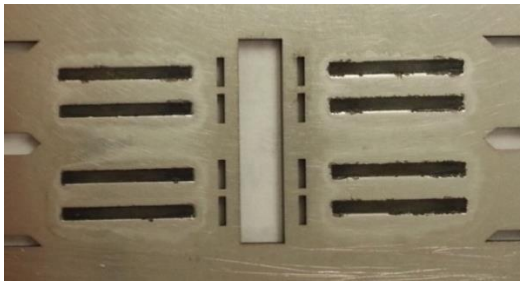

Figure 22. Catalyst deposited on back side of a shim

Catalyst activation device assembly*:* When the shims were ready and covered with the catalyst, they were put into a device for activation. The activation device consisted of two aluminum blocks instead of the PEEK parts and used cartridge heaters to provide the heat necessary to raise the temperature to 600 ^{o}C. Since O-rings cannot operate at these high temperatures, two gaskets were made from high temperature Mica sheet to surround and seal inlets and outlets. Following this, the layers of the combustor were stacked on top of each other (Fig. 23) followed by a second mica sheet and the top aluminum block.

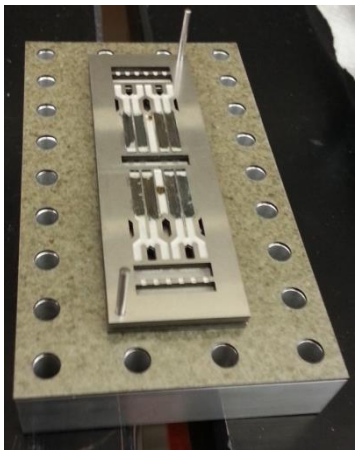

Figure 23. Assembly process of the activation setup showing the bottom aluminum block, the mica gasket and catalyst layers on the top

Two aluminum heater blocks with cartridge heaters were then located on the sides of the device. Custom clamps ensured that a good contact exists between the heater blocks and the layers. The heat blocks are separated from the holders with a layer of Mica to reduce heat loss.

Experimental facility*:* The existing experimental facility was modified to use cold nitrogen. Figure 24 shows a schematic of the modified experimental facility. Liquid nitrogen was used to reduce the temperature of the nitrogen stream. Liquid nitrogen was poured in a dewar with a coiled tube located inside (Fig 25). Before entering the µCHX, cold nitrogen was mixed with a bypass line of room temperature nitrogen to achieve the desired temperature (200 K). PFA tubing was used to reduce heat conduction and heat losses via the fittings and tubing system.

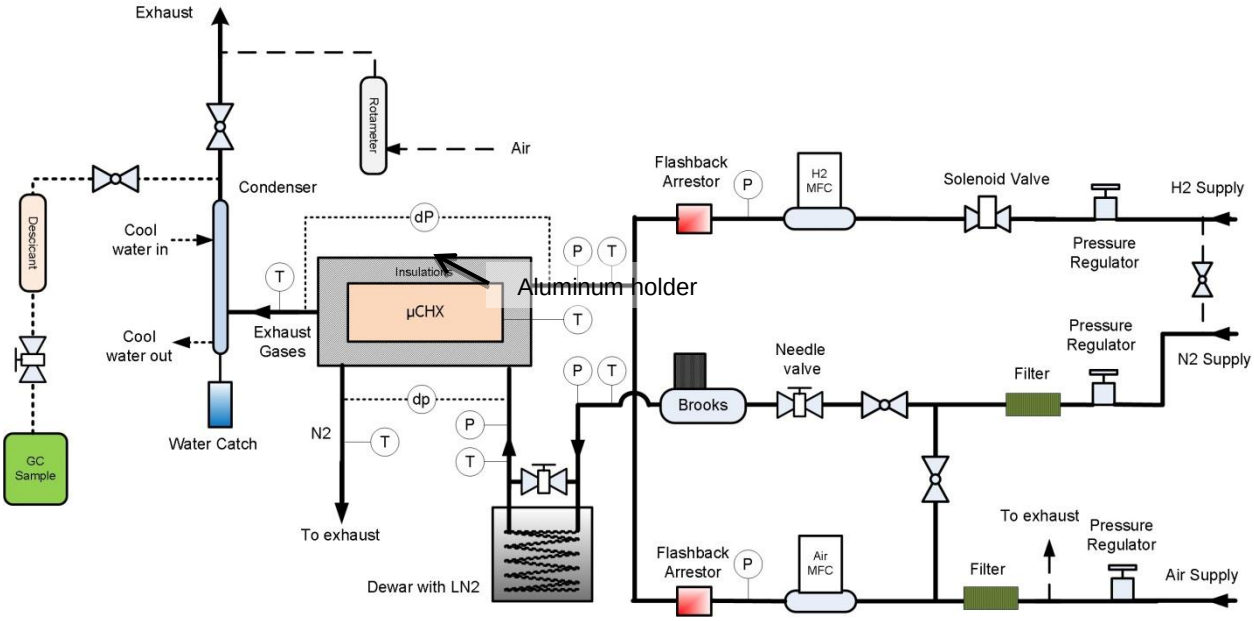

Figure 24. A schematic view of the experimental facility

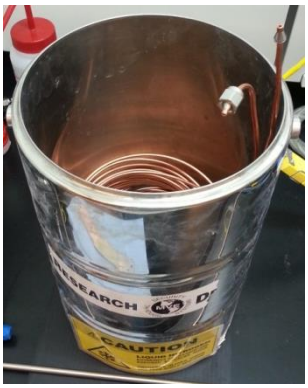

Figure 25. Nitrogen dewar with the coiled tube

A chiller was used to calibrate the thermocouples for the range of -20 ^{o}C to 100 ^{o}C (Fig. 15). In addition to that, thermocouples were immersed in a liquid nitrogen dewar to achieve -195 ^{o}C calibration point. A laboratory oven will be used to calibrate some of the thermocouples at higher temperatures. Hydrogen and air flow rates in a single unit cell were very small and the existing mass flow controllers were not used for testing a single unit cell. When multiple unit cells were considered for testing, current mass flow controllers were used for flow rate measurements of air and hydrogen streams.

Experiments

During the activation process, the device layers were bolted together with top and bottom aluminum headers to prevent leaks. The activation process took 7 hours and occurred at 600 ^{o}C. Figure 26 shows the µCHX layers after going through the activation process.


Figure 26. µCHX layers after activation

Being at high temperatures and under pressure for 7 hours caused a weak bond between layers which minimized leaks during the testing phase. Leak tests showed that there was no need to exert too much pressure to have a leak proof device, therefore the aluminum blocks designed to exert uniform pressure on the PEEK headers were

removed to reduce the device size and heat loss. A final assembly of the device for testing is shown in Fig. 27.

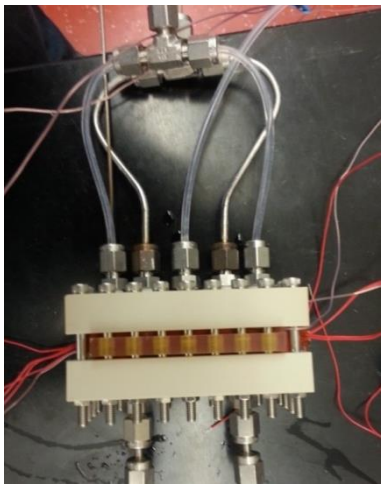

Figure 27. Assembly of the test section

Temperatures on four sides of the combustor were measured by T-type thermocouples shown in Fig. 5. Four 12-ohm thick film heaters were used to preheat the device to a temperature of around 120 ^{o}C to start the reaction (Fig. 28). To reduce heat loss, inlets and outlets were also covered with Cryogel insulation.

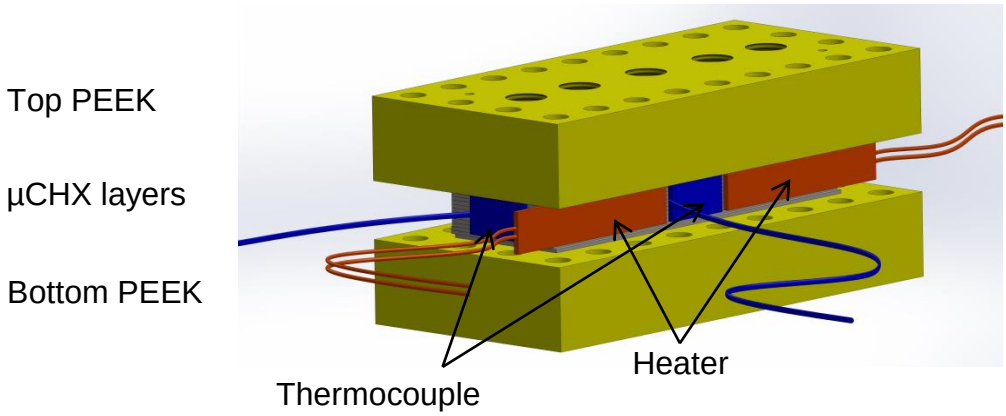

Figure 28. Detailed picture of the assembly

Hydrogen and air were premixed before entering the device at room temperature while nitrogen stream was routed to the device at a low temperature after exchanging heat to liquid nitrogen within a Dewar. Water vapor was removed from the exhaust gases using a condenser and desiccant filters. Samples were taken from the dry exhaust gases to quantify the amount of uncombusted hydrogen in the exhaust. Hydrogen conversion was defined as the ratio of the amount of hydrogen combusted to that of input hydrogen,

$$H_2 \text{ Conversion} = \frac{Y_{H_2,in} - Y_{H_2,out}}{Y_{H_2,in}} \quad (3)$$

Inlet and outlet temperatures, pressures and flow rates of the streams were measured using digital data acquisition. The gathered data were used to calculate the overall efficiency of the μCHX, defined as the ratio of the amount of heat transferred to nitrogen to the chemical energy of input hydrogen,

$$\eta = \frac{\dot{m}_{N_2}\left(h_{out} - h_{in}\right)_{N_2}}{\dot{m}_{H_2}\Delta h_{reaction} / M_{H_2}} \quad (4)$$

Heat losses are calculated by subtracting the heat transferred to nitrogen from the heat produced in the combustor by the spent hydrogen.

$$Q_L = \frac{\dot{m}_{H_2}\Delta h_{reaction,spentH2}}{M_{H_2}} - \dot{m}_{N_2}\left(h_{out} - h_{in}\right)_{N_2} \quad (5)$$

Temperature of the body of the device is measured at four different locations. To determine the body temperature, readings from two of the thermocouples that are located closest to the catalyst section of the μCHX are averaged.

Results and Discussion- Varied parameters include the inlet temperature of cold nitrogen (150-273 K), mass flow rate of cold nitrogen, mass flow rate of the combustible gas mixture and equivalence ratio. The equivalence ratio is defined as the ratio of the molar fuel-to-air ratio at the test conditions to that at stoichiometric conditions. The performance of the device was characterized using three parameters- pressure drop across the combustor and recuperator channels, hydrogen conversion, and efficiency.

Effect of residence time

One of the important factors in hydrogen conversion is the residence time over the catalyst for reactions. Residence time is defined as the time a hydrogen molecule has to react before leaving the catalyst region,

$$t_r = L_{Cat} / \bar{V} \quad (6)$$

where L_{Cat} is the catalyst bed length and $\bar{V}$ is the averaged velocity of hydrogen/air mixture in a channel. $\bar{V}$ is calculated by dividing the total flow rate by the number of channels and channel cross section area. Figure 7 shows the effect of residence time on H_2 conversion and device efficiency. In these experiments, the equivalence ratio was one and inlet nitrogen stream temperature was kept constant at -19 ^{o}C. Table 1 summarizes the key parameters.

It can be seen that H_2 conversion increases by about 10% with increasing residence time from 9 - 56 ms. However, the efficiency of the device drops from 82% to 66% due to heat losses. When the power generated in a device is small, the effect of heat losses

Table 6. Test conditions related to Fig. 29.

t_r (ms)	Input Power (W)	H_2 Conversion	η	Q_L (W)	r_{Q_L}
55.8	19.8	0.941	0.663	5.49	0.277
49.9	22.1	0.938	0.696	5.33	0.241
27.2	40.5	0.912	0.786	5.11	0.126
11.7	94.3	0.868	0.820	4.51	0.048
8.64	127.2	0.858	0.822	4.57	0.036

on the overall efficiency of the system can be significant. The body temperature was kept approximately the same between all experiments at about 186 ^{o}C and therefore there is not much difference between heat losses (in watts, see Table 1). However, the ratio of the heat loss to total power ratio which is defined as,

$$r_{Q_L} = \frac{Q_L}{\dot{m}_{H_2} \Delta h_{reaction} / M_{H_2}} \tag{5}$$

increased with an increase in residence time. Since the total length of the catalyst and the equivalence ratio were fixed, in order to achieve different residence times the flow rate of hydrogen/air mixture had to be varied (see Eq. 4). Different hydrogen/air flow rates resulted in different input power to the system (Table 1). Therefore, that heat loss ratio was different for different cases as is shown in Figure 7. The higher the heat loss ratio; the lower is the efficiency of the µCHX.

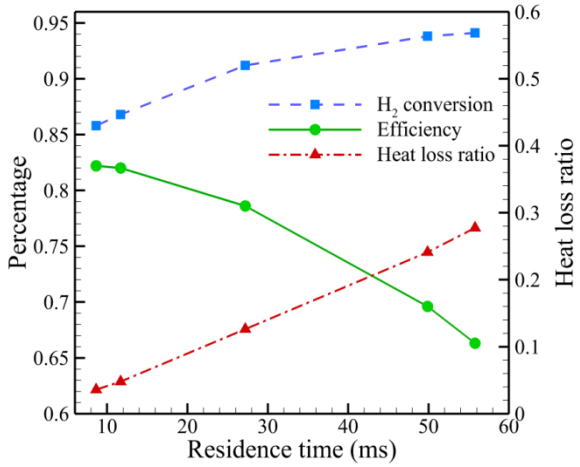

Figure 29. Variation of H_2 conversion, efficiency and heat loss ratio by residence time

Effect of body temperature - The body temperature of the combustor is a second important factor in conversion and device efficiency since higher reaction temperatures result in higher reaction rate and hence conversion. Figure 30 shows an increase in H_2 conversion with an increase in body temperature where body temperature is varied from 124 ^oC to 196 ^oC while keeping the residence time and equivalence ratio the same; 9 ms and 1, respectively. In these experiments, the inlet nitrogen stream temperature is kept fixed at -70 ^oC. The heat loss values vary from 1.1 W for the body temperature of 124 ^oC to 4.6 W for the body temperature of 196 ^oC. Since the power input is high in these cases (120 W), although heat loss increases, the heat loss ratios are small numbers and have insignificant effect on the overall efficiency of the system. Therefore the efficiency also increases with increasing the body temperature.

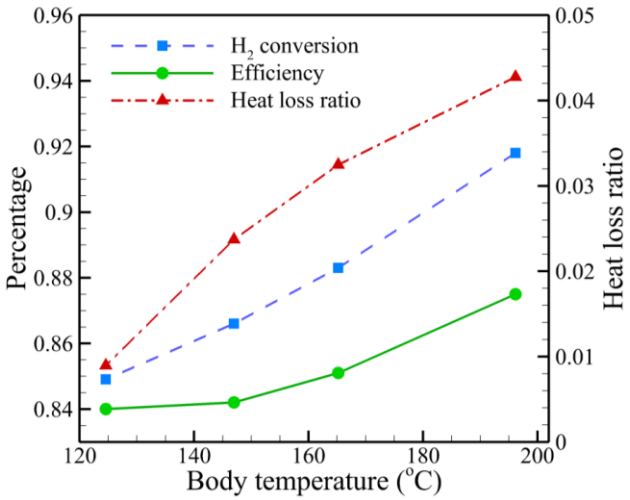

Figure 30. Variation of H_2 conversion, efficiency and heat loss ratio by body temperature

Effect of equivalence ratio - The effect of variation of equivalence ratio on the efficiency of the device was also investigated. Equivalence ratio was varied from 0.2 to 1 while residence time was kept constant at 10 ms. The body temperature as well as the inlet nitrogen temperature were kept fixed at 186 ^oC and -70 ^oC, respectively. Figure 31 illustrates an increase of about 10% on hydrogen conversion as the equivalence ratio decreases to 0.6. However, by decreasing the equivalence ratio, the efficiency increased at first but then decreased when the equivalence ratio reaches 0.4 and lower. The reason behind the fall of efficiency at lower equivalence ratio was the increase of heat loss ratio by a decrease in equivalence ratio. When the flow rate was kept the same, lower equivalence ratio means lower hydrogen was entering the device, therefore input power is less. The input power varied from about 110 W (for ϕ=1) to 29 W (for ϕ=0.2) and for the same body temperature the heat loss was almost the same. Thus the heat loss ratio was higher at lower equivalence ratios.

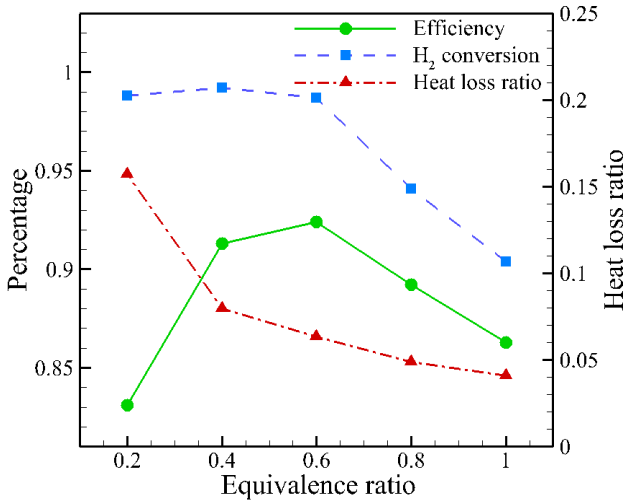

Figure 31. The effect of equivalence ratio on efficiency

It can be seen that the efficiency peaked at equivalence ratio of 0.6 with the value of 92.4%. This was the optimum operating conditions however, the input power is less (72 W) than equivalence ratio of one (109 W), therefore the size and weight of the system will be higher for the same power output. The size and weight comparison is shown in Table 2.

Table 7. Size and weight of a 1kW device for different equivalence ratios

Equivalence ratio	*Efficiency*	*Number of unit cells*	*Size (L)*	*Weight (g)*
1	86.3%	152	0.116	717.4
0.8	89.2%	200	0.151	879.6
0.6	92.4%	224	0.168	1035.6
0.4	91.3%	288	0.214	1318.5

The stated SMART goal is to develop and demonstrate a 1 kW catalytic combustor heat exchanger having > 85% efficiency, having a dry mass less than 0.9 kg and volume less than 0.65 liters. Table 7 clearly shows that if the device operates at equivalence ratios of 0.8 or higher, all goals were met while the size of the system was one quarter of the desired size.

3.4. Pressure drop- Another factor for the performance of the device is pressure drop. For the specific application identified by DOE, pressure drop on the working fluid side was not an important issue. The device pressure drops on the nitrogen side were high and varied between 50 kPa (for 15 slpm) to 180 kPa (for 48 slpm). Pressure drops on hydrogen/air mixture side, on the other hand, were much smaller and for the maximum flow rate was 20.1 kPa. High flow rates and complex headering system caused high pressure drops on nitrogen side. In using nitrogen in place of hydrogen for these tests, the heat capacity rate was kept identical. This meant that, due to the significantly larger specific heat capacity of hydrogen compared to nitrogen, the flow rate of nitrogen was 13 times larger than that which is anticipated in the actual application. Hence, pressure

drop on the heat transfer fluid side was not expected to be a major impediment in the actual device.

Key Findings: *Key findings from Task 2.1 include: 1) The use of a microchannel architecture for the adsorption system supplemental heater resulted in an extremely compact design that added little weight, volume or cost to the storage system, 2) Experimental investigations validated the simulations of the device and confirmed that the extremely small size was in fact attainable.*

Task 2.2. Cryogenic Integrated Test Apparatus Development: The Phase 1 test apparatus, (the Integrated Test Apparatus) was focused on experimental investigations of the complete charge and discharge process including both heat and mass transfer and adsorption. Phase 2 integrated experimental investigations were focused on the use of cryogenic liquid nitrogen (~70K) to remove the heat generated from the adsorption of gas during each experiment. While the general scope of adsorption experiments to be performed in the apparatus was not altered, the change of operating temperature (cryogenic range) required modifications of some elements of the experimental apparatus. A number of design enhancements are incorporated into the updated apparatus to improve safety, data collection, and experimental control. The first generation experimental device utilized three pressure transducers and seven thermocouples to monitor changes during each experimental trial. The second generation device used three pressure transducers to monitor the pressure change through the adsorbent bed and was capable of monitoring the temperature at 25 locations along: i) the liquid nitrogen flow path; ii) gas flow path; iii) the surface of the heat exchange device; iv) inside the adsorbent bed, and in v) the void spaces of the pressure vessel. Temperatures of the gas entering and exiting the pressure vessel will be continuously monitored at multiple locations along the flow path. These temperature measurements will allow for a more complete understanding of inlet and outlet conditions for each experiment and, therefore, will improve the accuracy of the mathematical models developed.

The system was designed to investigate gas adsorption (nitrogen and hydrogen) at cryogenic temperatures using both densified and powdered adsorption media. The symbolic information flow diagram of the cryogenic test apparatus is shown in *Figure 32*.

Inside of the 50 bar pressure vessel two cylinders of glass-filled PTFE are positioned, separated by a coil of $^{1}/_{8}$" stainless steel tubing designed to pre-cool the pressure vessel prior to experiments using liquid nitrogen or liquid nitrogen vapor. The microchannel heat exchange and gas distribution device is placed in the bottom of the inner PTFE cylinder and the packed bed of adsorption material is placed on the surface of the microchannel cooling plate/distributor. Figure 33 shows a photograph of the cooling/distributor plate installed at the bottom of the pressure vessel.

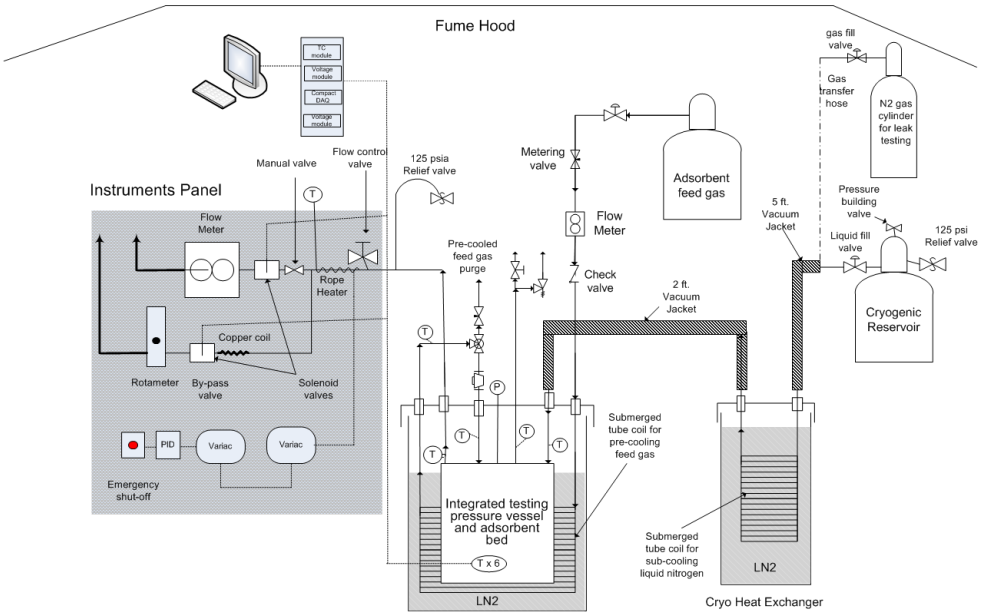

Figure 32: Schematic Diagram of Integrated Test Apparatus

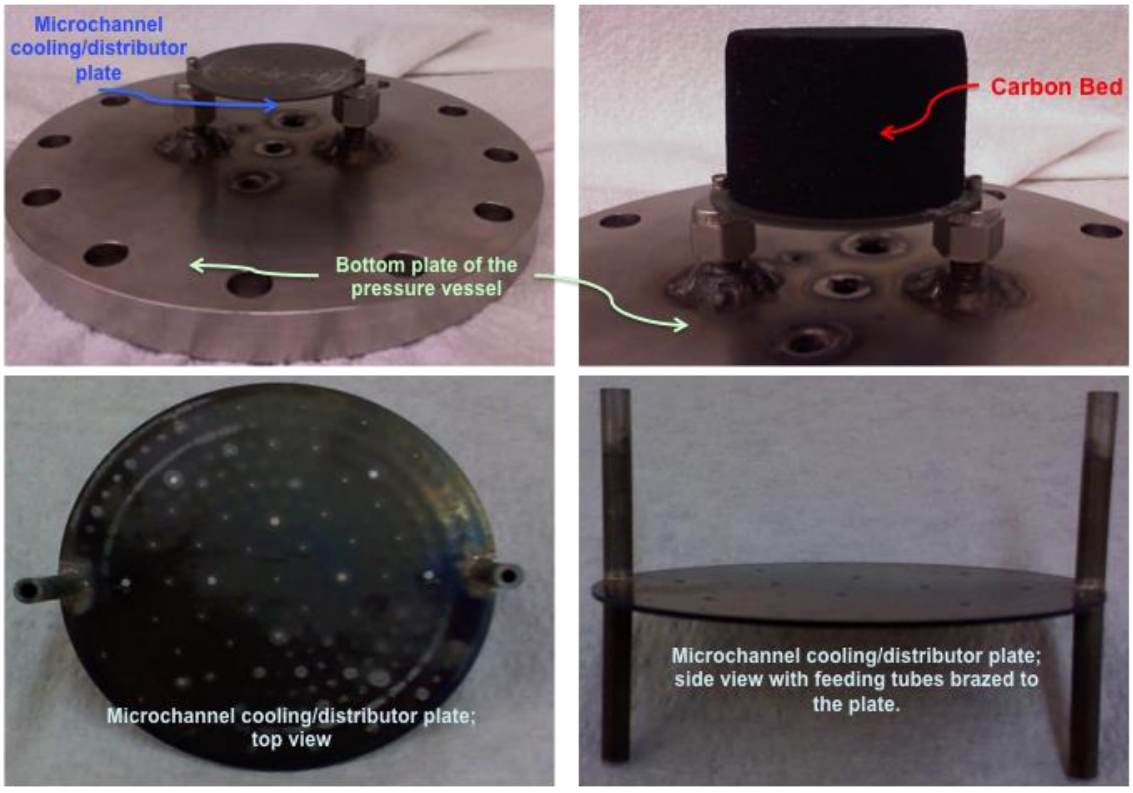

Figure 33.: Cooling/distributor plate assembly with carbon bed.

In Figure 34 we show the experimental set-up used to measure the pressure drop through the cooling plates.

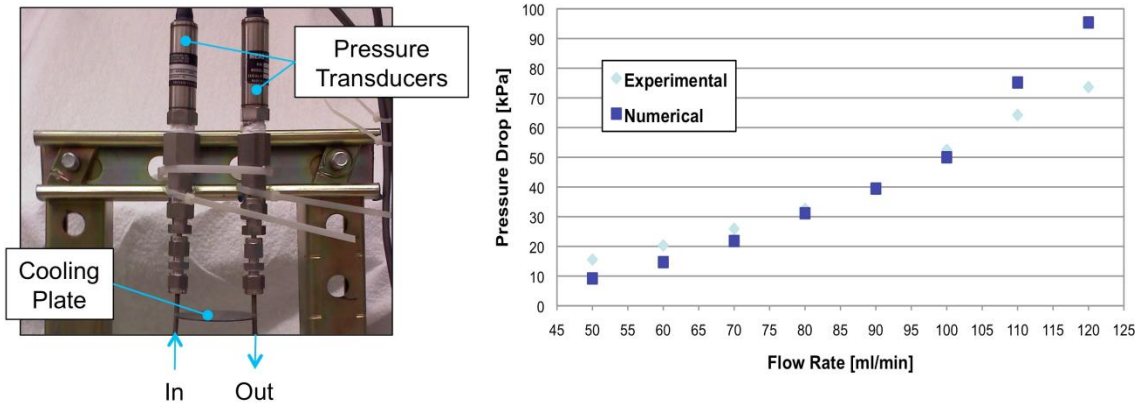

Figure 34.: Experimental set-up for pressure drop measurements in the cooling plate. (experimental data and numerical simulation)

We obtained experimental data on pressure drop with water and the data validated our numerical model, which will be used to predict pressure drop through the scaled-up version of the cooling plates to be used as insert in the hydrogen tank. The overall pressure drop through the cooling plates and feeding assembly is very small, which demonstrates successful design of the cooling subsystem.

The adsorbing gas used in this investigation will be supplied from pressurized gas cylinders at room temperature. Thus, it is necessary to cool the incoming gas to cryogenic temperatures prior to entering the pressure vessel. Pre-cooling of the feed gas will be accomplished by submerging 45 feet of stainless steel tubing in a research Dewar filled with liquid nitrogen.

The bed of approximately 3.2 [cm] height (20.9 [g] after machining) MOF-5 was chosen and machined for the initial testing within the integrated system. The MOF-5 compact was activated prior to assembly of the integrated system by placing in a vacuum (5.0 [in] Hg) for six hours and subsequently heated at 140 [^{o}C] for 24 hours in 5.0 [in] Hg vacuum. Final assembly of the integrated system was completed inside of a fume hood with constant flow of nitrogen gas above the sample. Once fully assembled and placed within the testing facility the house vacuum (12 [in] Hg) was connected to the outlet of the pressure vessel until testing began. In the unlikely event of a ruptured cryogenic delivery hose or spray of liquid nitrogen, a sheet metal structure encloses the test facilities to minimize the opportunity of human contact with cryogenic liquid, Figure 35.

Figure 35: Fully assembled integrated testing system inside of sheet metal enclosure.

The MOF-5 compact adsorbent material that was received from our partners within the Center has been stored in a vacuum glove box and all necessary machining of thermocouple holes and header cutouts were performed in fume hood with constant flow of nitrogen gas over the sample.

The bed of approximately 3.2 [cm] height (20.9 [g] after machining) MOF-5 was chosen and machined for the initial testing within the integrated system. The MOF-5 compact was activated prior to assembly of the integrated system by placing in a vacuum (5.0 [in] Hg) for six hours and subsequently heated at 140 [^{o}C] for 24 hours in 5.0 [in] Hg vacuum. Final assembly of the integrated system was completed inside of a fume hood with constant flow of nitrogen gas above the sample. Once fully assembled and placed within the testing facility the house vacuum (12 [in] Hg) was connected to the outlet of the pressure vessel until testing began

Multi-Module Testing: Once we decided to fabricate and test a multi cooling plate MATI test article we needed to modify the integrated test apparatus to accommodate the larger multi cooling plate test article. The integrated adsorption testing facility needed to accommodate an adsorption system containing three MATI cooling plates, two complete beds (approximately 3 cm tall), and two MPTN structures. The original integrated testing system was designed to minimize void space inside of the pressure vessel while allowing for testing of densified adsorbent beds of various heights and orientation with respect to cooling/gas feed, however, the internal height of the current pressure vessel body is unable to accommodate the three cooling plate structure. In addition, subsequent MATI revisions have moved away from the use of 3mm OD stainless steel headers in favor of 4mm OD headers, requiring the fabrication of custom

Swagelok fittings to allow for fluidic connections between the vessel cap and cooling plate stack.

To accommodate the increased height of the three cooling plate stack and avoid the major and costly tasks of fabricating a larger pressure vessel, a stainless steel spacer was fabricated and used to increase the internal height required for the multi-module testing. To insert the assembled multi-module stack into the pressure vessel and cylinder of PTFE tube (used for insulation) 3mm plugs were fabricated and welded to the bottom portion of the header tubes, similarly to the previous experimental system. A representation of the assembled integrated pressure vessel, including spacer and multi-modular device, is seen in Figure 36.

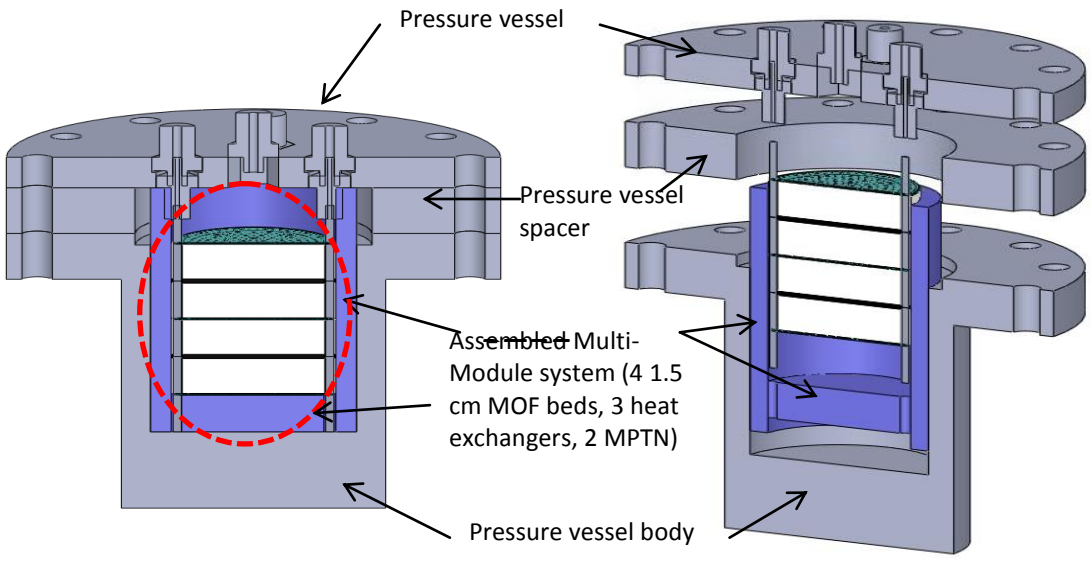

Figure 36: Representation of fully assembled Multi-module testing apparatus.

Separate Effects Test Facility for Heat Transfer and Pressure Drop: The separate effects test facility is separate from the integrated test facility described above and is focused on experimentally determining the heat transfer and pressure drop in cooling plated at cryogenic conditions. Figure 6 shows a schematic of the initial test facility, which consisted of a cryogenic pressurized reservoir, a dewar for fluid subcooling, and a dewar containing the test section. Fluidic lines connecting the reservoir and dewars are vacuum insulated. During system start-up a number of changes were made to this system. These are summarized below and the final system is shown in figure 37.

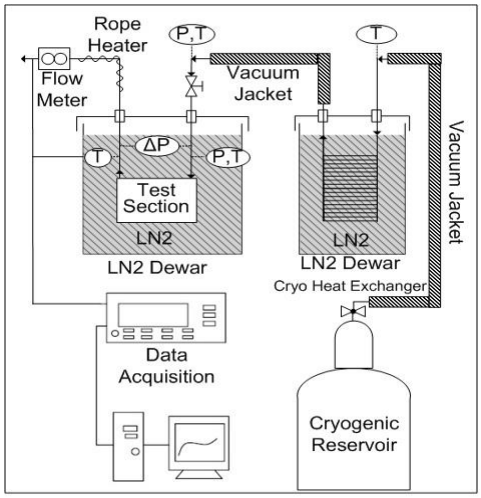

Fig.37: Schematic of the Initial separate effects heat transfer cryogenic test facility

During testing, liquid nitrogen in the cryogenic reservoir was pressurized between 4 bar and 8 bar, depending on the heat flux applied to the test section. Liquid nitrogen then entered the first dewar within a coiled tube at saturation temperature at the set pressure in the reservoir, and exchanged heat with liquid nitrogen in the dewar at atmospheric pressure. The exiting liquid nitrogen in the tube was subcooled at the set pressure prior to entrance into the second dewar which contained the test section. The test section was immersed in liquid nitrogen within this dewar in order to minimize heat losses. A flow control valve was used to regulate the mass flow rate of liquid nitrogen into the test section. Upon exiting the test section, the liquid nitrogen in the line was vaporized using rope heaters and the volumetric flow rate of the gaseous nitrogen was measured using a precision venture type flowmeter. Temperature was recorded at the inlet and exit of the test section and heat exchangers as well as near the venture flowmeter. Gage pressure was measured at the reservoir, while absolute pressure and pressure drop was recorded at the inlet of, and across, the test section respectively.

The test section was designed with several considerations in mind in order to ensure accurate temperature and heat flux measurements. The goal of the separate effects test was to quantify heat transfer rates in single-phase liquid nitrogen flows as a function of flow velocity by determination of the heat transfer coefficient. In non-dimensional terms, the experiments sought to provide a relationship between Nusselt number (Nu) and Reynolds number (Re) for liquid nitrogen flow through the microchannel cooling plate. The data was also be used to validate the detailed CFD simulations using ANSYS FLUENT. Local heat transfer coefficient was determined using Newton's law of cooling,

$$h(x) = \frac{q''(x)}{(T_w(x) - T_b(x))}$$

where x denotes the axial location in the cooling plate, q" denotes the heat flux, T_w denotes the wall temperature, and T_b denotes the bulk fluid temperature. Local heat transfer coefficients were then area averaged to obtain a global heat transfer coefficient. In order to determine h(x), local heat flux, local wall temperature and local bulk fluid temperature needed to be known. The local heat flux and wall temperatures were

determined using a heat flux meter however issue related to the conductivity of the titanium used in the flux meter introduced significant errors and we ultimately used electrical power corrected by deducting the heat losses to estimate the heat input to the heat sink. The local bulk fluid temperature were determined using local energy balance

The microchannel cooling plate was comprised of two shims that have been chemically etched to form the pattern of the generation 2 design of the modular adsorption system. Since hydrogen distribution holes were not of concern for the heat transfer tests, simplifications in the design were made by eliminating these holes. Also, since the inlet and exit ports were sealed using o-rings, the outer dimension of the plates was enlarged. Figure 38 shows the top and bottom plates, which were bonded together to form the microchannel cooling plate.

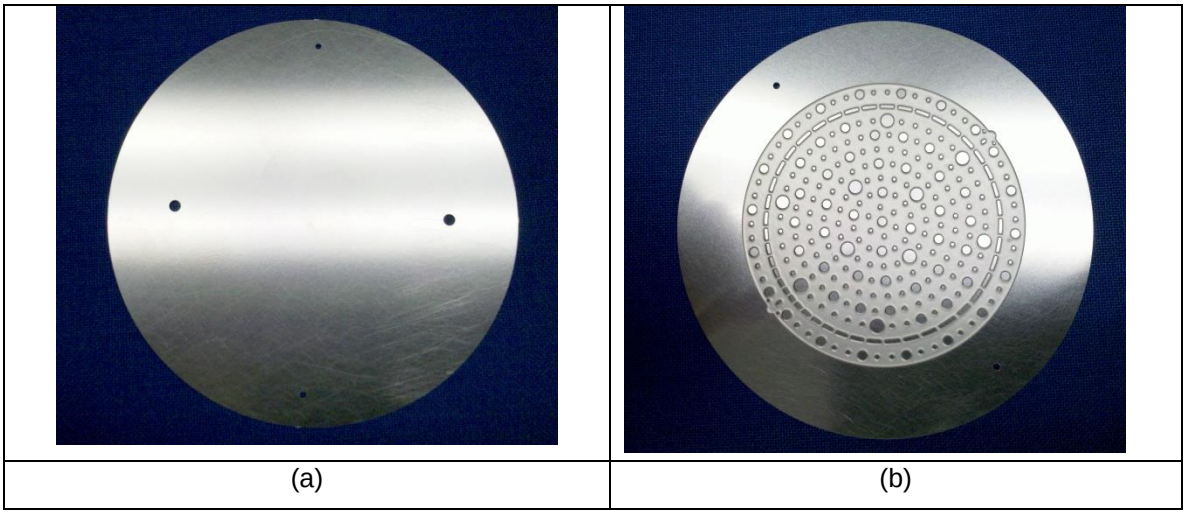

Fig. 38. Microchannel cooling plate (a) top plate showing holes for headers and alignment, (b) bottom plate with etched Microchannel and pin fins.

The debugging was completed and as a result, heat balance of test section matches quite well and stable conditions inside the microchannel are achieved for a range of flow rates. Key modifications to the test apparatus are summarized below.

- Removing the titanium flux meter and using electrical power corrected by deducting the heat losses to estimate the heat input to the heat sink.
- Applying a CPVC plastic insulation to reduce the amount of heat loss from the bottom side of the heater.
- Controlling wall superheat and running tests when all the six T-type thermocouples mounted on the bottom plate of the MATI heat sink were showing temperatures less than T_{sat}.
- Replacing the existed header with one without DP pressure ports to eliminate the fluctuation in inlet pressure.
- Developing a heat loss calibration curve

Liquid nitrogen is a very volatile fluid and small heat loss into the fluidic lines could cause phase change and local subcooled boiling. Hence, the lines had to be as short as possible and fully insulated. Based on the flow loop design we had two stages of subcooling before entrance of the flow into the test section. First stage was in the heat exchanger dewar and second through a copper coil immersed into the test dewar. We decided to exclude the first heat exchanger dewar from the flow loop and connect the 80L cryo-cylinder directly to the test dewar using 5ft vacuum jacket insulated tube. Thus, the fluidic lines would be much shorter and subcooling would only take place in test dewar. The result was dramatic reduction on fluctuations and very stable flow conditions at the inlet. Figure 39 shows the updated schematic of the separate effects heat transfer experimental facility following debugging.

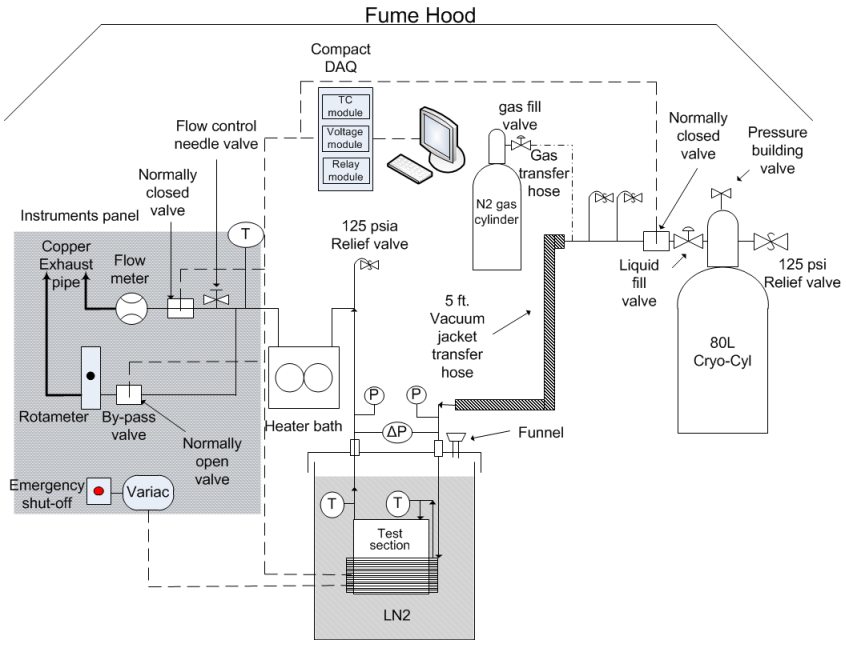

Figure 39: Schematic view of debugged separate effects test facility

Key Findings: *Key findings from Task 2.2 were that both test apparatus were successfully designed, assembled and debugged and there then used for the experimental investigations described below.*

<u>Task 2.3 Test Article Design and Fabrication</u>: The phase 2 objective of this task is to develop thermal management system test articles. The test articles will demonstrate the feasibility of our design. There are five key requirements that have guided the design of the thermal management system: 1) timely removal of the heat of adsorption generated by storing 5.6 kg H_2 in an adsorbent bed; 2) minimize mass and cost; 3) withstand 50 atm differential H_2 pressure; 4) maintain an LN_2 pressure drop of less than 4 atm

through a cooling plate; and 5) hermetically seal LN_2 circuit from the 50 atm hydrogen atmosphere.

The Phase 2 design of the thermal management system is shown below in Figures 40-41. Inlets and outlets have been brought inside the diameter of the cooling plates so the headers can fit within a 30 cm inner diameter pressure vessel. Plate thicknesses were reduced to microchannel dimensions to reduce mass and optimize heat transfer. Pillars have been reduced to sub-millimeter diameter in size and increased in number to reduce the span between pillars to the required span as calculated below.

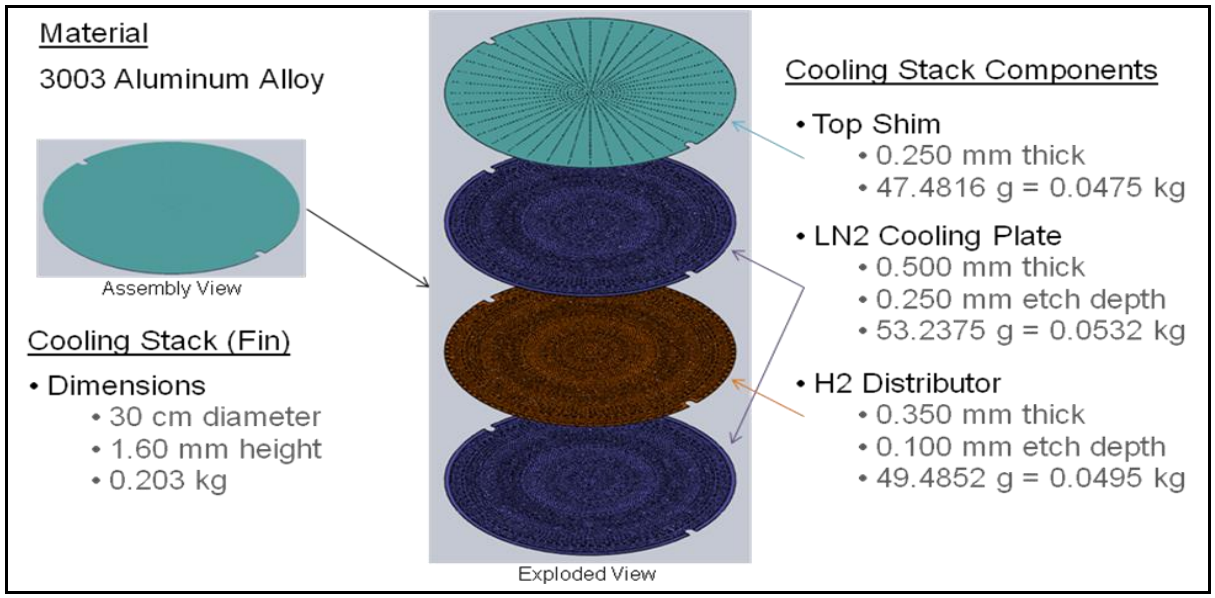

Figure 40: Exploded view of current cooling/H2 distributor plate with dimensions and mass.

Additional changes to reduce the mass and volume of the thermal management system have included reducing the fin thicknesses and LN_2 channel heights to 0.250 mm and the height of the H_2 distribution channel to 0.1 mm. The above dimensional changes required refinements to the cooling plate deflection analysis and the pressure drop analysis. Deflection calculations were used to find the span between pillars that would allow for less than 5% max channel deviation. Plate mechanic calculations for a simply-supported (conservative) circular disk with constant thickness and a uniformly distributed pressure across one surface showed that a distance of 2.9 mm between pillar centers was acceptable for 3003 aluminum. Improvements in the inlet and exit LN2 plate headers have reduced pressure drop through the plates.

Ultimately this task was focused on the development of thermal management system test articles for validation. A 5 cm diameter test article (Figure 42) was developed that incorporates all of the design features present in the full scale design presented above. The first test article was built from 316 stainless steel and comprised three cooling/distribution plates as shown below. This test article allowed the demonstration multiple cooling plates integrated with the header.

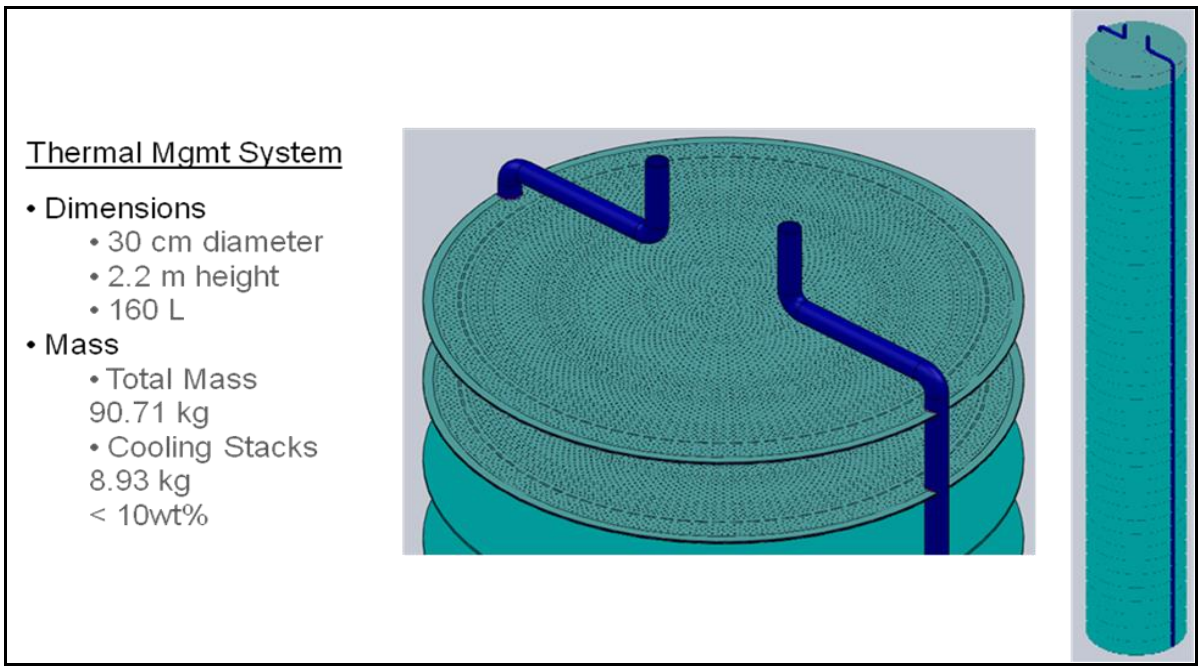

Figure 41: Current thermal management system concept with dimensions and mass.

Figure 42 shows the inlet/outlet, an area of critical importance in the design. Several failure modes and design features were considered here. Failure modes included thermal shock and thermal fatigue from repeated, instantaneous changes in temperature (from 295K to 70 K) across the braze joint which possessed a coefficient of thermal expansion different from the base stainless steel. Experimental evaluation of the effect of thermal shock on the braze joint included tensile testing of brazed joints. Further, a brazed joint configuration simulating the joint was also exposed to cryogenic temperatures for multiple times to assess effects on hermiticity under tank pressures. Finite element analysis (FEA) using Abaqus was used to numerically evaluate the thermal stresses encountered during the temperature swings for comparison with yield and thermal fatigue strengths.

Single-Plate Test Article: This section outlines the design, simulation and fabrication of the integrated cooling/hydrogen distribution plate test articles. The cooling plate has been analyzed for functionality based on heat removal, flow characteristics and failure modes of the plate.

Figure 43 shows the design of the integrated cooling/hydrogen distribution plate. It consisted of a bonded stack of four 5 cm dia. shims: a top shim, two LN_2 cooling channel shims (dark blue – 2nd and 4th shims from top) and one H_2 distribution shim (orange). Fabrication was completed as follows: photochemical machining (fluid channels in LN_2 shims and H_2 shim), laser cutting (shape, H2 holes) and diffusion

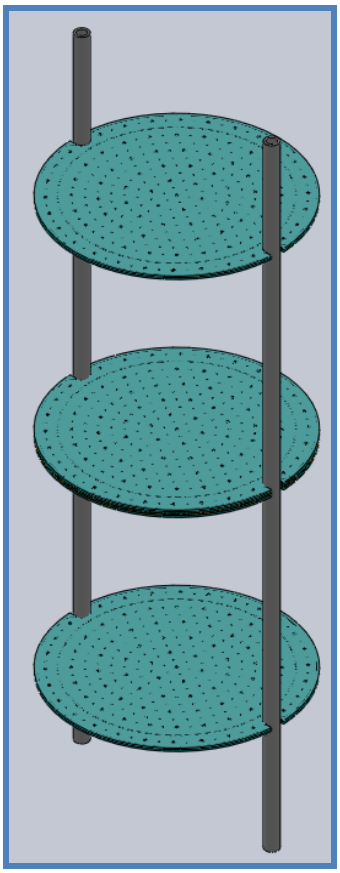

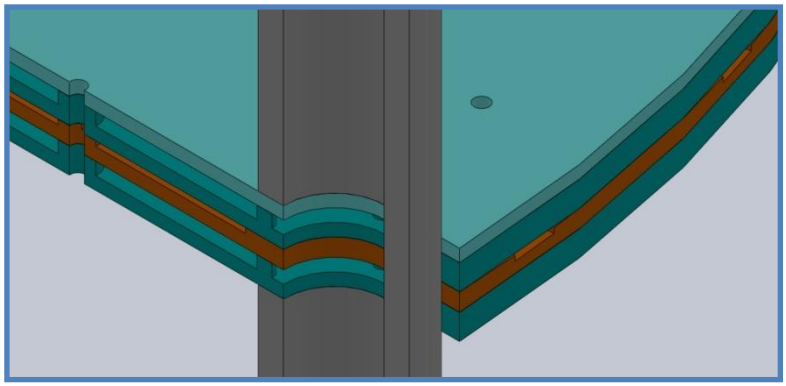

Figure 42: Left: Isometric view of the 5 cm test article; Above: Isometric section close-up view of the tube-plate joint.

bonding. The plate, below, has two cooling channels to remove heat from beds on both sides of the integrated plate. The hydrogen distribution shim allows for rapid radial transport of hydrogen into the storage beds. Holes through the cooling plates allow for axial distribution of the H_2 into the bed. Analyses performed on the cooling plate are pressure drop, LN_2 flow and thermal distribution, channel deflection due hydrogen charging pressure, and thermal shock (T_R to 70 K).

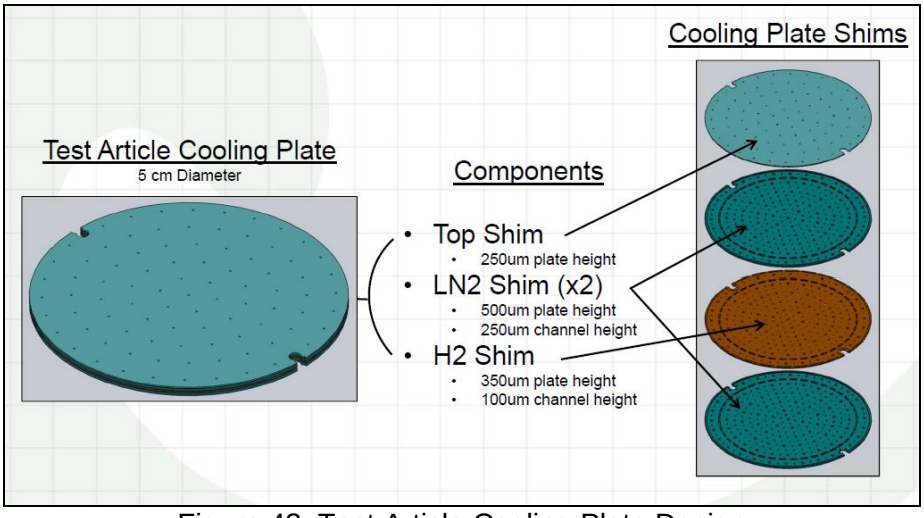

Figure 43: Test Article Cooling Plate Design

Two computational analyses were conducted on the cooling plate design: 1) CFD to map fluid flow distribution, thermal profile, and pressure drop across the cooling plate; and 2) FEA to evaluate the deflection of the cooling channel due to hydrogen charging pressure.

Figure 44 shows the pressure profile obtained using computational fluid dynamics (CFD) by applying required inlet flow rates of 0.85 liters/min. Flow characteristics were solved interactively. The pressure drop across the previous plate design was approximately 200 kPa (2 atm). As shown, the pressure drop across the cooling plate has been greatly reduced with the new header design to 5 kPa (0.05 atm). Figure 45 shows that the majority of the pressure drop in the plate is from the entry and exit headers. The dimensionless Reynolds number, which is the ratio of inertial and viscous forces, was reduced from 655,000 to 25,000 at the inlet and from 640 to 62 at the center of the plate. These reductions result from the increased cross-sectional area at the inlet port and the reduction of support pillars within the cooling plate.

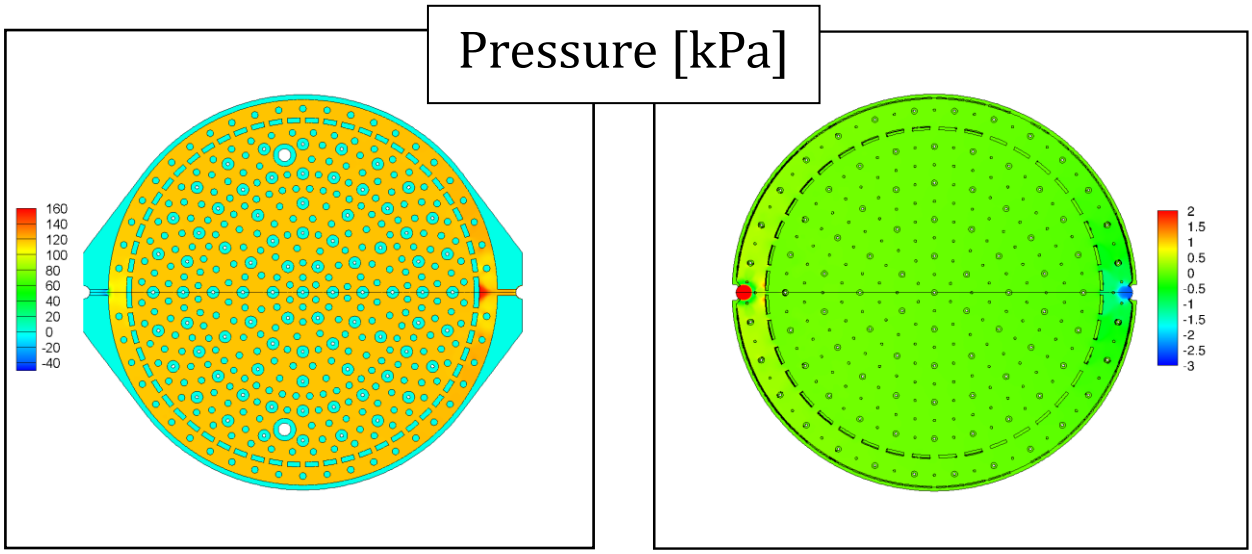

Figure 44: Pressure profile of previous (left) and new (right) cooling plate design. Current inlet/outlet design shows reduced pressure drop of nearly 2 atm.

Using the same flow conditions, the velocity and temperature profile across the plate was determined as shown in Figure 19. The velocity profile (left) gave insight into the potential for flow maldistribution and erosion effects. Flow was found to be reasonably symmetrical with little maldistribution. Erosion is mitigated by low velocity around the pillars. The model showed that the maximum velocity around the pillars was 1.5 m/s, with water as the working fluid. Erosion has been shown to be minimal under average flow velocities of 5 to 7 m/s [1,2,3]. Erosion at low temperatures with liquid nitrogen is not well documented in the literature and requires further investigation. Figure 46 shows the thermal profile within the cooling plate. This figure shows that at the required heat flux and current coolant flow rate, the liquid nitrogen does not exceed the boiling point of 77K.

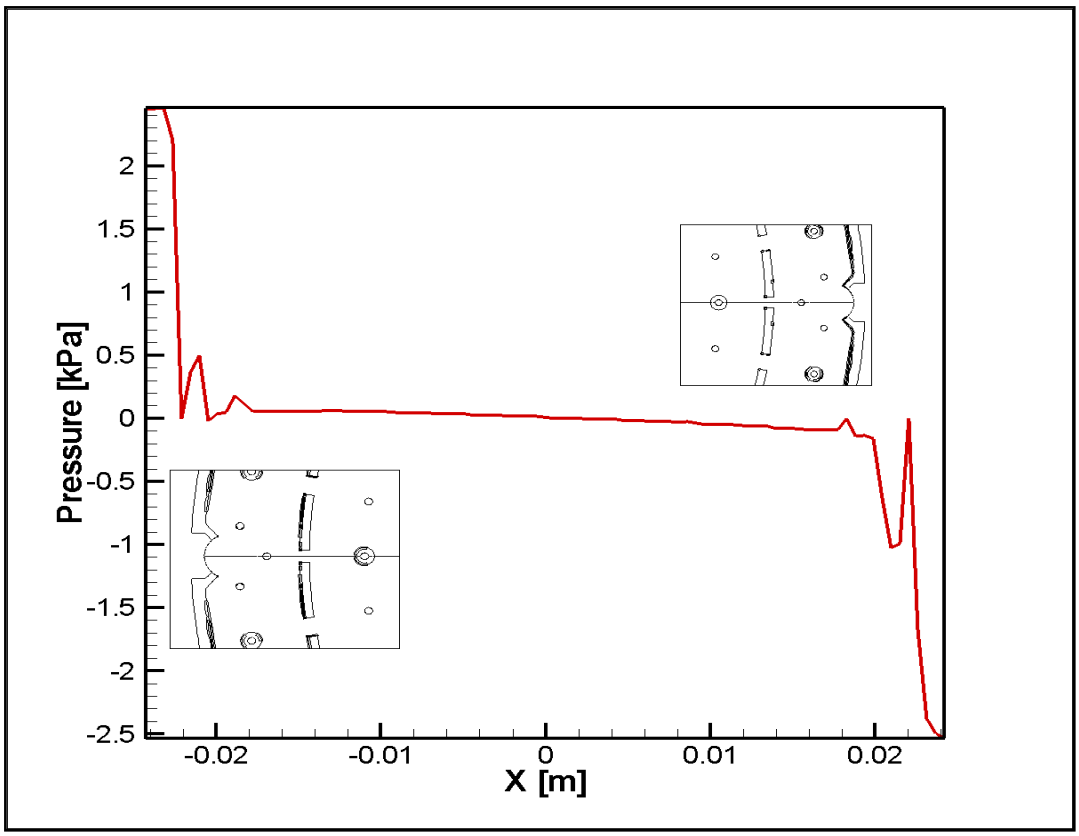

Figure 45: Pressure drop across center line of cooling plate (current design). Nonlinear pressure behavior occurs near non-uniform plate features.

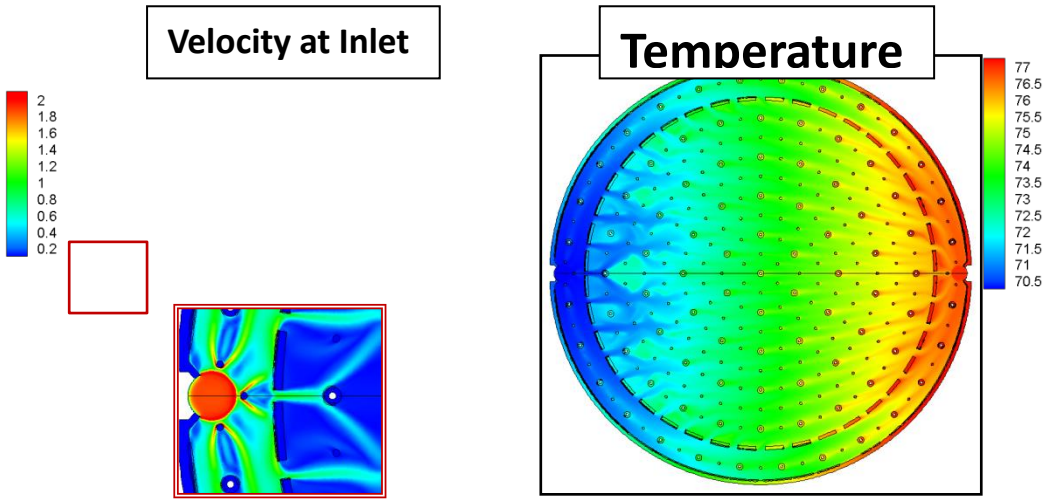

Figure 46: Thermal distribution within cooling plate from CFD Model

Abaqus FEA was used to verify that pillar spacing was adequate to support 50 atm hydrogen pressure with minimal deflection (Figure 47). In prior heat exchanger studies, average channel deflection of less than 5% of the channel height was found to minimize the effects of flow maldistribution on heat exchanger performance [4]. Results show that the maximum deflection, found in the center of the cooling plate (upper right image of the figure below), is less than 9 µm (3.5% average deflection) suggesting that flow maldistribution should not be an issue. Analysis was conducted with 316 SS, symmetrical borders, and 50 atm pressure normal to the bottom surface.

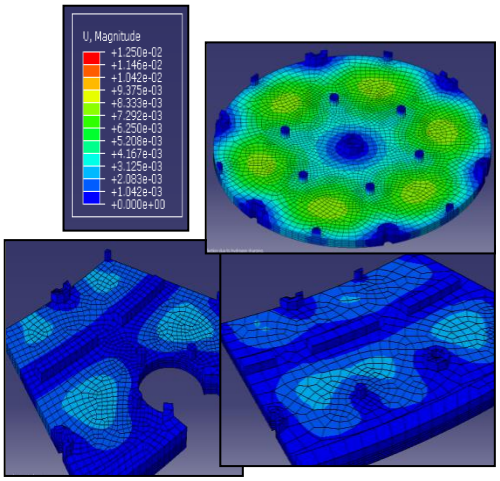

Figure 47: Abaqus FEA results showing maximum deflection of <9 um (3.5% of the channel height).

Micro-scale features on stainless steel shims were created with photo chemical machining performed by Great Lakes Engineering. Two designs were manufactured, a single flow channel plate with gas distribution capabilities,(micromachined by diffusion bonding of two shims), and a device consisting of two flow-through channels and a gas distribution channel (micromachined by diffusion bonding of four shims).

A CFD analysis was conducted using Fluent to evaluate the flow distribution at the flow rates (4.7 L/min per plate) and cooling capacities (656 W per plate) required to remove all of the heat of adsorption from two 1.5 cm high x 30 cm diameter modules with a single cooling plate. This level of heat removal represents a heat flux of 4.65 kW/m^2 for the cooling plate. The model was used to evaluate the worst case for thermal distribution and pressure drop of LN_2 in the cooling plates.

CFD was conducted using a k-epsilon model with laminar, transitional, and turbulent flows. The simulation was first run as a laminar model to determine the initialization parameters for the laminar and turbulent model. A tetragonal mesh was used and refinement was conducted using the turbulent refinement algorithm in Fluent.

The Reynolds number at the inlet and outlet were found to be around 23000 suggesting turbulent flow, though a Reynolds number of around 1000 was found across the majority of the plate suggesting laminar flow. Inlet velocity was found to be 9 m/s to generate a flow rate that would remove the heat of adsorption of two adjacent adsorbent beds without inducing boiling in the microchannels by limiting the delta T to 7 K.

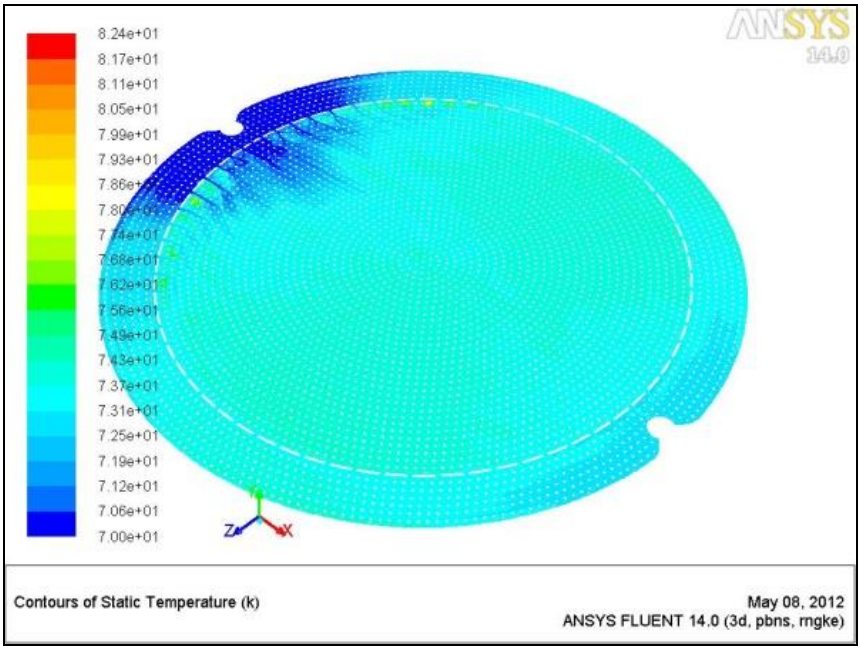

Figure 48: Temperature profile of the LN2 plate from CFD simulation

Figure 48 shows a steady-state solution of the thermal profile for liquid nitrogen in the cooling plate that occurs during hydrogen storage. The simulation investigates the thermal effects of hydrogen storage and shows how the cooling fluid removes the heat of adsorption. The thermal profile shows that the cooling fluid flow is evenly distributed across the plate. Also, Figure 18 shows that the thermal gradient from the inlet to the outlet is 7 K across the cooling plate, indicating that boiling in the microchannel is not an issue. The pressure drop was found to be 336 kPa (3.32 atm, 48.81 psi) across the cooling plate, with the majority of the pressure drop occurring at the inlet and outlet. These pressure drops were expected to be reasonable for an automotive platform.

Further CFD investigations showed that by considering the H_2 cooling, the pressure drop was reduced to 245 kPa (2.4 atm, 35.5 psi) with a temperature difference of less than 7 K using a flow rate of 3.2 L/min and an inlet velocity of 6.2 m/s. The high liquid nitrogen velocities at the inlet and outlet may cause concern due to erosion of the pillars, however, erosion requires particulate matter and it is assumed that the LN_2 is delivered without particulate.

Multi-plate Test Article: As showed above**,** a multi-plate modular adsorption tank insert (MATI) test article that was developed comprising three 5 cm microchannel plates and two header tubes with an internal diameter of 2 mm. Images of the test article can be found below. The joint was created by brazing with a nickel-based alloy.

The design of the cooling plates for the multi-plate test Article was conducted using CFD. A half model of the prototype cooling plate was used with symmetry across the centerline. A k-epsilon model was used with Reynolds numbers averaging below 3200. Inlet temperatures were set at 70 K and a heat flux of 4635 W/m2 was applied to the top and bottom surface of the cooling plate. Heat was allowed to conduct through interior pillars and the sidewall is assumed perfectly insulated with no slip condition on each wall.

Figure 49, below, shows that flow and temperature within the current design is well distributed with no boiling. Average velocity was found to be about 2.5 m/s. Pressure drop was found to be around 40 kPa (Figure 50).

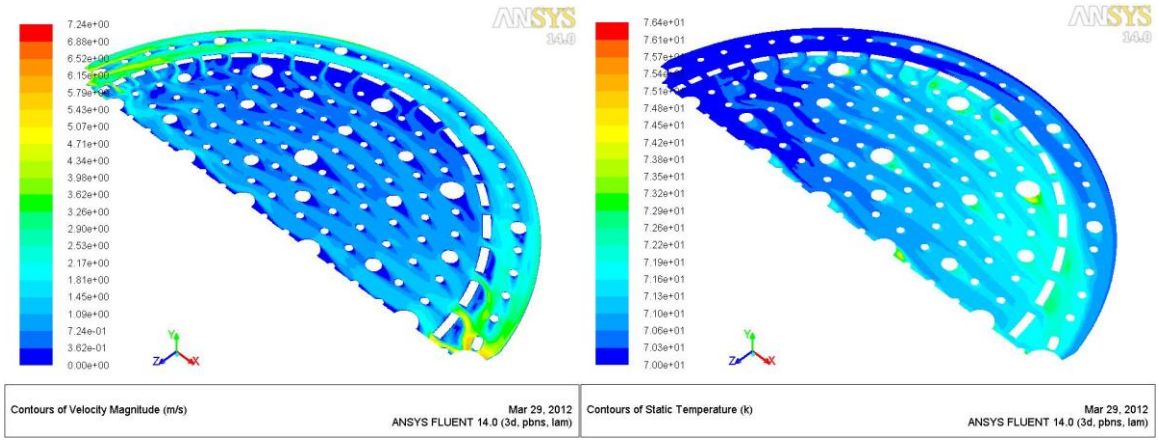

Figure 49: Thermal distribution and velocity across the prototype cooling plate

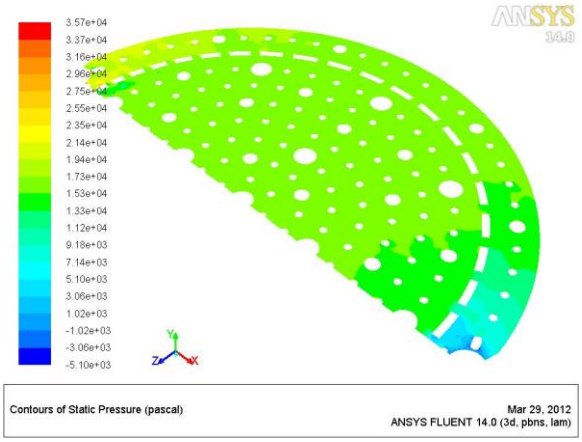

Figure 50: Pressure drop of the prototype cooling plate

Evaluation of the flow distribution between the three plates was solved using CFD by combining the single plate model detailed above and a three plate model including the headers and plates but none of the fine features (e.g. mechanical support pillars etc.) in the plate geometry. This two model approach was necessary owing to the three orders

of magnitude in length within the system. The pressure drop at the system flow rate (0.85 liters/min) was found within a single plate using the model above. Flow distribution was initiated by assuming one third of the overall flow (3 x 0.85 liters/min) entered each plate. Then the three plate model was solved and pressure drop within the headers was found. By replacing the dummy pressure drop across each plate from the three plate model with the pressure drop across the plate from the single plate model, a full pressure drop map was produced. From this map the pressure drop across each of the three plates was found and the flow rates through each plate were calculated and are compared in Table 8. This table shows excellent distribution of flow using a header with a 2 mm inner diameter.

Table 8: Flow distribution between plates		
System Location	Pressure Drop [kPa]	Percent of Flow
Plate 1	5*	34.1
Plate 2	5*	33.5
Plate 3	5*	32.4
Header Inlet	0.044**	100
Header Outlet	0.248**	100

* Denotes pressure drop from single plate model.
** Denotes pressure drop from 3 plate model.

Ansys FEA was used to evaluate the deflection of the cooling plate fins caused by the pressurized hydrogen environment. A pressure of 50 atm was applied uniformly, normal to all exterior surfaces. Symmetry was applied to the mid-plane and the tube-plate interface was fixed. The analysis showed that the hydrogen pressure has a negligible deflection with a maximum deflection of 3.6 um equally a 1.1% change in channel height. This effect is expected to be negligible on pressure drop. In addition, even if certain areas do not deflect, this level of variation across the microchannel plate should not cause significant flow maldistribution of cooling fluid during hydrogen filling.

A simplified steady state thermal model was developed involving two 316 SS tube sections connected by a BNi2 (Braze 820 – Lucas Milhaupt) braze alloy ring. The preliminary model was developed to evaluate worse case conditions i.e. a maximum thermal strain due to fully cooling of one plate to 70 K while all other plates are at the pre-fill bed temperature of 160 K and a maximum thermal gradient across the braze joint of 90 K. The braze joint was designed based on input from the braze vendor indicating that the braze length needs to be at least three times the smallest braze width to impart braze properties in excess of the parent material. Therefore, yield strength of the braze was assumed to be in excess of 316 SS. Symmetry was placed on the bottom of the tube assembly and a frictionless support was placed on top. The frictionless support acted as a surface to rest on and allowed the tube to contract freely. Ambient temperatures were initially set at 160 K. To produce the greatest possible thermal gradient across the braze joint, the inner surface of the top tube section was fixed at 70 K and the inner surface of the bottom tube section was fixed at 160 K. These boundary conditions were expected to be conservative, estimating the effect of the thermal gradient caused by introducing the 70 K fluid into a tube at 160 K. Results (See

Figure 51) show that stresses reached only 190 MPa, which is just below the yield strength of 316 SS (205 MPa).

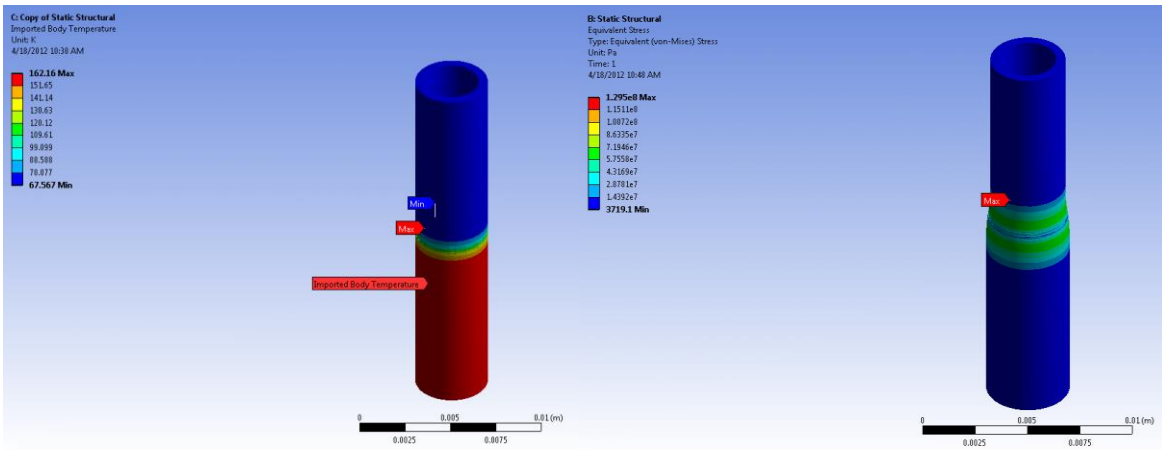

Figure 51: Screen shots from Ansys showing the thermal gradient focused on the braze joint (left) and the stress profile (right)

Three sub-scale MATI prototypes were fabricated for experimental validation and to evaluate the manufacturability of the design and proposed manufacturing processes. The three 5 cm diameter cooling plates were designed to remove at least 52 W (4.4 kW/m^2per cooling surface x 2 surfaces per plate x 3 plates) of heat at a water flow rate of 149 mL/min, an inlet temperature of 291 K and an outlet temperature of 296 K. The hydrogen plates were not included in the fabrication because the experiments were designed to evaluate the operational performance of the hermetic fluid network. To assess manufacturability of the MATI, the prototypes were fabricated using the same manufacturing plan established for the full-scale MATI. The design of the plates and headers were similar to the full-scale models to closely assess the functionality of the full-scale model. A difference that is present in the prototype is the inclusion of through holes in the liquid nitrogen plates. These holes were designed as thermocouple ports in case the plates were used to experiment with adsorbents. Cooling plate shims were photochemically machined (PCM) to a depth of 250 µm from 500 µm thick sheet stock to create the fluidic channel. Through holes were etched by PCM on both sides of the shims. The perimeter of the top shim and the etched shim were laser cut.

Prior to fabrication, the shims were characterized for etch depth. An optical profilometer was used to verify the etch depth. Ten samples were taken from 5 different cooling plate shims. Average etch depth was found to be 261.3 µm with a standard deviation of 9.1 µm which at a 95% confidence interval is an etch variation of 6.9%.

The shims were diffusion bonded using a vacuum hot press (See Figure 52). Critical parameters of diffusion bonding were time, temperature, pressure and atmosphere. The shims were bonded at 975 °C for 180 min with 1000 lbf at atmospheric pressures below $5x10^{-5}$torr. Fixtures were made from graphite and plates were gang pressed to bond three cooling plates in one bonding cycle. Fifteen cooling plates were bonded with a 100% yield based on hermeticity testing described below. All shims were visually

inspected with an optical microscope to verify the bond along the outer faying surfaces of the shims. Pressure uniformity on the shims appeared to be excellent based on the parallelism of the graphite brazing platens and ram used during the hot pressing cycle. Each platen was machined to have a flatness and parallelism of less than 0.0005 in (12.7 µm). The cooling plates were found to have a parallelism and flatness of around 13 µm after bonding. Out of parallelism could be caused by misalignment with the pressing rams, non-parallel surfaces of the pressing rams or due to the out of parallelism of the bonding fixtures.

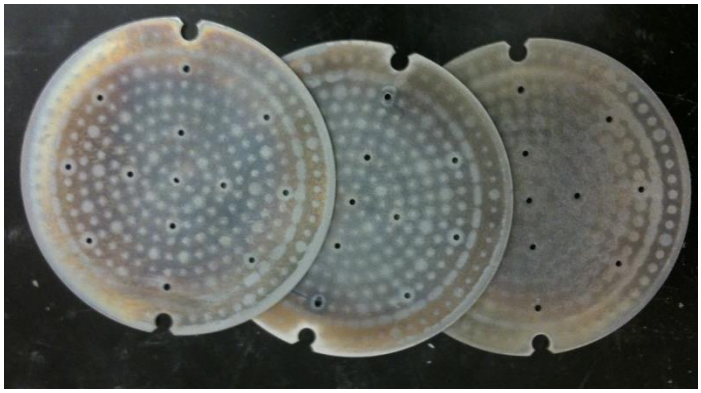

Figure 52: Bonded LN2 plates

The header tube was made from rolled 316 stainless steel tubing and had a 3 mm inner diameter with a 0.5 mm wall thickness. Tubes were machined using a vertical end mill and fixtures were designed to enable the fabrication of the tubes without structural failure due to the cutting forces. The fixture allowed for the tube to be clamped in place for the first cut then rotated to make the second cut, forming the faying surfaces of the tube.

The slits were designed so that a first cut would cut half-way through the tube, the fixture would rotate 45° and then a second cut would be made half-way through the tube. The result is a slit where, in cross section, 75% of the tube section is removed to fit up with the cooling plates. The shape of the cut only allowed the tubes to be fit onto the plates in one direction so assembly errors due to misplacement of the header were eliminated. Tube slits were required to be 750 µm high plus a 25 µm clearance for brazing joint fit-up. A 0.03” (762 µm) wide end mill was used to cut the slits. Slit width was measured using an optical microscope. An average slit width of 767.7 µm was produced with a standard deviation of 5.9 µm for 18 slits.

The prototypes were joined using Braze 820 (BNi-2), a nickel based braze material supplied from Lucas Milhaupt. Critical parameters for brazing were temperature hold time, vacuum, joint fit-up and joint cleanliness. The shims were prepared and cleaned with deionized water, acetone, methanol and deionized water wash prior to brazing. The brazing cycle followed the temperature profile in Figure 53 using a CamCo J-12 Combo Furnace.

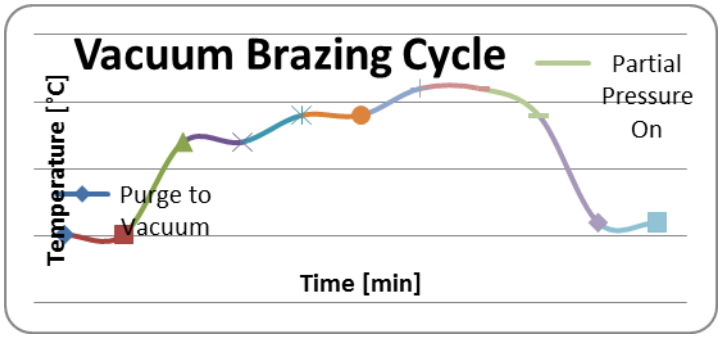

Figure 53: Vacuum brazing temperature profile

Initial brazing results were assessed using 100 psia air by leak testing the prototypes in water. Bubbles indicated any issues with hermeticity. The leak testing was used to evaluate both the bonding and brazing cycles. Two of the three prototypes were leak proof and one had a minor leak in one braze joint which was subsequently repaired by running a second cycle. In total, 17 of 18 braze joints were hermetic which is a 94.4% braze joint yield and a 67% device yield (See Figure 54

Figure 54: Fabricated MATI Prototypes

***References*:**

[1] Haake J. M. , Faircloth B. , 2005, Requirements for long life micro-channel coolers for direct diode laser systems, Proc. SPIE, Vol. 5711, pp.121-131.
[2] Bonati G., et al., 2003, A new heat exchanger concept for high power diode laser systems, Proc. SPIE, Vol. 4947, pp. 270-277.
[3] Bonati G. , Hennig P. , Schmidt K. , 2004, Passively cooled laser diodes for high power applications, Proc. SPIE, Vol. 5336, pp.71-76.
[4]B. K. Paul, “Micro energy and chemical systems and multi-scale fabrication,” in *Micromanufacturing and Nanotechnology*, 1st ed., N. P. Mahalik, Ed. Berlin, Germany: Springer-Verlag, 2006, pp. 323-352.

Conduction Enhancement of Adsorbent: It was determined that for optimum performance of the MATI, the spacing between cooling plated needed to be at least 5

cm. Cooling a 5 cm thick puck required two design changes. First, hydrogen distribution was taken out of the cooling plate and it was moved to the middle of the 5 cm MOF-5 puck allowing hydrogen to cool the interior of the 5 cm puck resulting in two 2.5 cm pucks separated by a hydrogen distribution plate. The second change was to introduce conduction enhancement in the puck which consisted of small diameter aluminum pins inserted in the puck. It was critical to know the limitation from the MOF-5 bed and manufacturing process. This section explores the feasibility of fabricating a MOF-5 puck with conduction enhancement.

OSU is collaborating with Ford on a test program with the goal of demonstrating the ability to fabricate pucks with embedded pin shaped fins. A preliminary design of the pin-based enhancement test articles and an outline of our proposed test plan were sent to Ford for input. While smaller feature size will have less impact on the MOF5 bed, it could be insufficient to enhance the conductivity of the bed. The goal is to find out the critical dimensions and features that maximize the conduction enhancement while maintaining the integrity of the “hockey pucks”.

Three key parameters were identified. These include the diameter of the pins, the spacing between pins and the shape of the pins. Hollow pins were initially thought to have the highest chance of success – minimal impacts on the MOF5 beds, although it provided reduced conduction enhancement compared to solid pins of the same size. Figure 55 shows the concept of using 1/16” hollow. Figure 56 shows the concept of using small nails which have the diameter of 0.035”. Additional test pieces using bigger nails (0.060”) were also be considered. For the pieces using nails, 3 different nail spacings were evaluated. The current MATI design assumes two 2.5 cm MOF5 pucks separated by a hydrogen distribution plate using Micro Pyramid Truss Networks (MPTN). Based on preliminary discharge cycle simulation using Comsol, the length of the conduction enhancement pins needed be around 1 cm. Thus, the goal is to demonstrate the capability of fabricating 2.5 cm thick pucks with 1 cm long pins.

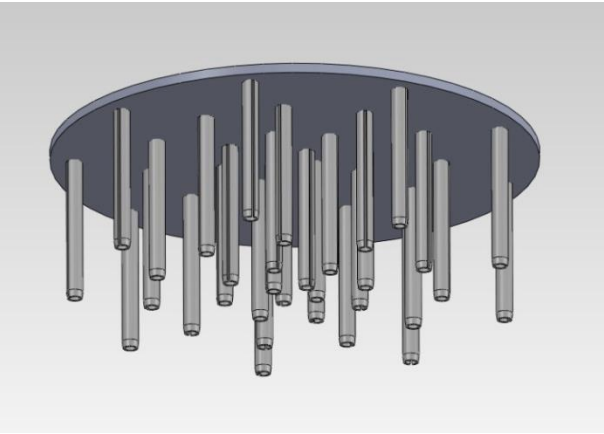

Figure 55: Conduction enhancement using hollow pins (1/16”)

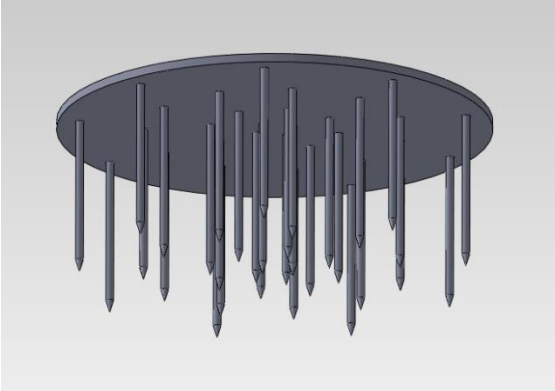

Figure 56: Conduction enhancement using nails (0.035”)

The proposed test plan was sent to Ford for guidance. After receiving inputs from Ford, it was decided for OSU to conduct an initial assessment of pin insertion using existing MOF5 beds. A delicate cutting process was used to obtain a 3 cm (length) bed from the current 7 cm (length) bed. The initial insertion test was to use syringe needles with sharp tips, since it was expected to have the minimal impact on MOF5 beds. Two types and two sizes of syringe needles were used for the insertion test with a 3 cm bed. The pictures after the insertion are shown in Figs. 57 and 58. A summary of the findings are listed as follows:

- The 23 Gauge (0.025”) needles seem to work well at the tested distance (0.5” – 0.75”). However, it becomes questionable as more needles being put in or the required pin density is increased.
- Most of the cracks were caused by the 21 Gauge (0.032”) needles, indicating there is a size limitation for current MOF5 bed regardless of the density of the needles.
- Sharp tip is not required for the needles to insert successfully. However, it became fairly obvious that the same size solid pins will be extremely challenging without making cracks because of large displacement or compression of MOF5. Thus the previously suggested design using 0.035” and 0.06” nails as the conduction enhancement pin will unlikely to work.
- The insertion depth was typically over 1.5 cm, although it is clear that shorter insertion depths will likely have less chance to form cracks.

Based on these findings, the team switched to an alternative fabrication approach were the pins were inserted in the uncompacted MOF-5 and the pucks were compacted around the pins.

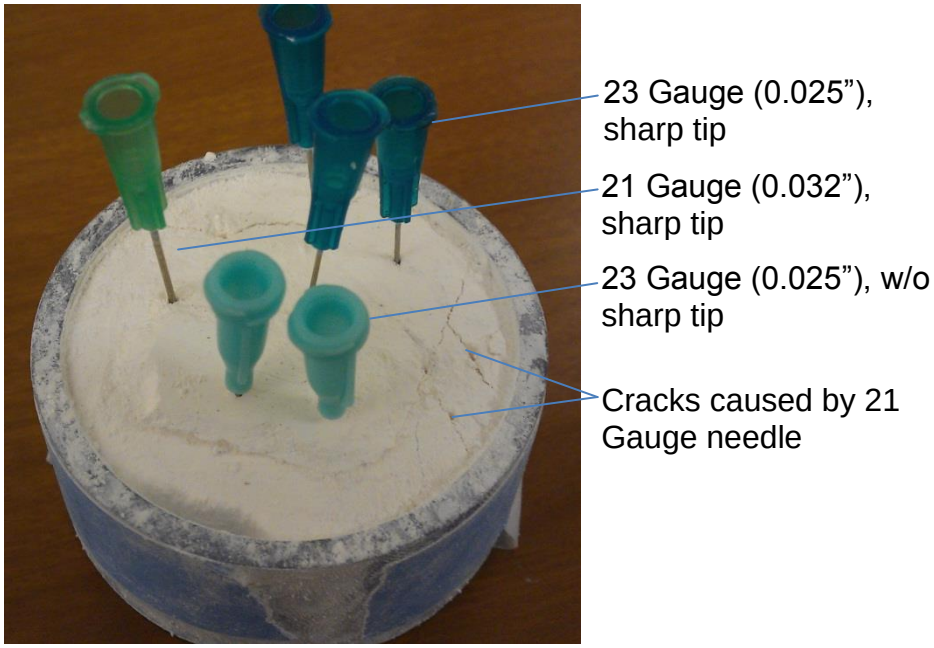

Figure 57: Picture 1 after the needle insertion

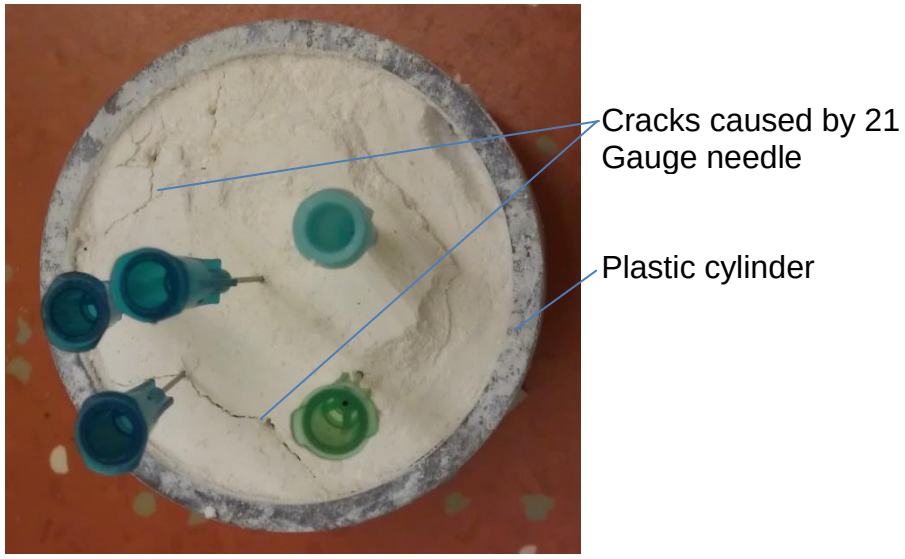

Figure 58: Picture 2 after the needle insertion

Key Findings: *Key findings from Task 2.3 include: 1) based on modeling the microchannel cooling plate was capable of operating at the design operating pressure with no significant deflections and was capable of providing the design flow rate at a reasonable pressure drop with good flow distribution, 2) The multi cooling plate test article was could be brazed and the resulting design was predicted to have good flow distribution between plates and 3) The insertion of pins into a densified puck was not a good way to fabricate a conduction enhanced puck and we should focus on forming the puck around the pins during the densification process.*

Task 2.4 Experimental Investigations: Experimental investigations involved separate effects testing using the separate effects test apparatus described above with the focus of determining the performance of individual cooling plates and the integrated test apparatus, also described above and focused on the performance of the complete system including heat and mass transfer effects. The results of each set of experimental investigations are presented below.

Separate Effects Testing (Cooling Plate) Experimental Results: Once the separate effects test apparatus had been assembled and debugged (as described above) a number of heat transfer and pressure tests on cooling plates were performed. Three sets of test were run while ensuring that the surface temperatures were less than T_{sat}. The saturation temperature was estimated using the temperature and pressure at the exit of MATI heat sink. Figure 59 shows the heat transfer coefficient for the tests conducted as a function of mass flow rate.

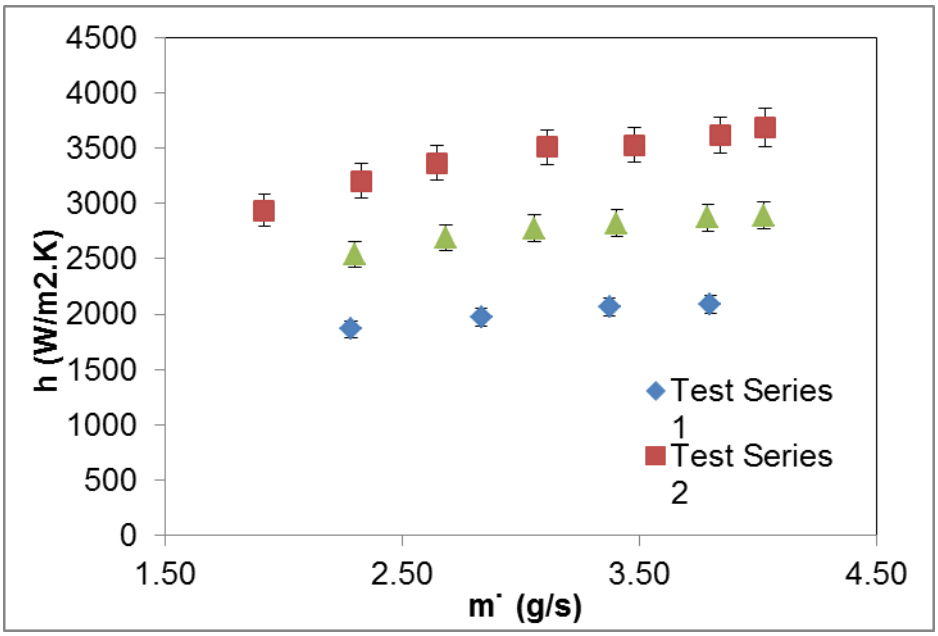

Figure 59: Averaged heat transfer coefficient through MATI heat sink at heat flux range of 15400 – 21700 (W/m^2) including uncertainty estimates of measurements

The only difference between test series is the average amount of imposed heat flux. The test series 2 which had the higher heat transfer coefficients belonged to the higher heat fluxes while test series 1 had lower heat fluxes. All three series of data showed a modest increase in heat transfer coefficient with flow rate. If the flow within the microchannel were laminar, we would not expect to see a variation in heat transfer coefficient with mass flow rate. Since the flow within the heat sink was diverging from the inlet and then converging to the exit, the cross sectional velocity varies at any location within the channel.

Fluid passage cross section area was calculated based on the design of MATI microchannel at three locations. The first location corresponds to the inlet of heat sink right before reaching the pin fins. The second location was 4.5 mm from the inlet toward the center of microchannel and third location was equidistance from the inlet and outlet of MATI heat sink. Using the equation below to obtain hydraulic diameter in internal flows (Eq. 1), the Reynolds number associated with data points shown in Fig. 59 were calculated and listed in Table 9.

$$D_h = 4\frac{A_{cross}}{P} \tag{6}$$

Where A_{cross} is cross sectional area and P is perimeter of fluid passage.

Table 9: Cross-section area of fluid passage in MATI and corresponding Re number range

Distance from Inlet (mm)	A_{cross} (mm^2)	Re number range
0	1	6650 – 13592
4.5	6.18	1064 – 2146
23.87	9.78	673 – 1376

One can see that fluid flow entered turbulent. However, within 4.5 mm into the heat sink, the Re number suggested laminar flow. When the flow converged towards the exit, the flow once again turned turbulent. This change from turbulent to laminar and back again to turbulent could explain the modest change (increase) in heat transfer coefficient with mass flow rate seen in Fig. 59.

Pressure drop along the microchannel is depicted in Fig. 60. These pressure drop data were measured using a differential pressure transducer and show that the pressure drop increases continuously with flow rate.

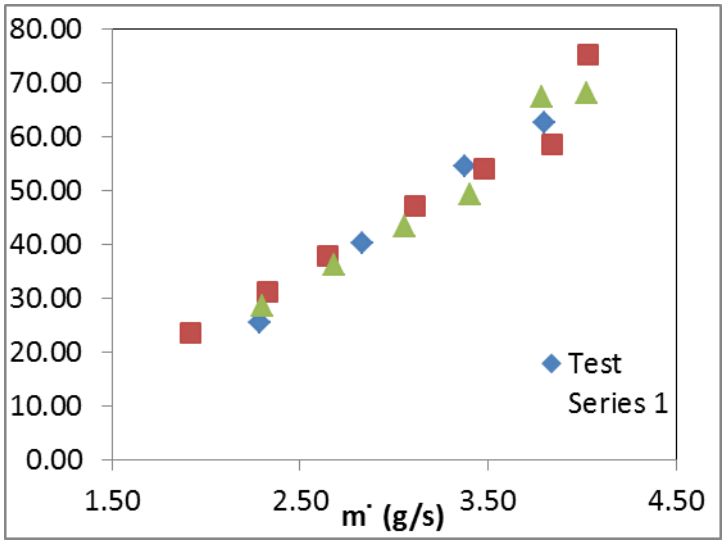

Figure 60: Pressure drop through MATI heat sink at heat flux range of 15400 – 21700 (W/m^2)

Multi Cooling Plate Test Article Experimental Results; The thermal system evaluation investigated the flow distribution characteristics of the MATI prototype using water as the working fluid. Four criteria were used to assess the functionality of the MATI system design:

1. Cooling capacity;
2. Flow distribution across a cooling plate;
3. Flow distribution between multiple cooling plates; and
4. Pressure drop through the system

The experimental setup to assess these functional criteria is shown in Figures 61 and **Figure** . The block diagram shown below is representative of the experimental setup.

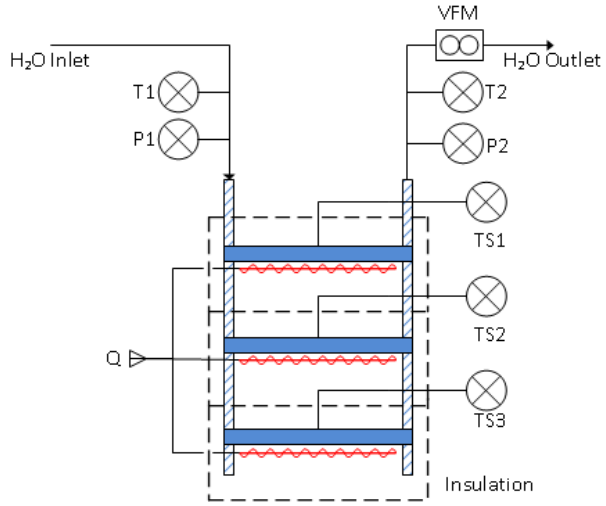

Figure 61: Block diagram of the fluidic system evaluation

The thermocouples outside of the insulation were for determining the thermal gradient of the system when a known heat load is applied. The pressure transducers showed the differential pressure of the cooling fluid. The thermocouple sets on the top surface of the cooling plates were to show the thermal distribution and the resistive heaters on the bottom of the cooling plates supply the heat load. Thermocouples were calibrated using digital thermometers attached to a heat source, pressure sensors were calibrated with an Omega DPG400 pressure gauge, the Malema M-1500 mass flow meter was calibrated by catching and weighing the water over a specified amount of time, and the power supply to the heaters was calibrated with a digital multimeter. Thermocouples were evaluated at room temperature to show no deviation from the specified error of ± 0.2 °K.

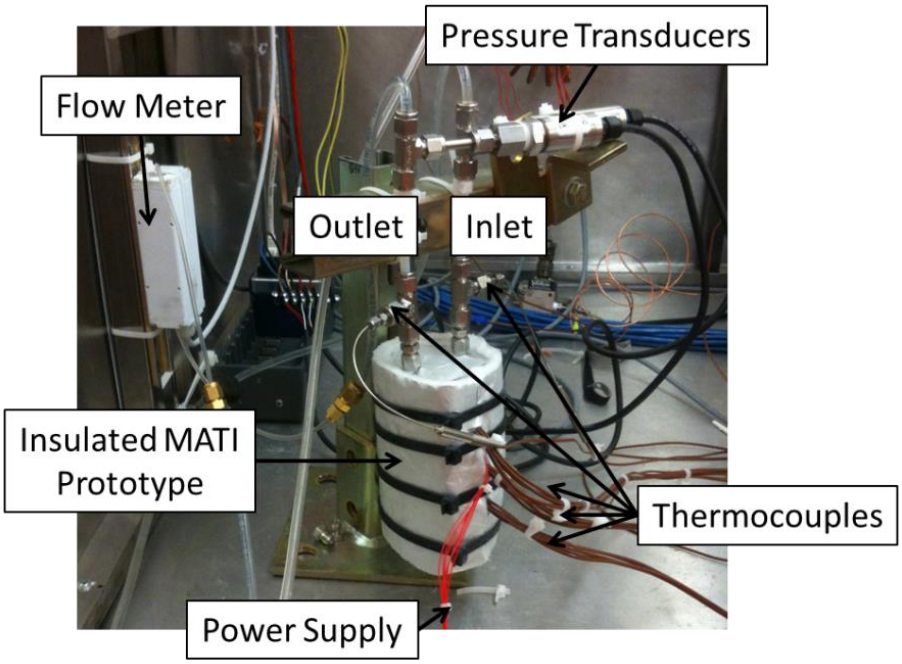

Figure 62: Experimental setup for fluidic system evaluation

Cooling capacity was evaluated by applying 17.33 W per heater (from two cooling surfaces at 4.4 kW/m^2) for a total heat load of 52 W across the three resistive heaters (Figure 34) and running the water mass flow rate through a range of values. The temperature difference from the inlet and the outlet was measured and compared with calculations. It was calculated that 149 mL/min would remove the applied heat load using the density of water at 1000 kg/m^3 and a constant heat capacity of 4185.5 J/kg-K. Flow distribution was evaluated during the cooling capacity tests. Thermal profiles were logged and charted from the top of each cooling plate (Figure 63). The data was collected and compared across each cooling plate as well as between the cooling plates. The temperature profiles across each plate indicate the flow distribution for each plate, while temperature profiles between plates indicate flow distribution of the headers to and from each cooling plate.

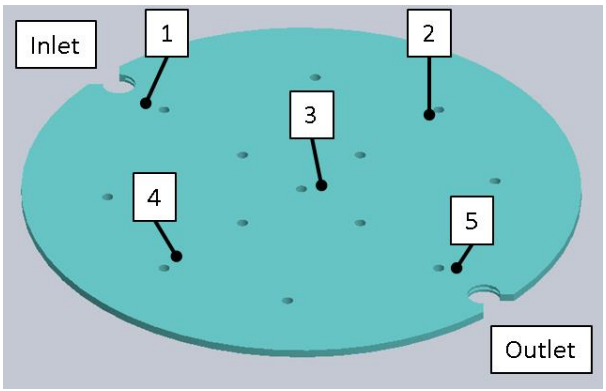

Figure 63: Thermocouple placement for thermal distribution tests (on top side of cooling plate)

Pressure drop was evaluated using pressure transducers connected to the inlet and the outlet of the prototype test loop. Pressure was instantaneously measured and the data was plotted against flow rate. The pressure drop of the MATI prototype was found by subtracting the total pressure drop found with the MATI unit in the test loop by the pressure drop obtained by substituting a large diameter tube in place of the MATI. The experimental pressure drop was used to validate the CFD model of the MATI prototype.

Thermal stress evaluation: The second set of experiments was designed to assess the effect of thermal stress on the prototypes. Each joint was visually inspected and tested for leaks according to AWS C3.3:2002[i] prior to the experiments. The MATI was then subjected to a worst case scenario thermal stress test, where two thermal shock and thermal cycling failure modes were evaluated caused by any one of the following:

1. Thermal gradients;
2. Differential thermal expansion/contraction of the braze joint; and
3. Failure due to mechanical constraint.

The largest thermal gradient expected in the storage tank is 90 K, from the temperature before fill (160 K) down to the temperature of the incoming liquid nitrogen (70 K). However, to be conservative, the MATI prototypes were exposed to liquid nitrogen from room temperature (294 K). The integrity of the joints was evaluated by the hermeticity of the joints either during or after testing. Two methods were used to evaluate the mechanical integrity of the joints due to thermal shock and thermal fatigue as described below.

First, to assess thermal shock effects, a dewar was filled with liquid nitrogen and the prototypes were subjected to ten controlled dunks in which the prototypes were submerged one cooling plate at a time. Each cooling plate was held submerged for 5 seconds before moving to the next cooling plate. This evaluated not only the effect of large thermal gradients and differential thermal expansion across the braze joints; it also evaluated the effect of mechanical constraint from one cooling plate to the next. Once the prototype was fully submerged, it was held below the surface for 30 seconds before being removed and left to air dry. These tests were performed 10 times in order to assess thermal cycling effects. Leak tests were conducted after each dunk by plugging the outlet and pressurizing the MATI prototype with air at 100 psi while submersing the prototypes in water to check for bubbles.

A second set of experiments were conducted to provide a more realistic assessment of thermal stress buildup within the MATI unit. This test was performed by connecting the MATI unit to a LN2 test setup and flowing LN2 through the system until the channels reached temperatures below 80 K. Leak testing was used after the test to assess the impact on hermeticity.

Experimental results

A CFD simulation was conducted to establish the expected results of the experiments. The results showed that a pressure drop was expected to be 1.01 psi at a flow rate of 149 mL/min with the addition of the pressure drop calculated through the headers on the MATI prototype. A heat load of 17.3 W was applied to the cooling plate (4.4 kW/m^2 per surface). Figure 64 shows the thermal distribution of the cooling fluid in the cooling channel and also shows the inlet and outlet temperatures for the cooling capacity calculations. The thermal gradient was expected to be linear from 291 K at the inlet and 296 at the outlet, showing a temperature gradient of 5 K. The thermocouples perpendicular to the flow direction was expected to be uniform at 293.6 K. Probed points at the specified points were used to compare against the experimental results for thermal distribution.

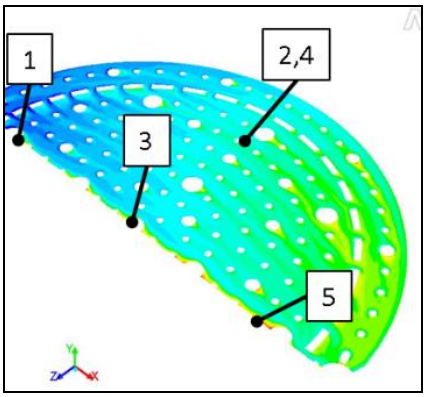

Figure 64: CFD results for pressure cooling capacity and thermal distribution

As expected, inlet thermocouples (X-1) had the lowest temperature while the outlet thermocouples (X-5) had the highest temperature. With an inlet temperature of 291 K average across the plates, the average outlet temperature was 296 K. The middle thermocouples (X-2, X-3, X-4) were uniformly grouped and were slightly higher than the expected value of 293.5 K which is likely due to the thermocouples being placed directly over the heaters. The middle thermocouple has a higher temperature which is likely due to the heater being square rather than round. The thermal profile of the thermocouples in the flow path show good agreement with the expected results suggesting that the expected cooling capacity of the plates were achieved.

Experimental results also implies that there was good distribution across and between plates. The temperatures for each location are within about 0.5 °K of each other, showing good agreement. The temperature differences are close to the error limits of the thermocouples (±0.2 °K). The error bars show the standard error of the thermocouples.

Experimental cooling capacity results were obtained by measuring the temperature difference from the inlet to the outlet using the Omega type T thermocouples and calculating the cooling capacity at a given flow rate

The required flow rate was calculated to be 149 mL/min to remove the 52 W across the three plates. Results show that the heat was effectively removed at flow rates of 149 mL/min and beyond which is in agreement with calculations. Below a flow rate of 149 mL/min, the flow is not able to remove enough heat. Consequently, heat is lost via axial conduction or through the insulation. The error bars are set at the standard deviation from four test runs.

The experimental pressure drop through the MATI prototype was determined as a function of flow rate. The expected pressure drop of the prototype cooling was estimated by CFD. Expected values were 1.03 psi and 4.13 psi for flow rates of 150 and 400 mL/min, respectively. Experimental results showed that the MATI prototype had a pressure drop of 1.42 psi at 150 mL/min compared to a computational solution of 1.03 psi resulting in an experimental error of 27 %. At a flow rate of 400 mL/min, results showed 5.58 psi versus 4.13 psi from the computational solution resulting in an experimental error of 26 %. A significant portion of this error can be explained by channel deviations of approximately 13 μm (5.2%) detected after diffusion bonding using external profilometry. These deflection are due to creep of the microchannel fins caused by bonding pressure being applied to unsupported spans. As the pressure drop as a function of flow rate is related to hydraulic diameter by a relationship of $1/D^4$, a five percent reduction in the hydraulic diameter would increase the pressure drop by about 18 %. The remainder of the difference can be explained by the prototypes having filleted edges due to PCM which further reduce the hydraulic diameter and because of the slight out of parallelism. In future efforts, pressure drop can be ameliorated through the use of shaped platens to apply bonding pressure only on supported regions of the cooling plate during diffusion bonding.

Per the experimental protocol for investigating thermal stress, the two successful prototypes were submerged 10 times in liquid nitrogen from room temperature with no observable failures during hermetic testing. Next, the two prototypes were setup on the cryogenic test loop and liquid nitrogen was run through the channels for 5 minutes without hermetic failure (Figure 65). Afterward, the MATI prototypes were left on the experimental setup overnight to heat back up to ambient temperature so as to not cause any failures in the cryogenic test setup. Again, the prototypes were subjected to hermeticity testing without failure. Throughout testing, no observable changes in the geometry of the prototypes were observed. These results suggest that thermal shock is not a concern in the MATI prototypes since the maximum temperature gradients are expected to be only 90 K compared to the temperature gradients of 220 K experienced in these tests.

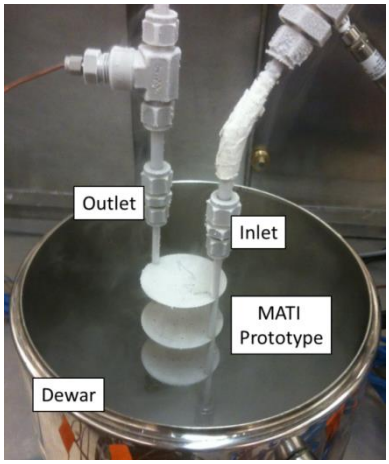

Figure 65: LN2 flow through test

Integrate Testing – Adsorption experiments were performed with MOF-5 material at room temperature in the absence of coolant flow and at cryogenic temperatures with and without liquid nitrogen coolant flow. The experiments were on a ~3.2 [cm] tall MOF-5 bed to verify that the MATI designed heat exchanger has the ability to improve the removal of generated heat during the adsorption process. The MATI's ability to remove heat is compared to adsorption experiments performed in the absence of liquid nitrogen flow through the heat exchange unit.

Cryogenic adsorption experiments were performed with a 180 [s] H_2 charging time and total of 300 [s] liquid nitrogen flow, when applicable. The locations of the thermocouples inside of the MOF-5 bed are depicted in Figure 66 and the direction of liquid nitrogen flow in comparison to the MOF-5 bed.

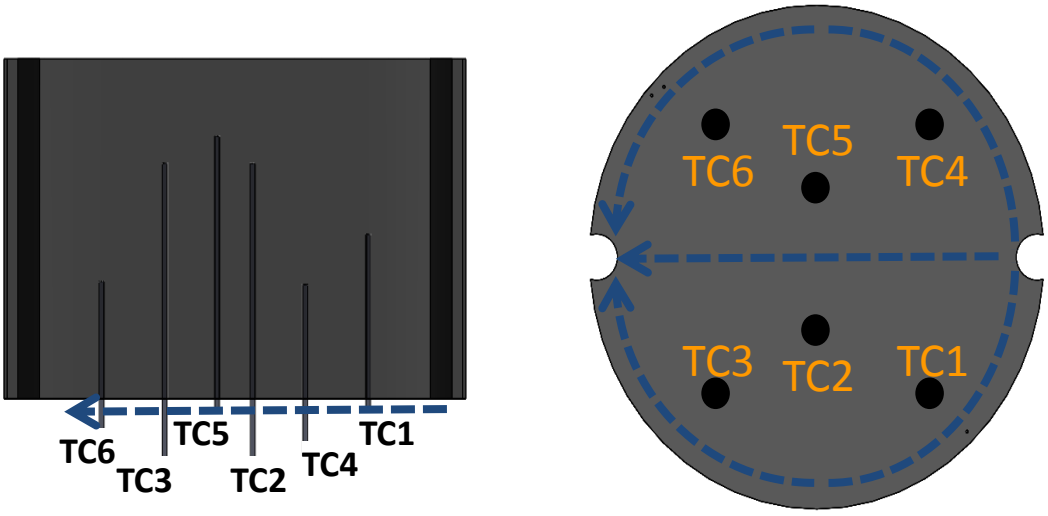

Figure 66: Thermocouple locations in compact MOF-5 bed.

Figures 67-68 depict the observed temperature rise inside of the MOF-5 bed during hydrogen gas charging, entering at approximately 130 [K] with and without liquid nitrogen cooling through the MATI, respectively. Although the overall response maintains a similar shape for each case, the thermocouples located closest to the MATI surface (TC 1, 4 and 6) experienced a significantly lower temperature rise during charging (11 [K], 12 [K], and 9 [K], respectively) with the presence of liquid nitrogen cooling compared to the charging without cooling. The temperature rise during charging for TC-2 and TC-3 were also lower than in the experiment without cooling, while the thermocouple located highest in the bed, TC-5, experienced an approximately the same temperature during charging with cooling compared to charging without cooling.

In both experiments, the maximum temperature at each thermocouple was reached at approximately the same time as the maximum pressure was observed. However, with approximately 0.0025 [kg/s] (~150 [mL/min]) of liquid nitrogen flow through MATI the thermocouples located closest to the MATI, TC-4 and TC-6, are sub-cooled by 16 and 20 K, respectively at 300 [s]. The same thermocouples, TC-4 and TC-6, were 6 [K] and 7 [K], respectively, above their initial temperature at the same time of charging/cooling cycle (300 [s]). Only thermocouples TC-2 and TC-5 did not cool below their initial temperatures within 300 [s] with liquid nitrogen cooling. However, at 300 [s] their respective temperatures were only 2 [K] and 6 [K] above their initial temperatures. This is still much better from the case without cooling in which temperatures of approximately 16 [K] above initial temperatures were recorded at both TC-2 and TC-5 at 300 [s].

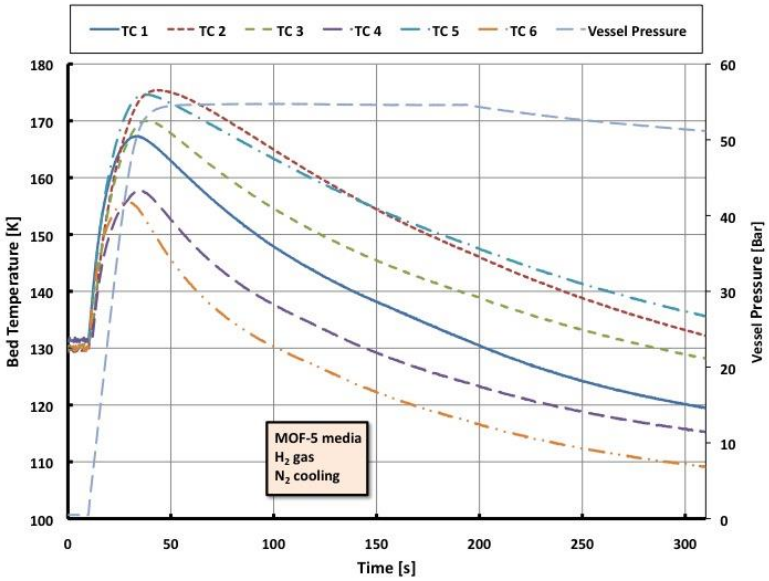

Figure 67: Temperature rise in MOF-5 compact bed during H_2 gas charging entering at 130 [K] with liquid nitrogen cooling.

In addition to the improvement in heat removal in the bed with liquid nitrogen flow through the MATI, the pressure vessel stored 10.9% more hydrogen inside with cooling compared to the system without cooling. When the major void space within the vessel

(not including voids within the bed) is subtracted from the total hydrogen in vessel the system stored 11.2% more hydrogen in the MOF-5 bed with liquid nitrogen flowing through the MATI.

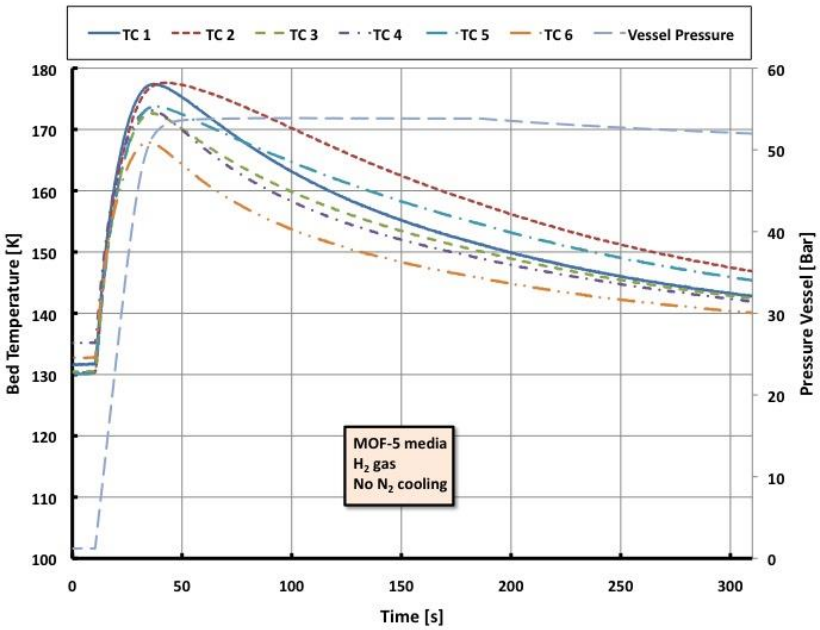

Figure 68: Temperature rise in MOF-5 compact bed during H_2 gas charging entering at 130 [K] without liquid nitrogen cooling.

It is important to notice that all the data presented in this section, does not attempt to illustrate the maximum performance of the bed, because the experimental conditions do not match the best operating parameters of a hydrogen storage system. Experimental conditions used in this study: H_2 inlet temperature in the range 90 [K] – 130 [K], and N_2-inlet temperature of 87 [K] are somewhat away from more favored operating parameters which will be, most probably, used in a hydrogen storage system. Implemented experimental conditions reflect experimental convenience and operating capabilities of our experimental apparatus.

Further hydrogen adsorption experiments were performed with and without cooling using compacted activated carbon bed. The activated carbon experiments were performed with only a 180 [s] hydrogen charging and liquid nitrogen cooling, when applicable, and can be seen in Figures 69 and 70.

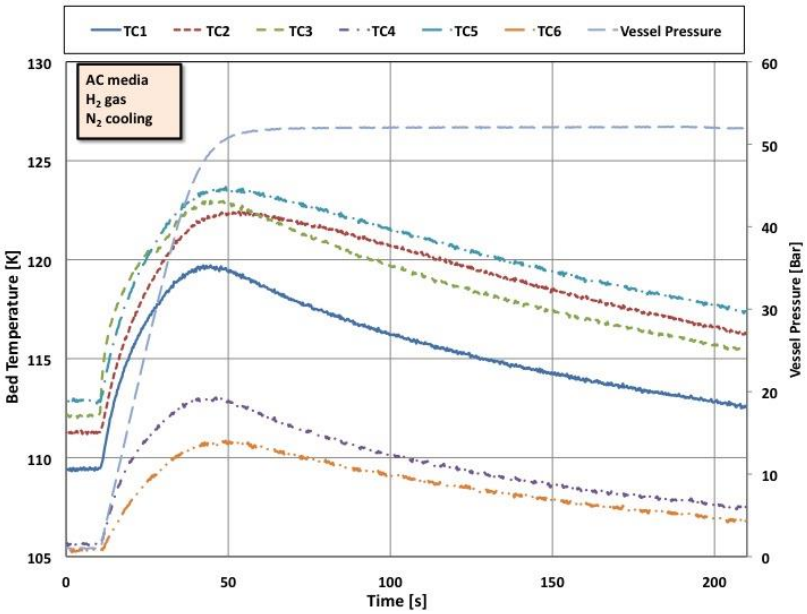

Figure 69: Temperature rise in activated carbon compact bed during H_2 gas charging at ~110 [K] with liquid nitrogen cooling.

Comparison of Figures 69 and 70 clearly shows a considerable increase in bed cooling with the addition of liquid nitrogen flow through the MATI. Each thermocouple locations returns within 5 [K] of its initial temperature at approximately 200 [s] after charging and cooling began. Figure 75 illustrate a minimal temperature change throughout the bed within the same time period (200 [s]) in the absence of cooling. Thermocouple locations and heights within the adsorption media are the same for both: the activated carbon bed and the MOF-5 bed. Additionally, a lower temperature rise during charging was observed at each thermocouple location with cooling.

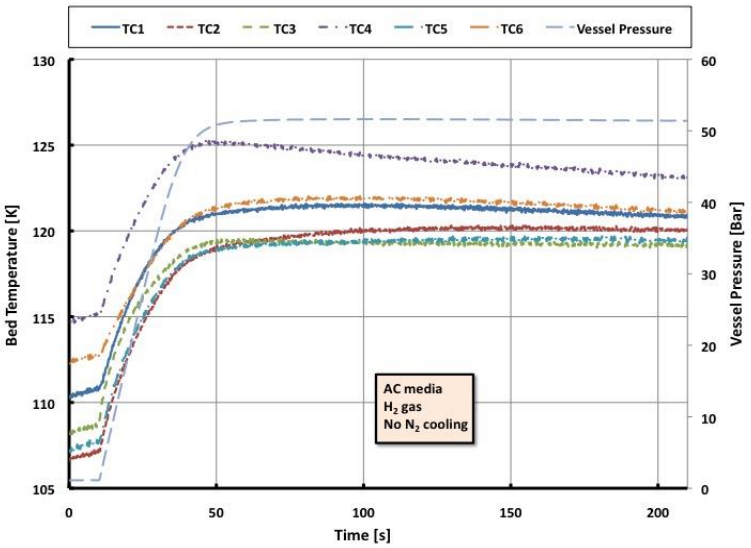

Figure 70: Temperature rise in activated carbon compact bed during H_2 gas charging entering at ~110 [K] without liquid nitrogen cooling.

The differences in temperature rise and cooling rates during the hydrogen adsorption experiments with and without cooling in both materials for the thermocouple highest in bed (TC-5, furthest from the MATI) and the lowest in the bed (TC-6, nearest to the MATI) can be seen in Figure 71. below.

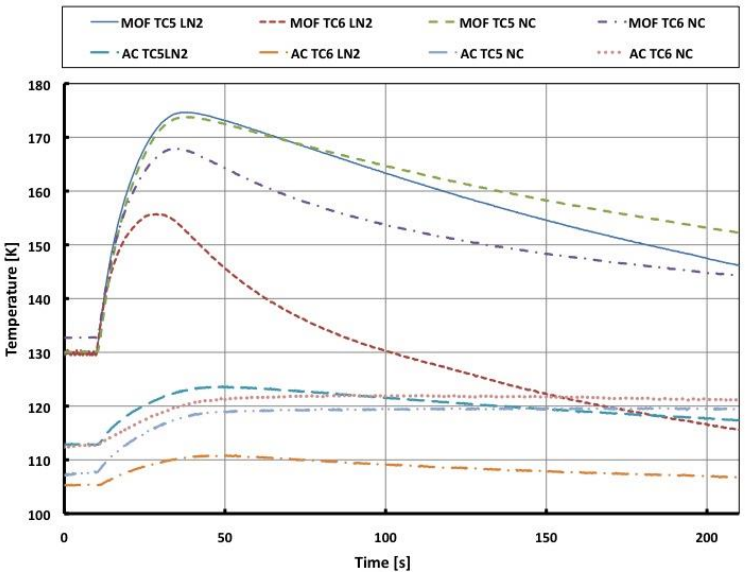

Figure 71: Comparisons of thermocouple readings (TC-5 and TC-6) with liquid nitrogen cooling (LN_2), and without (NC) cooling during hydrogen adsorption in both compacted MOF-5 and activated carbon beds.

These experiments show that liquid nitrogen cooling resulted in a 7.5% increase in total hydrogen inside of the vessel, 6.3% increase after hydrogen in major void area has been subtracted, compared to the trial without cooling.

Finally, adsorption experiments were performed in similar fashion on both MOF-5 and activated carbon with nitrogen as adsorbing gas. Figures 72 through 75 illustrate that a similar trend in temperature profile is observed in both beds with N2 and H2 as adsorbing gases, and with and without liquid nitrogen cooling. A lower temperature rise is observed throughout both beds with cooling and is followed by a lower final temperature at each thermocouple location compared to the observed profiles of each bed in the absence of cooling. Also, it does appear that greater temperature fluctuations are induced at each thermocouple location during nitrogen charging with cooling than charging without cooling for both bed materials (AC and MOF-5).

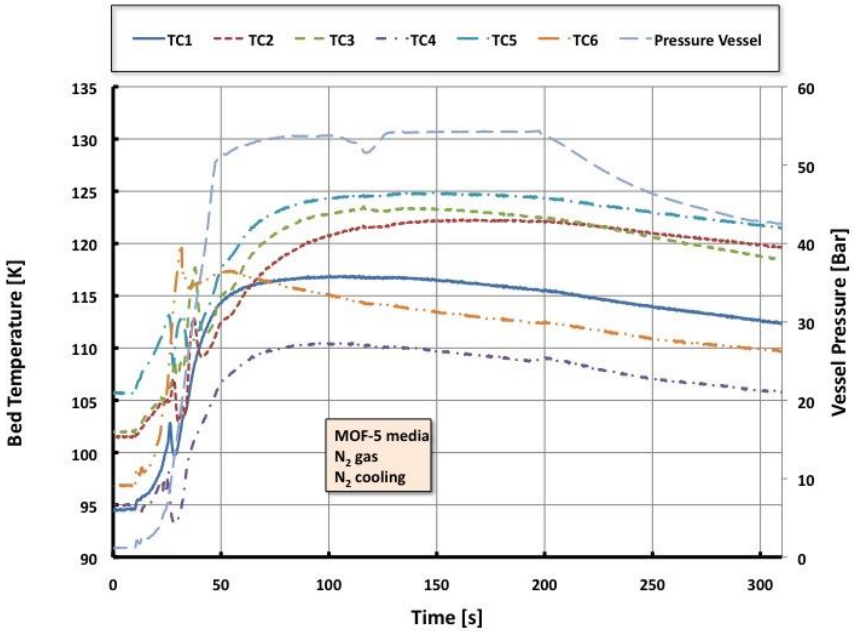

Figure 72: Temperature rise in MOF-5 compact bed during N_2 gas charging at ~100 K with liquid nitrogen cooling.

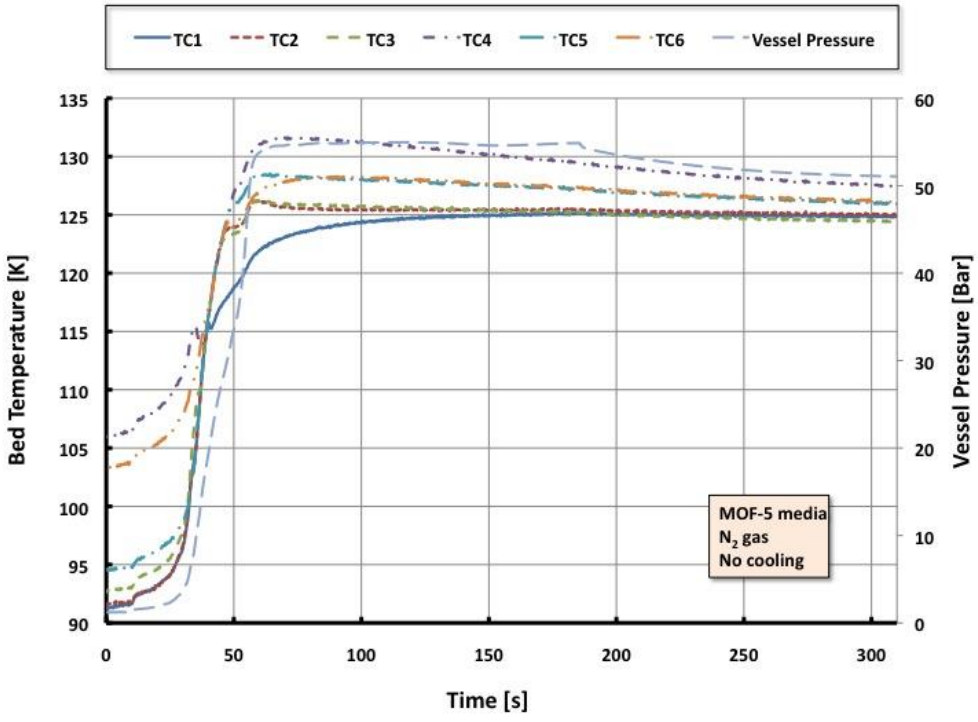

Figure 73: Temperature rise in MOF-5 compact bed during N_2 gas charging at ~100 K without liquid nitrogen cooling.

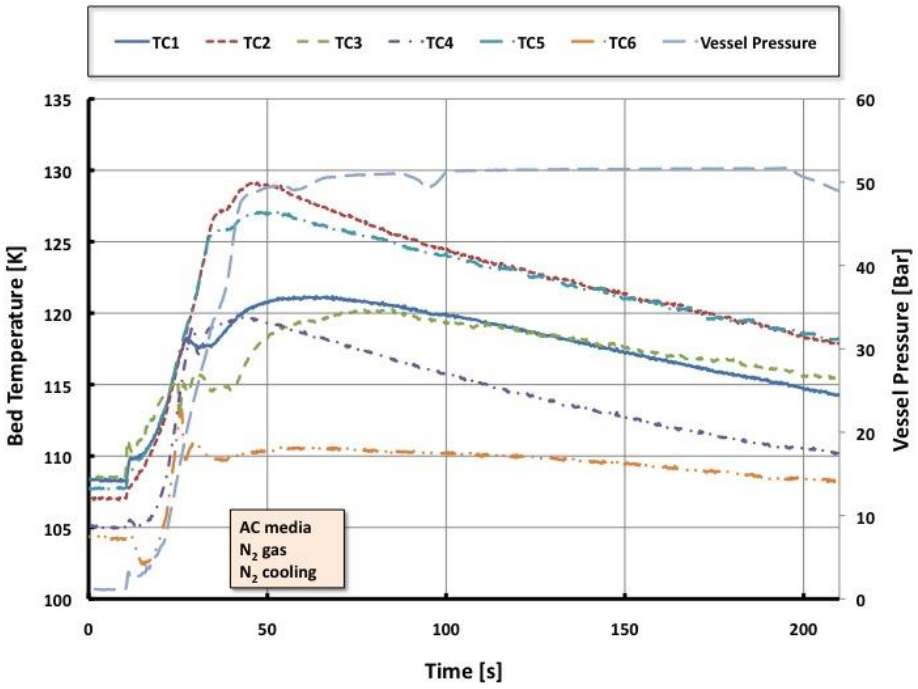

Figure 74: Temperature rise in activated carbon compact bed during N_2 gas charging at ~105 K with liquid nitrogen cooling.

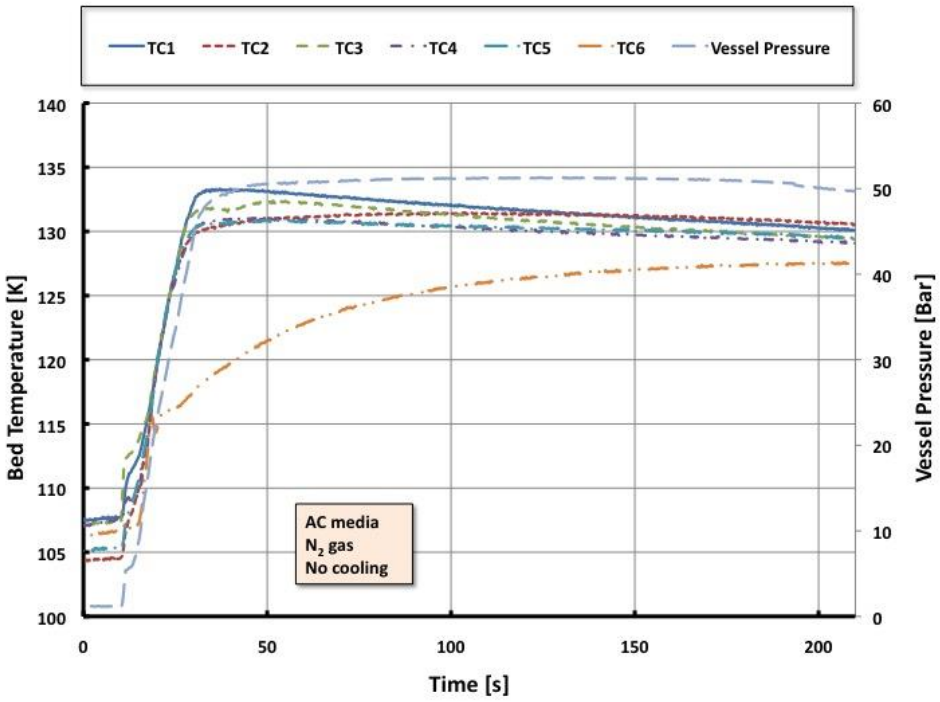

Figure 85: Temperature rise in activated carbon compact bed during N_2 gas charging at ~105 K without liquid nitrogen cooling

Key Findings: *Key findings from Task 2.4 include: 1) The pressure drop and heat transfer results from the separate effects testing confirm our design and modeling of the individual cooling plates, 2) The thermal performance and pressure drop in the multi-cooling plate test article confirm our heat transfer and pressure drop calculations for this device. The mechanical testing provided limited confirmation of the mechanical design but longer duration testing is needed for a final conclusion can be drawn, 3) Integrated testing results demonstrated the impact of the thermocouple penetrations on heat and mass transfer in the device. Generally the integrated test results confirmed our expectations for the test article which was confirmed in Task 2.5 by comparison to simulation results.*

Task 2.5 Model Development and Validation: In addition to the integrated test simulation described in our Phase 1, we developed a second simulation which could be used for design studies on the commercial scale MATI. This model also modeled heat transfer, mass transfer and the adsorption reaction in one puck along with modeling the cooling plate and hydrogen distribution. This model was primarily used to model the impact of conduction enhancement but was also used to model hydrogen discharge. The results of the experimental validation of the integrated test simulation and the development of the commercial scale design model are discussed below.

Subtask 2.5.1 Validation of Integrated Test Simulation: As reported in the Phase 1 part of this report, a three-dimension (3-D) model was created in COMSOL *Multiphysics 4.2a* to simulate the hydrogen adsorption process on a 5-cm diameter, 3.3-cm tall packed bed of MOF-5, bulk density 0.34 [g/cc], at cryogenic conditions with the addition of a sing MATI device.

The simulated temperature profile produced by COMSOL is compared to the experimental data at each of the six embedded thermocouple locations given above.

The void region between the gas entrance and the single MATI device in Figure 76 was divided into three regions to allow for closer inspection of the transport phenomena taking place near the gas entrance, expansion of entering feed gas, and near the MATI device, liquid nitrogen heat removal, and their effects on the freely flowing gas.

External elements of the experimental pressure-vessel, insulation layers and external cooling with LN_2, are reduced to the *averaged temperature boundary condition* which is estimated from a few temperature readings from thermocouples embedded in the pressure-vessel shell. The insulation layers, and external cooling with LN_2 were also accurately modeled with convective/conductive energy balance equation; but these portions of the simulation model were replaced with a flux boundary condition. This allowed us to reduce computational time requirement.

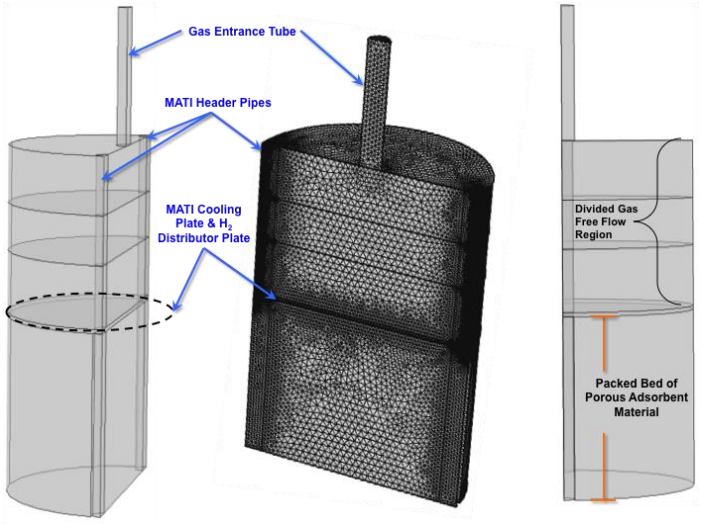

Figure 76: Simulated adsorption environment and applied meshing.

The overall objectives of this effort, was to validate the mathematical model and numerical simulations of the adsorption bed (representing the exact architecture of the adsorption bed and distribution of instruments throughout the experimental apparatus) with experimental data. One important element in this effort is to model and simulate all secondary and tertiary effects that may emerge from a realistic design and construction of the adsorption bed with imbedded MATI. For example: the influence of instruments, and instrumentation surfaces needed to be modeled independently and flexibly. It was inappropriate to perform model and simulation validation by *lumping* these effects into overall performance of the bed

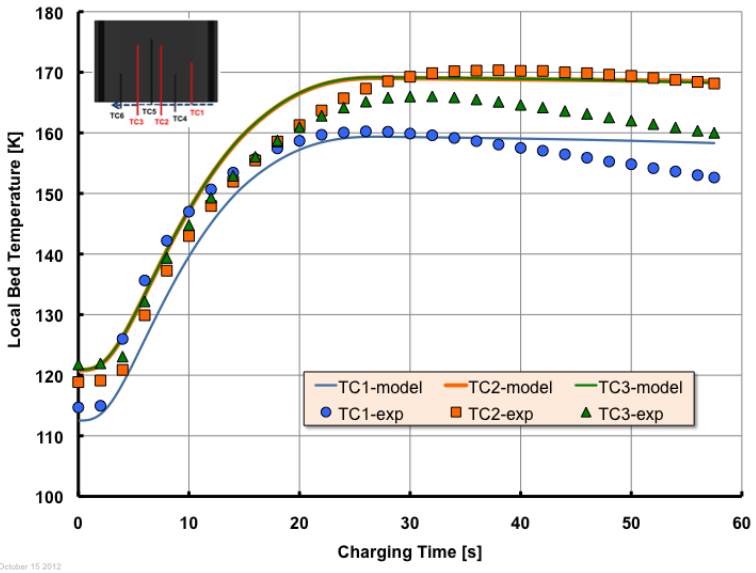

Figure 77 Comparison of simulated and experimental temperature responses for TC1, TC2 and TC3 in the initial simulation.

The initial numerical simulations closely matched the experimentally observed temperature profiles throughout the bed for the first 30 seconds of simulated time, however, the simulation proceeded to diverge from the experimental data after this time, (Figure 77 and Figure 78), indicating an increase in the experimentally observed cooling rate that was not captured by the simulation. An increase in thermal conductivity of the thermocouples compared to the adsorbent bed and the presence of preferential gas flow along the thermocouples resulted in the divergence of simulated data compared to experimental results. These effects were related to technical implementation of thermocouples insertion and may vary from location to location in the bed.

To account for differences in porosity and thermal conductivity in the adsorbent bed region, resulting from the insertion of thermocouples, in the simulation geometry, local property variations are embedded in the adsorbent bed domain to increase the conductive and convective heat transfer at thermocouple locations, Figure #84. The embedded variations allow COMSOL to interpolate porosity or increased effective conductivity as a function of location within the bed

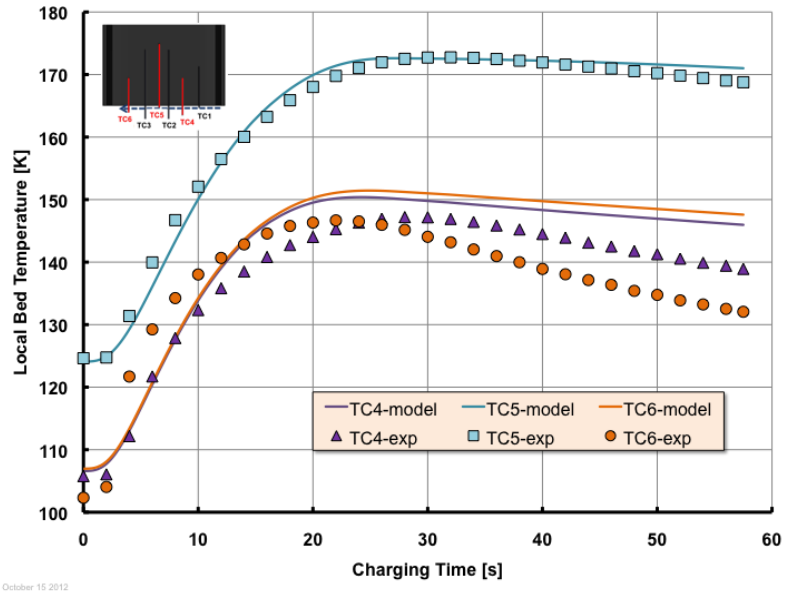

Figure 78: Comparison of simulated and experimental temperature responses for TC4, TC5 and TC6 in the initial simulation.

The simplified simulation geometry was employed to reduce the computational time required during the fine-tuning of the simulation tool. Temperature flux boundary conditions were utilized to transfer heat to and from the adsorbent bed and segregated free flow regions. The simulation and experimental results demonstrate an improved performance for the liquid nitrogen cooled system (Figure 80).

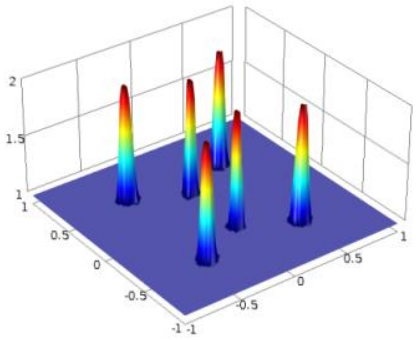

Figure 79**:** Example of embedded property as a function of geometric location inside of adsorbent bed domain.

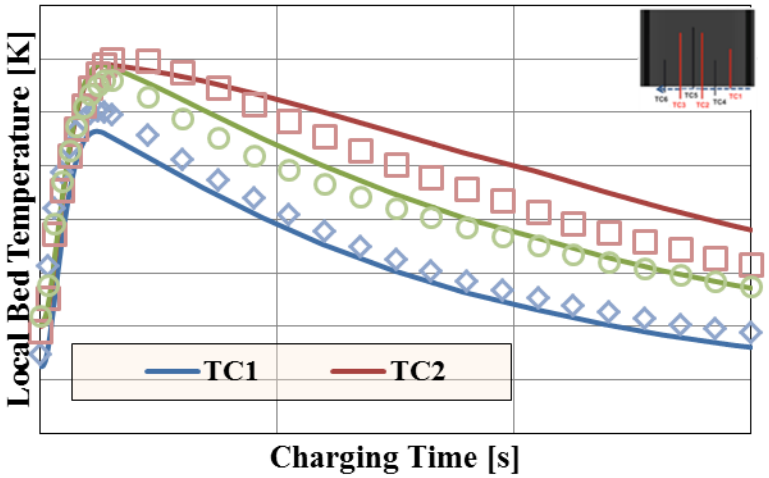

Figure 80: Comparison of simulated and experimental temperature responses for TC1, TC2 and TC3 with liquid nitrogen flow through a single MATI device (Solid lines are model data and symbols of the same color are experimental data).

As seen in Figure 81 the simulation demonstrated the general trend associated with the experimental cooling rate at all locations with the exception of TC2. While the experimentally observed cooling was similar at both TC2 and TC5, the simulation predicted a more linear cooling at TC2. Still, the predicted temperature at 300 seconds was within 5% of the observed temperature.

The greatest discrepancy between the experimental and predicted temperature response was observed at TC4. Although the temperature response shares the same general trend, the maximum and final temperatures were lower in the simulation compared to the experimental results. TC4 was inserted to a lower depth than TC6 and was positioned closest to the liquid nitrogen inlet of the single MATI device, which resulted in a lower observed temperature compared to TC6, therefore, the difference between the simulation and experimental results appeared to result from an experimental anomaly.

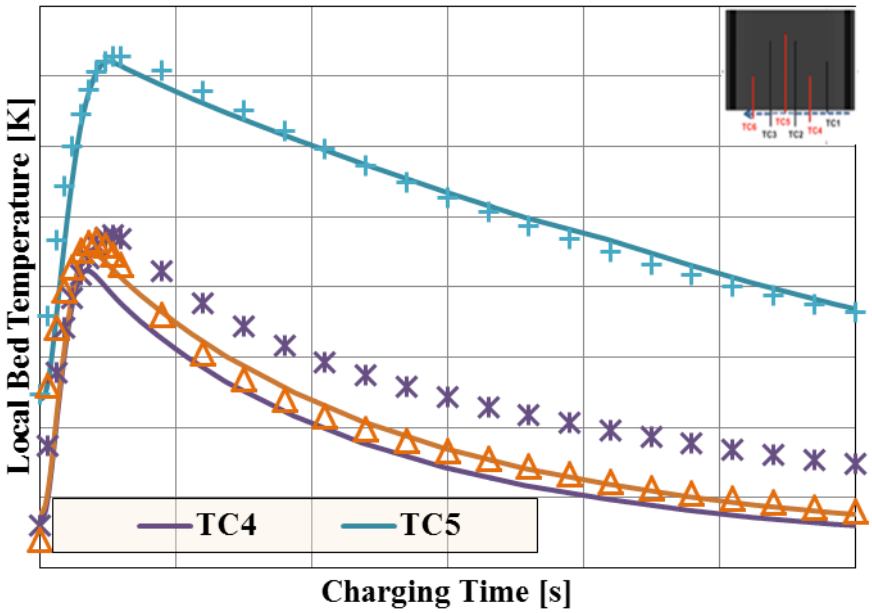

Figure 81: Comparison of simulated and experimental temperature responses for TC4, TC5 and TC6 with liquid nitrogen flow through a single MATI device. (Solid lines are model data and symbols of the same color are experimental data)

An experimental trial conducted in the absence of liquid nitrogen flow was simulated with the numerical model developed in COMSOL (Figure 82 and Figure 83). The simulated temperature response of the adsorbent system conformed to the experimental data with high precision at all thermocouple locations.

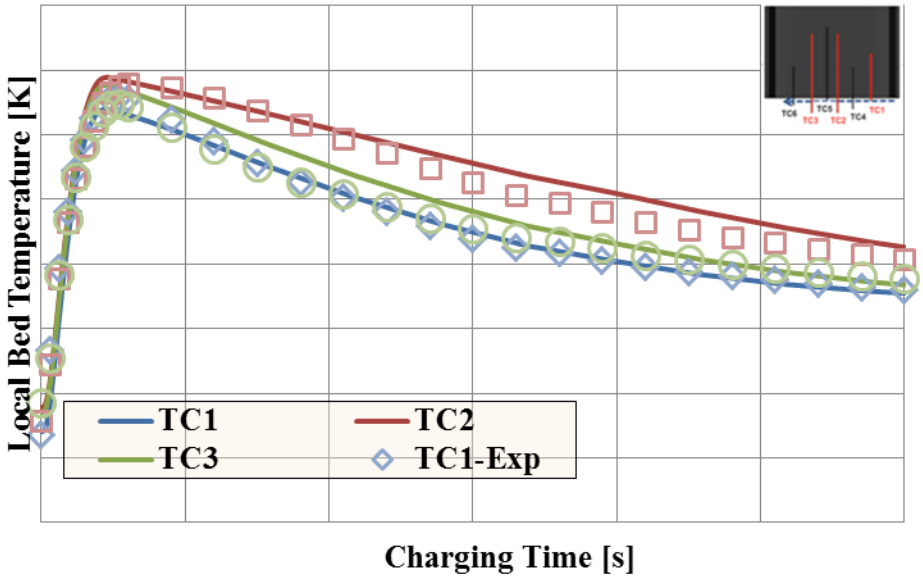

Figure 82: Comparison of simulated and experimental temperature responses for TC1, TC2 and TC3 without liquid nitrogen flow through a single MATI device (Solid lines are model data and symbols of the same color are experimental data)

The main discrepancies between the experimental and simulated data appeared with TC1 and TC3, which demonstrated similar response during charging despite the difference in insertion depth between the two probes.

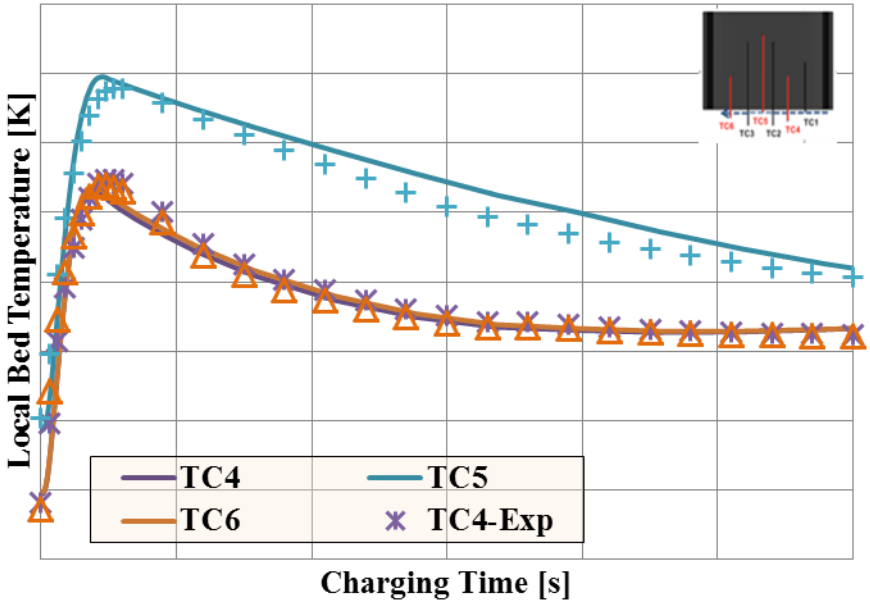

Figure 83: Comparison of simulated and experimental temperature responses for TC4, TC5 and TC6 without liquid nitrogen flow through a single MATI device. (Solid lines are model data and symbols of the same color are experimental data)

Subtask 2.5.2 Commercial Design Model: The overall goal of this activity was to provide a 3-D numerical simulation program that could be effective in implementing formal optimization procedures in search of improved bed performance based on innovative MATI approach and full scale size bed simulation. First the model is described and then we present the results for two design studies. The first is focused on the evaluation of the effectiveness of using aluminum pins to enhance conduction in the densified MOF-5 pucks and the second investigates adsorption bed discharge.

Simulation Mathematical Model: The mathematical model is given below.

Hydrogen Distribution Plate*: Mass balance* – continuity equation since the diffusion effects are considered negligible in the distribution plate:

$$\frac{\partial \rho_{H_2}}{\partial t} + \nabla \cdot \left(\rho_{H_2} \mathbf{u}_{H_2} \right) = 0 \quad \left[\frac{\mathrm{kg}_{H_2}}{\mathrm{m}^3_{H_2}\,\mathrm{s}} \right]$$

Momentum balance – transient, laminar, compressible flow with continuity of fluxes on the plate-porous bed interface and neglected inertial terms (Stokes flow) as well as gravity effects:

$$\rho_{H_2}\frac{\partial \mathbf{u}_{H_2}}{\partial t}=\nabla\cdot\left[-p_{H_2}\mathbf{I}+\mu_{H_2}\left(\nabla\mathbf{u}_{H_2}+\left(\nabla\mathbf{u}_{H_2}\right)^{T}\right)-\frac{2}{3}\mu_{H_2}\left(\nabla\cdot\mathbf{u}_{H_2}\right)\mathbf{I}\right]\quad\left[\frac{\mathrm{kg}_{\mathrm{H}_2}}{\mathrm{m}^3_{\mathrm{H}_2}}\frac{\mathrm{m}}{\mathrm{s}^2}\right]$$

Inlet of hydrogen was modeled as a pressure ramp that lifted the pressure from initial 1 $[bar]$ to final 50 or 60 $[bar]$ during the entire filling time, i.e. 3 minutes.

Energy balance – transient, convection dominated with continuity of fluxes on the bed/plate interface and the inlet temperature boundary at (40 K):

$$\rho_{H_2}C_{p,H_2}\frac{\partial T_{H_2}}{\partial t}+\rho_{H_2}C_{p,H_2}\mathbf{u}_{H_2}\cdot\nabla T_{H_2}=\nabla\cdot\left(k_{H_2}\nabla T_{H_2}\right)\quad\left[\frac{\mathrm{J}}{\mathrm{m}^3_{\mathrm{H}_2}\mathrm{s}}\right]$$

In all three balances above the bottom of the plate was modeled with symmetry boundary condition.

Porous Adsorption Bed: *Mass balance* – continuity equation:

$$\varepsilon\frac{\partial \rho_{H_2}}{\partial t}+\nabla\cdot\left(\rho_{H_2}\mathbf{u}_s\right)=\gamma_m\quad\left[\frac{\mathrm{kg}_{\mathrm{H}_2}}{\mathrm{m}^3_{\mathrm{bed}}\mathrm{s}}\right]$$

Momentum balance – transient, laminar, compressible flow through porous media with continuity of fluxes on the plate-porous bed interface and neglected inertial terms (Stokes-Brinkman equations) as well as gravity effects:

$$\frac{\rho_{H_2}}{\varepsilon}\frac{\partial \mathbf{u}_\mathbf{s}}{\partial t}=\nabla\cdot\left[-p_{H_2}\mathbf{I}+\frac{\mu_{H_2}}{\varepsilon}\left(\nabla\mathbf{u}_\mathbf{s}+\left(\nabla\mathbf{u}_\mathbf{s}\right)^{T}\right)-\frac{2}{3}\frac{\mu_{H_2}}{\varepsilon}\left(\nabla\cdot\mathbf{u}_\mathbf{s}\right)\mathbf{I}\right]-\left(\frac{\mu_{H_2}}{\kappa}+\frac{\gamma_m}{\varepsilon}\right)\mathbf{u}_\mathbf{s}\quad\left[\frac{\mathrm{kg}_{\mathrm{H}_2}}{\mathrm{m}^3_{\mathrm{H}_2}}\frac{\mathrm{m}}{\mathrm{s}^2}\right]$$

Here, $\mathbf{u}_\mathbf{s}=\varepsilon\mathbf{u}_{H_2}$ is the superficial velocity with $\varepsilon=V_{void}/V_{bed}=V_{H_2}/V_{bed}$ being the porous bed void fraction. The mass sink/source term is the adsorption/desorption rate modeled through Dubinin-Astakhov adsorption kinetics:

$$\gamma_m=-\rho_{bed}\left(\frac{\partial n_a}{\partial t}\right)\qquad\left[\frac{\mathrm{kg}_{\mathrm{H}_2}}{\mathrm{m}^3_{\mathrm{bed}}\mathrm{s}}\right]$$

$$n_a=n_{\max}\exp\left(-\left(\frac{A}{E}\right)^2\right)\left[\frac{\mathrm{kg}_{\mathrm{H}_2}}{\mathrm{kg}_{\mathrm{MOF\text{-}5}}}\right],\ A=RT\ln\left(\frac{p_0}{p}\right)\left[\frac{\mathrm{J}}{\mathrm{mol}_{\mathrm{H}_2}}\right],\ E=\alpha+\beta T\ \left[\frac{\mathrm{J}}{\mathrm{mol}_{\mathrm{H}_2}}\right]$$

As one can see the momentum equations in COMSOL are inconsistent with the outcome of rigorous derivation. Also, in order to keep the mass balance correct, one has to accept an error in source/sink term units in the momentum balance. These inconsistencies have been shown to be unimportant since the terms they influence mostly play a negligible role except near the boundaries. Therefore, we expected them not to affect our results in any significant manner. Edges of the bed and metal plate boundary were modeled as walls with zero velocity condition.

Energy balance – transient with continuity of fluxes on distribution plate/porous bed and aluminum plate/porous bed interfaces. We have assumed thermal equilibrium conditions:

$$\left(\varepsilon\rho_{H_2}C_{p,H_2}+(1-\varepsilon)\rho_{MOF-5}C_{p,MOF-5}\right)\frac{\partial T}{\partial t}+\rho_{H_2}C_{p,H_2}\mathbf{u}_s\cdot\nabla T=\nabla\cdot\left(k_{eff}\nabla T\right)+Q_m+W_p \quad \left[\frac{\mathrm{J}}{\mathrm{m}^3_{\mathrm{bed}}\mathrm{s}}\right]$$

Here Q_m represents heat generated/consumed due to adsorption/desorption and W_p is the pressure work:

$$Q_{ads}=\frac{\rho_{bed}\left(\frac{\partial n_a}{\partial t}\right)}{M_{H_2}\times 10^{-3}}\times\Delta_{ads}H \quad \left[\frac{\mathrm{J}}{\mathrm{m}^3_{\mathrm{bed}}\mathrm{s}}\right],\ W_p=-\varepsilon\frac{T}{\rho_{H_2}}\left(\frac{\partial\rho_{H_2}}{\partial T}\right)_p\left(\frac{\partial p}{\partial t}\right) \quad \left[\frac{\mathrm{J}}{\mathrm{m}^3_{\mathrm{bed}}\mathrm{s}}\right]$$

In this model, it was assumed that the heat of adsorption, has a constant value of $\Delta_{ads}H = 4.0\ [\mathrm{J/mol}]$. This is a conservative estimate since the heat of adsorption should vary as a function of mass of hydrogen adsorbed. We are planning to incorporate this dependence into our future model.
Effective thermal conductivity of the bed was set to its maximum theoretical value,

$$k_{bed}=\varepsilon k_{H_2}+(1-\varepsilon)k_{MOF-5}$$

which will also be a subject to further change.
Bed edges were modeled as insulated.

Aluminum Plate and Fins: Both plate and fins were impermeable to hydrogen and liquid nitrogen.

Energy balance – conduction with continuity of fluxes on metal/bed and metal/cooling plate interfaces and insulation on the system edges

$$\rho_{Al}C_{p,Al}\frac{\partial T_{Al}}{\partial t}=\nabla\cdot\left(k_{Al}\nabla T_{Al}\right) \quad \left[\frac{\mathrm{J}}{\mathrm{m}^3_{\mathrm{Al}}\mathrm{s}}\right]$$

Liquid Nitrogen Cooling Plate: *Mass balance* – continuity equation:

$$\frac{\partial\rho_{N_2}}{\partial t}+\nabla\cdot\left(\rho_{N_2}\mathbf{u}_{N_2}\right)=0 \quad \left[\frac{\mathrm{kg}_{\mathrm{N}_2}}{\mathrm{m}^3_{\mathrm{N}_2}\mathrm{s}}\right]$$

Momentum balance – transient, laminar, compressible flow with neglected inertial terms (Stokes flow) as well as gravity effects:

$$\rho_{N_2}\frac{\partial\mathbf{u}_{N_2}}{\partial t}=\nabla\cdot\left[-p_{N_2}\mathbf{I}+\mu_{N_2}\left(\nabla\mathbf{u}_{N_2}+\left(\nabla\mathbf{u}_{N_2}\right)^T\right)-\frac{2}{3}\mu_{N_2}\left(\nabla\cdot\mathbf{u}_{N_2}\right)\mathbf{I}\right] \quad \left[\frac{\mathrm{kg}_{\mathrm{H}_2}}{\mathrm{m}^3_{\mathrm{H}_2}}\frac{\mathrm{m}}{\mathrm{s}^2}\right]$$

Boundary conditions were inlet flow rate, pressure outlet, zero velocity at the metal plate wall and symmetry in the middle, i.e. on the top boundary.

Energy balance – transient, convection dominated with continuity of fluxes on the bed/plate interface, temperature boundary at the inlet (80 K) and insulation/symmetry boundary elsewhere:

$$\rho_{N_2}C_{p,N_2}\frac{\partial T_{N_2}}{\partial t}+\rho_{N_2}C_{p,N_2}\mathbf{u}_{N_2}\cdot\nabla T_{N_2}=\nabla\cdot\left(k_{N_2}\nabla T_{N_2}\right) \quad \left[\frac{\mathrm{J}}{\mathrm{m}^3_{\mathrm{N}_2}\mathrm{s}}\right]$$

Material Properties Used in Commercial Design Model: The material properties used with the commercial design model are summarized below.

Hydrogen: *Hydrogen properties* were fitted based on NIST database, http://webbook.nist.gov/chemistry/fluid/
Hydrogen density – ideal gas until pressure of 50 [bar] and 2D fit as a function of pressure and temperature above 50 [bar];
Heat capacity – 2D fit as a function of pressure and temperature;
Viscosity – 2D fit as a function of pressure and temperature;
Heat conductivity – 2D fit as a function of pressure and temperature;

MOF-5: *Heat capacity* – temperature dependence of the form,

$$\log_{10} C_{p;MOF-5} = \sum_{n=0}^{8} c_n (\log_{10} T)^n$$

Kumar, V., S., Raghunathan, K., Kumar, S., "Lumped parameter model for cryo-adsorber hydrogen storage tank", International Journal of Hydrogen Energy, 34 (2009) 5466-5475

Bed Characteristics

Void fraction $\varepsilon = 0.246 \left[m^3_{H_2} / m^3_{bed} \right]$ Permeability $\kappa = 2.04 \text{x} 10^{-12} \left[m^2 \right]$

Particle diameter $D_p = 108 \left[\mu m \right]$ Bed density $\rho_{bed} = 300 \left[kg_{MOF-5} / m^3_{bed} \right]$

Permeability was calculated as inverse of Ergun permeability (SRNL - H_2 adsorption model)

$$\frac{1}{\kappa} = 150 \frac{(1-\varepsilon)^2}{D_p^2 \varepsilon^3} + 1.75 \frac{\rho}{\mu D_p} \frac{(1-\varepsilon)}{\varepsilon^3} \left| \mathbf{u}_s \right|$$

Second term (representing turbulent contribution) in the above equation could be safely neglected in the simulation, as it is several orders of magnitude smaller than the first term, which represents laminar contribution.

Liquid nitrogen: Density, viscosity, thermal conductivity and heat capacity as a 1D fit with temperature at constant pressure of $50 \left[bar \right]$. Data was collected from NIST database,
http://webbook.nist.gov/chemistry/fluid/; Flow rate: $1.0 \text{x} 10^{-4} \left[\text{m}^3 / \text{s} \right]$;

Aluminum: Density: $2700 \left[kg / m^3 \right]$; Heat capacity: $900 \left[J / kgK \right]$;
Number of aluminum fins used: 12, 24, 48. *Fin length - L=12.5[mm]; Fin thickness* t_h*=125 [μm]*

Evaluation of Conduction Enhancement Using Aluminum Pins: For comparison purposes, we have used a two-dimensional approximation of the real system and modeled one half of a MATI unit cell (See Figure 84). Supercritical hydrogen entered the bed from the side at an inlet temperature 40 K and then penetrates the porous bed through the entire bed length up to a final pressure of 50-60$[bar]$ in 3 minutes (180 s). This was an attempt to model the actual microscale distribution plate. Heat generated by adsorption and to the minor extent, compression, was continuously removed with liquid nitrogen flowing through a microchannel cooling plate at an inlet temperature of 80K.

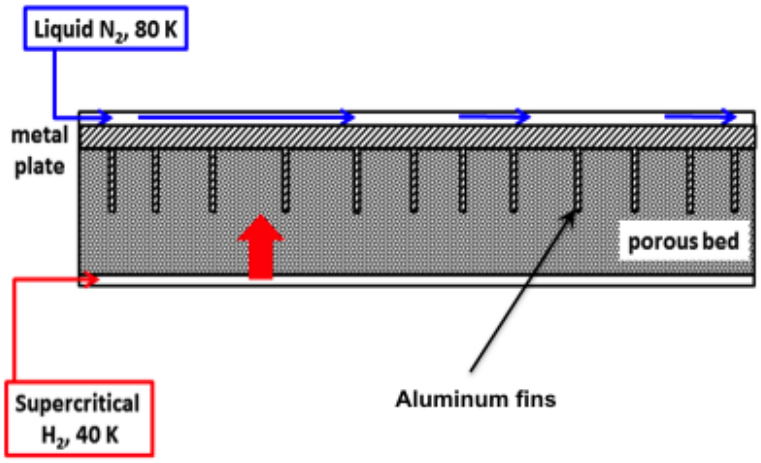

Figure 84: Schematic representation of a 2D model.

The liquid nitrogen flow rate assumed to be was 1x10^{-4}$\left[m^3/s\right]$ which corresponds to maximum velocity of around 2$[m/s]$. An aluminum plate was separating the cooling plate from the adsorption bed. Aluminum plate was considered impermeable to hydrogen. Aluminum as thermal conductivity enhancement was introduced in form of numerous fins connected to the metal plate at the top. Adsorption bed materials included pure MOF-5 (0 wt.%ENG), MOF-5 with 5 wt.% ENG and MOF-5 with 10 wt.% ENG. Initial temperatures were 40 K in the distribution plate, 160 K in the adsorption bed and 80 K in the metal plate, fins and cooling plate. Bed was 30$[cm]$ long and 2.5$[cm]$ high. Distribution and cooling plates were 125$[\mu m]$ thick since only half of them were modeled for symmetry purposes. Aluminum plate thickness was 250$[\mu m]$. Fins were about half of the modeled bed height long, around 1.25$[cm]$. Thickness of the fins was either 125$[\mu m]$ or 250$[\mu m]$ and their number varied from 12 to 48.

2D Numerical Simulation Results with 12 Aluminum Fins: This section presents the results for a bed containing 12 fins. Results include the average bed temperature and total mass of hydrogen adsorbed (Figure 85) and bed temperature profiles as a function

bed composition (1)no enhancement, 2) 5% ENG, 3) fins, 4) 10% ENG, 5) fins with 5% ENG and 6)fins with 10% ENG (Figure 91). We also presented the results for a bed with a conductivity of 3W/mK which based on earlier simulations had been selected as our target bed conductivitiy.

Total mass of hydrogen in the system was calculated as:

$$n_{H_2,vol} = n_a \rho_{bed} + \varepsilon \rho_{H_2} \qquad \left[\frac{\mathrm{kg}_{\mathrm{H}_2}}{\mathrm{m}^3_{bed}} \right]$$

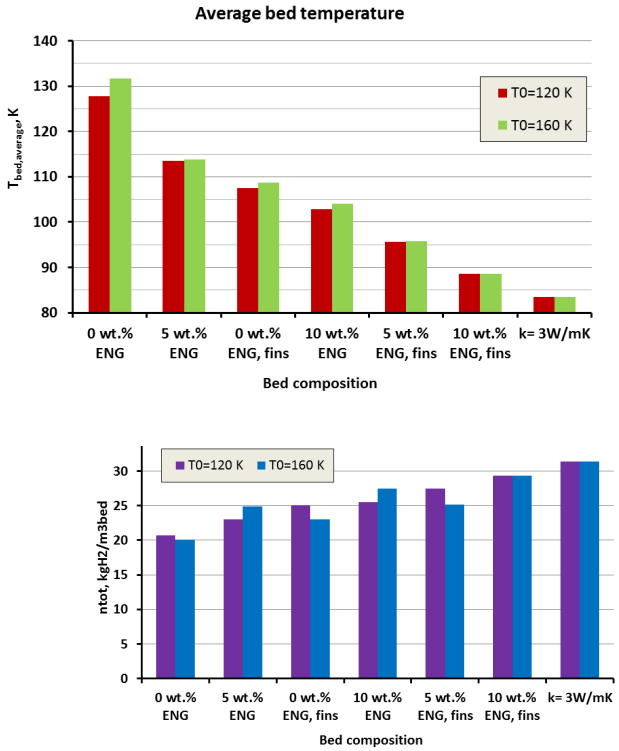

Figure 85: 12 Pin Average bed temperatures and total mass of hydrogen in the adsorption system:

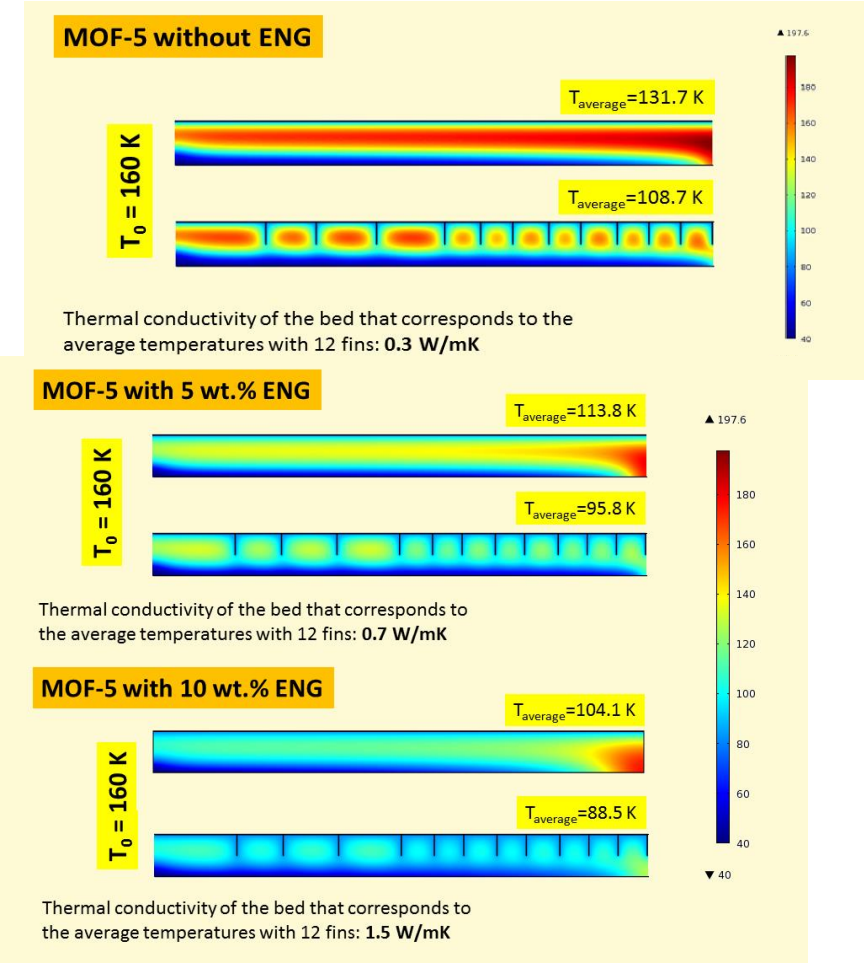

Figure 86: 12 Pin Bed Temperature Profiles:

2D Numerical Simulation Results with 24 Aluminum Fins: This section presents the results for a bed containing 24 fins. Results include the average bed temperature and total mass of hydrogen adsorbed after a three minute charge cycle. (Figure 87) and bed temperature profiles as a function bed composition 1) fins, 2) fins with 5% ENG and 3) fins with 10% ENG (Figure 88).

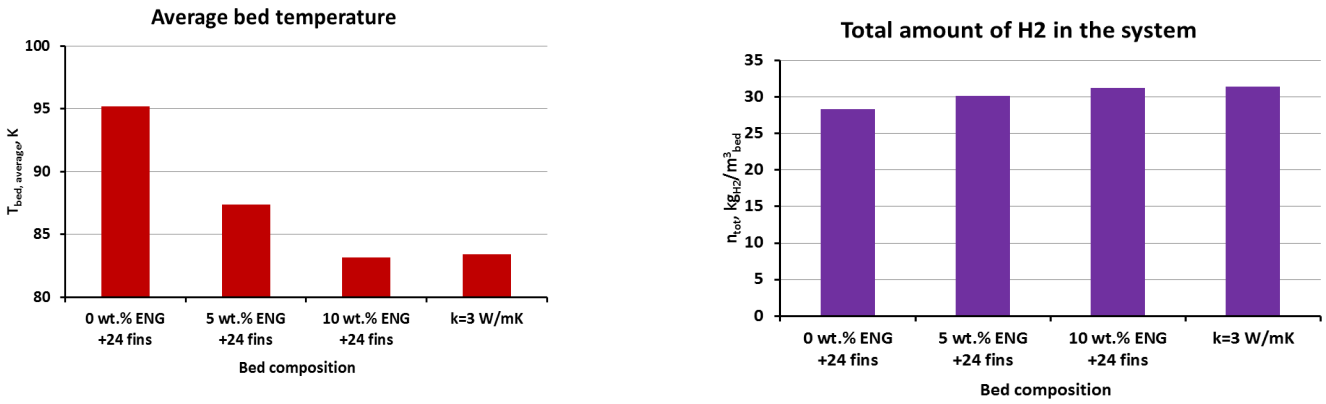

Figure 87: 24 Pin Average bed temperatures and total mass of hydrogen in the adsorption system after a three minute charge cycle:

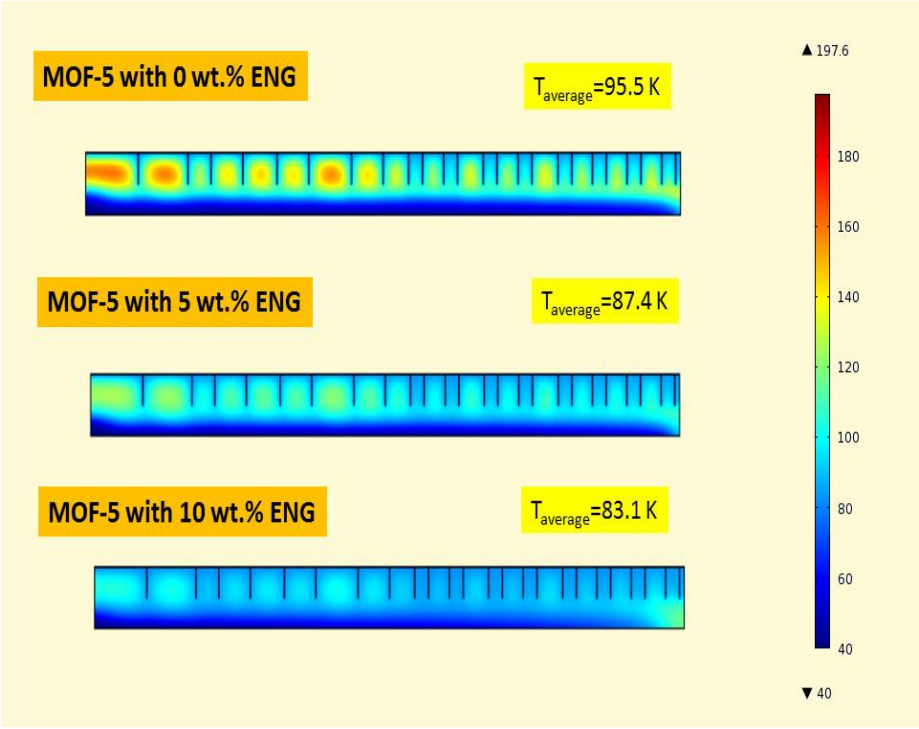

Figure 88: 24 Pin Bed Temperature Profiles

2D Numerical Simulation Results with 48 Aluminum Fins: This section presents the results for a bed containing 48 fins. Results include the bed temperature profiles (Figure 89). Only the case of pure MOF-5 with fins was modelled.

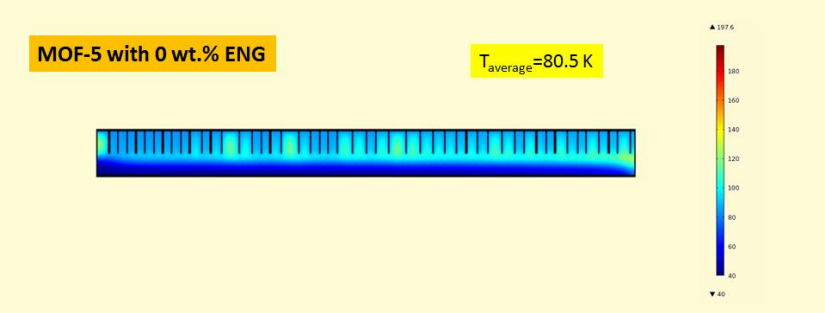

Figure 89: 48 Pin Bed Temperature Profiles

In this parametric study we have demonstrated that addition of highly conductive component into the bed structure, like aluminum fins, we were able to reach the target adsorption performance even with MOF-5 as bed material.

Discharge Studies: One advantage of the MATI is that we can use discharge heat from the fuel cell, augmented by limited combustion of hydrogen to discharge hydrogen storage avoiding the need for an electric heater. The concept involves taking the hydrogen desorbed by adsorption storage system, heating it with fuel cell thermal energy to 40^{o}C and then using the hydrogen combustor described above to heat the hydrogen to 120^{o}C. The hot hydrogen passes through the MATI in the header and heat transfer plates where the heat in in hot hydrogen is used to desorb the bed. The hydrogen then goes to the fuel cell where it is used to generation motive power for the automobile. The investigations described below model this process in a single MOF-5 puck to insure that the thermal performance of the MATI system can supply the required hydrogen.

We have investigated the behavior of a 1.5 [cm] high bed anticipating the possibility that a bed with this height may not need conduction enhancement elements. Our current results are preliminary and include several sets of fin numbers and bed without fins. All numerical simulations extend to only one hour of discharging process.

Hydrogen discharge operation was facilitated with a supply of hot hydrogen up to 120 [^{o}C] (obtained in the hydrogen combustor) flowing through the heat exchanger while maintaining overall pressure in the tank at 60 [bar]. At the end of the discharge operation the pressure in the hydrogen storage tank was slowly reduced to 5 [bar], while maintaining all the time the same hydrogen mass flow rate at the exit of the bed. Hydrogen in the heat exchanger flows at a constant mass flow rate of 0.0031 [g/s] in all cases presented below. This flow rate was the one calculated for half of the unit cell (1.5 cm high), which was providing a nominally needed hydrogen-discharge rate for the period of 4h for the entire tank. The constant flow rate was kept at bed outlet (distribution plate) by careful adjustment of the heat exchanger hydrogen inlet temperature and subsequent pressure decrease in the bed. Based on the hydrogen mass flow rate from the bed the temperature is slowly increased to 383.15 [K]. After that

pressure swing desorption starts and it is maintained until the bed pressure is lowered to 5 [bar] and the desired mass flow rate is no longer achievable. Cases presented here did not reach the final stage of discharge. Our initial goal was to demonstrate the impact of enhancement elements on the average bed temperature and compare hydrogen exit and inlet temperature in the heat exchanger. All simulations were done in two-dimensional rectangular coordinate system and for a bed of densified (0.5 [g/cm^3]) MOF-5.

Figure 90 illustrates how closely hydrogen exit temperature from the heat exchanger 'followed' the *average* bed temperature. It is reasonable to conclude that there was still substantial capacity for the heat transfer between hydrogen in the heat exchange and bed. Figures 91 and 92 provided insight of how inlet (red) and outlet (blue) hydrogen temperatures were changing in the heat exchanger for bed with 17 and 54 heat conductive fins respectively. It was obvious that the performance of the heat exchanger was dramatically improving with the addition of the heat conductive fins.

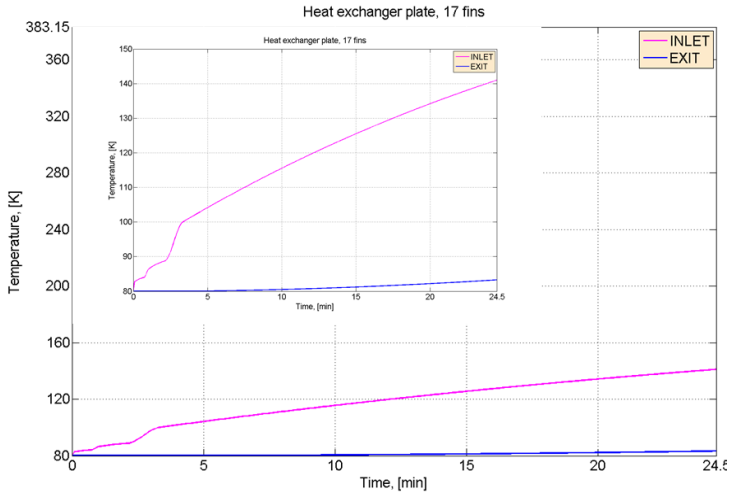

Figure 90: Hydrogen exit temperature from the heat exchanger (blue), and average bed temperature (red) in bed without heat conductive fins.

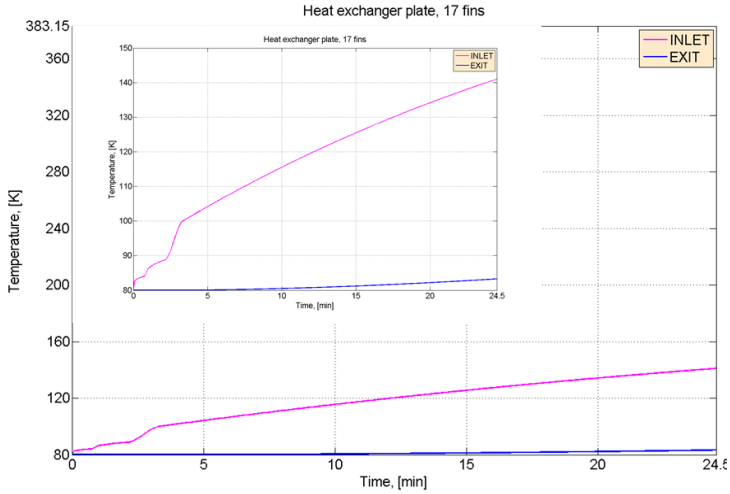

Figure 91: Hydrogen exit temperature (blue) from the heat exchanger, and average bed (red) temperature for bed with 17 heat conductive fins.

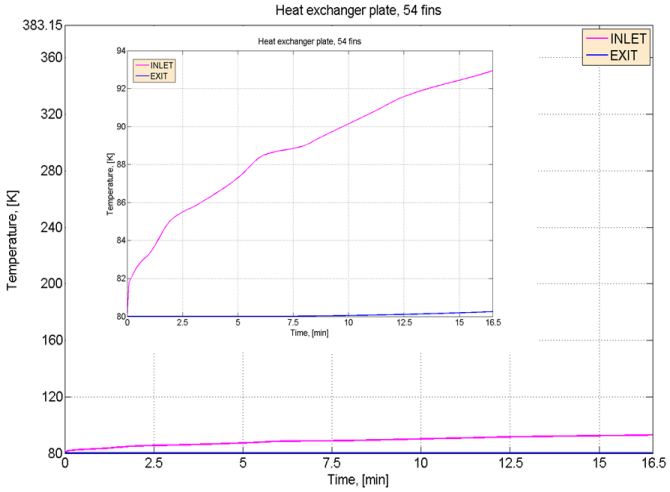

Figure 92: Inlet and outlet hydrogen temperature in the heat exchanger (with zoom) for bed with 54 heat conductive fins.

Key Findings: *Key findings from Task 2.5 include: 1) When compared with experimental results the integrated simulation did an excellent job predicting the results from the integrated testing, 2) Design simulation results suggested that conduction enhancement could significantly improve the charge and discharge performance of the MATI. Plate spacing could be increased to 5 cm if the pucks contained aluminum pins/fins separated approximately 1 cm apart.*

Task 2.6 Fabrication Investigations – This task consisted of number of studies focused on fabrication issues that helped establish the technical feasibility of large scale manufacturing of a MATI concept. The focus was on establishing the feasibility of using aluminum as a material of fabrication. The use of aluminum in a MATI required the demonstration of 1) the ability to bond aluminum lamina to form cooling plates (Welding Studies), 2) the ability to pattern aluminum lamina to form cooling (Stamping studies),

and 3) the ability to attach the cooling plates to the headers (brazing studies). Each of the studies is summarized below.

Laser welding studies – This task was focused on the laser welding of 6061 aluminum alloy. A literature review of laser welding identified several major issues associated with the laser welding of aluminum including oxidation, gas porosity, heat affected zones, susceptibility to cracking and undercutting or humping among others. Oxidation can be managed by using shielding gas (such as argon) during welding and use of proper cleaning methods prior to welding. Cracking can be controlled by controlling the speed of welding. Literature reported that the cracking susceptibility is increased up to a certain velocity limit and then drops to zero beyond that limit. Simultaneously, porosity formation, undercutting or humping and heat affected zones can be controlled using proper welding parameters including power, welding speed and spot size.

Laser welding experiments were performed on 6061-O aluminum alloy to evaluate the weldability of the aluminum alloy. The objective of the welding study was to determine if two shims 0.5 mm in thickness could be lap welded using laser keyhole welding. The guideline for the lap weld joint was to have the weld nugget penetrate 1.5 times the thickness of the shims, suggesting a weld depth requirement of 750 µm. Based on preliminary results, four parameters were selected based on a weld depth requirement of 750 µm. The four parameters were tested for the joint strength using a lap shear test. The effect of using shielding gas and heat treatment on the bond strength was also evaluated.

The parameters selected for lap shear testing were 900 W and 350 mm/s, 800 W and 240 mm/s, 600 W and 85 mm/s and 500 W and 10mm/s. Each level was tested for all four combinations of using or not using shielding gas and heat treatment. Lap shear tests were performed on the samples with 3 replicates for a total of 16 samples per level. A mixed level, full factorial design was generated for the experiments and randomization was incorporated for performing the experiments. Table 10 shows the factors and levels in the experiments.

Table 10. Brazed joint design at the inlet of cooling plate

Factors	Level 1	Level 2	Level 3	Level 4
Joining Efficiency/ (Welding Parameters)	0.34 mm^2/J	0.30 mm^2/J	0.18 mm^2/J	0.03 mm^2/J
Power	900	800	600	500
Speed	350	240	85	10
Duty Cycle	90	80	60	50

The same weld depth can be attained in laser welding under different combinations of parameters. Furthermore, for the same energy input different weld depths can be achieved. Joining efficiency was used to define how much weld area (length by depth) can be attained per unit energy as follows:

$$Joining\ Efficiency\ \left(\frac{mm2}{J}\right) = \frac{Weld\ depth(mm) \cdot Welding\ speed\ (\frac{mm}{s})}{Average\ power\ (W.\frac{s}{mm})} \quad (1)$$

The higher the joining efficiency, the more energy goes into the weld meaning less energy goes into creating a heat affected zone. At or beyond a joining efficiency of 0.18, the joint ultimate shear strength remains reasonably constant. The drop off in joint strength below this joining efficiency was associated with failure in the heat affected zone of the weld. Thus, to obtain the highest joining efficiency and highest utilization of energy, the highest power and highest speed should be used that provides a continuous weld. This minimizes process cycle time for the welding operation. For comparison with the parent material, an approximation of the theoretical ultimate tensile strength was found by dividing by 0.65.In so doing, all three values for ultimate tensile strength of the joint at or above a joining efficiency of 0.18 were found to be above the accepted handbook value for the ultimate tensile strength for 6061-T6 of 310 MPa. This suggests excellent joint strength.

The strength of the welded joint increased through the use of shielding gas suggesting that the shielding gas method is effective at reducing gas porosity.

Heat treatment was carried out on the welded test articles. The material was solution heat treated at 530 ^{o}C for 40 mins and quenched in cold water followed by age hardening at 160 ^{o}C for 16 hrs. Heat treatment results in a significant increase in the ultimate shear strength and yield shear strength of the welded joint.

Based on the preliminary experiments described above an additional set of experiments was performed to determine good parameters for lap welding of 6061-O aluminum. Table 11 shows the parameters used for these experiments.

Table 11. Welding parameters investigated**.**

Sample no.	Power [Watt]	Speed [cm/s]	Sample no.	Power [Watt]	Speed [cm/s]	Sample no.	Power [Watt]	Speed [cm/s]	Sample no.	Power [Watt]	Speed [cm/s]
1	400	0.5	**19**	500	7	**37**	600	11.5	**55**	700	25
2	400	1	**20**	500	8	**38**	600	12	**56**	700	30
3	400	1.5	**21**	500	9	**39**	600	15	**57**	800	17
4	400	2	**22**	500	10	**40**	600	20	**58**	800	19
5	400	2.5	**23**	500	15	**41**	700	7	**59**	800	21
6	400	3	**24**	500	20	**42**	700	8	**60**	800	23
7	400	4	**25**	600	5.5	**43**	700	9	**61**	800	24
8	400	5	**26**	600	6	**44**	700	10	**62**	800	25
9	500	1	**27**	600	6.5	**45**	700	11	**63**	800	30
10	500	2	**28**	600	7	**46**	700	12	**64**	800	35
11	500	2.5	**29**	600	7.5	**47**	700	13	**65**	900	20
12	500	3	**30**	600	8	**48**	700	14	**66**	900	25
13	500	3.5	**31**	600	8.5	**49**	700	15	**67**	900	30
14	500	4	**32**	600	9	**50**	700	15	**68**	900	35

15	500	4.5	**33**	600	9.5	**51**	700	16	**69**	900	40
16	500	5	**34**	600	10	**52**	700	17	**70**	900	45
17	500	5.5	**35**	600	10.5	**53**	700	18	**71**	900	50
18	500	6	**36**	600	11	**54**	700	20	**72**	900	55

Metallography was performed on all samples. Experimental results show a general trendline in Figure 93 between bonded and unbonded regions of the weld power-weld speed plot. The criterion for determining whether a sample was bonded was fixed at a weld depth of 1.2 times the thickness of the shim i.e. 0.6 mm. The trendline suggested a linear relationship between power, speed and weld depth. Given that the welding was performed with a constant beam diameter, the slope of the line is the condition of constant fluence necessary to satisfy the weld depth criterion. This curve suggests that a minimum amount of energy must be deposited to be bonded. To minimize the heat affected zone while maximizing throughput, it would be desirable to operate at the highest power and weld speed possible which, in this case, was 900 W and 400 mm/s.

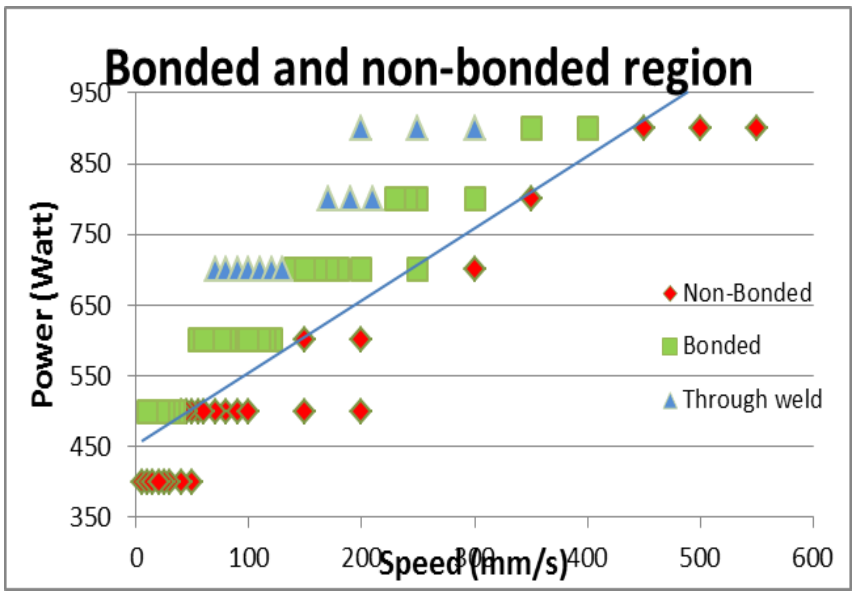

Fig 93. Graph showing the bonded and non-bonded regions.

Figure 94 shows the effect of weld width and weld speed at different powers. This graph shows that at a particular power, weld depth decreases as weld speed is increased leading to lower fluences and lower energy dosage within the material.

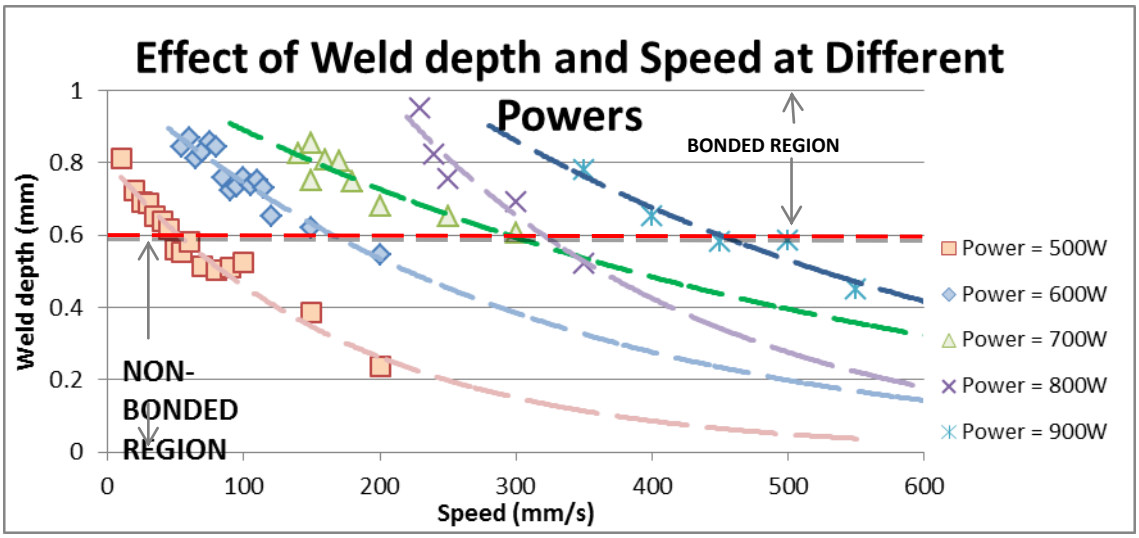

Fig 94. Graph showing effect of weld width and weld speed and different powers.

Figure 95 shows some of the cross-sections obtained by metallography. Several defects such as porosity, cracking, and discontinuous weld lines were observed in the microstructure and on the top surface of the welds. Gas porosity and voids are caused by the molten aluminum absorbing atmospheric gases. Porosity and voids can be controlled by proper cleaning of welding surfaces, the use of cover gas, providing good fit up between laminae and running fast welding conditions. Thermal phenomena such as cracking and warpage are caused by excessively high thermal gradients and can be controlled with welding parameters. Discontinuous weld lines are caused by fluences being too low and also can be controlled using welding parameters.

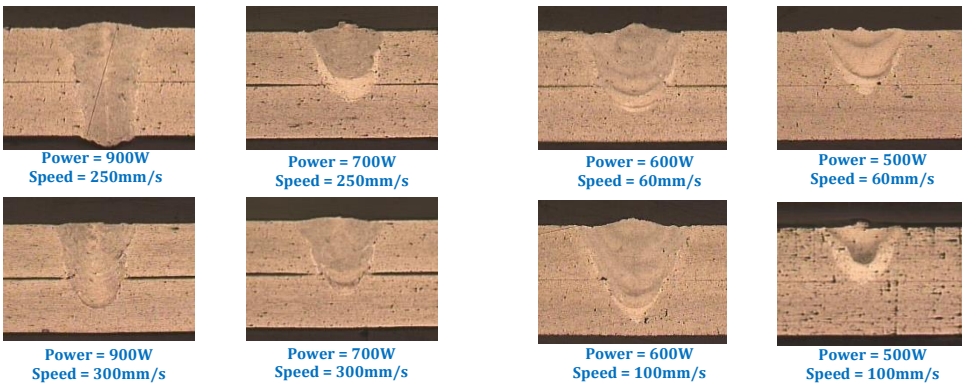

Fig95. Laser welding parameters for good weld

Stamped aluminum investigations: A low cost MATI design based on stamped aluminum plates was developed for the design conditions of 50 bar and a charge time of 180 seconds. Further, the stamped design was evaluated from a manufacturing point of view with the help of Ford engineers. No changes were made in the flow features of the plate design. In the latest design, the thickness of the LN_2 plate was 300 µm and the channel height 250 µm. The thickness of the H2 plate was 300 µm with a channel height of 100 µm. A current bend radius of 0.3 mm was used for all stamped features.

Several changes were made to the design corresponding to the changes in requirements and manufacturability and reliability feedback from Ford engineers. In the latest design, the thickness of the LN_2 plate was reduced to 300 µm from 500 µm and the channel height was reduced to 250 µm from 500 µm based on the decreased H_2 pressure requirement. Similarly, the thickness of the H_2 plate was reduced to 300 µm with a channel height of 100 µm. Fig 96 shows the features in the revised design. As a result of manufacturability feedback from Ford engineers, we made these changes.

1. The bend radius of all stamped features were increased to avoid tearing and to allow a free flow of material during stamping;
2. The hem around the circumference of the plate was changed to a stamped feature.

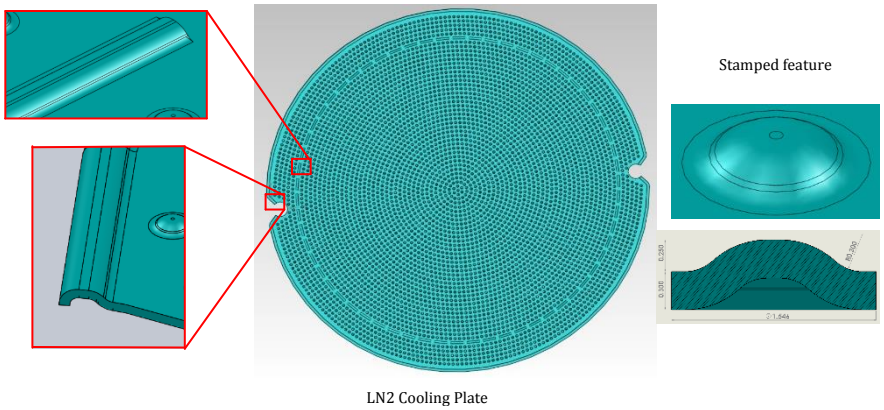

Figure 96: Stamped MATI features

FEA analysis was performed on the stamped plate to evaluate the deflection of the plate under pressurized hydrogen. FEA analysis predicted a 4.5% deflection in the plate and analytical calculations using plate mechanics predicted a 5.5% deflection. Even if other areas of the cooling plate did not deflect, this level of deflection would not cause significant flow maldistribution

Comparing the stamped design with the a PCM design under the same set of design conditions of 50 bar pressure and charge time of 180 seconds, the channel height of both designs was kept the same. The major difference between the two designs was the thickness of the plate and the span between the features/pillars. The plate thickness for the stamped design was 0.3 mm and for the PCM design is 0.25 mm. This was because the distance between the pillars was larger for the stamped design due to restrictions imposed by a minimum bend radius for the stamping of 6061 Al. Therefore, in order to hold the flow cross-section constant without increasing the depth of the channels, fewer pillars were inserted into the stamped design.

Brazing Studies: Three concepts were evaluated in terms of robustness of the system and the rigidity of the brazed joint. Figure 97 shows the brazed joint concept chosen, with the help of Ford engineers, to be incorporated into the design. The bottom cooling plate was stamped with a vertical flange along the circumference of the inlet. This

feature aided in alignment of the header in the horizontal direction and provides extra surface area for brazing. The top plate was stamped with a “speed bump” feature close to the inlet of the cooling plate. The area between the inlet and the speed bump aids in vertical alignment of the cooling plate with the inlet. In all, these features helped to improve joint rigidity reducing stresses induced on the brazed joint resulting in a more reliable brazed joint.

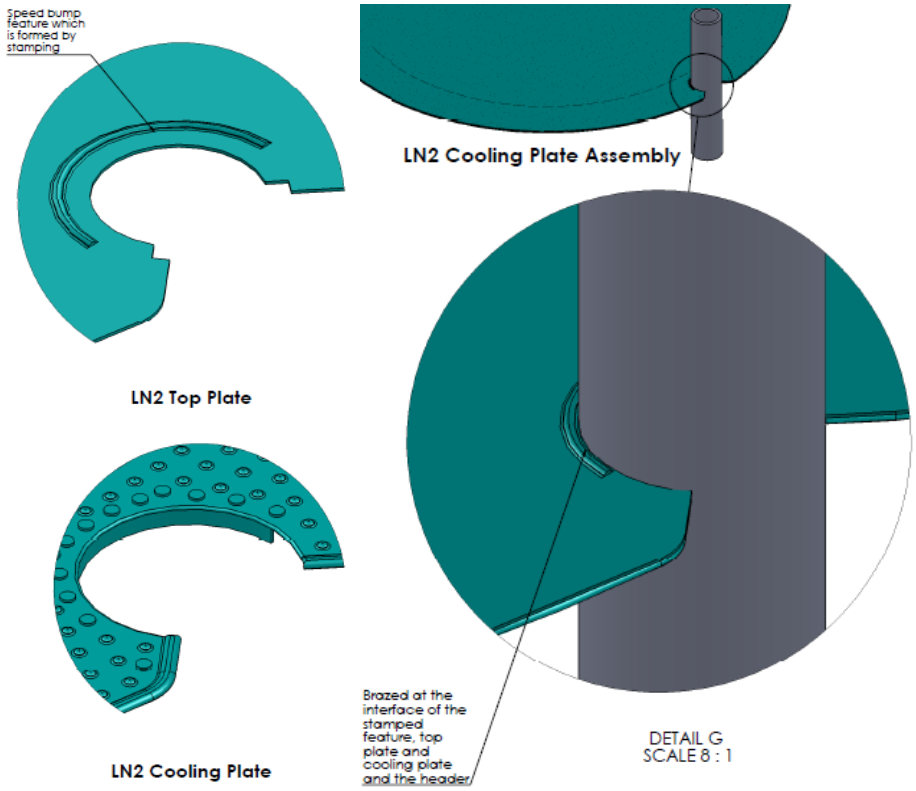

Fig 97. Brazed joint design at the inlet of cooling plate

The critical issue for fabricating the MATI test article was creating a hermetic seal at the interface of the cooling plates and the headers. Brazing was found to be the only suitable joining technique because of the joint’s unique shape (limited access to all sides) and thermal expansion concerns of the stainless steel. Requirements to select the appropriate braze material were: similar CTE to stainless steel, withstand cyclic thermal shock of 220 K (290 K to 70 K), operate at cryogenic temperatures and resist hydrogen permeation. With these requirements, brazing options were limited to copper or alloys based on nickel or silver. Because of the limited access and irregular shape of the joint, a braze paste was selected as a means to obtain a hermetic joint. Copper was not available as a paste. Further, oxygenated copper can be reduced in hydrogen leading to embrittlement. Silver was not selected due to its high cost. Nickel-based alloys were found to be suitable as several brazing fabricators reported using nickel-based brazes for the cryogenics industry.

Brazing was conducted with Braze 820 (BNi-2; Lucas-Milhaupt) and Nicrobraz LM (Wall-Colmonoy Corp.) in an Argon filled inert gas furnace. Both were heated and

cooled at 5 °C/min (max. heating and cooling rate of the selected furnace). The BNi-2 was held at 1100 °C for 25 minutes. The Nicrobraz was held at 1100 °C for 5 minutes. Three critical issues were considered in producing the braze joints: cleanliness, fit-up and surface roughness. For a braze paste to form a solid joint, the braze paste must reach its transition temperature, wick into the joint and evaporate off any binder and/or flux. Capillary action required clearances between 0.002 and 0.004" (25 to 50 μm) for the selected material. Test article header tubes were fabricated with these tight tolerances to ensure hermeticity.

After brazing, joints were visual inspected (with a microscope to check for filleted edges and no bubbles or cracks on the braze surface) and leak tested. Both alloys were found to produce high quality joints that were leak proof before and after they were soaked in a liquid nitrogen bath. Multiple samples were produced showing repeatability of the procedures to produce leak-free joints.

Braze joints were further tested for failure due to thermal effects in liquid nitrogen. The experiments evaluated two failure modes at cryogenic temperatures. First, failure due to a temperature gradient across the stainless steel cooling plate when the liquid nitrogen initially enters the apparatus. Second, failure due to CTE mismatch between the braze material and the stainless steel cooling plate.

Figure 98 shows the test article used to evaluate Braze 820 and Nicrobraz LM braze joints under cryogenic conditions. Tests were performed by dipping the test article in liquid nitrogen for 5 minutes and then removing the test article into ambient conditions. The orientations shown in Figure 8 were used to test for the two modes of failure. After exposure to liquid nitrogen, the brazed test joints were air leak tested up to a pressure of 100 psi without any failure or leakage. This suggests that both braze materials may be suitable for withstanding cryogenic conditions of the MATI device.

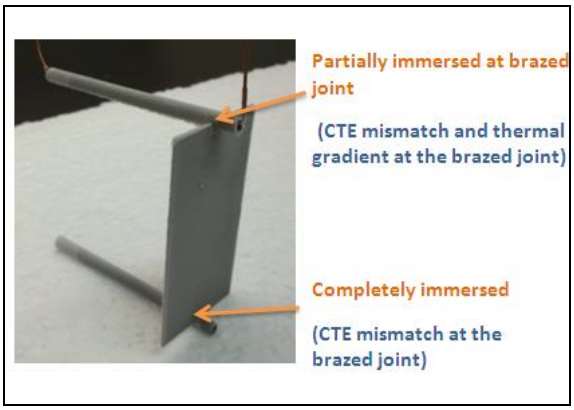

Figure 98: Test article apparatus used to leak test braze joints after cryogenic application.

Key Findings: *Key findings from Task 2.6 include: 1) both patterning using stamping and bonding using laser welding were successfully demonstrated for aluminum 6061. These are critical findings and open the way for the use of low cost and light aluminum for the MATI material of fabrication. Stamping in particular is a low cost alternative to*

photochemical etching, 2)The technical feasibility of brazing the cooling plates to the headers was successfully demonstrated. This is a wildly used manufacturing process and is a low cost way of connecting the cooling plates to the headers.

Task 2.7 System Studies: The design of the First Generation MATI began with the following basic requirements given by the US Department of Energy: store 5.6 kg H_2 using adsorptive media, remove heat of adsorption, add heat for desorption and refill the H_2 storage tank in less than 250 seconds. Evaluation parameters included system volume, mass of non-adsorptive materials and cost of goods sold. By coupling the basic requirements with the evaluation parameters, requirements were identified for driving the design of the MATI. Key requirements for driving the geometry of the MATI include removal of heat of adsorption, provision of heat for desorption, provision of radial access of H_2 to the adsorptive bed, hermetically sealed fluid paths, and the ability to withstand 50 atm H2 pressure. These requirements led to a system concept that uses liquid nitrogen cooling. Key material requirements included high modulus at low temperatures (70 K), the ability to resist H_2 permeation and embrittlement, a low coefficient of thermal expansion, joinability, and the ability to resist erosion due to high liquid nitrogen velocities. 300 series stainless steel and 3000/6000 series aluminum alloys were chosen to meet these requirements largely due to the cost of materials. Stainless steel 316 was tentatively selected due to its commercial availability. Aluminum alloy 3003 were evaluated another task.

Figure 99 shows the initial calculations which were performed to determine the flow rates to be used through a single cooling plate. Assumptions included an overall modular bed height of 5 cm and an overall modular bed diameter of 30 cm. Assuming cooling plates on both the top and bottom of the adsorbent module, a 2.5 cm bed height was assumed for each cooling plate. A flow rate of 2.7 liters/min was determined for each cooling channel. It was determined that 43 adsorbent beds were need for an overall liquid nitrogen flow rate of 232 liters/min for the MATI.

The MATI was designed to fit within a 30 cm inner diameter cylindrical pressure vessel. The system was composed of several stacked microchannel plates, sandwiched between adsorptive beds. Header tubes, which feed and remove liquid nitrogen from the microchannel cooling plates were located on opposite ends of the microchannel plates and fit within the 30 cm diameter. The SolidWorks image below is a rendering of the 30 cm diameter MATI (Figure 100).

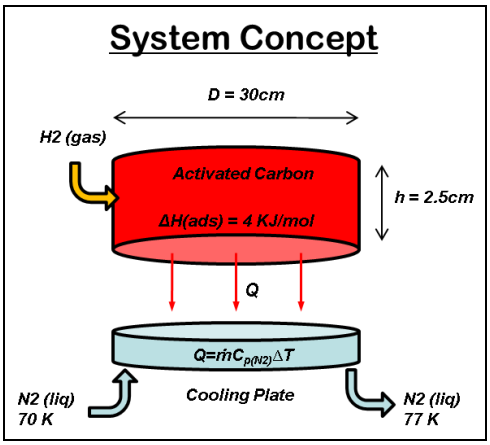

Figure 99: MATI system concept

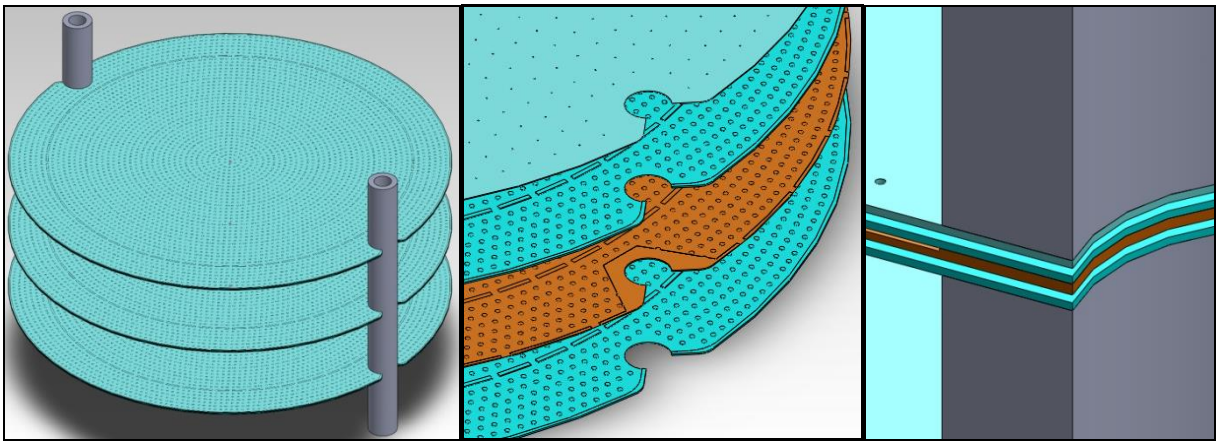

Figure 100: Left - MATI concept; Center – Exploded view of the cooling plate shims; Right - Close up section view to show LN2 paths from the header

The cooling plate was composed of four shims providing three functions. The plates have the ability to remove heat, add heat and allow hydrogen to access the beds in an axial direction. The LN_2 shims (second and fourth from top, blue) have a channel for cooling and heating of the bed. The H_2 plates allow hydrogen to be introduced between the two cooling plates. The LN_2 shims and top shim (top, light blue) have holes for axial access of hydrogen from the H_2 plate to the beds. Joining of the four shims provides hermetic seals between the H_2 and LN_2.

The following processes were used to produce the MATI: photochemical machining (PCM) the fluidic paths of the cooling plate shims, laser cutting the H_2 access holes, diffusion bonding or laser welding of the shims into a microchannel plate, machining the slits for the header tubes and brazing or soldering the header tubes to the cooling plates. All processes implemented are established in industry processes for high

volume production and have established tooling costs and step yields. Consequently, a cost model was developed for estimating the cost of goods sold (COGS) for the MATI. The cost model was a bottom-up process-based cost analysis that obtains a COGS based on tool usage, throughput, capital costs, power usage, etc. for each process step. All data in the cost model was based on real parameters that have been obtained in practice or based on quotes.

Figure 101 shows the results of the cost modeling analysis assuming different manufacturing approaches. Each manufacturing approach evaluated in the graph is represented by a combination of the material, the joining process and the work envelope (x-y dimensions of the shim stock panel). The first bar (left most) represents a stainless steel system that is diffusion bonded on a 24" envelope. The last bar (right most) represents an aluminum alloy system that is laser welded on a 48" envelope. Results suggest that a full-scale MATI can be manufactured using PCM/laser welding at a 48" scale for a cost of goods sold of $279.36 per system assuming a production volume of 500,000 units per year assuming 5.6 kg of hydrogen stored

The first iteration (red) shows a high MATI cost because of large amounts of wasted raw material (recycling and remanufacturing of raw material waste is not considered in the model). By increasing the work envelope to 48" (dark blue), the cost per system drops by a factor of four due to better use of the raw material. The third (light blue) iteration reduced the cost by 50% from the previous by gang pressing three cooling plates at a time within the diffusion bonding step (further research is required to verify gang pressing is a robust process). Iteration four (yellow) showed a cost decrease due to the use of laser welding. This drastically reduces bonding cycle time and electricity usage over the previous diffusion bonding methods. The final iteration (green) is modeled using aluminum. The reduced cost of the aluminum versus stainless is the cause of the reduced cost versus the previous iteration. It is also important to note that laser welding is also likely required for aluminum alloys.

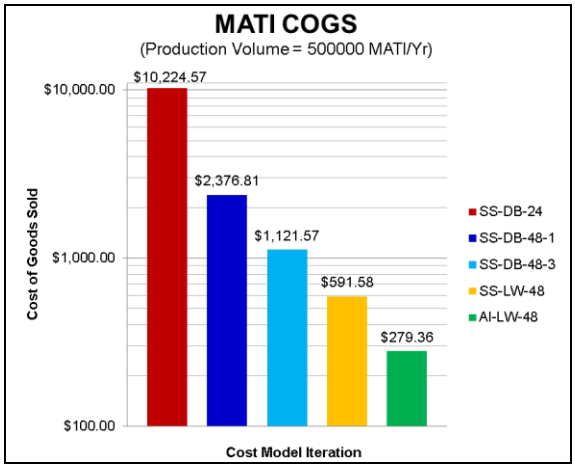

Figure 101: Cost of goods sold (COGS) for the MATI device assuming different material-processing architectures.

Figure 102 shows a breakout of the COGS for PCM/laser welding of 48” aluminum. All categories except for raw materials and utilities contain elements that are production-rate dependent. That is, when production increases, the cost per unit decreases, as seen below.

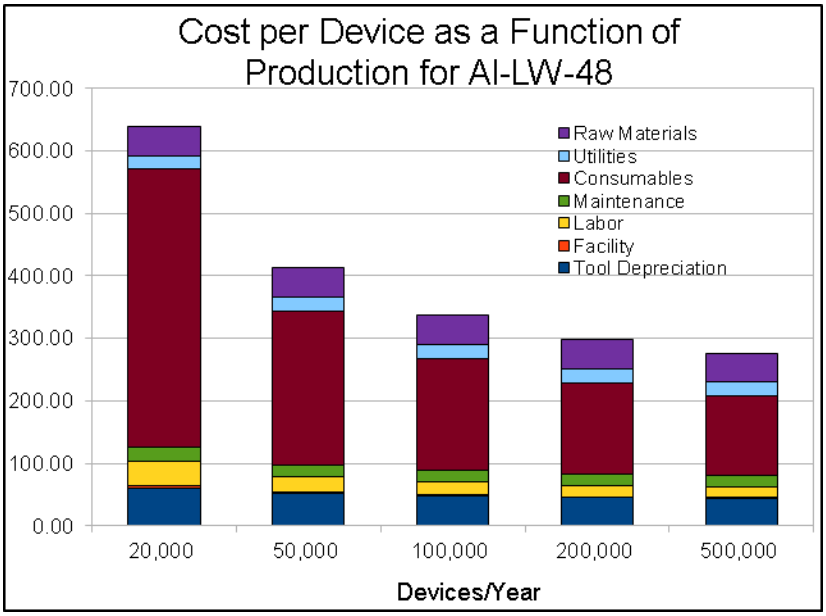

Figure 102: Cost of goods sold (COGS) as a function of production volume per year for the MATI device assuming a 48” aluminum architecture using photochemical machining and laser welding.

The manufacturing plan for producing the First Generation MATI system and inserting it within an aluminum tank is shown below. As discussed above, the cooling plates were designed to be stamped from shim stock and assembled together using laser welding. Slots were machined into headers for assembly with cooling plates via brazing using a process similar to how headers on automotive radiators are joined to cooling fins and plates. This manufacturing plan was then integrated with the aluminum tank manufacturing plan to show all processes required for the production of the MATI hydrogen storage system. The final manufacturing plan is shown in Figure 103.

Revised System Design with Enhanced Puck Separation – It was determined that for optimum performance of the MATI, the spacing between cooling plated needed to be at least 5 cm. Cooling a 5 cm thick puck required two design changes. First, hydrogen distribution was taken out of the cooling plate and it was moved to the middle of the 5 cm MOF-5 puck allowing hydrogen to cool the interior of the 5 cm puck resulting in two 2.5 cm pucks separated by a hydrogen distribution plate. The second change was to introduce conduction enhancement in the puck which consisted of small diameter aluminum pins inserted in the puck. A MATI design is shown in the figure(Figure 104) below in which the hydrogen distribution plates have been separated from the cooling plates. The hydrogen distribution plates better contribute to the overall cooling capacity

of the system resulting in an increase in bed height from 2 cm to 3 cm and a reduction in the MATI system mass and displacement volume as reported last period. The addition of conduction enhancement allows plate spacing to increase to 5 cm.

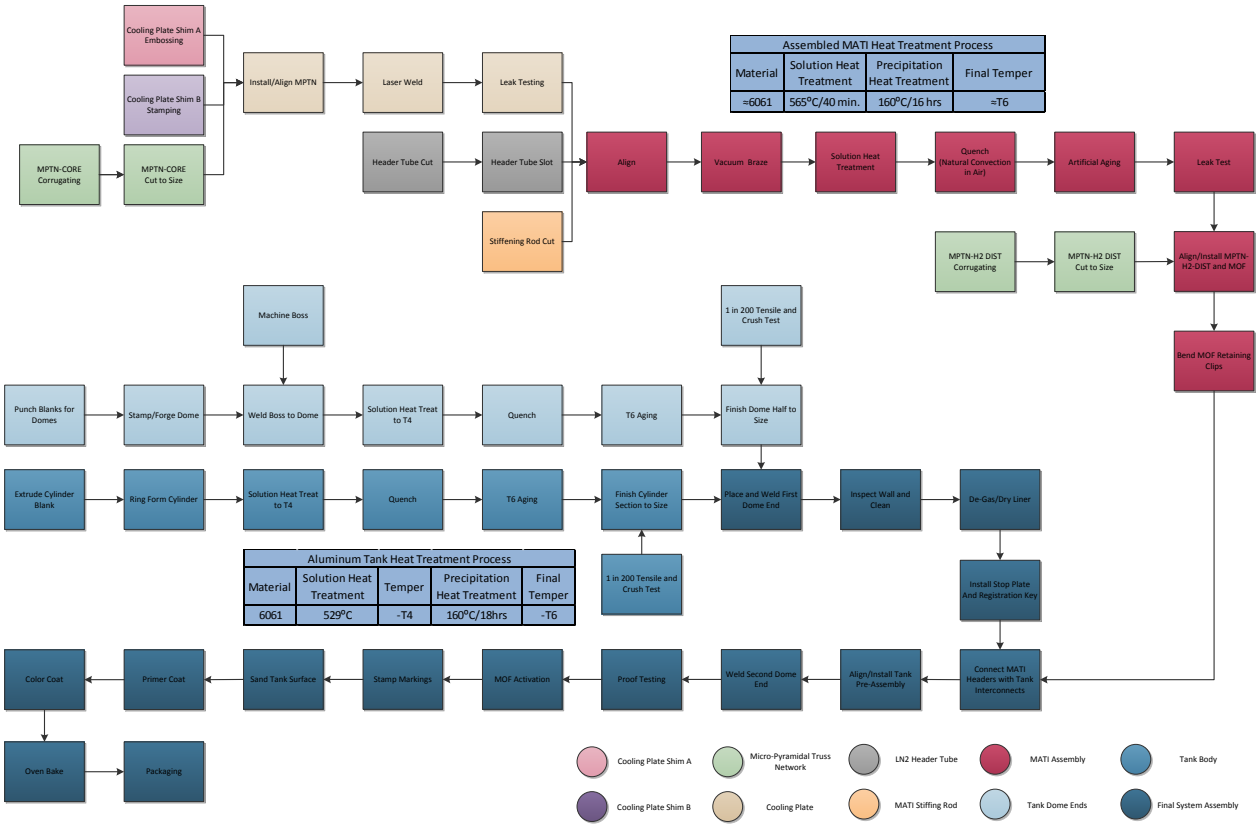

Figure 103: MATI Manufacturing Plan

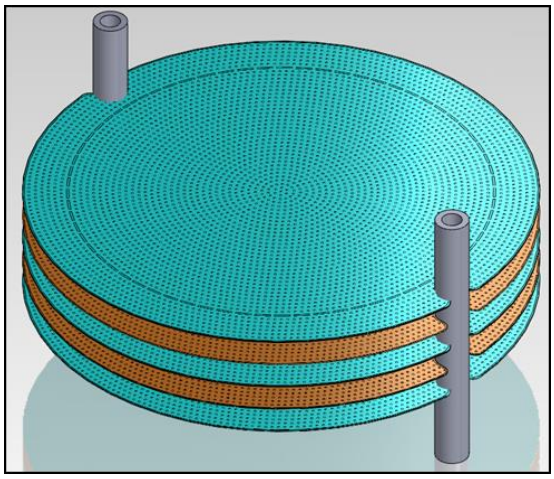

Figure 104. 30 cm diameter MATI system design at 6 months into phase 2.

In order to insure that we could distribute flow between a large number of cooling plates, an Excel model was developed to predict flow maldistribution. It was shown that with an header inner diameter of 23 mm, a flow non-uniformity of less than 5% could be attained across all 72 cooling plates. Previously, 5% flow variation was determined as the tolerance at which heat exchanger effectiveness significantly decrease.

Two new MATI system designs were developed: the MATI v2.2 and v3 system designs. The v2.2 design was developed in 316L SS to increase efficiency by introducing the H2 into the middle of the packed bed . In addition to this, the v3 design was developed in 6061 aluminum for H2 pressures of 50-200 bars and hydrogen and a charging time of 180 seconds. These requirements led to a system concept of a fin and tube type heat exchanger that uses liquid nitrogen cooling (storage density increases with decreased temperatures). Key material requirements included high modulus at low temperatures (70 K), the ability to resist H_2 permeation and embrittlement, a low coefficient of thermal expansion, joinability, and the ability to resist erosion due to high liquid nitrogen velocities. 6061aluminum was chosen to meet these requirements largely due to the low cost of materials and low density.

The MATI was designed to fit within a 30 cm inner diameter cylindrical pressure vessel. The system is composed of several stacked microchannel plates, sandwiched between adsorptive beds. Header tubes, which feed and remove liquid nitrogen from the microchannel cooling plates were located on opposite ends of the microchannel plates and fit within the 30 cm diameter.

The updated design with separated cooling (MATI v2.2) and distribution required identical fluid flow rates as the cooling channels have not changed. However, the number of cooling channels was decreased and therefore the overall mass and volume of the storage tank that was consumed by the MATI was reduced. The current design can be seen below in Figure 105.

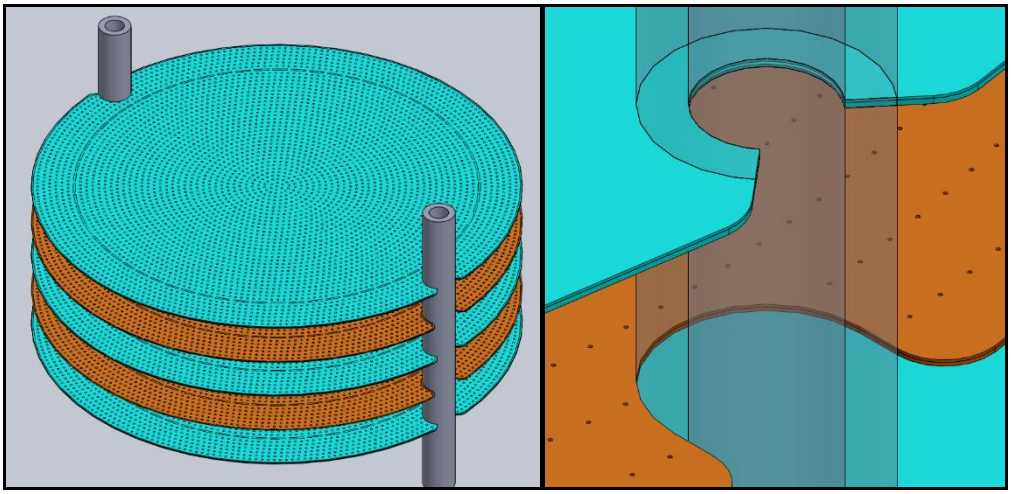

Figure 105: MATI v2.2 (left) and close-up view of the LN_2 plate and H_2 plate joints (right)

The LN_2 plate inlets and outlets were designed to fit into slits machined into the header tubes to create a hermetic seal upon brazing. The H_2 plates are simply press fit onto the header and can be placed between adsorbent sections. By re-designing the MATI to separate H_2 and LN_2 plates, the mass of the MATI decreased by 26% and the volume by 5%. By going to an aluminum architecture, possible mass savings could be up to 71% though volume would remain the same.

The following processes were assumed to be used to produce the SS v2.2 MATI: photochemical machining (PCM) to pattern the fluidic paths of the cooling plate shims, laser cutting the H_2 access holes, diffusion bonding or laser welding of the shims into a microchannel plate, machining the slits for the header tubes and brazing or soldering the header tubes to the cooling plates. All processes implemented are established in industry for high volume production and have established tooling costs and step yields. Consequently, a cost model was developed for estimating the cost of goods sold (COGS) for the MATI. The cost model is a bottom-up process-based cost analysis that obtains a COGS based on tool usage, throughput, capital costs, power usage, etc. for each process step. All data in the cost model was based on real parameters that have been obtained in practice or based on quotes.

The Cost of Goods Sold (COGS) can be reduced by 50% if we replaced the stainless steel by aluminum using PCM and laser welding. Further, the MATI design was redesigned (v3) for stampability and laser weldability for 6061 Al. Further, design requirements were changed from 50bar to 200bar and the charge time from 240 seconds to 180 seconds. The MATI v3 30cm LN_2 cooling plate design is shown in Figure 106 below.

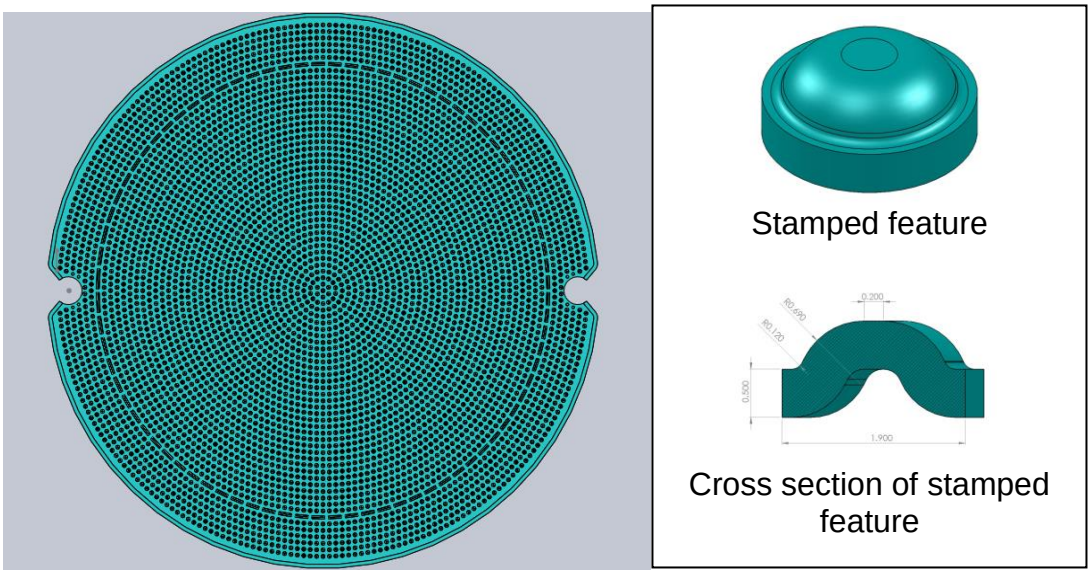

Figure 106: Left – LN_2 cooling plate design; Right top- Stamped feature; Right bottom- cross section of the stamped feature.

To deal with the new H_2 pressure requirements, the thickness of the LN_2 plate was increased to 500µm and the stamped feature height was made to be 500 µm i.e. the channel height was increased to 500µm. The pillars were spaced based upon a deflection analysis performed on the plate. The threshold for channel deflection was kept as 5% of channel height. Higher deflection in the channel was expected to cause a large change in pressure drop across the plate. Due to lower modulus of the material (versus v2) and the higher pressures acting on the plate, the spans between features were found to be too small which would lead to increased pressure drop across the cooling plate. In order to reduce the deflection, the thickness of the plate was increased. In this design, the spans between the pillars were found to be 3.5 mm. Plate mechanics was found to predict a 5.4% deflection of the channel while FEA analysis predicted a 2% deflection.

In the current reporting period, system studies were conducted to visualize the impact of design changes with regards mass and volume. Phase 2 SMART goals for the MATI unit are a mass of 9.4 kg and a displacement volume of 4.2 L. Three designs were developed to show progress towards meeting the SMART goals. The Phase 1 MATI design uses a four shim integrated cooling and hydrogen distribution plate.

The first improvement over the Phase 1 design allows incoming hydrogen gas to flow half-way through the adsorbent bed to enhance cooling capacity. This allowed for an increase in plate spacing to reduce system weight and displacement volume. This design was the state of the MATI unit approximately 6 months into Phase 2. This concept is shown below in Figure 107.

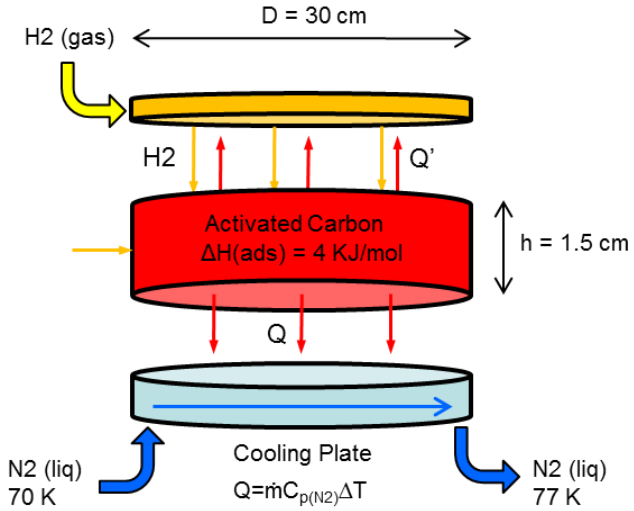

Figure 107: Concept of MATI design at 6 months into Phase 2.

Beyond this, two additional enhancements were developed for reducing the size, weight and cost of the MATI to be developed by 18 months into Phase 2. First, the 18-month design includes a conductivity enhancement within the adsorption bed which will increase the modular bed height to 5 cm still keeping the hydrogen distribution plate in the middle of the modular bed. Second, the material to be used in the 18-month design

will be aluminum. A summary of the changes between each design can be seen below in Figure 108.

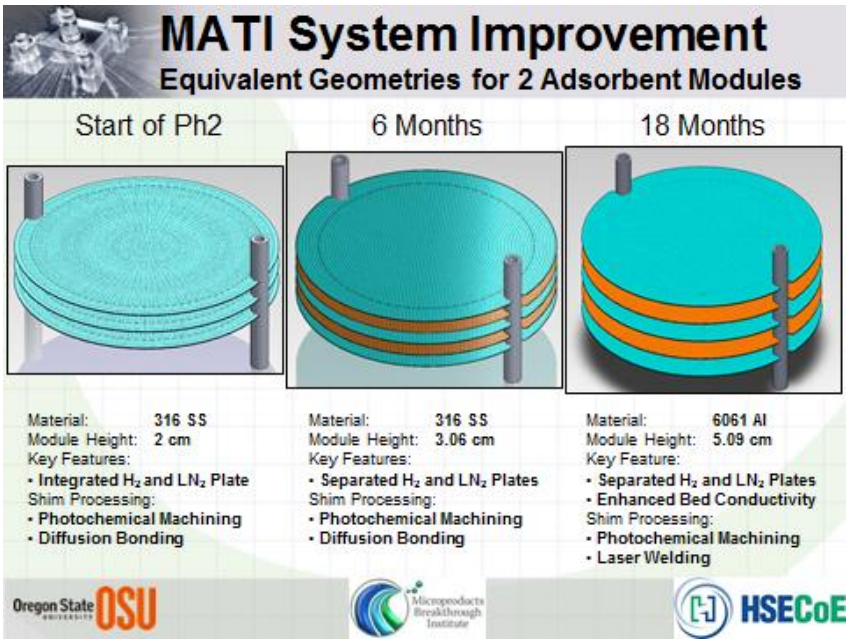

Figure 108: Comparison of design changes needed to meet SMART goals.

As a summary, plate spacing changed from 2 cm in the initial design to 3 cm in the 6 month design by introducing hydrogen cooling half way through the adsorbent bed. Spacing changed from 3 cm to 5 cm in the 18 month design by raising the conductivity within the modular adsorbent bed to 3 W/mK. These increases in modular bed height reduce both system mass and displacement volume by reducing the number of cooling plates required per unit volume. Finally, additional weight savings are achieved by producing the MATI system in aluminum. Figure 109 shows how the designs lead to an overall volume and mass reduction comparable with MATI SMART goals.

Two aluminum manufacturing routes were evaluated for producing the 18 month MATI cooling and distribution plates: 1) PCM and laser welding; and 2) stamping and laser welding. Cost models indicate that stamping would be significantly cheaper than PCM due to a reduction in the process consumables and raw materials. The effect of these two designs on size and weight of the MATI is shown in the figure 110 below. It is observed that the use of stamping increases the system mass and displacement volume by approximately 13% and 11%, respectively. As explained above, this is largely due to increases in material thickness caused by required increases in fin spans between pillars due to the larger pillars required within stamping operations.

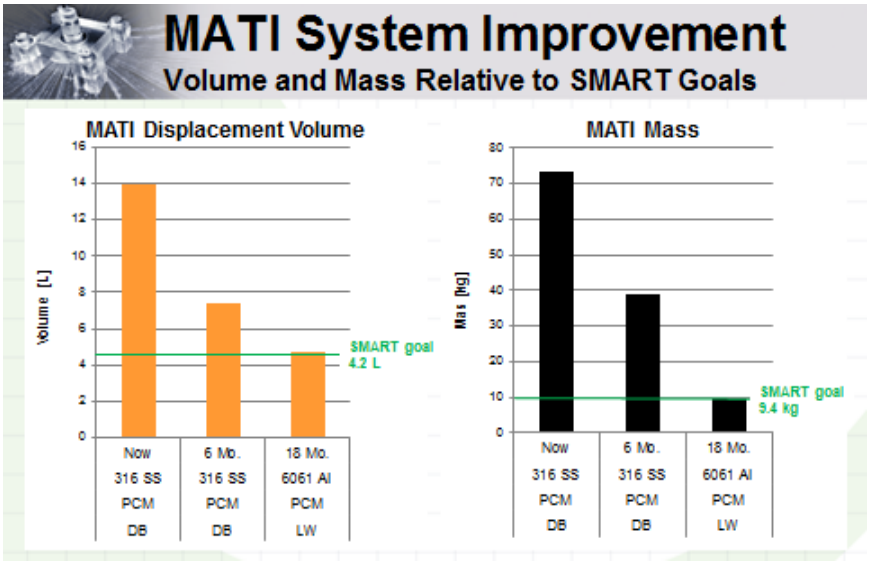

Figure 109: Mass and displacement volume reduction by design

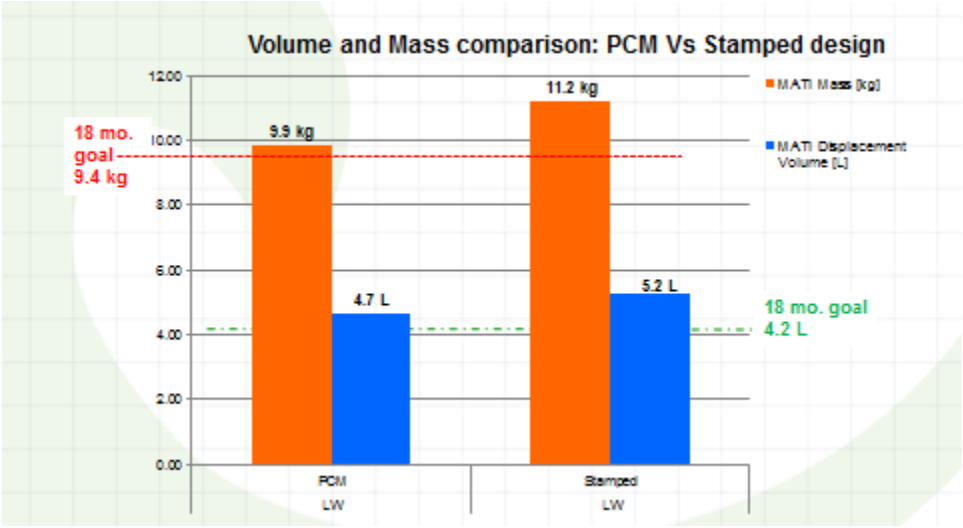

Figure 110: Displacement volume and mass comparisons between PCM and stamped designs.

The 18-month Phase 2 MATI design incorporating the MPTN technology was found to meet SMART goals for both displacement volume and mass. Figure 111 shows the design iterations for the Phase 2 design where PCM is photo chemical machining, DB is diffusion bonding, H_2 plate means the hydrogen plate was separated from the cooling plate, stamped mean the cooling plate was manufactured by stamping, LW is laser welded and MPTN means that the micro-scale pyramidal truss network was used. Incorporation of the MPTN into the Phase 2 design reduced displacement volume and mass by removing material from the hydrogen distribution plate.

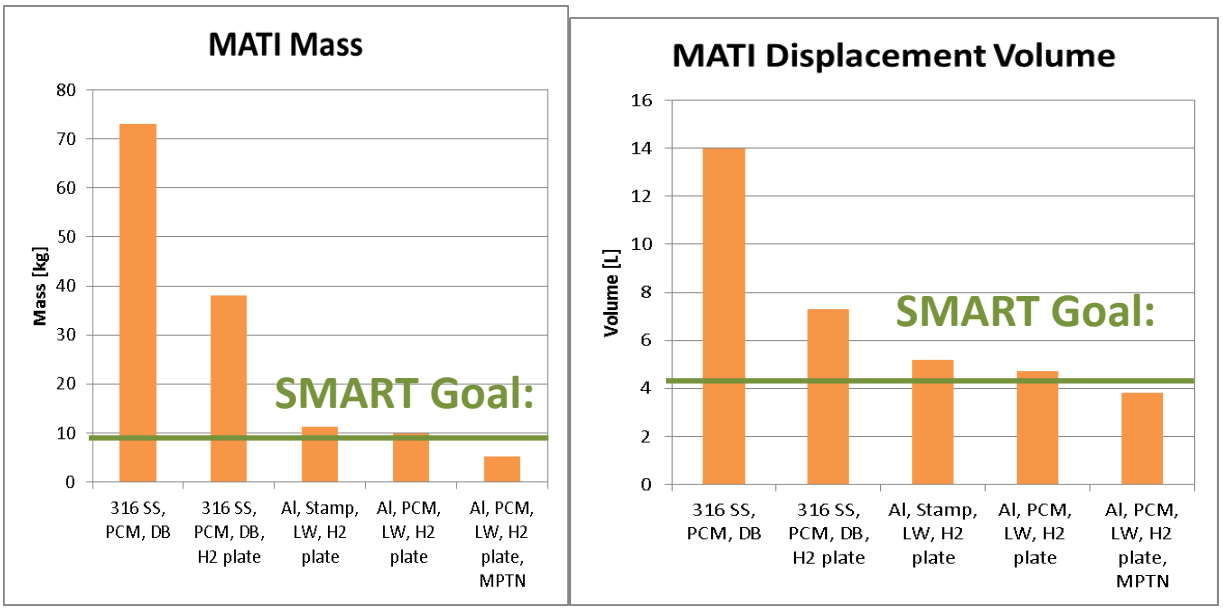

Figure 111: The change of mass and displacement volume with changes in MATI design

Previous studies showed stamping of cooling plates would slightly increase both system displacement volume and mass. Through the incorporation of a modified MPTN within the cooling plate to replace all of the islands within the cooling plate, it is expected that additional reductions in displacement volume and mass can be made while improving the manufacturability of the cooling plates.

Key Findings: *Key findings from Task 2.7 include: 1) A series of design modifications identified during Phase 2 led to a significant reduction in the MATI volume, weight and cost allowing the system to achieve the DOE smart goals for the device. The most important design modifications include:*

- *Take Hydrogen Distribution out of the Cooling Plate and add a Separate Hydrogen Distribution Plate in the middle of the pump allowing hydrogen to provide cooling at the most difficult part of the puck to cool. This allowed cooling plate spacing to increase from 2 to 3 cm.*

- *Use Aluminum 6061 in place of stainless steel for weight and cost reductions*

- *Use conduction enhancement using small aluminum pins in the densified pucks to improve heat transfer and allow cooling plate spacing to be increased to 5 cm.*

- *Replace the hydrogen distribution plate and the internals of the cooling plates with MPTN for weight reductions*

Production cost modeling confirmed that the MATI was suitable for high volume low cost production.

4.4 PHASE 2 CONCLUSIONS – Conclusions from the Phase 2 research are summarized below.

- **The microchannel Combustor/Heat exchanger Technology is an extremely attractive approach to providing combustion heat for discharging a hydrogen storage system**. – Simulation and experimental results confirmed that microchannel technology can result in an extremely compact device for providing thermal energy to a hydrogen storage system.

- **The MATI has several important impacts on the Adsorption System Design** – The use of the MATI has several important system impacts including 1) the MATI allows the use of densified media with a very high packing factor. The MATI allows up to 95% of the volume of the adsorption pressure vessel to be media and 2) Since the cooling fluid and hydrogen are separate, the MATI allows the use of fuel cell waste heat for discharge though a small amount of supplemental heating from hydrogen combustion is required.

- **The MATI concept is Technically Feasible** – Modeling and experimental results demonstrated that the MATI thermal and chemical performance is well understood and performs as expected.

- **The MATI concept is Manufacturable** – Fabrication studies demonstrated that the MATI could be fabricated out of aluminum 6061 using proven industrial processes amenable to high volume production.

- **The MATI concept can meet mass and weight goals for Adsorption Storage with a reasonable production cost** – The results of Phase two demonstrate that the MATI could meet the DOE Smart Goals for the device. To meet the smart goals, a number of important design modifications were required. These included the 1)The location of the hydrogen distribution plate needs to be in the middle of the puck to allow the hydrogen to provide cooling where it is most needed, 2) use aluminum 6061 in place of stainless steel, 3) use aluminum pins to enhance conduction in the pucks and 4) use microscale pyramidal truss networks for hydrogen distribution and for the internals of the cooling plates.

Based on these results the decision was made to further develop the MATI in Phase 3.

5.0 PHASE 3 ORGANIZATION AND RESULTS

This section presents an overview of Phase 3. Section 5.1 discusses the objectives of OSU's Phase 3 activities while Section 5.2 presents an overview of the MATI which is the primary technology focus of Phase 3. Section 5.3 discusses the Phase 3 scope of work while Section 5.4 presents the technical results by task.

5.1 OSU PHASE 3 OBJECTIVES: In Phase 3, OSU will design, fabricate and conduct acceptance testing on one or more MATI prototypes. The MATI prototype will be provided to SRNL by July 1st 2013 for performance testing. Testing is focused on demonstrating the feasibility of using microchannels for cooling adsorption based hydrogen storage systems and for model validation. OSU has two smart milestones associated with this scope of work. These include:

- Design a 2L adsorbent subscale prototype utilizing a MATI thermal management system having 54 g available hydrogen, internal densities of 0.10g/g gravimetric, and 27g/L volumetric.

- Demonstrate performance of subscale system evaluations and model validation of a 2L adsorbent system utilizing a MATI thermal management system having 54 g available hydrogen, internal densities of 0.10g/g gravimetric, and 27 g/L volumetric.

5.2 INTRODUCTION TO MATI: The preferred embodiment of the MATI is shown in figure. In this design, the tank is filled with densified adsorption media in the form of 1.5 to 2.5 cm thick disks (pucks) which have a diameter slightly less than the internal diameter of the tank. A standard unit cell consists of a stack of a cooling plate, a media puck, a hydrogen distribution plate, a second media puck and then a second cooling plate.

During charging, hydrogen is introduced into the hydrogen distribution plate and diffuses through the puck. As the hydrogen diffuses, it is adsorbed by the media producing heat that must be removed. Simultaneously, liquid nitrogen is passing through the cooling plates. As the heat of adsorption is produced, it is conducted through the media to a cooling plate where it is transferred to the liquid nitrogen which leaves the cooling plate at a slightly elevated temperature (90K) and is returned to the forecourt .The heat of adsorption is removed by two processes. First, the low temperature hydrogen being used for adsorption is at a temperature lower than the bed temperature and will remove some of the heat of adsorption as the hydrogen increases in temperature to the temperature of the bed. The balance of the heat of adsorption is removed by having the heat conduct through the bed to the cooling plates.

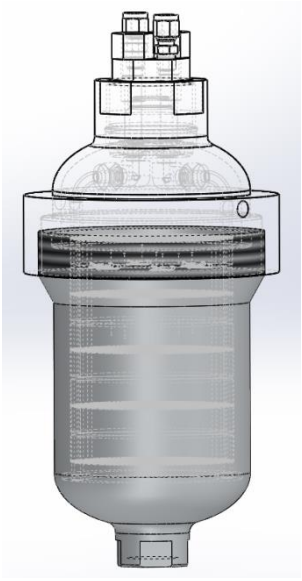

Figure 1: MATI prototype assembly inside of 2 L aluminum tank

The complete MATI consists of a number of cells (typically between 10 and 50) which are connected by headers to provide liquid nitrogen to the cooling plates and collect it so that it can be returned to the forecourt. In our current embodiment, the MATI has a diameter slightly smaller than the inside diameter of the tank, forming an annular region between the outside of the MATI and the inside wall of the tank. This allows hydrogen to flow in the annual region to the hydrogen distribution plates. An alternative configuration would eliminate the annual region and utilize distribution headers to deliver and collect the hydrogen. Use of distribution headers allows an increase in the diameter (approximately 2 mm or larger) and an improvement in the overall volumetric and gravimetric efficiency of the device.

The design of the cooling plate uses a micro pyramidal truss network (MPTN) to define the flow channels for the cooling fluid. The MPTN is enclosed between two plates to form the micro channel cooling plate. This approach to the cooling plate has the advantage of using an inexpensive stamped structure (MPTN) which is significantly less expensive other microchannels fabrication techniques, such as chemical etching. In addition, the use of MPTN's reduces the weight of the cooling plate. The cooling plate application requires that the MPTN is enclosed between two thin sheets of metal ensuring that the cooling fluid is separate from the hydrogen being adsorbed. However, the MPTN does not need to be enclosed for the hydrogen distribution application and this significantly reduces the weight of the hydrogen distribution plate.

Design studies have shown that the cost and weight of the MATI are strongly determined by the selected material. Stainless steel has been widely used for micro channel applications and is well understood for microlamination applications. However stainless steel is twice has heavy as aluminum and is twice as expensive. The Hydrogen Storage Center of Excellence conducted an evaluation of the suitability of

aluminum for the MATI and believes that the cooling and hydrogen distribution plates can be reliably and cost effectively fabricated from aluminum.

The MATI concept has several key advantages. These include:

- *Separates Cooling Fluid from Charging Hydrogen* – The MATI allows the use of a separate cooling fluid other than hydrogen. The alternative approach provides hydrogen for adsorption and requires excess hydrogen flow for cooling. The use of a micro channel heat exchanger in the MATI allows an alternate lower cost material (e.g., Nitrogen) to be used for cooling. The MATI is more flexible and allows the use of an alternative cooling fluid if this is desirable.

- *Allows Use of Densified Media* – The design of the MATI can be optimized for adsorption materials that are either densified or in a loose fill state depending on the design requirements of the overall system. Densified materials are generally preferred as compaction eliminates voids within the media and generally increases volumetric and gravimetric efficiencies.

- *Allows Use of Fuel Cell Waste Heat for De-adsorption* – During hydrogen discharge, the MATI can use waste heat from the vehicle's hydrogen fuel cell to provide most of the thermal energy needed to desorb the hydrogen in the tank. This is only possible in systems, such as the MATI, where the heating fluid (e.g., nitrogen) is kept separate from the hydrogen being discharged from the tank. The current embodiment of the MATI based storage system uses an electric resistance heater drawing electric power from the fuel cell. It is possible that some designs will require additional heating of the discharged hydrogen if the fuel cell waste heat is not capable of heating the discharged hydrogen to a sufficiently high temperature.

- *Enhances cooling with Separate Hydrogen Distribution Plate* – The cost, weight and volume of the MATI is determined in large part by the spacing between cooling plates. Using cooling and hydrogen distribution plates at the top and bottom of the puck, currently the largest attainable spacing is approximately 2 cm. The addition of a separate hydrogen cooling plate, located in the middle of the puck, introduces very cold hydrogen at the center line of the puck. This delivers cooling directly to the hottest and most difficult to cool part of the puck and enables the spacing between the top and bottom plate to be increased by 50% to 3 cm while maintaining the required charging and discharging rates. The spacing can be further increased by using aluminum heat transfer pins in the media puck to enhance the conductivity of the puck. This allows the spacing to be increased to 5 cm.

- *Compact and Light* – When using a MATI with densified media more than 97% of the tank volume can be filled with densified media. Typically, in a powder or packed bed design only 65-80% of the tank volume can be filled with media. Based on modeling and experimental results, we believe that the MATI with

densified media holding the DOE targeted 5.6 Kg of hydrogen will weight 9.3 kg and have a volume of 6 liters. The impact of the design features described above on the size and weight of the MATI are summarized on VG 6 through VG 9.

5.3 PHASE 3 TASK STRUCTURE: In Phase 3 the OSU activities related to engineering concept design, modeling and validation were organized into six activities:

Task 3.1. Prototype Design – This task focuses on the analysis and design of the MATI prototype

- **Subtask 3.1.1 Prototype Design** – Subtask 3.1.1 is focused on the overall design of the 2 MATI liter prototypes including instrumentation

- **Subtask 3.1.2 Cooling Plate Design** – This task involves the redesign, fabrication and separate effects testing to improve flow distribution in a 10 cm diameter cooling plate,

- **Subask 3.1.3 Hydrogen Distribution Plate Design** – Subtask 3.1.3 is focused on developing and conducting separate effects tests on the hydrogen distribution plate

- **Subtask 3.1.4 Header Design** – The focus of Subtask 3.1.4 is on the design of the nitrogen distribution headers and the attachment of the headers to the cooling plates

- **Subtask 3.1.5 Puck Design** – Working with University of Michigan and Ford Motor Company, this subtask is focused on the design of the densified MOF-5 puck. The pucks will be fabricated at Ford Motor Company and supplied to Oregon State University

- **Subtask 3.1.6 Pressure Vessel Design** – Subtask 3.1.6 is focused on developing the design for the pressure vessel which will be fabricated by Hexagon/Lincoln

Task 3.2. Prototype Fabrication and Assembly – Subtask 3.2 is focused on fabricating components such as the cooling plates and assembling the MATI prototype.

Task 3.3. Facilities Development – The redesign of our test facility to allow the preliminary testing of the 2 liter MATI prototype is included in Task 3.3.

Task 3.4. OSU Prototype Testing – Task 3.4 is focused on the preliminary testing and characterization of the 2 liter MATI prototype.

Task 3.5. Modeling – Model development and validation with prototype experimental results are included in Task 3.5.

5.4 RESULTS - Progress on each of these activities is reported below.

Task 3.1 Prototype Design – This task involves the design of the prototype MATI and consists of six subtasks. Progress on the subtasks is discussed below.

Subtask 3.1.1. Prototype Design – Originally the Phase III prototype was designed to utilize the aluminum 2L tank provided by Hexagon Lincoln and to be filled with compressed beds of MOF-5 provided by Ford Motor Company. The prototype will utilize an arrayed MATI design consisting of stainless steel cooling plates and H_2 distribution layers.

The pressure vessel was to be filled with approximately ten ½ height compressed MOF-5 bed sections (each ½ height section will be approximately 1.5 cm tall) inserted into a fully integrated MATI system consisting of six microchannel cooling plates and 5 H_2 gas distribution plates, Figure 2.

The MATI prototype was be constructed to be 10 [cm] in diameter and approximately 750 [μm] total thickness and utilizing ¼" stainless steel integrated headers to produce a flush perimeter design. The cooling plates were to be fabricated using photochemical machining and diffusion bonding following similar recipes used to produce the Phase II prototypes. The stainless steel headers will utilize a notched design to provide proper spacing between cooling plates, maintain structural integrity of the stacked device, and provide a uniform distribution of LN2 coolant and N_2 gas to each MATI plate. The H_2 distribution plate were be placed between the two ½ height beds (1.5 [cm]) and were approximately 1 [mm] total thickness, as depicted in Figure 3. The H_2 distribution plate served three functions: i) uniform distribution of H_2 between MOF-5 beds, ii) provided an additional cooling affect from the low temperature adsorbent gas during charging, and iii) provided structural support necessary to maintain contact between the compressed beds and respective cooling plates. The distributor plate provided necessary spring-type tension to accommodate for all tolerances in the production of the MOF-5 beds.

To help minimize the loss of MOF-5 material (cracked chunks, crumbles, etc.) the MATI stack was to be wrapped in a highly porous mesh to help maintain the overall mass of MOF-5 in the vicinity of the MATI structure, Figure 4.

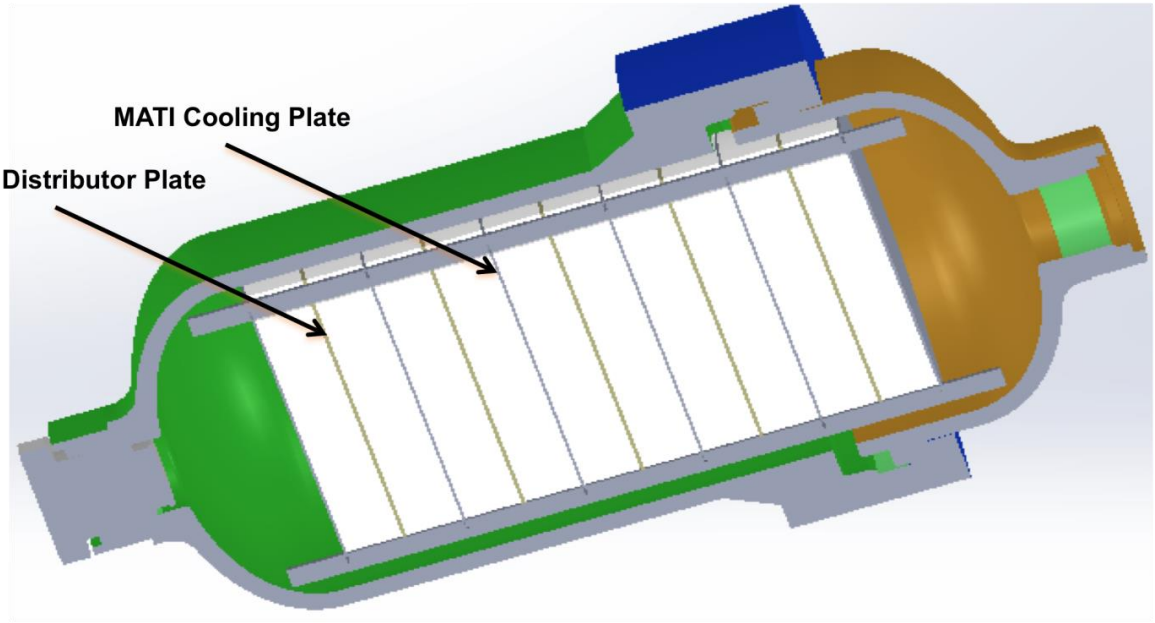

Figure 2: Representative MATI and compressed MOF-5 bed assembly inside of 2 L pressure vessel, shown without internal headers and inside original vessel design.

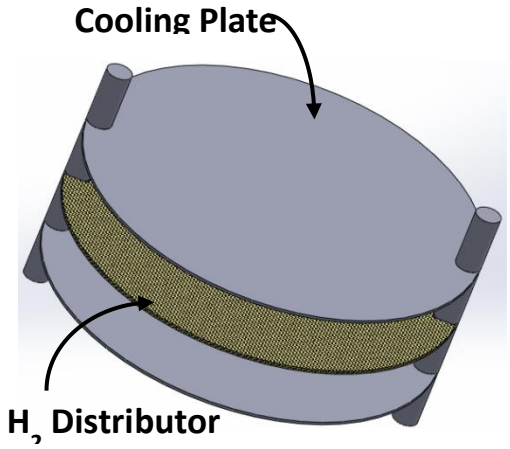

Figure 3: General representation of a single MATI stack

The fully constructed Phase III prototype was designed to store 54 g of H_2 between the adsorbed gas in the MOF-5 bed and compressed within the void space of the 2 L tank. The designed system gravimetric density was 0.10 g total H_2 per gram of MOF-5 and a volumetric density of 27 g total H_2 per L of tank.

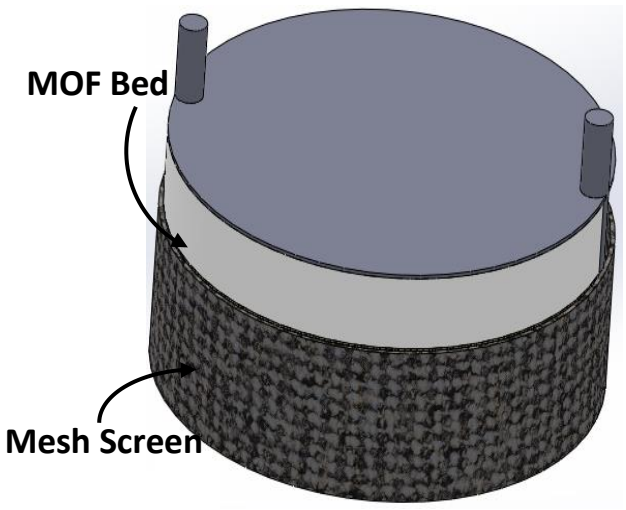

Figure 4: General construction of single MATI stack wrapped with mesh screen.

The Phase III prototype system will be used to validate the mathematical model created to represent the experimental system used throughout the Phase III investigation. Model validation will be completed using experimental data collected at SRNL. The data used to validate the model will consist of LN2 coolant mass flow, H_2 flow rate, system pressure, and temperature data collected during the charging/discharging trials. Inside the pressure vessel, temperature data will be collected at various locations along the inside wall of the pressure vessel, the outside of each MOF-5 half-bed, and inside each MOF-5 half-bed. In addition, one single MOF-5 bed will be additionally instrumented with thermocouples and the outside surface of a coolant plate, as depicted in Figure 5.

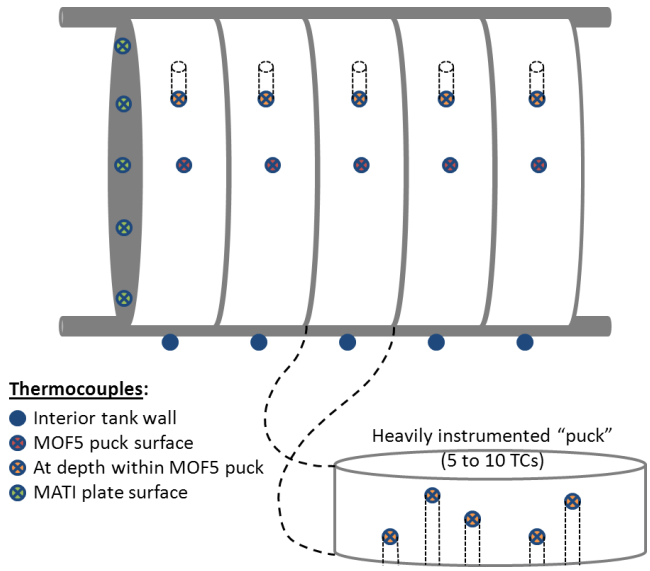

Figure 5: Representation of the proposed thermocouple installation throughout the MOF-5 beds and pressure vessel.

The Phase III MATI prototype design for the 2L aluminum pressure vessel was finalized and presented at the adsorption team meeting in mid-November 2013. The MATI assembly (except the PEEK ring shown in Fig. 6) has no physical contact with the housing interior wall, minimizing any possible heat leakage between MATI and tank. The assembly was attached to the big (2 inches) plug through Swagelok fittings as shown in Fig. 6. Key features of the phase 3 MATI include:

- LN2 in and out from the big plug
- H2 enters from the small plug
- Thermocouples feed in through the big plug
- 5 LN2 cooling plates with brazed ¼" tube headers
- 8 bed layers (two half beds/layer)
- H2 distribution plate/disc springs between two bed layers – take component tolerance and thermal expansion while help maintain better thermal contact
- Screen to wrap around the MATI to contain MOF
- PEEK ring at the end of tube header to provide additional structures support/thermal isolation between MATI and tank
- The two holes in the PEEK (CTE close to Al and SS) ring allow the header tubes to slide in and out to compensate thermal expansion
- During transportation thin shock absorbing foam can be inserted between MATI and tank

The MATI prototype is 10 cm in diameter and approximately 16.3 cm tall (including the header tubing and PEEK supporting ring). Details of the H2 distribution plate, cooling plate header and puck designs will be described in the following sections.

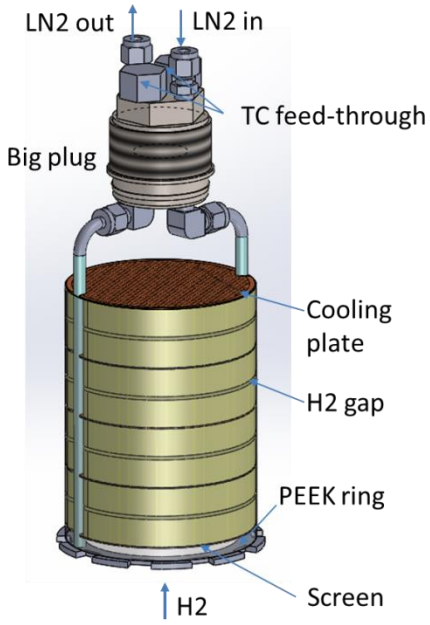

Figure 6: MATI assembly with components callout

Key Findings: *Key findings from Task 3.1.1 include: The overall design of the 2 liter prototype MATI was successfully completed and peer reviewed by other center members. All suggested modifications were included in the design.*

Subtask 3.1.2 Cooling Plate Design – The separate effects heat transfer experiments and simulations during phase 2 led to a verified simulation which could help us to characterize the cooling plate with acceptable accuracy. The verification was performed by doing LN_2 single phase convective heat transfer tests through the initial generation of stainless steel MATI microchannel heat sinks. At the end of Phase 2, a set of single phase experimental tests could be predicted with using our cooling plate CFD simulation using within following errors reported in Table 1.

Table 1. Mean average error between experimental and CFD simulations for single phase flow through the MATI heat sink

Mean Average Error (MAE) at q"=17600 (W/m^2)	**h_{num} vs. h_{exp}**	**ΔP_{num} vs. ΔP_{ex}**
	7.1%	**5.2%**

The velocity contours inside the heat sink are depicted in Fig.7a for one of the experiments performed at a mass flow rate of 3 g/s and an input heat flux of 17450 W/m^2. It is clear that a significantly higher velocity exists in the outer regions of the heat sink within the flow distribution ring formed by the tabs. Relatively higher velocity is also observed near the centerline, where flow from the tabbed outer region enters the pin fin region. Barring the center region, the velocity is nearly constant within the pin fin portion of the heat sink. Figure 7b presents contour maps of the local heated wall temperature. Commensurate with the larger fluid velocity in the outer regions formed by the tabs, the temperatures in these locations is also lower as well as the centerline region.

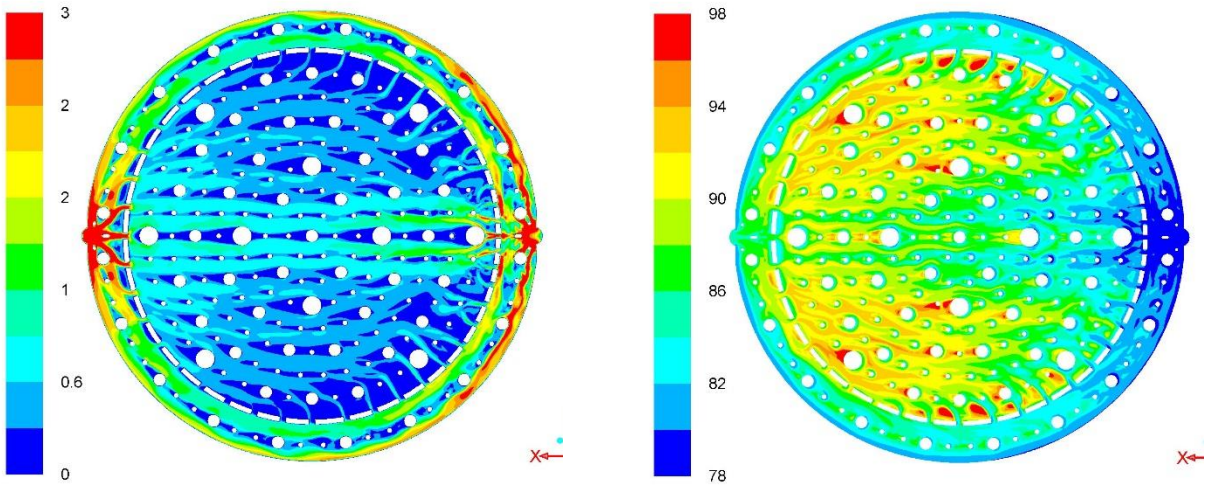

(a) (b)

Figure 7. Contour maps of velocity magnitude (a) and wall temperature (b) within the heat sink for a mass flow rate of 3 g/s and an applied heat flux to the bottom wall of 17450 W/m^2.

From the simulation results, it is clear that this heat sink design can benefit from further optimization to permit a more uniform flow, and hence temperature distribution. The Phase 2 MATI cooling plate design in Fig. 7 was developed with three different pin sizes. The largest pin size permitted placement of thermocouples through the heat sink and into the adsorbent bed to monitor temperature changes during adsorption or desorption. The mid-sized pins originally served the purpose of hydrogen distribution. Currently we perform the hydrogen distribution function in the hydrogen distribution plate which is located between two cooling plates. In phase 3, we instrumented the bed from the sides rather than through the cooling plate. Hence, a new cooling plate design needed to be developed to ensure uniform flow distribution.

The first step in redesigning the cooling plate was to generate design concepts that key design met constraints. The constraints include the following:

(a) The design should be able to withstand an external compressive pressure of 150 bar and an internal pressure of 5 bar.
(b) The design should be such that uniform flow distribution is achieved. This aspect will be considered satisfied using flow visualization experiments.
(c) The design should result in a low pressure drop across the cooling plate.
(d) The design should meet all the fabrication constraints associated with chemical etching and diffusion bonding.

A systematic design study was pursued beginning with identification of the possible pin geometries for the cooling plate. The designs included different pin fin parameters-pin spacing, pin fin size and the unit cell arrangement. During the selection of the possible geometries to be analyzed, fabrication constraints were considered. Next, a stress analysis of the identified unit set of pin geometries was performed. The outcome of this stress analysis would result in providing upper bounds on the pin spacing and lower bound on the pin diameter to ensure adequate bonding. Once designs that satisfy the stress requirements were down-selected, CFD simulations were performed to select the designs that have the lowest pressure drop.

Initial CFD simulations were performed to identify whether more uniform flow distribution can be achieved than that observed in the design in Fig. 7. The original design resulted in the following temperature contour maps, shown in Fig. 8. Figure 9 shows the velocity contours of four evaluated designs under the same flow conditions.

Area averaged temperature together with the highest observed temperature of each design in Figs. 8 and 9 are listed in Table 2. As seen from the Table, there is a about a 2.7 degree reduction in average wall temperature and in excess of an 11 degree decrease in peak wall temperature in the designs shown in Fig. 7 when compared with the original design.

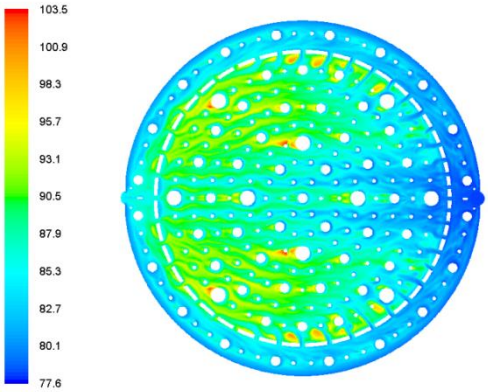

Figure 8. Contour maps of wall temperature within the original design of heat sink for a mass flow rate of 3.4 g/s and an applied heat flux to the bottom wall of 18530 W/m^2 with system pressure of 650 kPa.

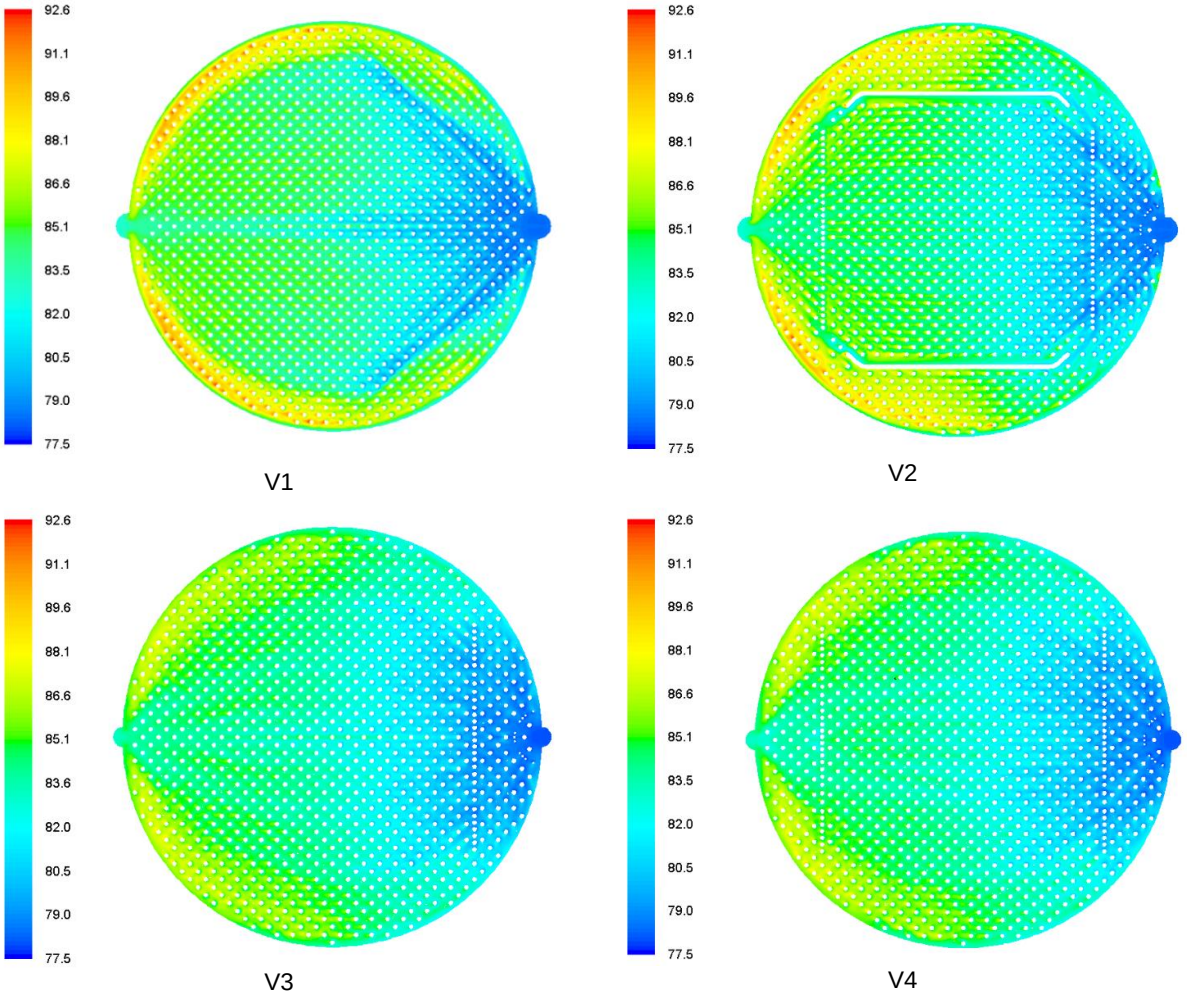

Figure 9. Contour maps of wall temperature within the different new design of heat sink for the same flow conditions as simulated in original design (Fig. 2).

Table 2. Comparison of the peak and average wall temperatures for the original and four new designs of cooling plates. The mass flow rate and applied heat flux is identical for all cooling plates.

Design model	Hot spot T_{max} (K)	Area averaged wall temperature (K)
Original	103.50	86.03
V1	92.61	83.86
V2	92.42	83.84
V3	89.26	83.27
V4	90.18	83.22

Based on the table 2 results, twelve possible cooling plate designs were identified with respect to fabrication constraints. These designs included two pin fin size variations, three different pin fin spacing, and two unit cell arrangements. Figure 10 is depicting two distinct pin fin pattern layouts depending on the direction of the flow. In Fig. 1a, the pins are in a staggered arrangement when the flow direction is horizontal and in-line when the flow direction is vertical. Similarly, in Fig. 1b, the pins are in a staggered arrangement when the flow direction is horizontal and in an in-line arrangement when the flow direction is at 45 degrees to the horizontal.

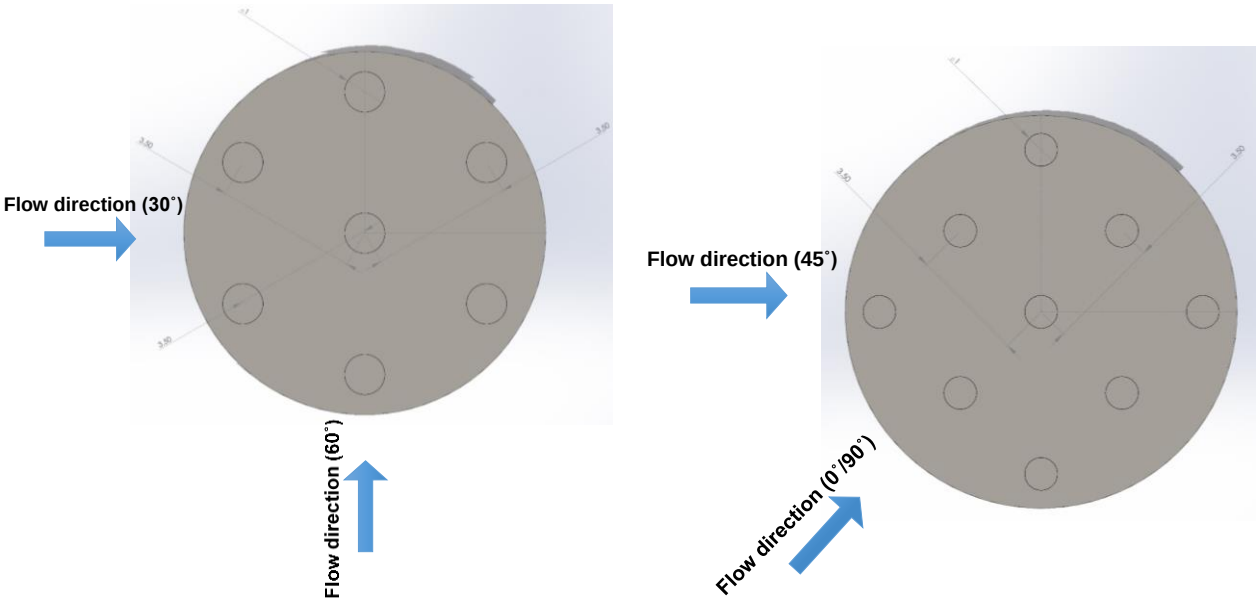

Figure 10. Different studied pattern layouts of a unit cell (a) 0˚/45˚/90˚ (b) 30˚/60˚

Table 3 is summarizing variable parameters values for studied designs. As first step, stress analysis under aforementioned working pressures were performed on a unit cell

using Ansys Mechanical V14.5. Solutions for equivalent (Von-Mises) stress and total deformation for each unit cell under two different boundary conditions (one with external pressure alone and the second with internal pressure alone) are presented.

Table 3. Unit cell design parameters values

Design #	Pin size (μm)	Pattern layout	Pin spacing/pitch (mm)
1	1000	45˚ with horizontal (0˚/90 ˚)	2
2			2.5
3			3.5
4		60˚ with horizontal (30˚)	2
5			2.5
6			3.5
7	500	45˚ with horizontal (0˚/90 ˚)	1
8			1.5
9			2
10		60˚ with horizontal (30˚)	1
11			1.5
12			2

In first mode, as is shown in Fig. 11a, 100 bar pressure (equivalent to 10 MPa) imposed on external surfaces of unit cells (top and bottom) while atmospheric pressure existed on internal surfaces. Large spacing between adjacent pins will result in high stress and deformation near the middle zone and may cause channel clogging. On the other hand, small spacing leads higher pressure drop. In mode two, as shown in Fig. 11b, the external pressure was set at atmospheric condition and internal pressure was increased to 35 bar (~3.5 MPa) on internal surfaces, marked in red. In this mode both pin fin size and pitch are dominant factors.

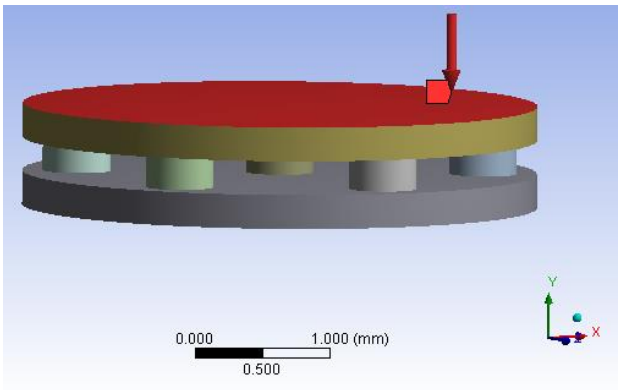

(a) Mode 1: External 10 MPa, Internal 0.1 MPa

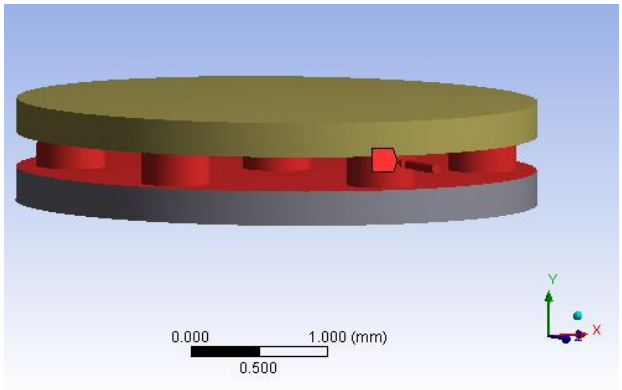

(b) Mode 2: External 0.1 MPa, Internal 3.5 MPa

Figure 11. Surfaces affected by high pressure boundary condition marked in red

To assess the accuracy of numerical results, grid independence was evaluated by repeating a simulation with 4 different grid resolutions ranging from 0.24 to 1 million cells. Comparing to the results using 1 million cells with that obtained using 0.25 million cells, the maximum deviations about 1.6% and 0.8% observed respectively for maximum stress and deformation. Hence, cells in the in range of 0.25 to 0.3 million cells used for all FEA simulations.

The outcome of this stress analysis resulted in providing an upper bound on the pin spacing and lower bound on the pin diameter to ensure adequate bonding. Figure 12 shows the maximum stress on areas of interest under both modes of boundary conditions for design number 11.

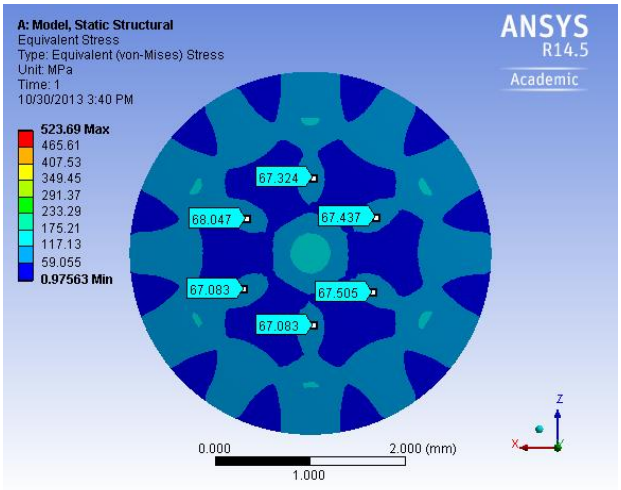

(a) Mode 1: External 10 MPa, Internal 0.1 MPa

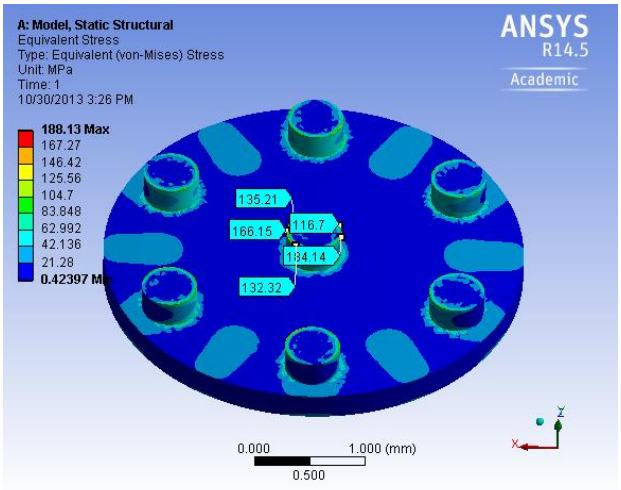

(b) Mode 2: External 0.1 MPa, Internal 3.5 MPa

Figure 12. Maximum stress for a unit cell with 500μm pin size, 30˚/60˚ pattern layout, and 1.5mm pitch (Design #11)

Maximum equivalent stress and total deformation values for all designs are listed in Table 4. For each design, two factors of safety are calculated corresponding to two yield stress numbers associated with room and liquid nitrogen temperatures. Stainless steel 316 will be used as MATI cooling plate substrate. Designs which are marked in yellow were down-selected because they satisfied the stress requirements with reasonable safety factor margin.

The two down-selected unit cell designs were applied over the 10 cm diameter cooling plate. CFD simulations were performed on these designs to compare flow distribution and pressure drop. The fluid flow conditions such as mass flow rate, heat flux, and system pressure were defined according to the operational conditions that MATI prototype would have based on 3 minutes charging time. A concept which helped better flow distribution, resulted from CFD simulations examined in last quarter, was implemented in these selected designs. The concept has two flow distribution locations. The first location is close to the inlet and consists of number of pins located with

variable spacing normal to the flow direction. The second location is in the middle of cooling plate.

Table 4. Safety factor numbers obtained for pin fin design unit cells

Design		Max stress (MPa)		Max deformation (μm)		Yield Stress of SS316 (MPa)		Factor of Safety			
								77 K		273.15 K	
#	Spec	M 1	M2	M 1	M2	77 K	273.15 K	M 1	M2	M 1	M2
1	1000μm, 45˚, 2mm	115	118.9	1.1	0.4	551	276	4.8	4.6	2.4	2.3
2	1000μm, 45˚, 2.5mm	208.8	225.7	3.3	1.1			2.6	2.4	1.3	1.2
3	1000μm, 45˚, 3.5mm	450.4	840.8	14.7	5.2			1.2	0.7	0.6	0.3
4	1000μm, 60˚, 2mm	75.2	92.7	0.6	0.2			7.3	5.9	3.7	3.0
5	1000μm, 60˚, 2.5mm	140.2	186.3	1.8	0.6			3.9	3.0	2.0	1.5
6	1000μm, 60˚, 3.5mm	345.6	521.9	10.2	3.5			1.6	1.1	0.8	0.5
7	500μm, 45˚, 1mm	23.9	44.6	0.1	0.03			23.1	12.4	11.5	6.2
8	500μm, 45˚, 1.5mm	79.5	163.8	0.6	0.2			6.9	3.4	3.5	1.7
9	500μm, 45˚, 2mm	165.2	370.1	2.4	0.8			3.3	1.5	1.7	0.7
10	500μm, 60˚, 1mm	19.9	51.7	0.1	0.03			27.7	10.7	13.9	5.3
11	500μm, 60˚, 1.5mm	68	184.1	0.6	0.2			8.1	3.0	4.1	1.5
12	500μm, 60˚, 2mm	133.2	401.4	1.9	0.6			4.1	1.4	2.1	0.7

The CFD model which was developed in phase 2 was based on laminar flow, because with the exception of the conditions at the inlet and exit, the flow throughout the heat sink remained under 2000. To make sure that the same was true for the current 10 cm cooling plate design, Reynolds number was calculated at several cross-sectional locations from inlet to the exit of the heat sink. The resulting Reynolds number ranged from 1100 to 1990 for 80% of length of channel. Also the heat balance of heat gain and input heat showed less than 1.5% deviation.

Area averaged temperature and highest observed temperature of each selected design along with fluid pressure drop are listed in Table 5. The inlet temperature was kept at 77.5 K, and the mass flow rate of liquid nitrogen was 6.9 g/s. A heat flux of 11,268 W/m^2

was applied to both sides of the heat sink. Based on the results in Table 5, design 11 was chosen since it exhibited the lowest peak wall temperature (See Figure 13).

Table 5. Fluid flow results in selected designs

Design model #	Hot spot T_{max} (K)	Area averaged wall temperature (K)	Pressure drop (kPa)
2	120	84	58.9
5	102.5	85.4	47.4
8	107	85	46.3
11	96.7	84.8	48.3

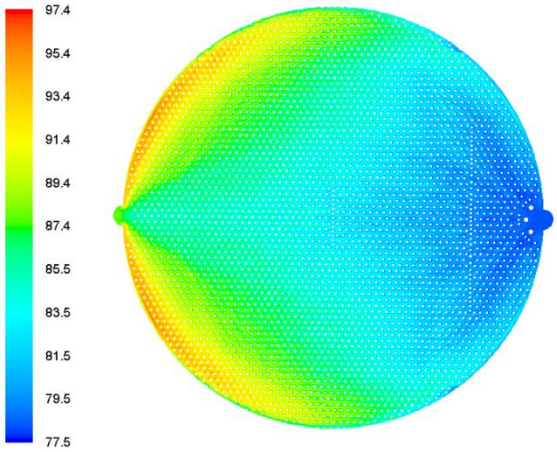

Figure 13. Contour maps of wall temperature within the design # 11 of heat sink for a mass flow rate of 6.9 g/s and an applied heat flux to top and bottom of 11268 W/m^2

The finalized design was fabricated on 10 cm stainless steel 316 shims by chemical etching process by an external vendor. Figure 14 shows a photograph of the top and bottom etched plates.

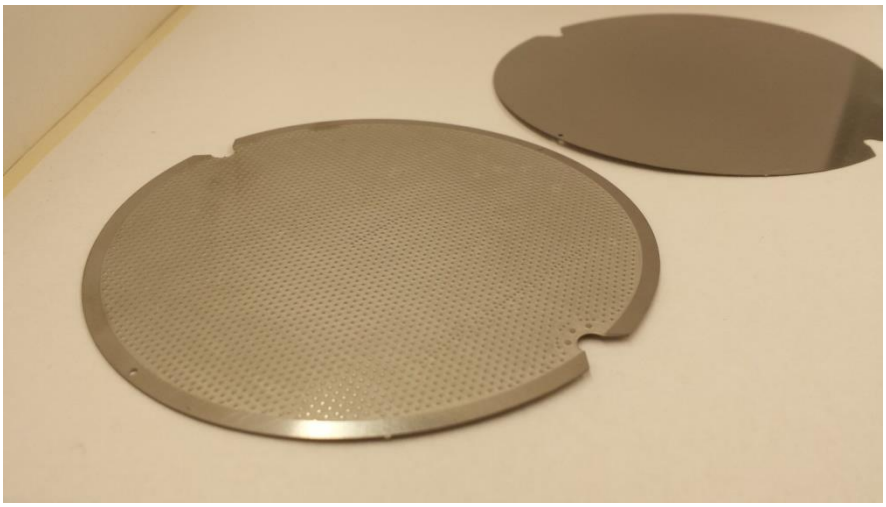

Figure 14. Fabricated MATI cooling plate

FEA and fluid flow simulations indicated that a pin fin size of 500µm in diameter, 250µm depth, 1.5mm diagonal spacing, and 60˚ pattern layout resulted in a reasonable factor of safety and flow distribution. Figure 15 is illustrating the finalized design which was fabricated on 10 cm stainless steel 316 shims by chemical etching process together with the diffusion bonded plates.

Figure 15: Fabricated MATI cooling plate

The chemically etched plates before being diffusion bonded were scanned by an optical surface profiler (Zygo 3D) to ensure that the etched pin fin dimensions corresponded with the design dimensions. Figure 16 shows the measured center to center distance between two adjacent pin fins to be 1.503 mm while the design dimension was 1.5 mm. The measured pin fin diameters showed above are in the range of 3 to 7% as a result of the etching process selected by the etching company. However noting that there was a reasonable margin on safety factor in the FEA simulations (FS was 4.1 and 1.5 for external 100 bar pressure and internal 35 bar pressure respectively), this variation was deemed tolerable.

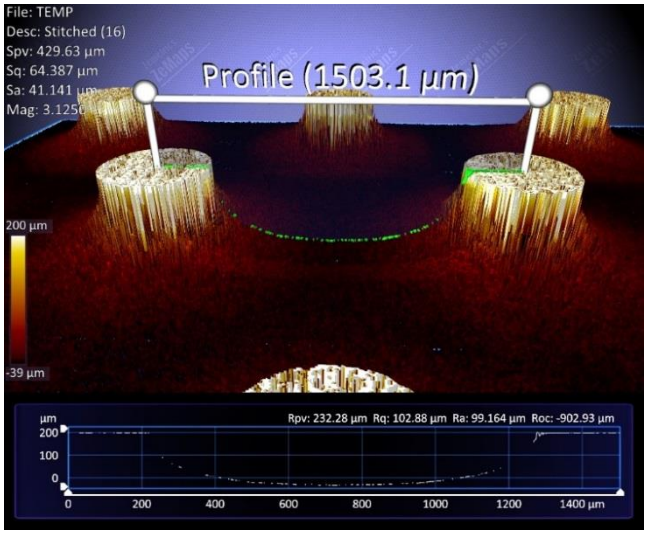

Figure 16: surface profile of the etched plate

To experimentally test the strength of diffusion bonded heat sinks over the range of anticipated internal and external pressures, a pressure testing facility was designed and assembled. The pressure test chamber, as is shown in Fig. 17, includes an inner air-tight stainless steel container surrounded by an outer metal container to ensure the safety of operator while performing pressure test at up to 100 bar. The tubing lines and pressure control valves were assembled in such a manner that both internal and external pressure tests could be performed with the same apparatus.

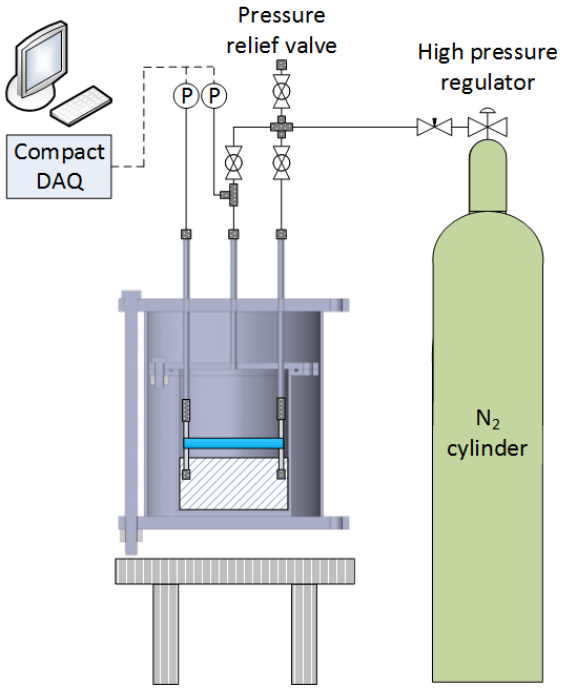

Figure 17: Schematic of designed pressure testing facility

Two ¼ in. stainless steel tubes were brazed to the heat sink. Before starting the pressure testing the surface of the bonded heat sink was characterized by the 3D surface profiler to have a reference on the surface evenness of the heat sink. Then the heat sink was assembled to the inlet and outlet lines and encapsulated into the inner chamber. Figure 18 shows the assembled pressure testing facility and cooling plate with brazed tubes. As the first step, a 100 bar external pressure test was performed while the inside of heat sink was at atmospheric pressure. Two absolute pressure transducers were used to track the chamber pressure (external pressure on the heat sink) and the heat sink internal pressure to make sure that there wasn't any leak from the external side to within the heat sink. While making sure that the system was leak free, the heat sink was kept in 100 bar external pressure environment for more than 20 minutes (Fig. 19). Then a second surface profilometery scan was performed and compared with the reference surface evenness for detecting any potential deformation. The internal pressure test was carried out in the same manner while the initial chamber pressure was set to atmospheric condition. The heat sink internal pressure was raised up to 35 bar and released after 20 minutes. The observed pressure change during the tests and

profilometery scan comparison on the surface of plate before and after each pressure test, showed neither leakage nor deformation.

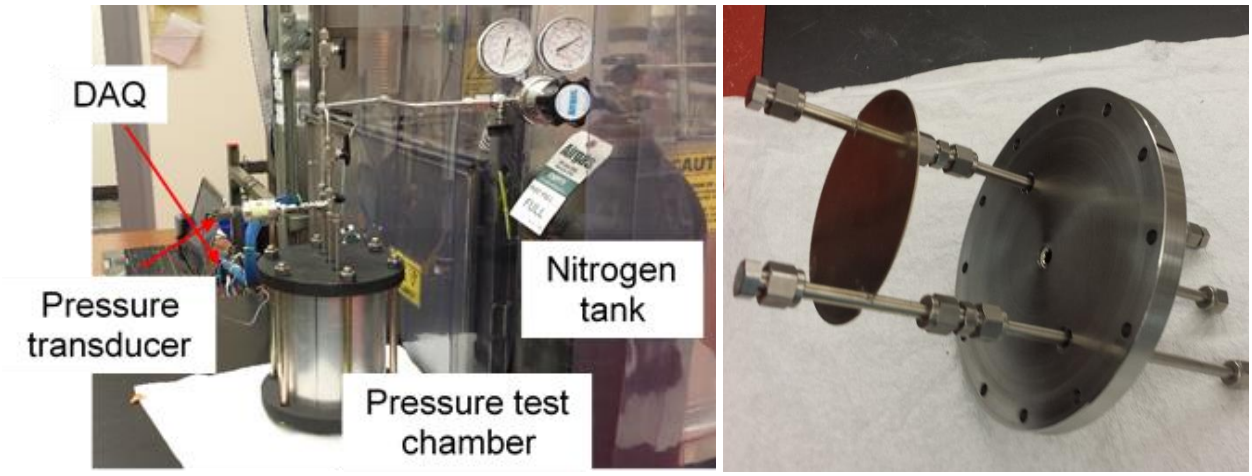

Figure 18: Pressure testing facility and tested MATI cooling plate

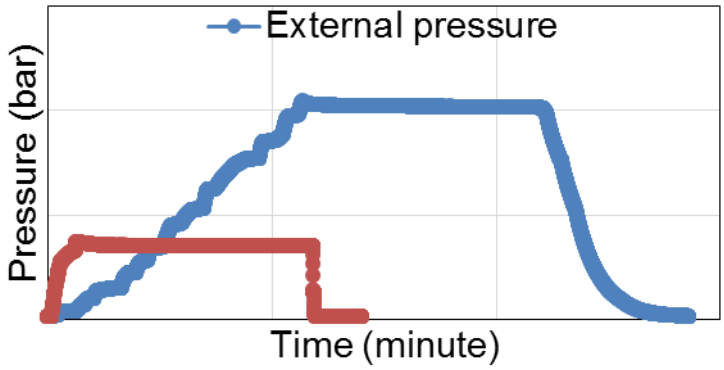

Figure 19: System pressure against time

As the next step in heat sink design validation, an experimental facility for testing uniformity of flow distribution was designed and assembled. Uniform heat flux was applied to the bottom of MATI heat sink while having the DI-water flow through the microchannel as a coolant. The top surface of the MATI was coated with flat black paint to increase emissivity. Using an IR camera, contour maps of the heat sink top surface temperature were recorded. This local temperature distribution could be compared qualitatively with the CFD simulations to observe the variations in contours.

In order to have uniform heat flux supplied to the entire of MATI heat sink bottom surface and also to be able to quantify it, a heat flux meter was designed and built (Fig. 20a). The platform dimensions of the heat flux meter were identical to that of heat sink. The height of flux meter had to be sufficient to achieve 1D conduction. To design the height of the fluxmeter, a heat conduction simulation was performed in Ansys Fluent. Figure 20b is depicting the temperature contours on the design of heat flux meter

verifying 1D heat conduction while each of five inch-long cartridge heaters embedded into its bottom were generating 19 W.

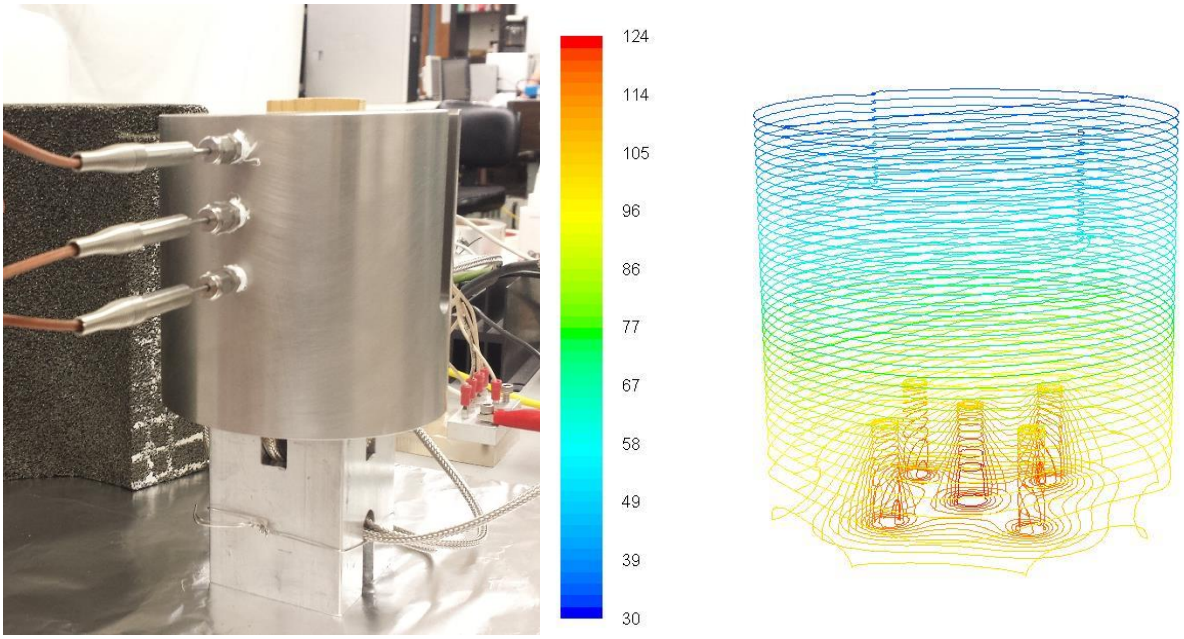

(a) (b)

Figure 20: a) Fabricated heat flux meter (HFM) mounted by thermocouples b) Temperature (°C) contours on the design of HFM showing 1D heat conduction, 19 W per cartridge heater

Heaters each with 100W power capacity were connected in parallel and powered by a variable DC power supply. The heat flux meter had three holes 20mm apart to determine the temperature gradient and hence the one-dimensional heat flux. The heat flux meter body material was machined out of stainless steel 316 with a certified alloy composition, so that thermal conductivity values estimated by Engineering Equation Solver (EES, Fchart Inc.) based on the average body temperature at each measuring section could be applied for precise heat flux measurement. The input heat flux to the heat sink was calculated by using Fourier's law for 1D heat conduction, based on the temperature readings of the upper two thermocouples embedded into the body of heat flux meter.

$$q" = k_{HFM} \frac{\Delta T_{tc}}{\Delta z}$$

In an initial experiment with average heat flux of 8600 W/m^2, the obtained heat flux from two bottom thermocouples showed less than 6% deviation from that calculated based on the upper two thermocouples.

The process of brazing the stainless steel tubes to the MATI could potentially cause channel intel/outlet port clogging. As a reference case to be used for examining the quality of heat sink's brazing, there was a need for a MATI heat sink connected to the fluid supply by another means that did not have any risk of clogging. The pressure drop

in certain flow rate through this test article could then be used as a baseline to evaluate other brazed cooling plates. Those brazed MATI heat sinks that showed similar pressure drop and temperature distribution as this baseline case would be used for making the final prototype. If one brazed tube MATI heat sink showed higher pressure drop, it could be interpreted as a defective heat sink and not used in the MATI assembly.

In order to make such a baseline test article with both ports fully open, two miniature plena were fabricated and adhered with J-B Weld epoxy to the sides of a MATI heat sink. Figure 21 is showing the CAD assembly of the design and the fabricated plenums mounted on the cooling plate. As indicated in Fig. 9, the top 1/8” tubes took the fluid into and out of the heat sink while the two on the bottom were used for pressure drop measurements along the cooling plate.

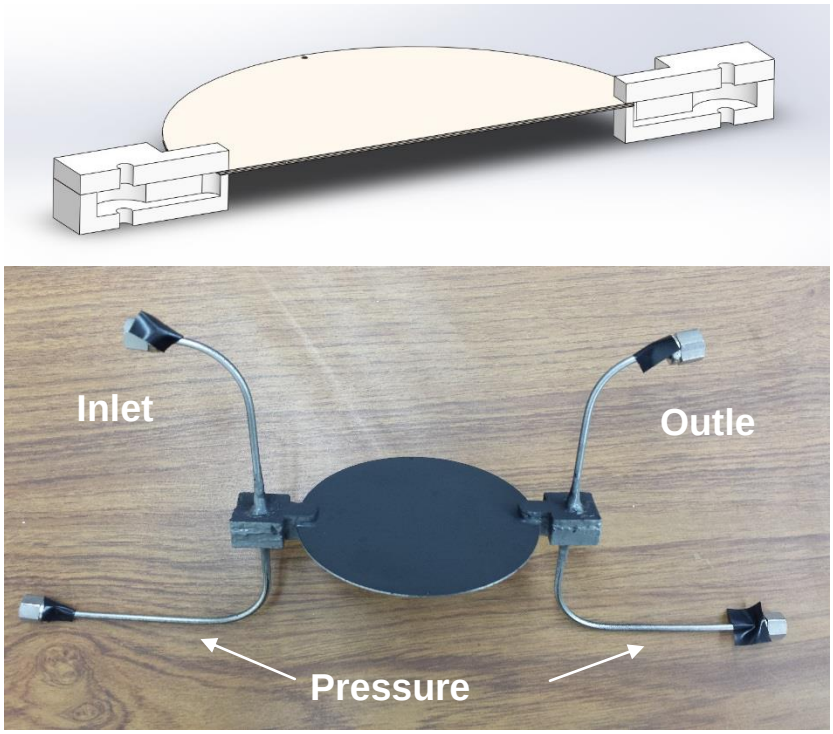

Figure 21: Miniature plena adhered to the MATI cooling plate

In order to reduce the thermal resistance between bottom surface of heat sink and top surface of heat flux meter, adequate amount of high temperature copper paste was applied. To eliminate the heat loss from the side of heat flux meter and help to achieve 1D heat conduction, 1.5 inch thick pre-formed cylindrical foam insulation was used. Appropriate holes and channels were carved into the insulation for guiding in and out the thermocouples and tubing lines through the insulation.

DI was pumped through the heat sink from a 4L reservoir by a peristaltic pump. The flow rate was measured with a Coriolis flow meter. The water flow then was passed through MATI heat sink, and after measuring inlet and outlet fluid temperatures and

pressure drop between two plenums, was drained into a collection tank. The pressure drop was measured using a handheld NIST-traceable pressure calibrator (Omega PCL-1B) with a plug in DP module rated to 508 cm of H2O (~49.8 kPa). All thermocouples used in the experiments were T-type SLE.

The experiment was initiated by flowing DI-water through the system in a fixed flow rate (0.85 g/s was used in this initial test). Electrical power was supplied to the five cartridge heaters to a level such that the fluid temperature difference measured by inlet and exit thermocouples was on the order of 15 ^{o}C (to reduce uncertainty in measurements). Steady state condition was determined by noting stable readings of heat flux meter body temperatures as well as fluid inlet and exit temperatures. Data on temperatures, pressure drop and mass flow rate were recorded at steady state.

Figure 22 shows the temperature distribution on the top surface of the MATI heat sink after reaching steady state together with CFD simulation of LN_2 flow reported in last quarterly report. The important test parameters are tabulated in table 6. The 18% heat loss was calculated by comparing the measured heat flux versus heat gain. The main reason of such significant heat loss was due to the uninsulated top surface of heat sink which was being imaged. Since the goal of the experiment was to characterize the flow and heat transfer distribution, heat loss from the top surface was not of concern. Furthermore, by using the upper heat sink surface temperature recorded by IR camera, one could correct for natural convective and radiative losses.

Although the heat flux and mass flow rate of flow distribution experiment was not matching to the simulation case, as is shown in Fig. 10, both contour maps are in good agreement. Based on these results and our confidence that the design resulted in acceptable flow distribution, this design was selected for the final MATI prototype.

Key Findings: *Key findings from Task 3.1.2 include: The redesign of the cooling plate resulted in nearly uniform flow distribution with improved thermal performance and mechanical strength necessary to accommodate both the required internal and external pressure.*

Subtask 3.1.3. Hydrogen Distribution Plate Design – As the MATI pucks (MOF5 beds) become bigger in diameter, it became more important to distribute H_2 evenly throughout the puck. The plan was to have H_2 flow radially inward from the circumference, and then enters the pucks axially. The H_2 distribution plate needed to be highly porous, adding as little flow resistance as possible and add little weight to the MATI.

Table 6: Flow distribution test parameters

$\dot{m}$ (g/s)	ΔP (kPa)	T_{in} (ºC)	T_{out} (ºC)	$q_{gain} = \dot{m}c_p\Delta T$ (W)	q'' (W/m^2)	Heat loss %	Ambient temperature (ºC)
0.85	5.8	28.7	44.4	55.6	8883	18	28.8

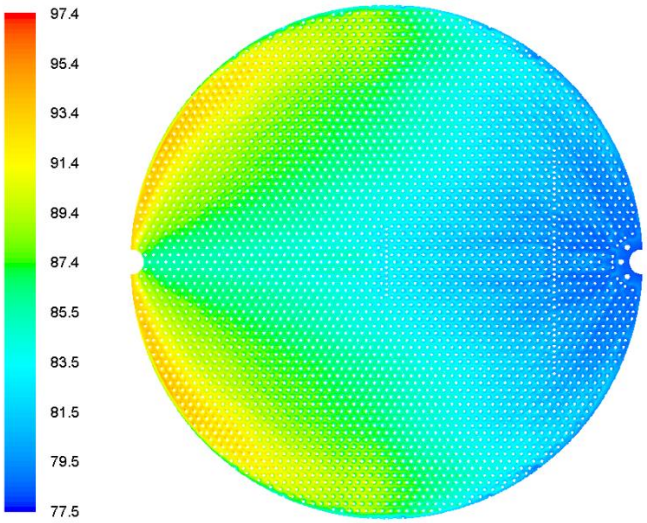

(a)

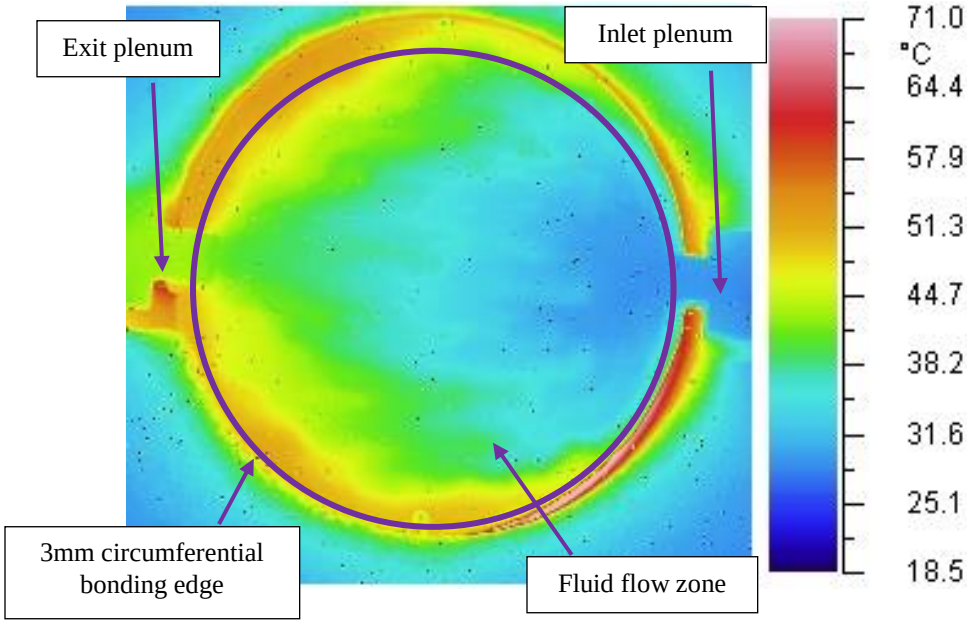

(b)

Figure 22: b) Contour maps of wall temperature for a LN2 mass flow rate of 6.9 g/s and an applied heat flux to both top and bottom walls of 11268 W/m^2 with system pressure of 8 bar. 10 million cells were used in this simulation. a) Contour maps of wall temperature for di-water flow through the fabricated MATI heat sink with test parameters listed in Table 1.

In evaluating the design options, several concepts were considered. Initially we focused on Dexmet expanded foil, corrugated & perforated plate and OSU micro pyramid truss network. However, the OSU team also evaluated some different concepts for the H_2 distribution plate. Using disc spring with low spring constant seemed to be a better solution than the dexmet foil. First, the disc springs created much open space for H_2 flow while adding little flow resistance and thus better flow distribution. Secondly, the light spring can adapt to any variability in puck dimensions and assembly imperfections making the assembly process easier. In addition, the disc springs put light pressure on

the half-pucks against the MATI cooling plates, creating better thermal contact between MOF beds and cooling plates. This was especially important when conduction enhanced pucks were used, where thermal contact resistance between pucks and cooling plates could play a role. Furthermore, the spring function of the disc/H_2 distribution plate could take some vibration loads during operation and transportation; potentially improve the puck's durability.

Fig. 23 shows an example of using three disc springs between the two half-pucks. During assembly of the half-pucks, the disc springs will be sandwiched between two half-pucks and compressed slightly before sliding them in between two MATI cooling plates.

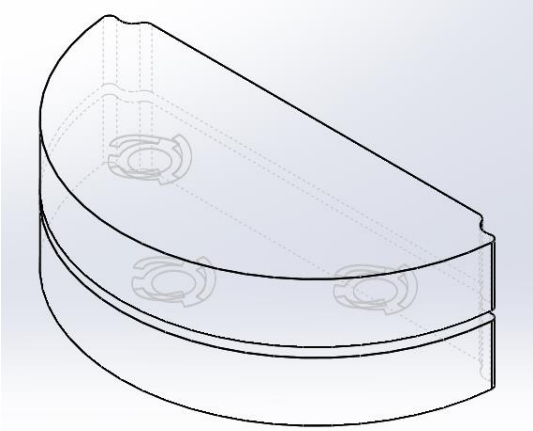

Figure 23: Example of disc spring/H2 distribution plate concept between two half-pucks

After receiving the half pucks from Ford, two half pucks were assembled between two plates with four disc springs separating them and creating the hydrogen passages. The springs created good amount of compression force between the plates and the half pucks. There were no sign of damage to the pucks due to compression. Fig.24 shows the assembly from two different angles.

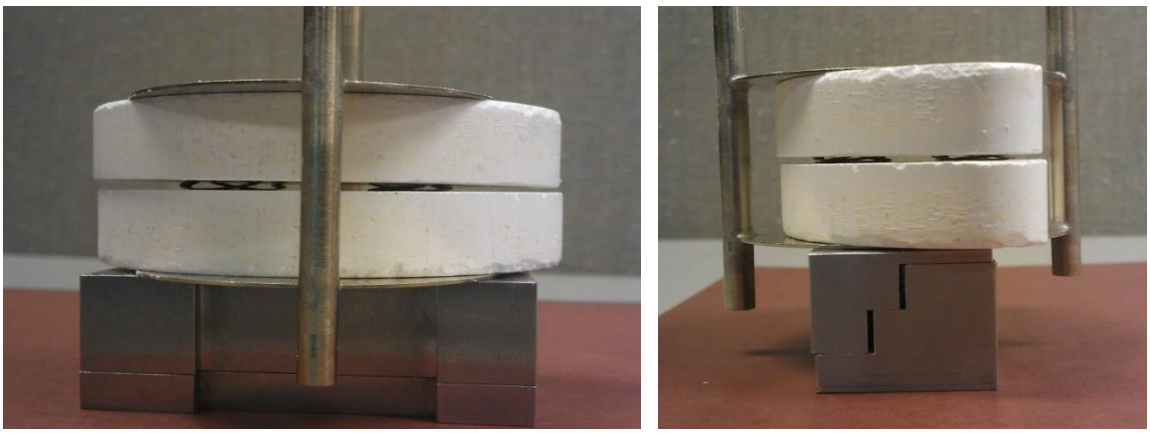

Figure 24: Plates and half pucks assembly with four disc springs in between half-pucks

Key Findings: *Key findings from Task 3.1.3 include: The use of flat springs as the hydrogen distribution system was a significant innovation which 1) created a low pressure drop flow passage for hydrogen, 2) allow assembly using pucks with some dimensional variation and 3) provided for good contact between the cooling plates and the MOF-5 pucks,*

Subtask 3.1.4 Header Design - Two MATI header designs were considered by the team. One leverages the past experience during Phase 2 that created high yield joints, which also potentially had higher H_2 storage capacity as the result of bigger pucks. A picture of the MATI with 3 cooling plates is shown Fig. 25. However, this created problem during assembly – a round puck cannot pass through the headers. As a potential solution, the shape of the pucks was modified as shown in Fig. 26.

An alternative header design moved the headers outside the cooling plate, as shown in Fig. 27. This allowed the shape of the puck to remain to be round. The down side of this approach was smaller puck size for a given tank, resulting in less H_2 storage.

Figure 25: MATI with 3 cooling plates

Figure 26: Puck Shape Options

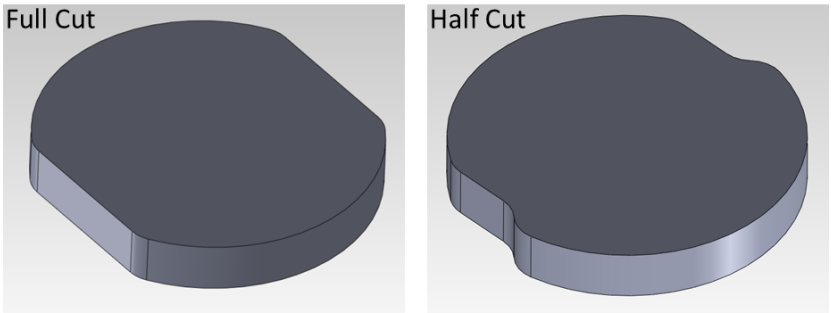

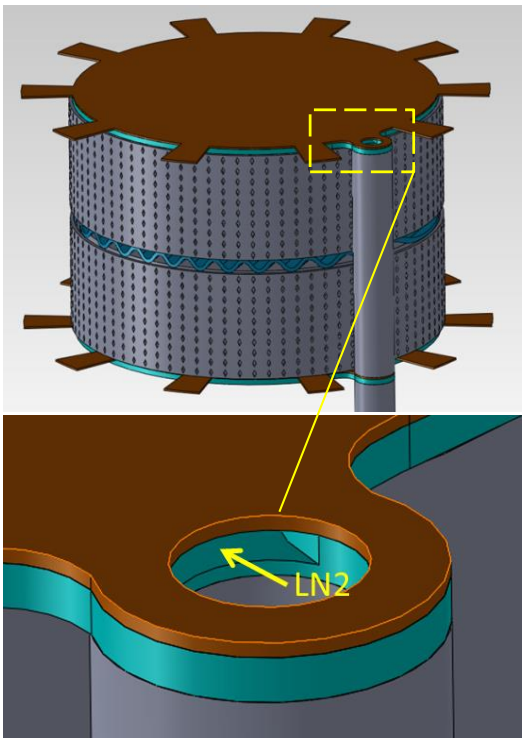

Figure 27: Alternative LN2 header design for phase 3 MATI

With input from other members of the Center, the team decided to change the single puck design to a two-half-puck design which made the bed assembly practical without significantly compromising H_2 storage capacity for a given MATI size design. As a result, the team decided to use the slotted header design which was used during phase 2 MATI development. The design of the slots closely matched the opening of the MATI cooling plates, in order to obtain a good brazing joint. A nickel-based brazing alloy from Lucas Milhaupt was selected to join the slotted tube headers and MATI cooling plates.

In order to confirm flow distribution and fluid pressure drop across the slotted openings for the increased LN_2 flows, a flow simulation of the slotted header design was conducted using CFD. The slotted header design and its flow simulation results are shown in Fig. 28.

Key Findings: *Key findings from Task 3.1.5 include: The use of the half puck concept allowed the use of a full size puck (not reducing the MOF-5 inventory in the storage system) while keeping the design of the headering system developed in Phase 2.*

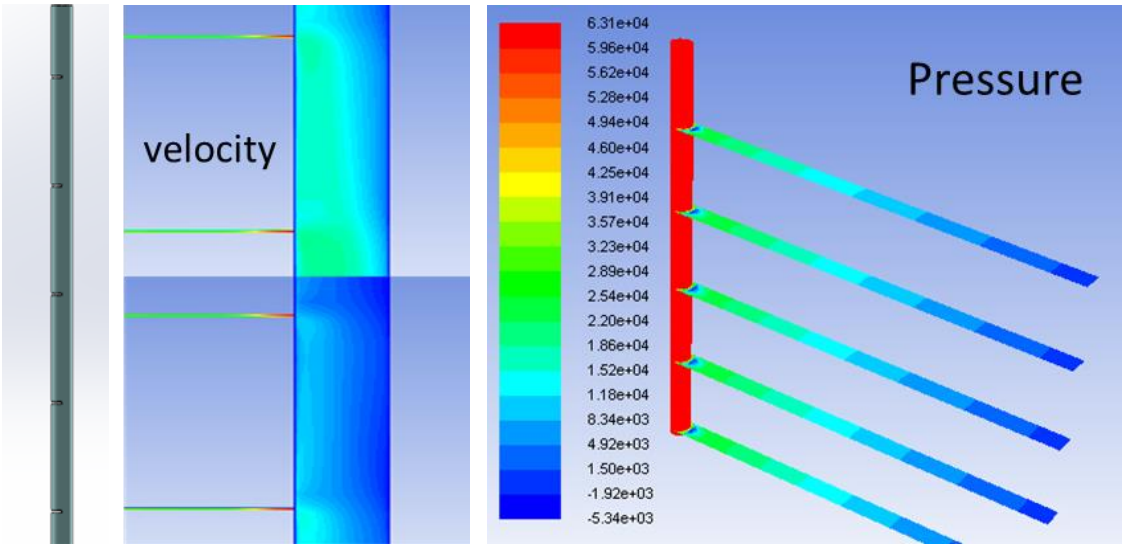

Figure 28: Slotted header and its flow simulation results

Subtask 3.1.5 Puck Design – There were a number of design decisions and factors that influence the design of the MATI puck. Two most important considerations were conduction enhancement and puck thickness. For the sake of model validation in Phase 3, the decision was made to not include any conduction enhancement in the pucks. This eliminated the complications associated with conduction enhancement, leading a simpler model for experimental validation. Midway through Phase 3, the decision was made to include a preliminary evaluation of conduction enhanced pucks and the later in this section we will describe the design of the conduction enhanced pucks and the results of the evaluation will be discussed in the experimental results section.

The next important design parameter was puck thickness. A series of adsorption simulations were conducted to evaluate the average bed temperature over 3-minute charge time. The model assumed 2D axisymmetric model geometry with constant temperature boundary conditions as shown in Fig. 29. The perimeter of the puck had adiabatic boundary condition. The bed was initially at 160 K and 5 bars in pressure. At the end of the 3-minute charge time, the bed pressure was increased to 60 bars. The puck had 10 cm diameter and its thickness was changed among 1, 1.5 and 2 cm. The preliminary result of the averaged bed temperatures are plotted in Figs. 30, given the cooling plate temperature was at 80 K.

As shown in the graph, all three-thickness beds cannot be cooled below 120 K. Thinner bed definitely had the advantage of lower averaged bed temperature, which was good for specific storage capacity. However, this could decrease both the volumetric and gravimetric H_2 storage capacities. In addition, thin MOF bed could pose challenges in manufacturing process and during testing and transportation.

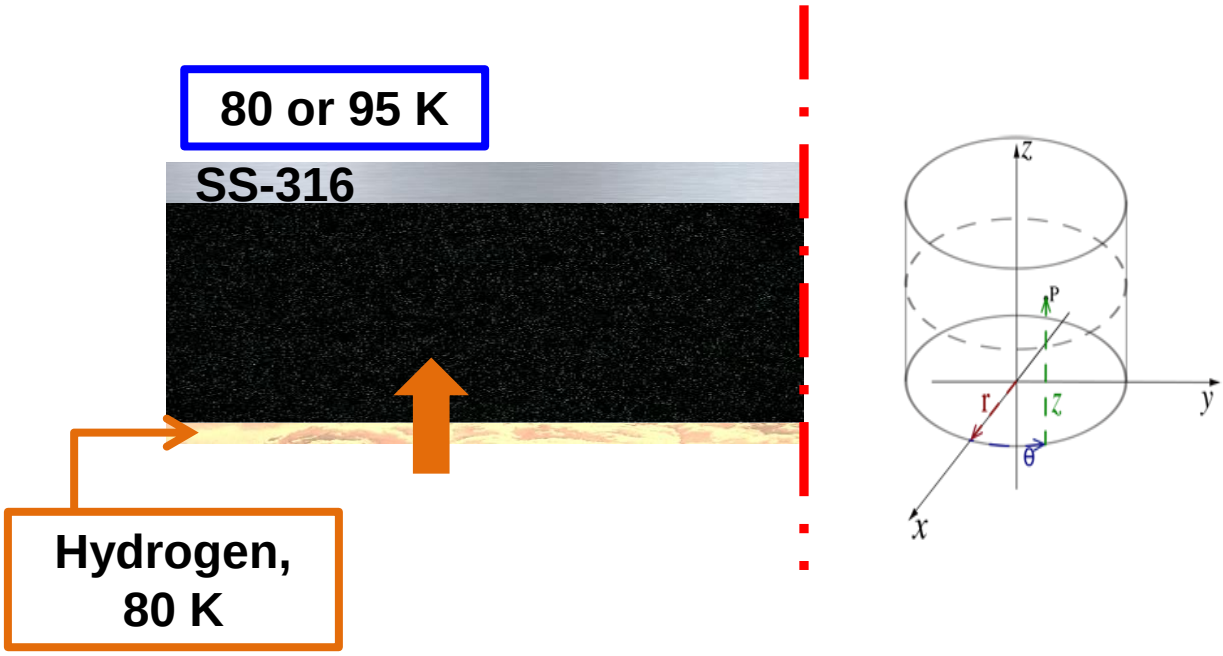

Figure 29: Comsol model for 3-minute adsorption cycle

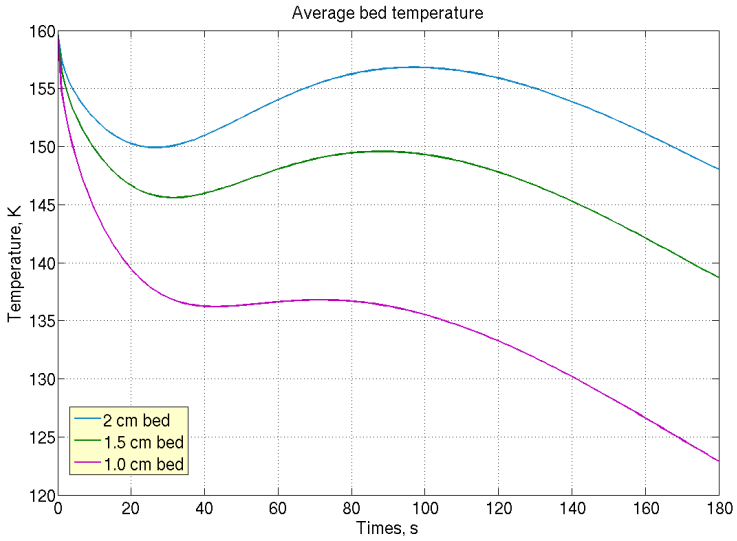

Figure 30: Modeling results of averaged bed temperature during adsorption

After taking into account the durability of puck design and preliminary adsorption simulations, the shape and dimensions of the puck were determined. The design of the half-puck and its relation to the header of the cooling plates is illustrated in Fig. 31. The tiny holes on top of the half-pucks represent the thermocouple holes for the two heavily instrumented half-pucks. The rounded edge design minimized stress concentrations while maintain as much MOF as possible for the sake of maximizing H_2 storage capacity. The diameter of the puck was 10 cm and its thickness is 1.5 cm. The bed density was expected to be slightly above 0.4 g/cc enhancing puck durability

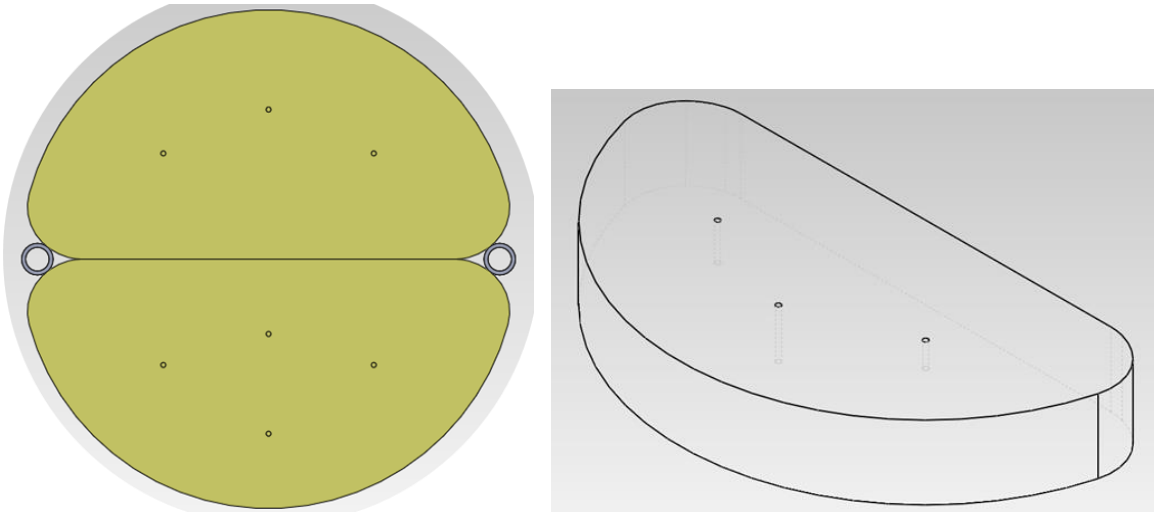

Figure 31: Half-puck assembly and half-puck with thermocouple holes

With the half puck design finalize, a die set was designed and machined at Ford. After the initial trial by Ford engineers to verify the compression process, six pucks were formed and delivered to OSU for further evaluation. The important characteristics and dimensions are defined in figure 32 and listed in Table 7, which show very precise and consistent dimensional control and reproducibility. The half pucks at density of 0.4 g/cc show better-than-expected durability. This was also confirmed by the compression test using four disc springs mentioned earlier.

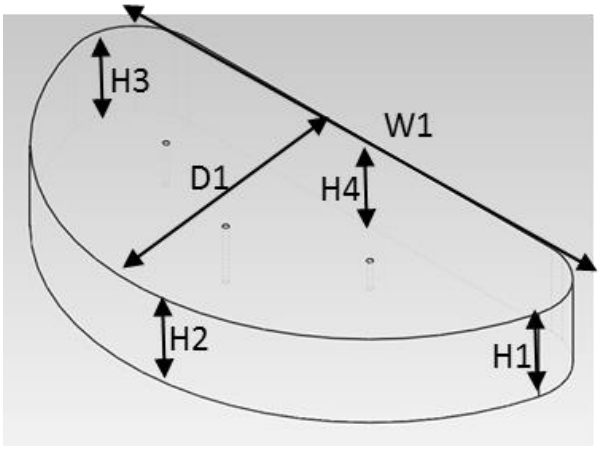

Figure 32: Half puck design with measured dimensions

Table 7: Half Puck Dimensions

	# of thermocouple holes	Weight (g)	Density (g/cc)	H1	H2	H3	H4	Avg Height	D1	W1
A	4	23.39	0.40	15.01	15.18	15.28	15.07	15.14	50.23	96.33
B	4	23.42	0.40	15.22	15.27	15.35	15.26	15.28	50.23	96.35
C	4	23.35	0.40	15.01	15.03	15.03	15.24	15.08	50.25	96.35
D	3	23.41	0.41	14.9	14.88	14.97	14.95	14.93	50.22	96.38
E	3	23.46	0.40	15.32	15.2	15.3	15.26	15.27	50.26	96.39
F	3	23.52	0.40	15.24	15.22	15.27	15.27	15.25	50.24	96.37

After the initial batch of six trial pucks were fabricated, Ford delivered another 34 half pucks. During transportation several of them broke into small pieces and few of them had edges worn off. After that Ford sent additional 10 half pucks which all were intact when they arrived at OSU. The following table shows the characteristics dimensions of the original 34 half pucks with very low standard deviations, indicating highly repeatable process over at Ford for making the pucks.

Table 8: Characteristics of MOF-5 Pucks

Puck ID No.	# of TC holes	Weight (g)	Density (g/cc)	H1 (mm)	H2 (mm)	H3 (mm)	H4 (mm)	Avg. Ht. (mm)	D1 (mm)	W1 (mm)
A	4	23.89	0.407	15.19	15.24	15.13	15.19	15.19	50.21	96.28
C2	4	23.82	0.403	15.24	15.19	15.21	15.50	15.29	50.19	96.13
D	3	23.90	0.407	15.25	15.13	15.16	15.21	15.19	50.17	96.13
F	3	23.84	0.406	15.18	15.16	15.27	15.19	15.20	50.16	96.11
2	1	23.85	0.406	15.28	15.15	15.20	15.19	15.21	50.16	96.10
3	1	23.85	0.404	15.18	15.25	15.29	15.30	15.26	50.17	96.14
4	1	23.88	0.406	15.21	15.12	15.17	15.28	15.20	50.17	96.18
5	1	23.87	0.406	15.16	15.11	15.27	15.24	15.20	50.19	96.19
6	1	23.78	0.403	15.23	15.25	15.34	15.29	15.28	50.21	96.23
7	1	23.73	0.405	15.10	15.12	15.16	15.17	15.14	50.24	96.22
11	1	23.74	0.406	15.05	15.06	15.18	15.22	15.13	50.18	96.17
12	1	23.66	0.405	14.97	15.02	15.23	15.22	15.11	50.22	96.21
13	1	23.71	0.404	15.17	15.10	15.21	15.25	15.18	50.15	96.18
14	1	23.73	0.404	15.10	15.17	15.27	15.20	15.19	50.19	96.19
16	1	23.76	0.404	15.18	15.27	15.20	15.21	15.22	50.24	96.19

17	1	23.76	0.405	15.11	15.06	15.25	15.26	15.17	50.20	96.19
18	1	23.69	0.403	15.28	15.11	15.18	15.25	15.21	50.20	96.19
19	1	23.70	0.405	15.05	15.10	15.17	15.21	15.13	50.19	96.16
20	1	23.73	0.403	15.17	15.17	15.27	15.25	15.22	50.21	96.22
21	1	23.72	0.403	15.22	15.21	15.22	15.19	15.21	50.20	96.21
22	1	23.74	0.405	15.10	15.15	15.23	15.22	15.18	50.15	96.16
23	1	23.66	0.401	15.24	15.20	15.28	15.30	15.26	50.26	96.22
24	1	23.73	0.403	15.12	15.25	15.26	15.25	15.22	50.22	96.21
25	1	23.71	0.404	15.15	15.13	15.21	15.27	15.19	50.22	96.2
28	1	23.67	0.405	15.01	15.12	15.14	15.21	15.12	50.19	96.17
31	1	23.73	0.404	15.20	15.14	15.19	15.20	15.18	50.22	96.18
32	1	23.76	0.405	15.14	15.11	15.20	15.23	15.17	50.23	96.19
35	1	23.73	0.404	15.19	15.11	15.23	15.25	15.20	50.17	96.2
37	1	23.71	0.403	15.12	15.15	15.27	15.26	15.20	50.18	96.19
39	1	23.72	0.405	15.16	15.06	15.19	15.23	15.16	50.23	96.18
42	1	23.76	0.406	15.10	15.00	15.20	15.22	15.13	50.22	96.15
43	1	23.80	0.407	15.08	15.04	15.24	15.19	15.14	50.19	96.2
44	1	23.74	0.405	15.11	15.04	15.24	15.18	15.14	50.21	96.2
45	1	23.74	0.406	15.02	15.07	15.18	15.21	15.12	50.23	96.18
	Average	23.76	0.405	15.15	15.13	15.22	15.24	15.18	50.20	96.18
	Standard Deviation	0.07	0.001	0.08	0.07	0.05	0.06	0.04	0.03	0.03

Following the completion of puck fabrication for performance testing, OSU initiated discussions with Ford and University of Michigan on conduction enhancement. OSU provided the design of pin-based conduction enhancements test articles to Ford, which includes both the aluminum pin array design and location of the thermocouples in the pucks. Ford then compressed MOF around the pin-based conduction enhancement to form the enhanced pucks. Due to a thin base plate for mounting the aluminum pins, the thickness (bed height) of the enhanced pucks was slightly less than 15 mm (the thickness of pucks without the plate). This also required Ford to make a few thinner pucks without the plate. The current design of the test article with reduced bed height is shown in Fig. 33. The pins are 1.6 mm in diameter and the spacing between pins was 10 mm, which is based on previous simulations. The pins were roughly 12 mm long extending the MOF bed.

In addition, Ford and University of Michigan developed means to incorporate ENG into the pucks along with aluminum pins. The idea is to enhance transverse thermal conductivity of the bed, thus minimizing the required pin density and reducing size and weight. Ten test articles with aluminum pins, shown in Fig.34 below, were sent to Ford as part of assembling the conduction enhancement pucks. Six varieties of pucks were made in early May, including combinations of bare MOF, pin and expanded natural graphite (ENG). Figure 35 shows the pucks during initial MATI assembly. Each puck has two thermocouple holes in the same locations and depth of penetrations for measuring bed temperature during the following sensible cooling and absorption experiments.

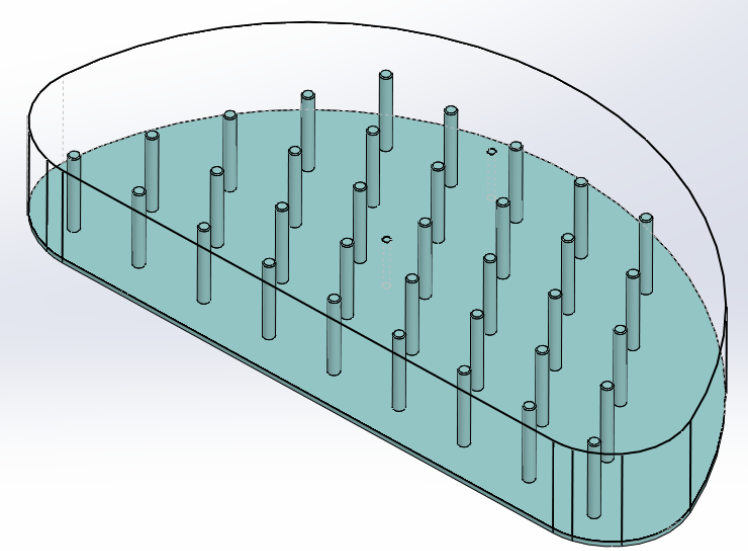

Figure 33: Conduction enhancement puck showing 2 thermocouple holes

Figure 34: Bed conduction enhancement test articles using aluminum pins

Key Findings: *Key findings from Task 3.1.5 include:*

1) *Pucks could be reliability fabricated with good dimensional control*
2) *Pucks were durable and we had few cases where pucks were cracked or broken*
3) *Compressing the media around conduction enhancing aluminum pins was successful and gives confidence that we can fabricate conduction enhanced pins using this approach.*

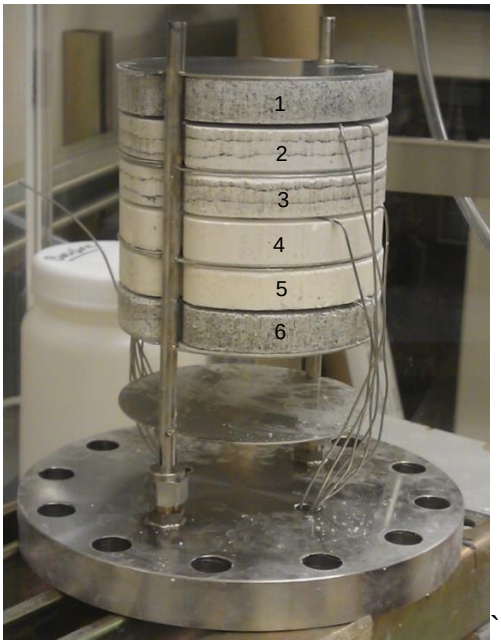

Figure 35: Pucks assembled for conduction enhancement study, from top down 1)bare+random ENG; 2)pin+layer ENG; 3)bare+layer ENG; 4)bare; 5)bare+pins; 6)pins+random ENG

Subtask 3.1.6 Pressure Vessel Design – Initially we planned to use a 2L pressure vessel provided to OSU by Hexagon Lincoln in the Phase III H_2 storage experiments. The pressure vessel consisted of two end caps, a collar, and two plugs. To accommodate the assembly and disassembly of temporary header connections between the vessel plug and MATI, the short end of the aluminum pressure vessel was redesigned to from an external plug connection, Figure 36, to an internal plug assembly, Figure 37.

The smaller plug, located on the longer end cap, was modified to allow H_2 gas to enter and exit the system during the charging and discharging experiments and to facilitate the passage of thermocouples into the body of the pressure vessel. The redesigned internally installed plug, located on the shorter end cap, was modified to allow liquid nitrogen coolant and heated N_2 gas to distribute to and from the MATI. The internal plug allowed both internal and external fluidic connections to allow complete assembly of the H_2 storage system and proper connection with the remainder of the test facility.

All changes in the 2L pressure vessel design were communicated and agreed on with the designers of the 2L vessel, Hexagon Lincoln.

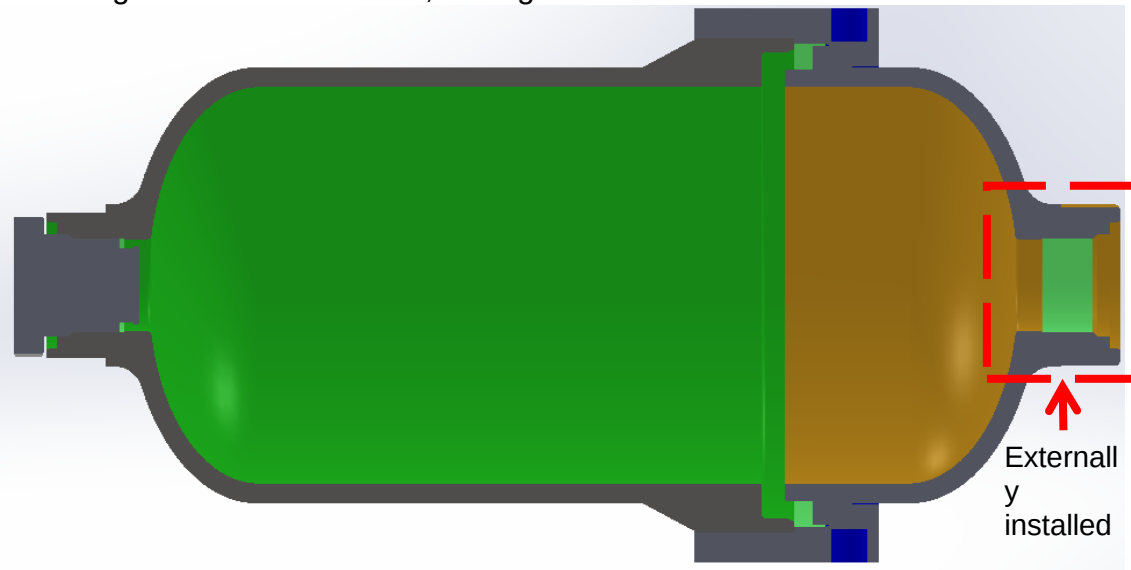

Figure 36: Original 2L tank design with externally installed plug.

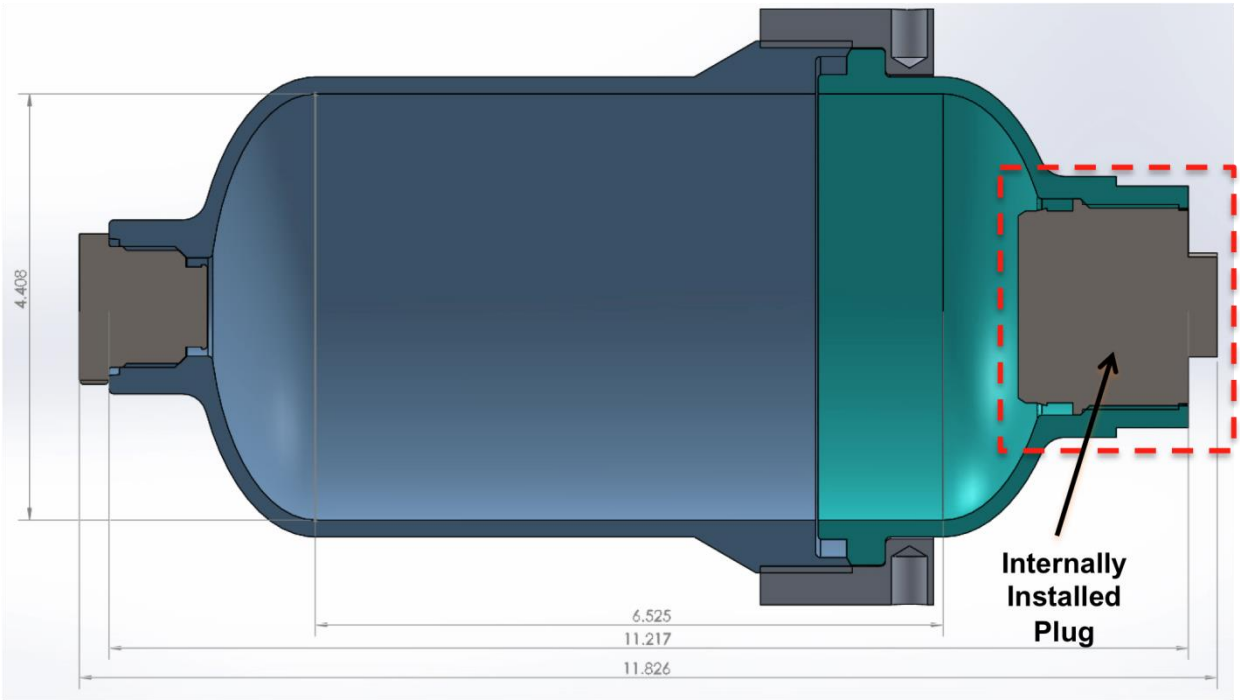

Figure 37: Redesigned 2L tank with internally installed plug.

Internally, OSU anticipates the use of 8 compressed beds of MOF-5 placed in contact with 5 cooling plates and 4 H_2 distribution plates as depicted in **Figure 38**, below.

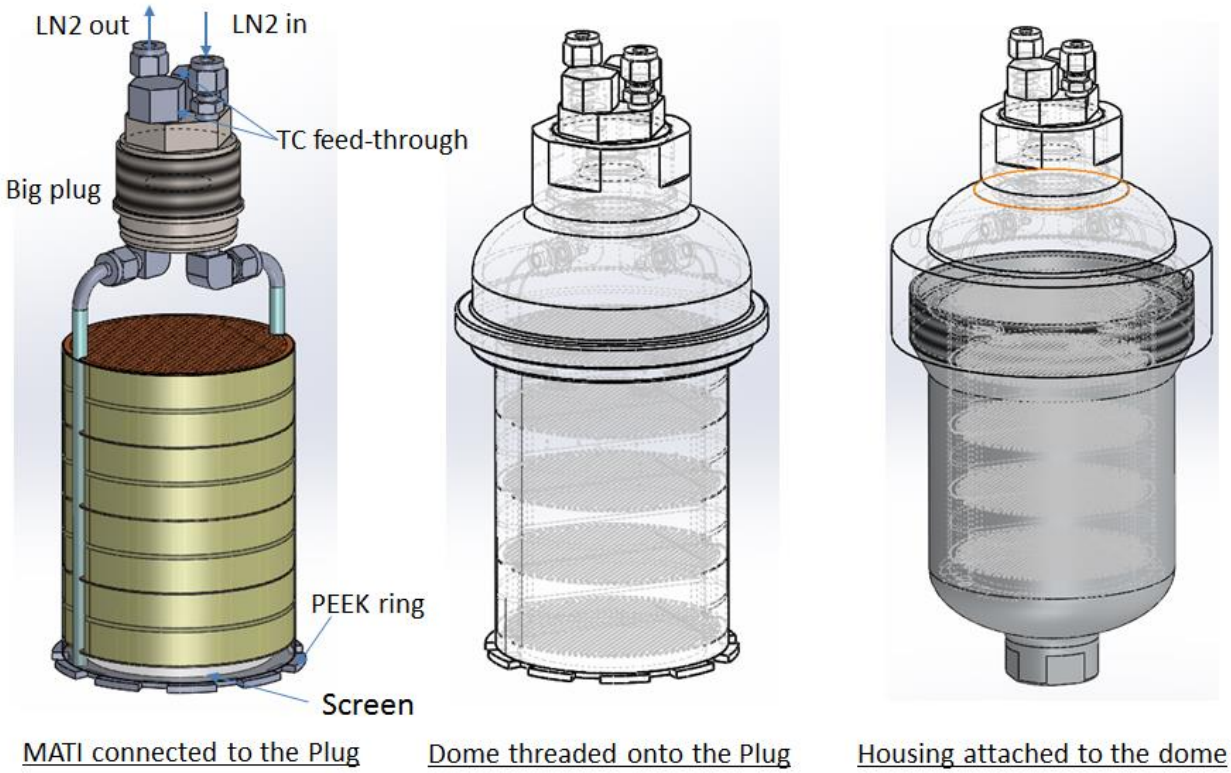

Figure 38: Proposed alignment and assembly of the MATI and MOF-5 beds within the pressure vessel.

The 2L pressure vessels were delivered to OSU by Hexagon Lincoln. However, serious seal leaks have been experienced at UQTR using the 2 liter Hexagon tanks and Teflon seals during the initial test. All three seals (one PTFE seal between the tank and dome; one PTFE seal for each plug) leaked upon submerging into LN2. Hexagon Lincoln also tested the new tank with larger port. Leaks also developed at cryogenic temperature, in particular from the 2" seal and the large one between the domes. A number of solutions were including crush seals were tried but no successful solution was identified for sealing the internally installed plug. Due to lack of near-term reliable solution for current tank leaks, the center decided to go with a more conservative flanged tank design in order to move remaining phase 3 activities forward. The new flanged tank design developed by Hexagon Lincoln is shown in Fig. 39.

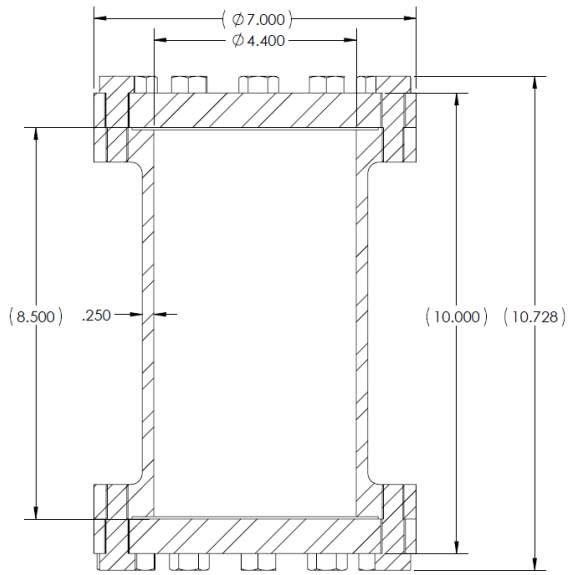

Figure 39: Cross-sectional view and dimensions of new flanged tank.

Two flanged tanks were delivered to OSU in later October 2014. Penetrations were added to both top and bottom flanges using TIG welding. Upon completing the whole MATI assembly with the tank, an unusual leak was found on the top flange during initial nitrogen leak check. The tiny void appeared to be at the center of the flange, roughly 0.5 inches apart from two adjacent welds (see Fig. 40). In consultation with the welding shop which did the penetrations, it was suggested that the void was caused by an initial material defect existed in the material that was later on enhanced by the welding process.

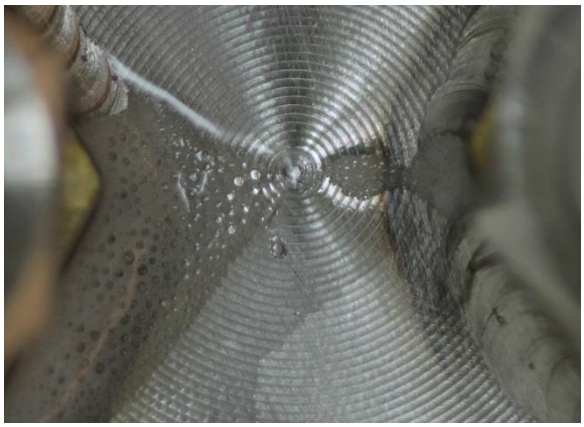
Figure 40.: Pinhole leak on flange

New penetrations were added to another flange. This time, before adding the penetrations, the flange was pressure checked to ensure no leaks. After adding the penetrations using the same welding process and welding shop, no leaks were found allowing the team to assemble the MATI for testing. The flanged pressure vessel design was completed and successfully pressure tested including all penetrations.

Key Findings: *Key findings from Task 3.1.6 include: Pressure vessel leaks were a major problem for every organization working on the MATI concept and probably resulted in a three to four month delay in testing. This coupled with staffing changes at OSU resulted in the cancelation of OSU acceptance testing with the MATI prototypes being shipped directly to SRNL for performance testing.*

Task 3.2. Prototype Fabrication and Assembly – As MATI cooling plates became available; the process of assembling cooling plates with the header tubes began. The initial task was to bond the inlet and outlet header tubes for a cooling plate using vacuum brazing, which will allow the team to evaluate the flow performance against simulation results.

The slits on the header tubes were initially cut using miniature end mill. The slits were not straight causing substantial gaps of the mating surfaces between the cooling plate and the header tube. As a consequence, the braze material got inside the inlet and outlet ports of the cooling plate through the “oversized” gap, causing both 0.25 mm (tall) ports plugged with braze material. In addition, it was learned that the brazing conditions were not tuned to this particular joint design. The set brazing temperature allowed too much of movement for the nickel-boron based braze alloy. Consequently the team started to take a closer look at the braze joint design. In addition, much more precise wire EDM was used to cut the slits instead of miniature end mill. The slits using wire EDM showed much better dimension tolerance. Furthermore, series of experiments were performed to find out the best brazing conditions instead of using the conditions suggested by the braze vendor. As a rule of thumb, higher brazing temperature or residence time at brazing temperature creates a uniform fillet at the joint; but it could create too much flow which gets into unwanted areas, which was critical to this case. In contrast, low temperature or less time will do the opposite. By running a series of brazing experiments, the desired brazing conditions for assembling MATI cooling plates and header tubes were identified.

It was also learned that the fit-up between the cooling plate and header tube must have high precision. No gaps above 0.001 inches were allowed anywhere in the assembly. The slits in the header tube had to have straight cut edges and their profiles needed to match those in the cooling plate. In addition, the rough edges on the cooling plates after diffusion bonding had to be smoothed out to eliminate any significant mating gaps. Figure 41 shows the joint and slit design.

To further minimize the risks associated with assembling the MATI prototype, the team also looked into the option of using orbital tube welding as part of the assembly process. Instead of brazing the five cooling plates and two header tubes in one process, there are advantages of brazing the cooling plate piece by piece (shown in Fig. (42)) and then use orbital welding to connect the tubes. This allows testing of each brazed cooling plate separately to insure that the brazing process was successful. A sample of a typical orbital weld and the relative size of the welding head are shown in Fig. 43. The team decided to use this combined brazing and welding approach to make the MATI prototype.

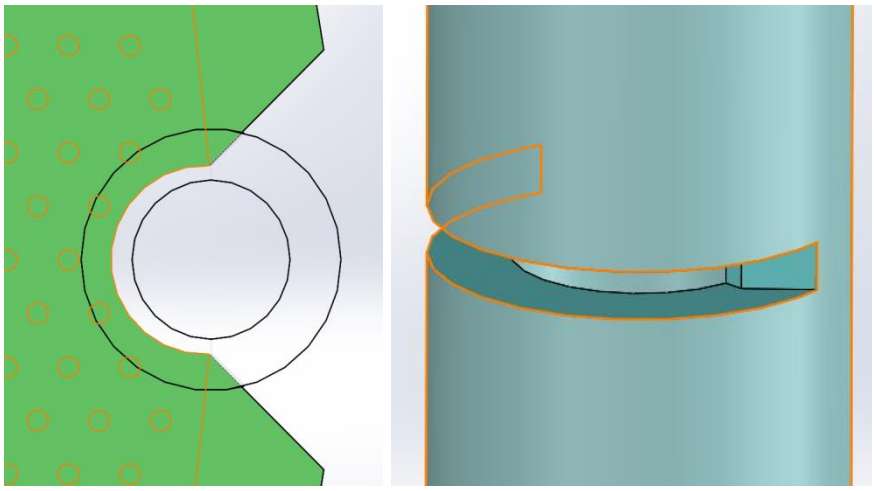

Figure 41: (Left) top view of cooling plate and header tube joint assembly; (Right) side view of the slit on the header tube with profile match on the cooling plate

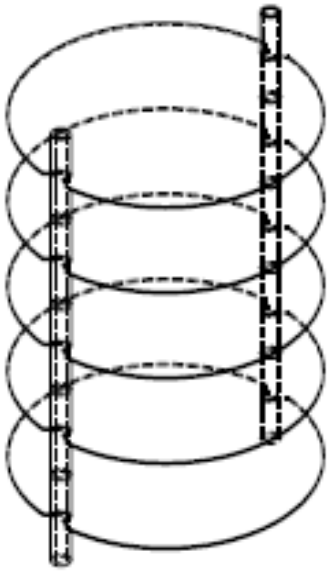

Figure 42: MATI assembly using both vacuum brazing and orbital welding

To mitigate the risk associated with braze joint fit-up, more precise wire EDM was used to make the slits on the header tubes. Once consistent fit-up was established, many vacuum brazing cycles were performed to find the best brazing conditions for the joint design. Two nickel brazing alloys were used during the design of experiment. One is BNi-2 that is boron based with relatively narrow melting temperatures, which requires slightly tighter component fit-up. The other is BNi-1 which is also boron based but has

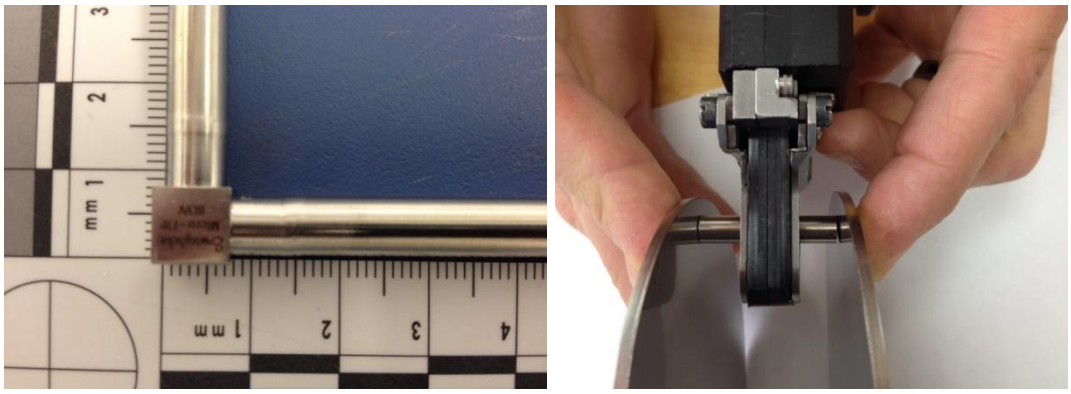

Figure 43: (Left) Typical orbital weld; (Right) Smallest welding head to perform the job

noticeable wider melting temperature. Similar joints were produced for a given range of brazing temperatures and dwell times, once proper fit-up was established for the braze joint. The suitability of a brazed bond was demonstrated by flowing compressed N_2, to demonstrate the lack of significant blockage of the MATI cooling plate ports by the braze material. This confirmed, that close component fit-up was essential. Figure 44 shows one of the MATI cooling plates used for brazing studies and typical N_2 flow during the flow verification test.

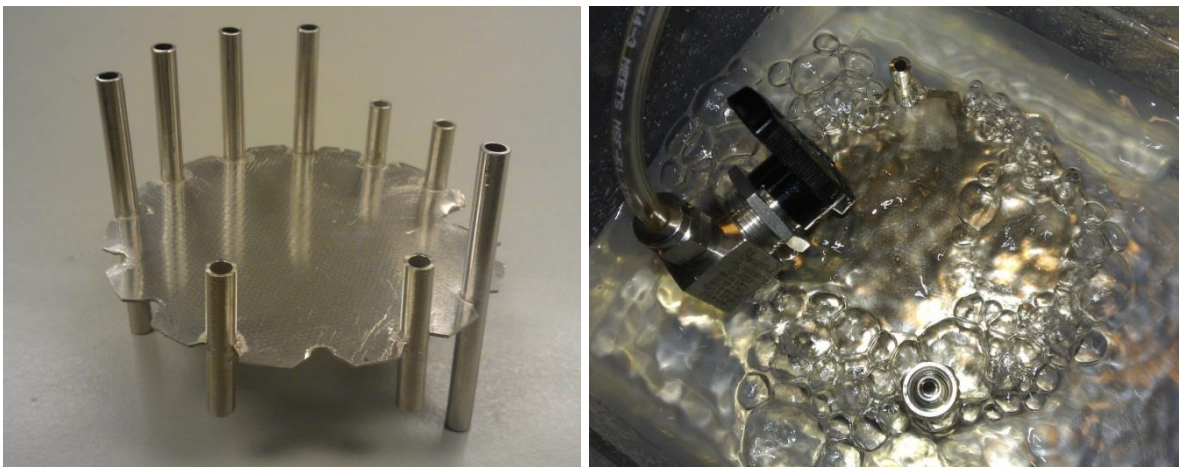

Figure 44: Picture of the MATI cooling plate for vacuum brazing DOE (left); Flow verification test after brazing (right)

Given the height of the cooling plate ports is only 0.25 mm, only small amount of brazing alloy would block or partially block the ports. Although BNi-1 is more viscous at the recommended brazing temperature thus with a lower chance to get inside the ports, BNi-2 was found to give more uniform joints and better fillets at significant lower temperature. Therefore, BNi-2 was chosen to be the brazing alloy and brazing

temperature of 1060 °C. In addition, the brazing temperature was held at 1060 °C for 4 minutes, a trade-off between joint bonding strength and risk of plugging the ports.

Using the brazing “recipe” and precisely cut tube slits, three MATI cooling plates were brazed the header tubes initially and additional two were brazed after confirming the flow and mechanical strength of the original three – all three MATI cooling plates were tested for 35 bar internal pressure and 100 bar external pressure. No physical damage or leaks were observed during the mechanical strength tests. A picture showing the 5 brazed MATI cooling plates is in Fig. 45.

Figure 45: Individually brazed MATI cooling plates

The flow measurement in terms of pressure drop across the cooling plates was used to identify the potential port blockage by the braze material. The blue curve (dots) shows the pressure drop of water for the baseline cooling plate (one with glued inlet and outlet plenums), which eliminated any additional pressure drops introduced by extra braze at the inlet and outlet ports. If more pressure drop occurred for a brazed cooling plate (e.g. MATI #5, 6, 7) for a given flow rate, it could be assumed that the brazed cooling plate was partially blocked. As shown in Figure 46, both cooling plate #6 and #7 had lower pressure drops than the baseline case indicating their ports are clear of braze material and ready for the next step. In contrast, the MATI #5 could indicate a partial blockage given its higher pressure drops.

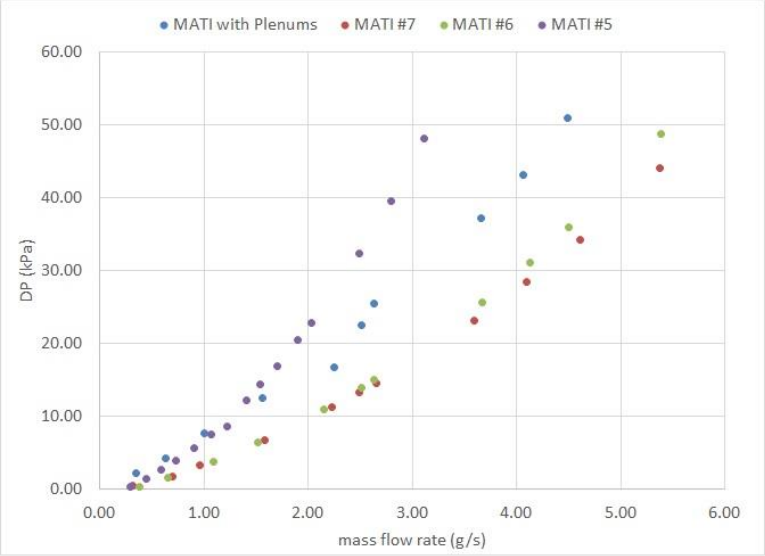

Figure 46: Pressure drop of water flowing across the MATI cooling plates

To demonstrate the assembly of multiple plates into a complete MATI two MATI cooling plates were welded together using an orbital welder to verify its performance with a picture shown in Fig. 47.

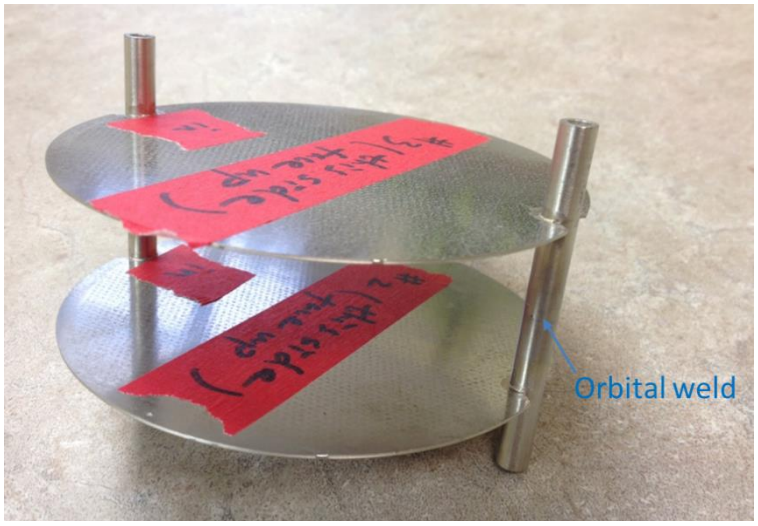

Figure 47: MATI cooling plates assembly using orbital welding

Following the demonstration of orbital welding, the first MATI was assembled. The five cooling plates were individually joined with headers using vacuum brazing. Orbital welding was used to connect the header tubes afterwards. A picture of the assembled MATI is shown in Fig. 48. The MATI was tested under 50 bars for over 5 minutes, no apparent deformation and leaks were identified. Pressure drop versus flow rate was also conducted to ensure good flow. As shown in Fig. 49, the data is consistent with that of single cooling plate reported during last quarter. Slightly higher pressure drop per

plate for the MATI assembly was likely due to extra pressure drops in the headers, as the flow rate was five times of that for the single plate.

Figure 48: 1st assembled MATI

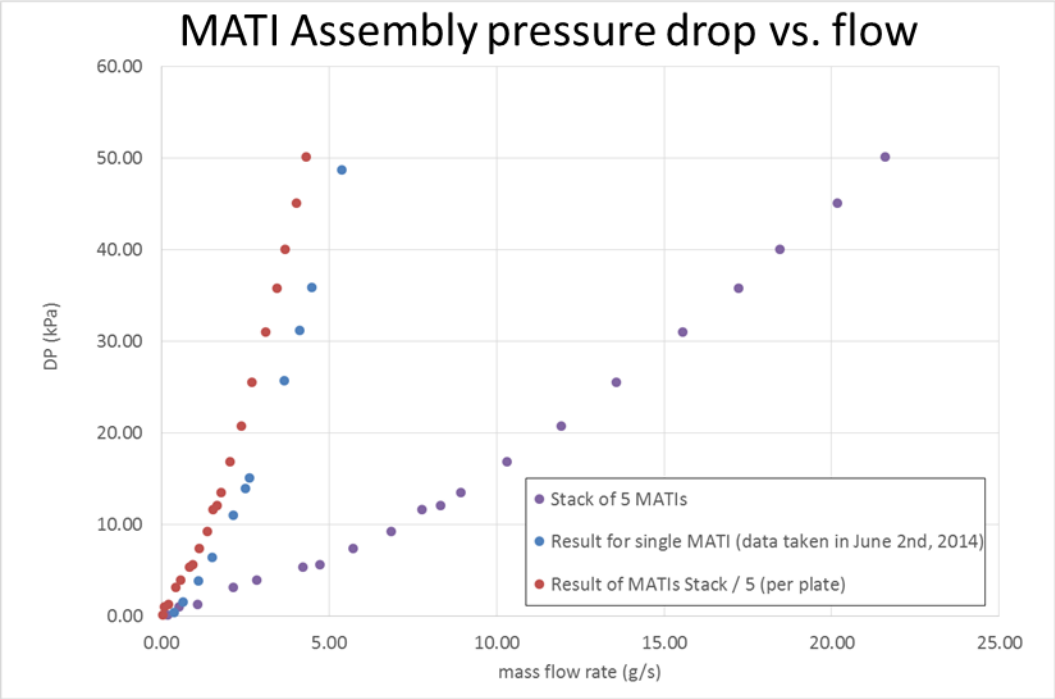

Figure 49: Comparison of measured pressure drops as function of flow rates

In addition, penetrations were added to both the large and small plugs earlier this quarter in order to be in the position to test the MATI when there is a seal solution to the current aluminum tank. A picture showing the large plug with MATI attached is shown in

Fig. 50. The same penetrations done on the large plug will be used for the flanged tank, in order to minimize changes on the assembled MATI.

Figure 50: Assembled MATI with large plug attached

Once the flanged pressure vessel was identified as our preferred pressure vessel design, We initiated the assembly of a complete MATI including MOF-5 pucks. The assembly process is shown in Fig. 51. The MATI was first attached to the flange. Two half pucks separated by three disk springs were slide in between two cooling plates and the thermocouples leads were fed through one of the two 3/8” tubes on the flange and inserted into the bed. The assembly process was conducted inside a glove box in order to minimize the beds exposure to air. Given the use of a glove box and the large number of thermocouples the assembly process took a significant amount of time. The thermocouple tree (total 34 TCs) shown below.

Figure 51**:** 1st MATI assembly process

In addition to assemble the 1st MATI, which was intended to be used for acceptance testing at OSU with subsequent shipment to SRNL, a 2nd MATI without MOF beds was also assembled. Similar to the 1st one, the five cooling plates were individually joined with headers using vacuum brazing. Due to contaminations from aluminum vacuum brazing, two of the five cooling plates were not bonded well onto the header tubes. After thorough cleaning of the vacuum furnace, the two cooling plate and header tube sub-assemblies were able to re-brazed. All five sub-assemblies were able to pass the flow check and low pressure leak check before conducting Orbital welding to put the whole MATI assembly together. After orbital welding, two cooling plates were observed to have pinhole leaks along the bonding perimeters upon pressurizing it to 50 bars. Using filler-less TIG welding, the pinholes leaks on two cooling plates were fixed. However, another pinhole leak in one of the braze joints were found. Using braze welding (filler material with significant lower melting temperature than nickel braze), the pinhole was sealed successful and the device passed 60 bars pressure check and it has been delivered to SRNL where SRNL was use it to complete start-up of their test apparatus.

The original MATI with MOF and instrumentation was assembled at OSU but due to continuing leaks around the thermocouple leads (discussed below) it was decided to forgo acceptance testing at OSU and this device was shipped to SRNL. Unfortunately the MATI was damaged during shipment and the 2nd MATI was assembled with MOF-5 pucks and instrumentation and is currently being used by SRNL for performance testing.

A 3rd MATI prototype was assembled using the similar assembly procedures as previous ones. After assembly, the MATI was used by OSU to assess various conduction enhancement approaches, including solid aluminum pins, random and layer ENGs.

Key Findings: *Key findings from Task 3.2 include: The key issues in assembly of the MATI related to brazing the cooling plates to the headers. After a number of tests we believe that we have developed an acceptable approach, but this is an area that needs additional research. Errors in brazing can lead to blockages in the cooling plates. This led to the decision to individually braze each header to the cooling plate and then assemble the MATI by using an orbital welder to weld the five cooling plate headers together.*

Task 3.3. Facilities Development – OSU's role in phase 3 initially included testing of the MATI prototype. This required significant modifications to our Phase 3 test apparatus. Alterations primarily included increased LN_2, H_2 gas, and N_2 gas flow capacities required for the Phase III preliminary testing. In general, the testing facility followed the piping and instrumentation diagram in **Figure 51**, below.

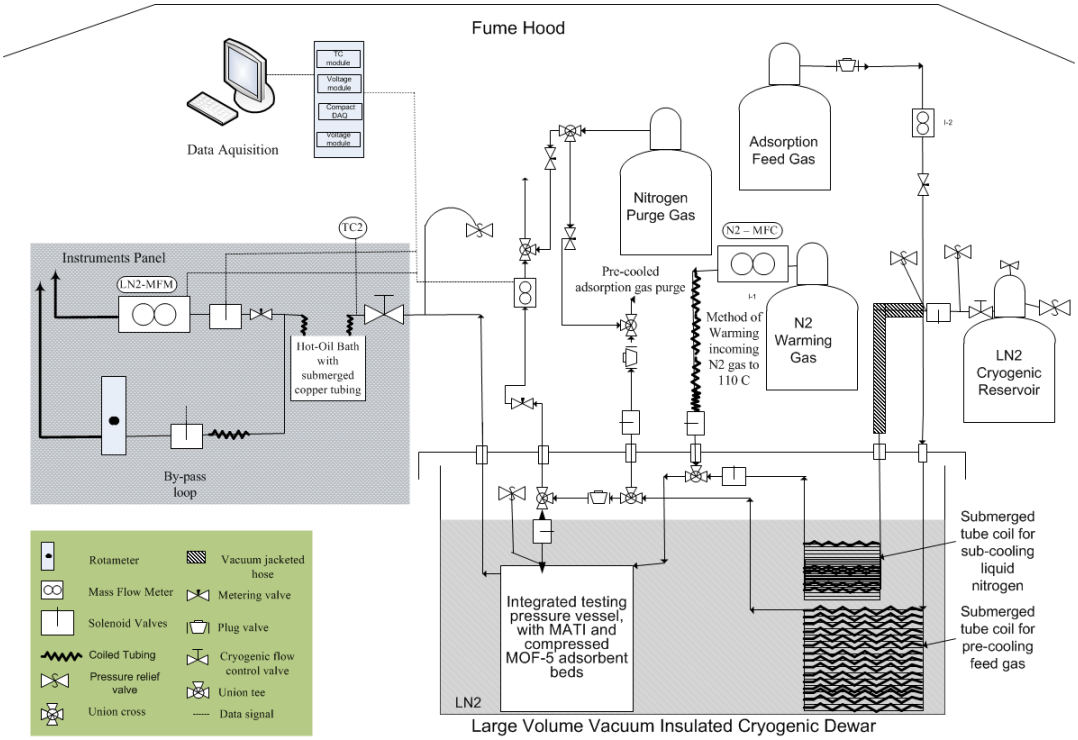

Figure 51: General piping and instrumentation diagram for Phase III testing facility.

Three separate manifold systems were installed to increase the overall capacity of the testing facility:

1) A pressurized (115 psi) liquid nitrogen manifold was installed to allow two 160 L pressurized liquid nitrogen tanks to be utilized for H_2 charging experimental trials;

2) A two tank N_2 gas manifold were installed to provide additional gas capacity required for discharging experiments; and,

3) A new H_2 gas manifold increased the capacity of adsorbent gas.

These manifold systems were necessary to allow the increased for gas flows during experiments and to reduce the number of gas refills and tank changes, thus reducing system downtime and improving efficiency.

Two vacuum insulated Dewar vessels was utilized throughout the experimental effort to house the integrated testing vessel, LN_2 sub-cooling system, and H_2 precooling system.

Placing secondary cooling systems in close proximity to the 2L pressure vessel containing the integrated MATI system helped to maintain a constant 80 K delivery temperature of LN_2 to the MATI and H_2 gas into the system itself.

Sub-cooling pressurized LN_2 coolant was achieved using coiled tubing submerged in atmospheric LN_2 in the research Dewar vessel. Providing sub-cooled LN_2 to the experimental system increased the allowable temperature change of the LN_2 flowing through MATI and minimized the potential for boiling LN_2 in the micro channel cooling plate throughout the charging experiments.

The Phase III hydrogen gas precooling was accomplished with the flow of H_2 gas through submerged tubing packed with stainless steel ball bearings to increase the contact surface area of flowing hydrogen gas, similar to the system utilized at UTQR. The length of submerged tubing for both LN_2 and H_2 was increased compared to Phase II to ensure proper cooling of increased mass flow throughout charging experiments.

Throughout Phase II, used liquid nitrogen coolant was subsequently heated upon exiting the integrated system and passed through a mass flow meter for analysis. To ensure continued heating of spent high flow rate liquid nitrogen throughout the charging experiments, a larger capacity heated oil bath was utilized to ensure an elevated temperature for phase change and continued heating. A high flow rate orifice plate replaced the electronic mass flow meter utilized in Phase II to analyze the mass flow rate of liquid nitrogen required throughout the charging process. Similarly, a mass flow meter was utilized to measure the mass flow rate of H_2 throughout pressurization and charging of the system.

Electronic mass flow controllers were utilized to control the flow rate of heat N_2 gas flowing through the MATI to desorb stored H_2 during the discharge process and to control the flow rate of H_2 exiting the pressure vessel. Similar to discharged LN_2 coolant, N_2 gas was heated with flow through submerged tubing in an oil bath.

The initiation of LN_2 coolant, heated N_2 gas, and H_2 charging and discharging streams was controlled with electronic solenoid valves via LabView software. Data collection and flow control (throughout discharging) was controlled and operated via integrated LabView software.

To ensure the safe discharging of used and unused H_2 gas prior to entering the pressure vessel and exiting during discharging, charging and discharging lines were purged with N_2 gas to significantly dilute H_2 gas prior to discharging into the fume hood.

After the design of the test apparatus was completed a more detailed piping and instrumentation diagram was completed and is shown in Figure 52.

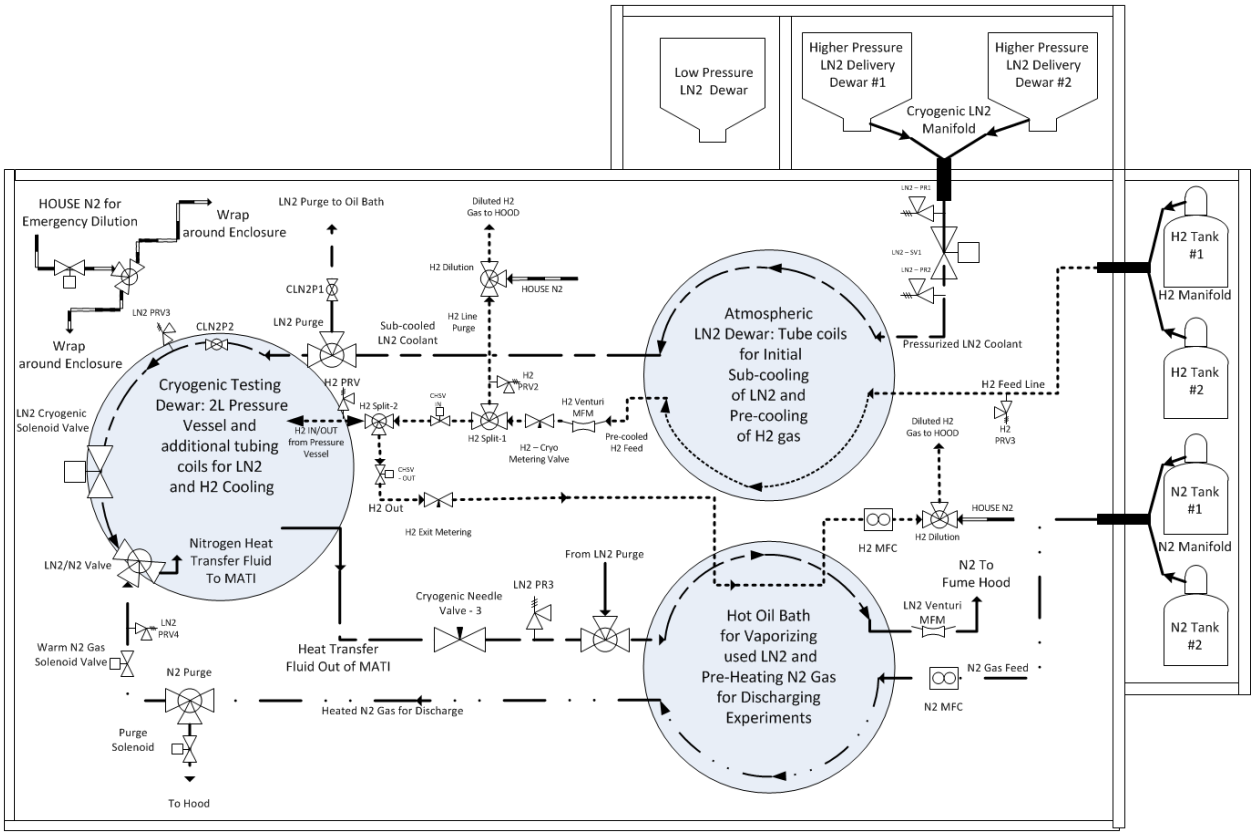

Figure1 52: General piping and instrumentation diagram for Phase III testing facility.

In December 2013, a design and safety review was completed via teleconference with the HSECoE Adsorbent team to discuss the proposed testing facility, system design, and safety overview. No major recommendations were brought to light throughout the discussion. Following the design review alterations to the testing facility were completed and the complete system is shown in Figure 52.

Key Findings: *Key findings from Task 3.4 include: The design and assembly of the test apparatus was successful and no significant modifications or upgrades to the system were required to conduct the conduction enhancement tests.*

Task 3.5 OSU Prototype Testing – The original plan for Phase 3 involved having initial performance and shakedown testing performed at OSU prior to final performance testing at SRNL. Both charging and discharging experiments were to be performed to ensure safe operation and proper functionality of all instrumentation and data collection devices. As discussed below, do to unresolved hydrogen leaks around thermocouple leads at OSU and personnel changes, it was ultimately decided to move shakedown testing to SRNL. In this section we will describe the plans for shakedown testing at OSU and the result of conduction enhancement testing which was completed by OSU

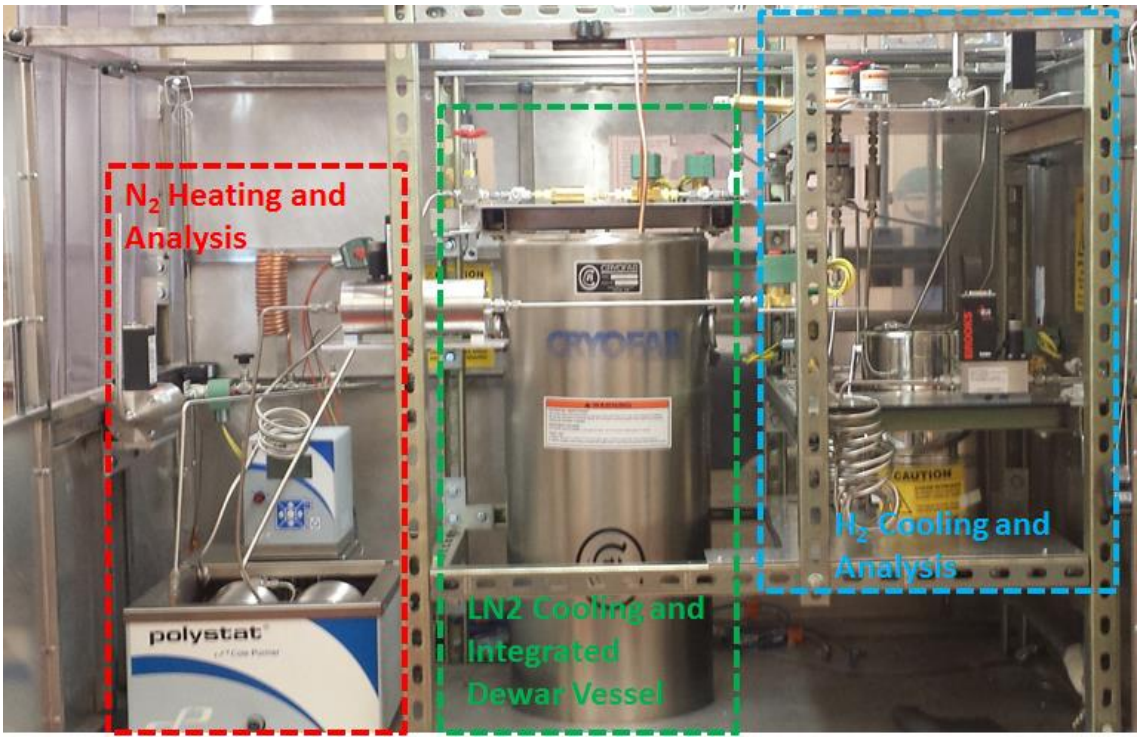

Figure 53: Constructed OSU testing facility.

OSU Planned Shakedown Testing – A shakedown test involves submerging the pressure vessel, liquid sub-cooling coil, and H_2 gas pre-cooling devices are submerged in LN_2 prior to initial charging of the pressure vessel with H_2 gas and allow the system to come to equilibrium. Discharging of the pressure vessel was to be accomplished through the flow of heated N_2 gas through the MATI at a constant flow rate, with the simultaneous constant flow discharge of gas from the system. Heated N_2 gas flow would continue until the pressure vessel reaches approximately 5 bar internal pressure and temperature in the range of 160 – 180 K.

With internal conditions maintained at 5 bar and 160 - 180 K, the H_2 charging experiments would proceed with simultaneous initiation of H_2 gas flow and LN2 coolant flow. Charging would proceed at constant LN_2 flow rate and constant H_2 gas cylinder pressure until the final conditions were reached within the pressure vessel and MOF-5 adsorbent.

Once multiple charging and discharging cycles had been completed the storage pressure was planned to be increased and the process repeated at 40 and 60 bars H_2 pressure.

The functionality and shakedown testing of the experimental system was performed using the collared two dome aluminum tank with the five plate MATI installed (Figure 54). The facility shake down was performed at a variety of operating pressures starting at ~20 bars He gas pressure and pressurized LN_2 to perform leak testing of all compression fittings and MATI unit.

Figure 54: Five plate MATI installed in the large plug and smaller dome of the collared pressure vessel for initial system debugging.

Following the functionality testing The MOF-5 beds were instrumented with fine gauge beaded wire thermocouples and installed into the five plate MATI within the flanged pressure vessel. The initial flange used in the installation was found to contain a material defect that rendered the system unusable. A second flange was fabricated to provide the penetrations necessary for heat transfer fluid connections and thermocouple pass-through. Figure 55, below, depicts the various steps of assembly for the integrated MATI system: including thermocouple insertion, MOF-5 assembly, and additional images of the thermocouples throughout the vessel and fluidic paths.

The fully assembled flanged vessel was inserted into the Dewar and all fluidic lines are connected. Activation of the compressed MOF-5 was performed prior to full assembly by exposing beds to vacuum at room temperature for 12 hours and an additional 8 hours at 115^{o}C under vacuum. Once the MOF-5 beds were installed with thermocouples into the flanged tanks, a secondary in-situ activation was performed by wrapping an electric heating tape around the outside of the flanged vessel and heating under vacuum for 8 hours at approximately 115^{o}C. Prior to performing a test, H_2 gas is introduced to the room temperature system at approximately 20 bars and allowed to equilibrate. Once the system pressure and temperature is stabilized, the tank is discharged to atmospheric conditions. Once temperatures stabilize within the vessel, this procedure is repeated four additional times to allow the MOF-5 system to be fully exposed to H_2 gas prior to the cryogenic adsorption experiments.

Figure 55: Various steps of assembly process and fully assembled flanged pressure vessel.

The fully assembled flanged vessel was inserted into the Dewar and all fluidic lines connected. A 100 bar He pressure decay test was performed over a 48 hour period with less than 1 bar of pressure change observed. An in-situ activation of the compressed MOF-5 was performed in the fully assembled system by exposing beds to vacuum at room temperature for 24 hours. An electrical heating tape was added to the outside of the pressure vessel and brought heated until all MOF-5 beds read approximately 115^{o}C, under vacuum, and was held for an additional 24 hours. Following the in-situ activation, a second room temperature pressure decay test was performed with similar result.

Following the second pressure decay test, preliminary adsorption experiments were schedule to begin. H_2 gas was added to the pressure vessel at room temperature up to 60 bars. As atmospheric LN_2 began to be added around the integrated pressure vessel a leak was observed in the custom made thermocouple pass-through, Figure 56. Gas leaks were observed along the thermocouple wire in three of eight required thermocouple pass-through. While the thermocouple pass-through used in the system were individually pressure tested at cryogenic conditions, and passed, and are located approximately 32” above the LN_2 dispensing tube, failure was observed after full assembly.

An attempted fix to the thermocouple pass-through was attempted by applying an additional application of epoxy approximately ½” below the tube end on the outside of the tube and extending approximately ½” above the tube end, the epoxy demonstrated repeated cracking upon exposure to LN_2 in this manner.

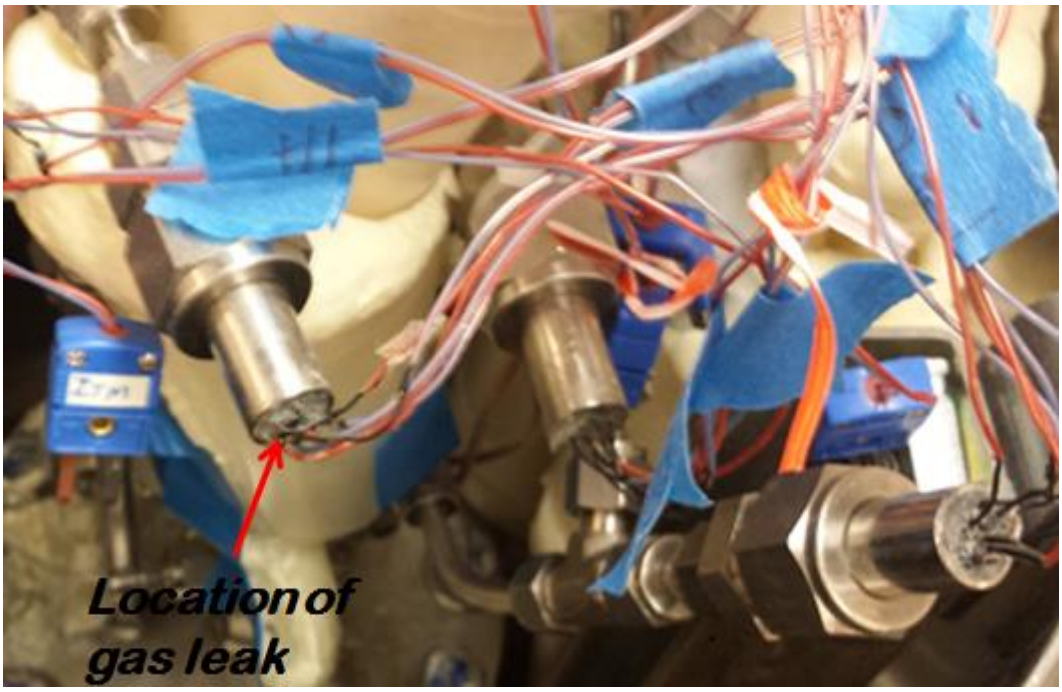

Figure 56**:** Custom made thermocouple pass-through that demonstrated leaks at wire upon the addition of LN_2 to research Dewar containing pressure vessel.

Simultaneously, SRNL successfully pressure tested an alternative thermocouple sealing solution at cryogenic conditions. It was decided, between OSU and SRNL, to ship the fully assembled MATI to SRNL and reassemble the MATI and MOF-5 beds with the solutions developed at SRNL and perform all performance testing at the SRNL site.

Conduction Enhancement Testing – While the hydrogen leaks around the thermocouple leads was sufficiently severe to prevent performance testing of the MATI, the OSU test apparatus was capable of conducting a more limited set of tests on conduction enhanced pucks.

Six kinds of pucks, with total of 12 pucks (two of each) were assembled into the MATI. Due to constraint of thermocouple pass-through and placement, six pucks (one of each kind) were selected for instrumentation – two 0.040" sheathed T-type thermocouples were inserted from the vapor channel between MOF beds to measure bed temperatures. One thermocouple was close to the center and the other was away from the center, which could capture flow related effects.

Initial conduction enhancement experiments began in the middle of May 2015 with sensible cooling and heating experiments (the flanged tank housing the MATI was only pressurized with 2 bar of N_2, thus minimized adsorption). The experiments started with sending LN_2 into MATI which was initially at room temperature. A picture of the experimental setup is shown in Fig.57. No subcooling (using atmosphere LN_2) was provided during the initial experiment. Figure 58 shows the two sets of temperatures for the beds during cooling. The results suggest that the pucks with pins and ENG had

faster thermal responses than unenhanced and less enhanced pucks (bare, or using pins or ENG alone).

Figure 57: MATI (left) and LN_2 manifolded tanks during initial experiment

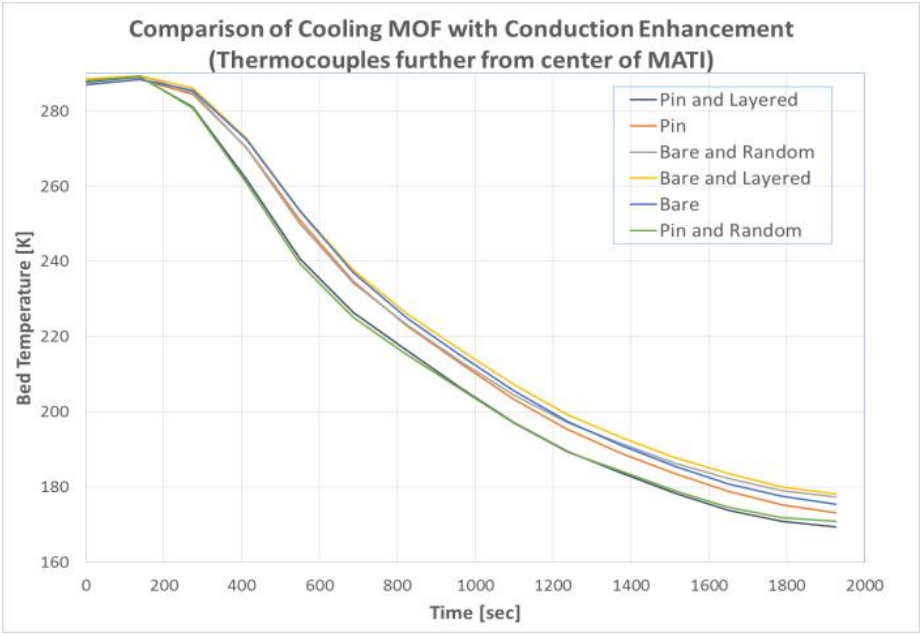

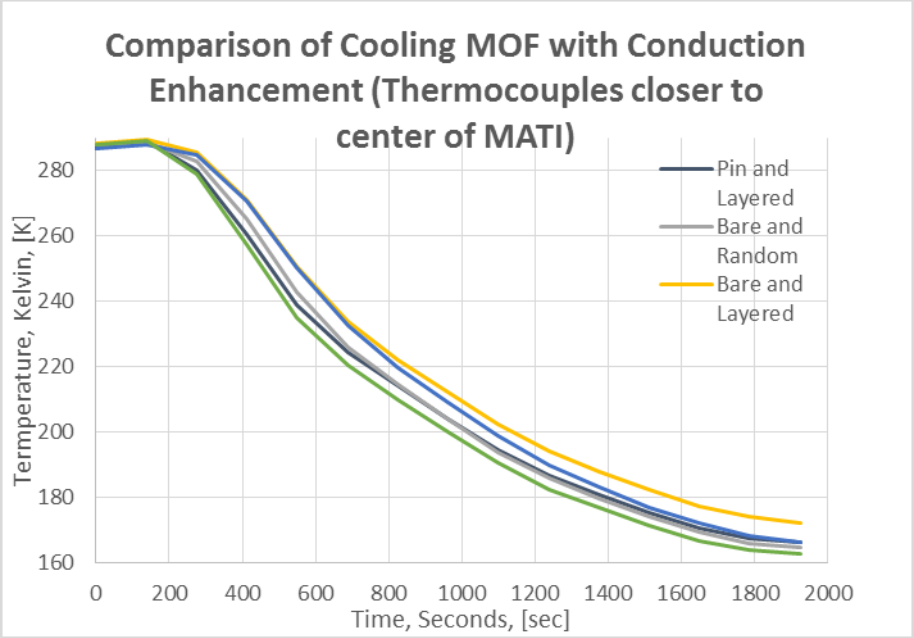

Figure 58: Bed temperature profiles with time during sensibel cooling. Left Plot – thermocouple measurements away from center; Right Plot – thermocouple measurement closer to the center

The next step was to add an adsorption process. N_2 was used as the absorbing gas in place of H_2. N_2 has higher heat of adsorption, which could compensate for low pressure adsorption. Compressed N_2 was cooled using LN_2 and introduced at 25 bars to simulate low pressure hydrogen adsorption. The LN_2 was subcooled in this experiment to minimize vaporization inside the MATI. Figure 59 shows the bed temperatures as a function of time. Compared with previous experiment without LN_2 subcooling, bed temperatures dropped significantly faster even though internal heat was also generated due to adsorption. This was also observed even when tank was significantly cooler shown in Fig. 60. Similar to earlier results, the beds with pins and ENG (both random and layer) performed the best. In addition, the thermocouples closer to the center have shown faster temperature decline.

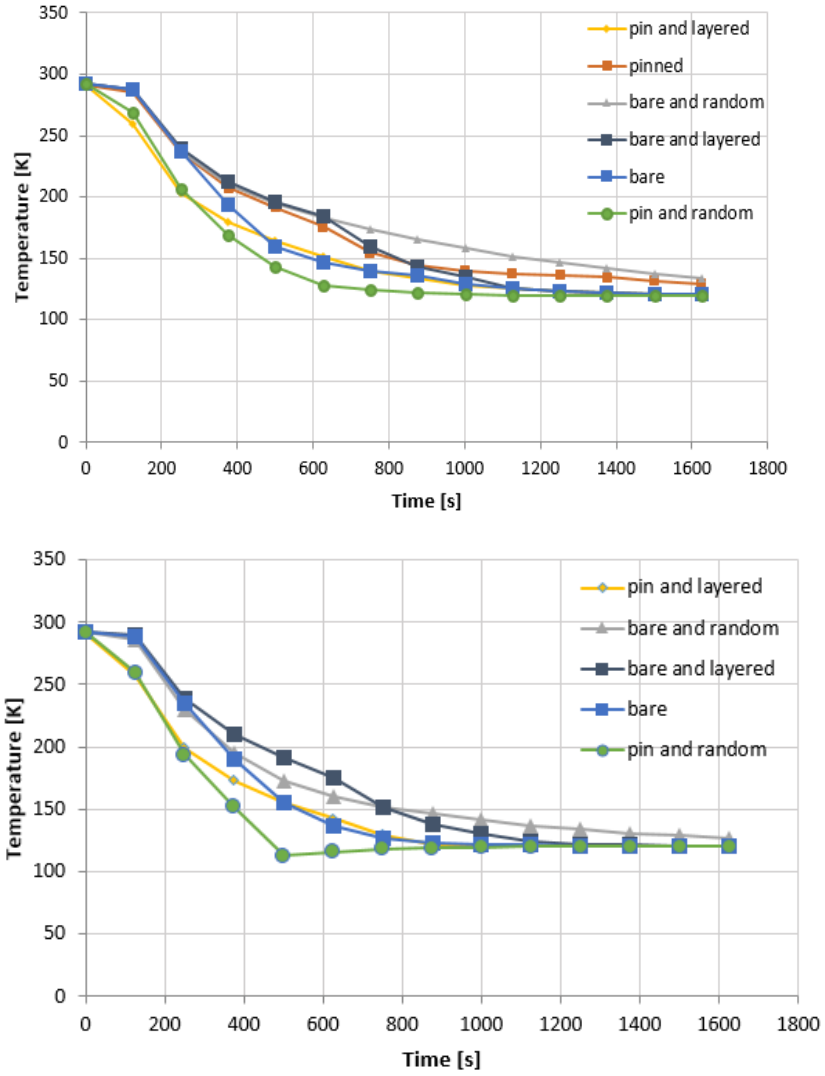

Figure 59: Bed temperature profiles with subcooled LN_2 cooling the beds. Left Plot – thermocouple measurements away from center; Right Plot – thermocouple measurement closer to the center

Figure 60: MATI during adsorption with subcooled LN_2 and precooled N_2 at 25 bars

Although the results were generally what we expected during the cooling experiments, the data showing the instrumented bare puck out-performing several enhanced pucks which was suspect. This prompted the team to open the MATI and inspect the pucks, especially thermocouple placements. Due to the rigidity of the thermocouples, several thermocouples were not fully inserted into the 7.5 mm thermocouple holes. In order to mitigate possible flow maldistributions between the cooling plates the several of the pucks (instrumented bare puck and pin puck) were relocated to different unit cells. Experiments using subcooled LN_2 for cooling and precooled 25 bar N_2 as adsorption gas was repeated following the reassembly. The bed temperature profiles are presented in Fig. 61. As shown, the enhanced pucks performed significantly better than the bare puck.

The last experiment that OSU team performed was to submerge the MATI tank within LN_2 dewar, eliminating thermal mass that both subcooled LN_2 and precooled N_2 had to interact with. This case was the closest to a actual charge cycle and is the best measure of the value of conduction enhancement. As shown in Fig. 62, trends similar to earlier experiements were achieved confirming the effect of conduction enhancement. Figure 10 shows the test apparatus during these experiements, documenting thelarge amount of LN_2 being vaporized. The newly assembled MATI is also shown in Fig. 63 (right). All of the conduction enhancements performed significantly better then the bare unenhanced puck. The best performing enhancement (pins with out any ENG) reached a steady state temperature in 1200 sec as compared to 2700 sec for the unenhanced puck. This is a significant improvement and suggests that puck conduction enhancement is both feasible and could lead to a significant improvement in the rate of charging and discharging an adsorption bed formed from densified adsorbing material.

We investigated a number of charging options and the multiple experiments conducted clearly demonstrated the benefit of conduction enhancement for current MATI design.

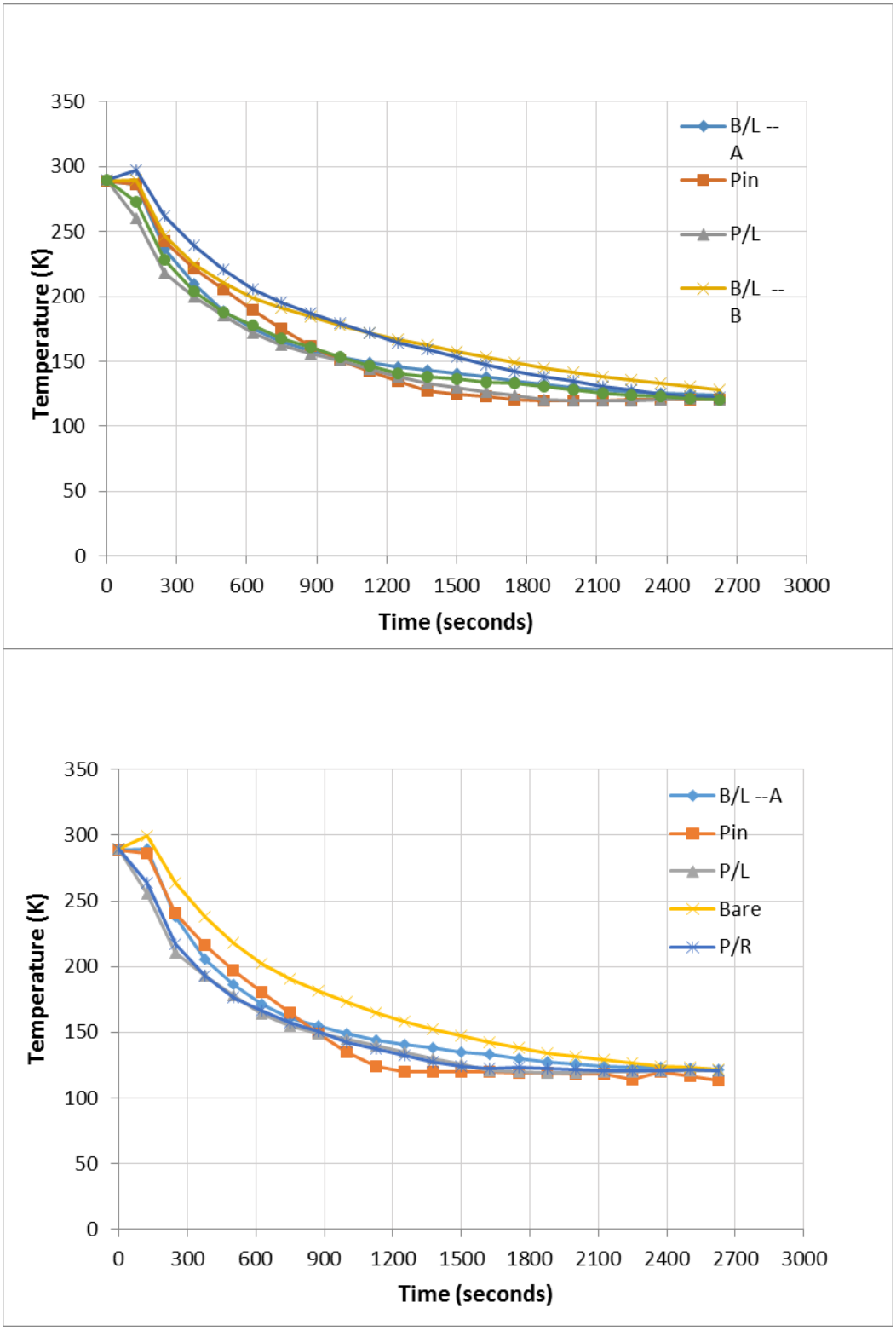

Figure 61: Bed temperature profiles with improved thermocouple placements and some pucks relocations. Top Plot – thermocouple measurements away from center; Bottom Plot – thermocouple measurement closer to the center

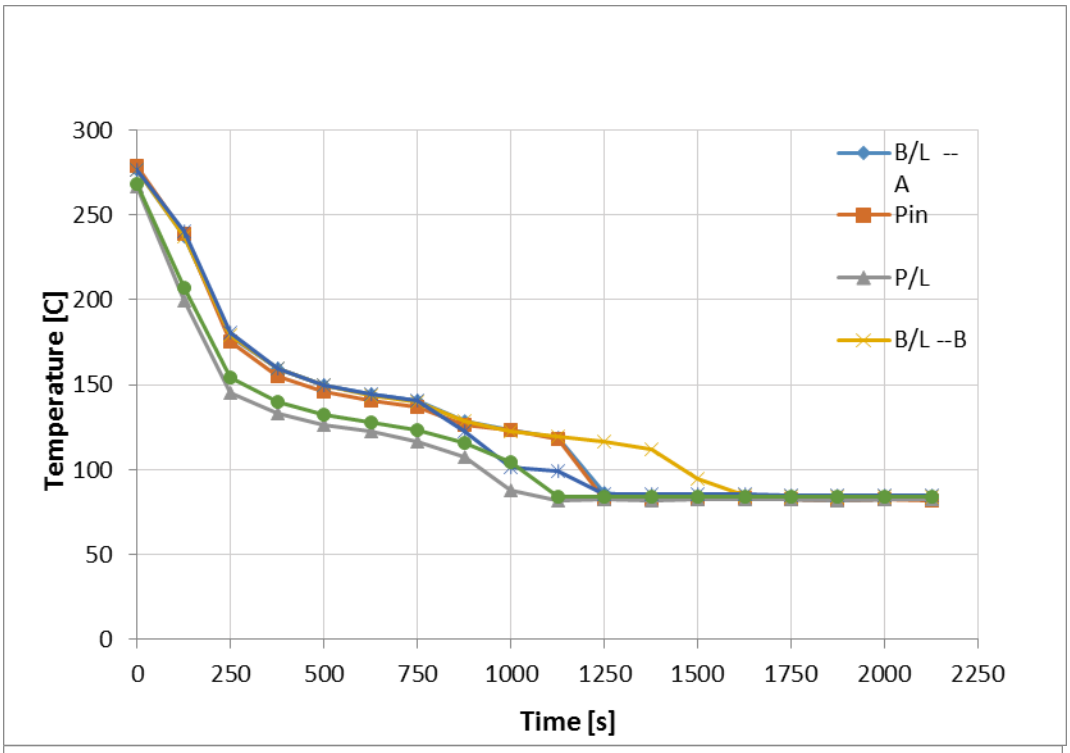

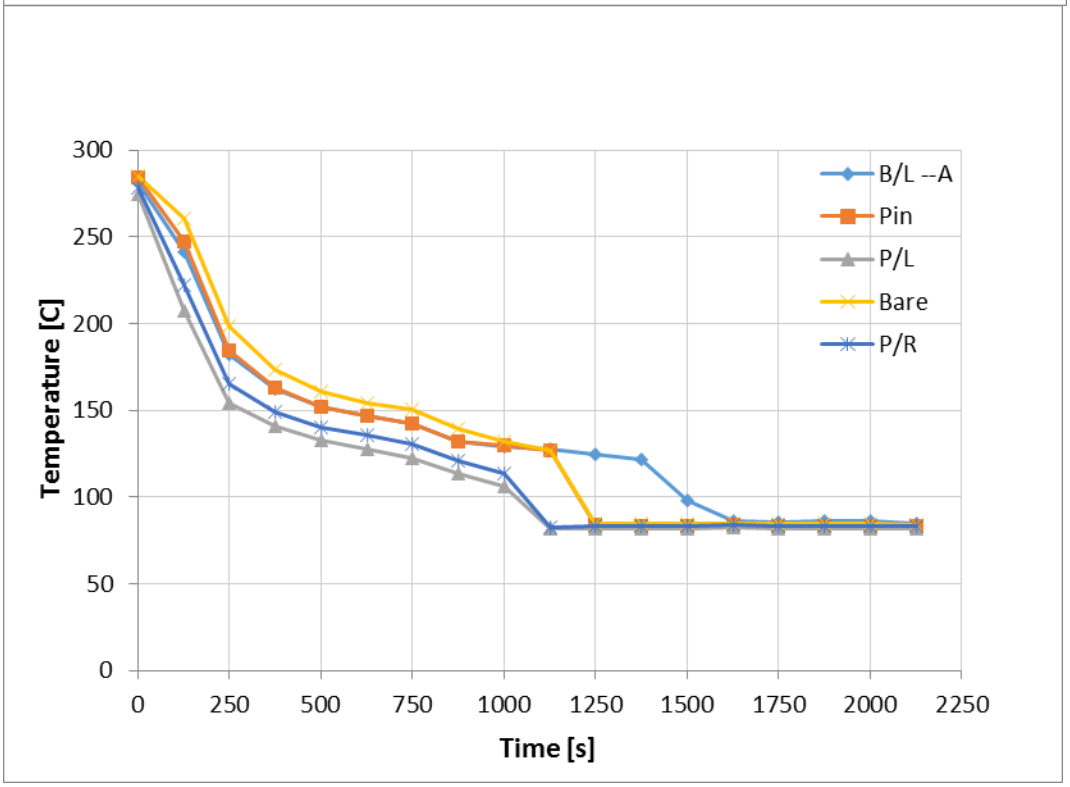

Figure 62: Bed temperature profiles with submerged MATI tank. Top Plot – thermocouple measurements away from center; Bottom Plot – thermocouple measurement closer to the center

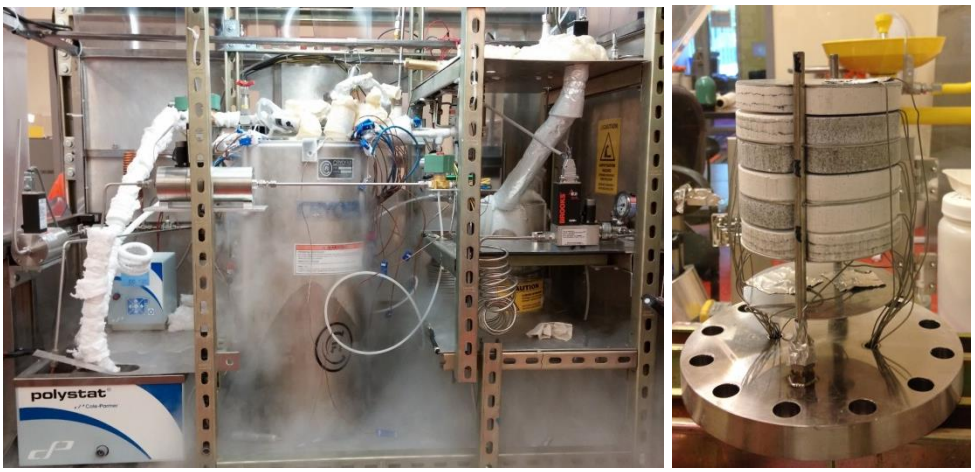

Figure 63: Experiment apparatus during submerged adsorption test (left); MATI with improved thermocouple placement and bed re-location (right)

Key Findings: *Key findings from Task 3.5 include:*

- *Hydrogen leaks from the pressure Vessel was the most significant problem we encountered. In any future testing, leak prevention from the pressure vessel and any penetrations needs to be address early in the design process. Hydrogen leakage ultimately forced the cancelation of acceptance testing at OSU with the project going directly to performance testing at SRNL.*

- *Conduction Enhancement Testing successfully demonstrated the impact of conduction enhancement on heat transfer from and to the MOF-5 pucks. As Figure 61 shows, the puck enhanced with pins reached thermal equilibrium in around 1100 seconds while the unenhanced puck required 2700 seconds*

- *The results of conduction enhancement testing were shown to be very sensitive to thermocouple location and uncertainty in thermocouple location can lead to significant errors*

Task 3.6 Modeling – Phase 3 modeling focused on two subjects. First, we used the conduction enhancement model described in Phase 2 to help select the height of the pucks that would be used in the prototype. Second, using our Phase 3 model of the complete adsorption process as a starting point, we refined our integrated system model are using this model to compare against experimental data being produced by SRNL.

2D Simulation for Determination of Half-Bed Height - During the design of the Phase 3 MATI prototype, there was a need to estimate the height of the half-bed to be used in the 2L pressure vessel with integrated MATI system. The objective of this effort was focused on the spatial and temporal resolution of thermocouple data that was expected to emerge from Phase 3 experimentation. It was important to determine if any particular

half-bed height (1, 1.5, or 2 [cm]) would yield temperature profile readings, which could be measured with enough resolution to successfully facilitate simulation effort.

Consequently, we have conducted a parametric study in order to determine optimal height of MOF-5 bed that was used in Phase 3 MATI prototype. We examined if it is reasonable to expect a sufficient temperature gradient within the bed as well as presence of zones where the half-bed would undergo significant cooling.
Bed bulk density was assumed to be 320 [$kg_{MOF\text{-}5} / m^3_{bed}$] with corresponding Dubinin-Astakhov adsorption kinetics parameters. Simulation was a 2D axis-symmetric approximation of the system as shown in **Figure 63**. Modeled system represented half-bed and included half of the hydrogen distribution plate, MOF-5 bed and SS-316 metal plate. The distribution plate was 500 [µm] high, metal plate thickness was 250 [µm] and bed height measured 1, 1.5 or 2.5 [cm].

Hydrogen entered the system at 80 [K] from the side of the distribution plate through which it penetrated the bed. Inlet boundary is set to pressure ramp. Pressure was increased in 3 minutes from initial 5 to final 60 [bar]. Upper boundary of metal plate was kept at a constant temperature of either 80 or 95 [K]. The latter temperature choice was somewhat unfavorable case scenario and represented highest allowable temperature in the liquid nitrogen heat exchanger channel. Numerical setup and boundary condition assume negligible changes of liquid nitrogen temperature. Other boundaries were symmetry or insulation boundaries. This was a conservative approach since in the actual experiments the radial side of the bed would be exposed to hydrogen and would therefore provide cooling through both conduction and to some minor extent convection. Initial temperature conditions were 160 [K] in the bed and 80 [K] in distribution and metal plates.

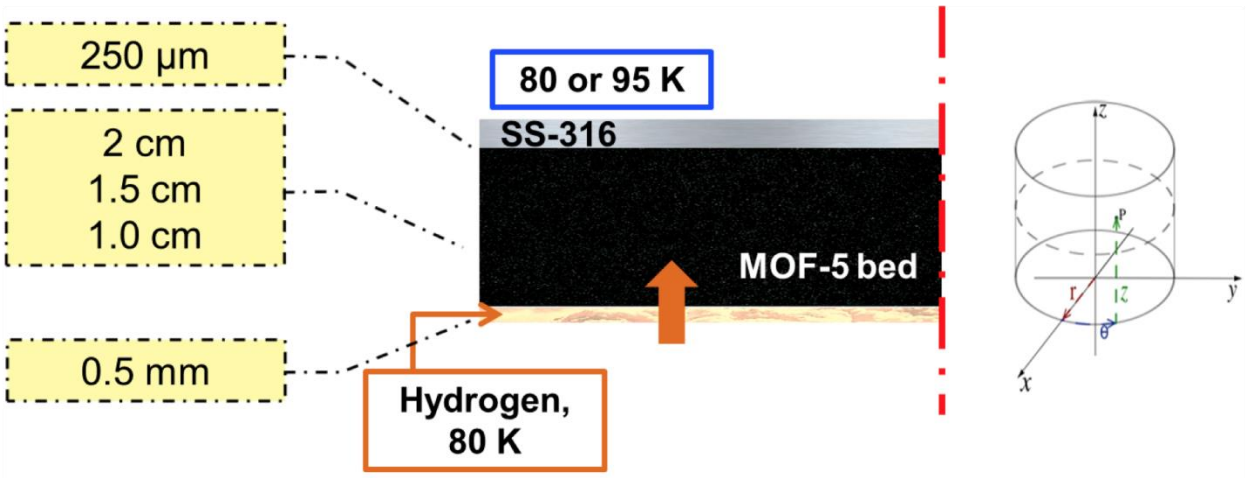

Figure 63: Modeled system with dimensions and major boundaries.

Results are presented as temperature profiles expected to be obtained at three different characteristic location of the half-puck (**Figure 64**). During evaluation of the simulation results other datasets were also considered, such as average bed temperature and temperature evaluation with time at fixed points in the bed. Simulation results show

several degrees of temperature increase when higher temperature metal plate boundary is used.

A

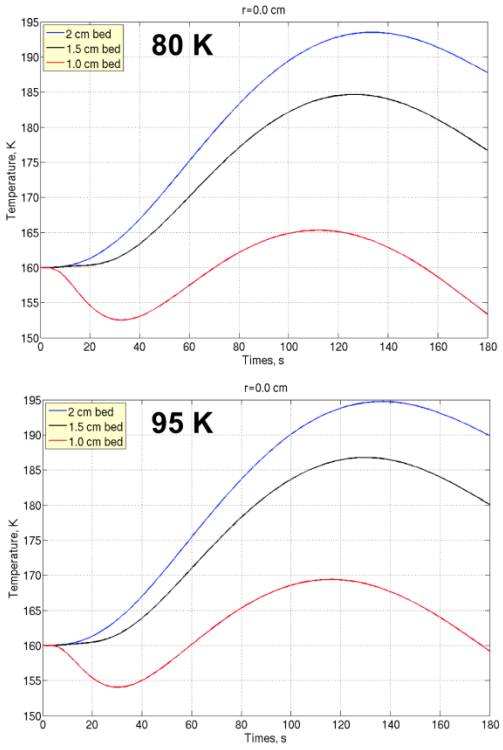

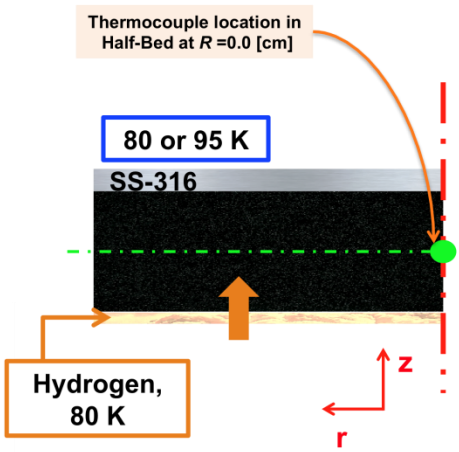

B

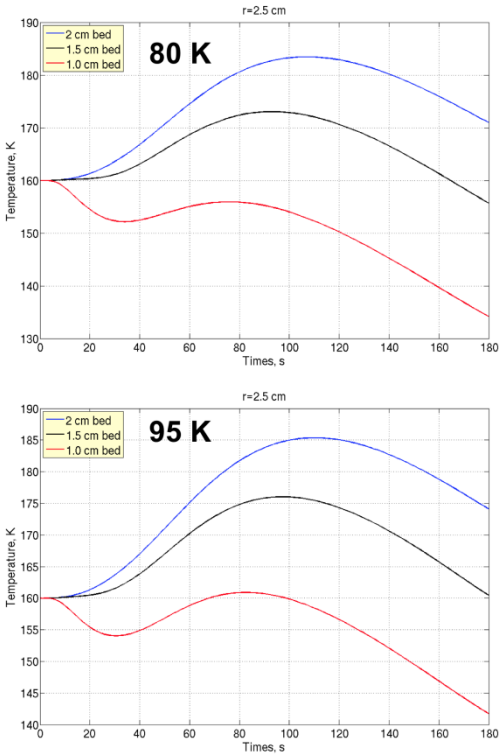

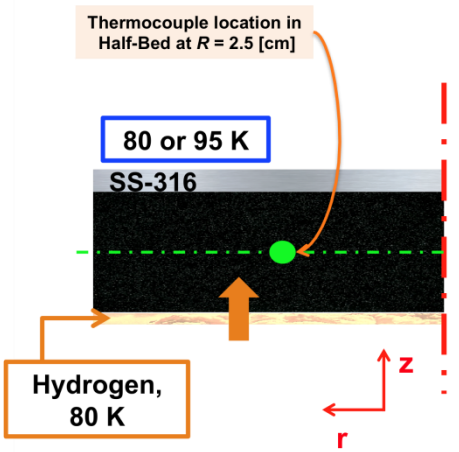

C

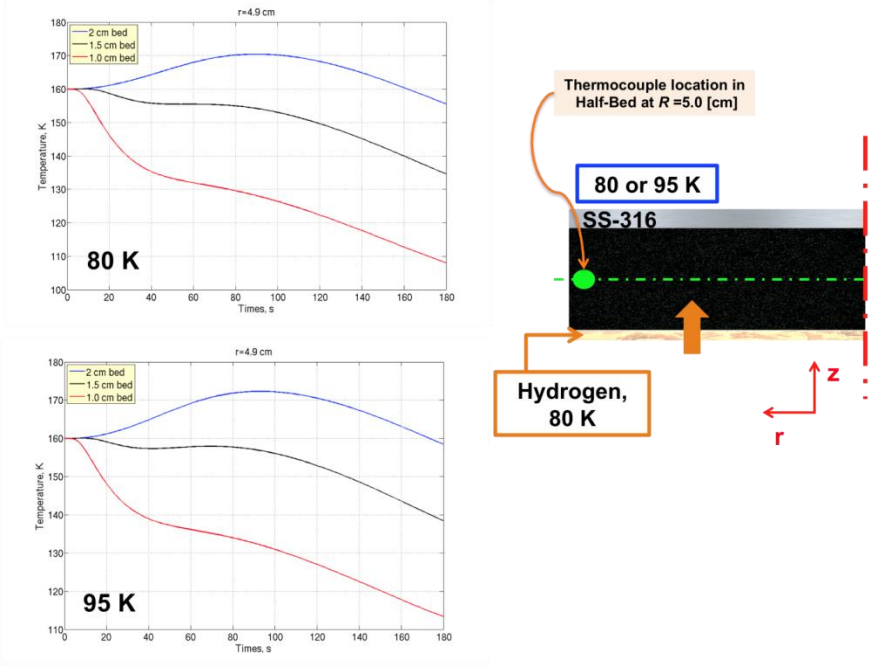

Figure 64: Temperature distribution at different positions of Half-Bed densified MOF-5.

From the entire simulation we concluded that appropriate experimental bed height was 1.5 [cm]. Higher half-bed structure would likely develop stagnant temperature regions and hot spots significantly above initial bed temperatures and target values. Lower height bed would result in somewhat better temperature profile resolution and cooling effects but at a price of increased number of half-bed cells in the actual experimental system. The 1.5 [cm] bed size provided reasonable trade-off between temperature resolution requirements and number of beds used in the planned experimental work.

Integrated System Model - Throughout Phase III, production and validation of a numerical modeling tool for the prediction of MATI system performance was conducted. The numerical simulation tool was developed in COMSOL Multiphysics 4.2a and was utilizing information obtained from previous modeling efforts at OSU (see Chris Loeb PhD Thesis 2013). We continued to use this simulation tool to ensure proper formulation, characterization, and accuracy of the experimental results. It is important to note that the mathematical model and its numerical simulation was entirely based on first principles. However, the model contained particular geometric characteristics of the experimental apparatus and particular material characteristics of the compressed MOF-5 material. Most of these material characteristics were imbedded in the parameters of the DA equation, which will require updating due to the increased density of the compressed MOF-5 bed compared to those used in Phase 2.

The Phase III numerical model will be developed and utilized to conduct a local simulation characterizing a half unit cell (**Figure 65**) of the adsorption system, taking advantage of the natural symmetry of the MATI design. The half unit cell geometry

contained a MATI cooling plate with headers, heat transfer fluid flow path, two compressed MOF-5 beds, and two half height H_2 distribution regions, annular region for H_2 flow between the MATI and steel vessel, the steel shell, and all H_2 void spaces resulting from the rounded edges of the compressed beds. The half unit cell geometry was utilized to perform simulations on a smaller scale, resulting in a more efficient use of computer resources and lowering computational time. The half unit cell was used as a first pass to ensure proper functionality, proper implementation of material characteristics, and application of boundary conditions.

A new machine has been procured by OSU for the development and validation of the numerical models of the MATI storage system. Oregon State University is no longer supporting or providing COMSOL 4.2a software that was used throughout the Phase II numerical investigations and has offered COMSOL 4.4 as a replacement. The Phase II models using updated properties and energy equations (provided by SRNL) was rerun on the new software to ensure that the solutions calculated compare accurately to those performed in Phase II.

Due to the complexity of the modeling geometry, the geometry was fully assembled using SolidWorks, to ensure proper fit of all required modeling domains and transferred to COMSOL using a COMSOL/SolidWorks LiveLink license.

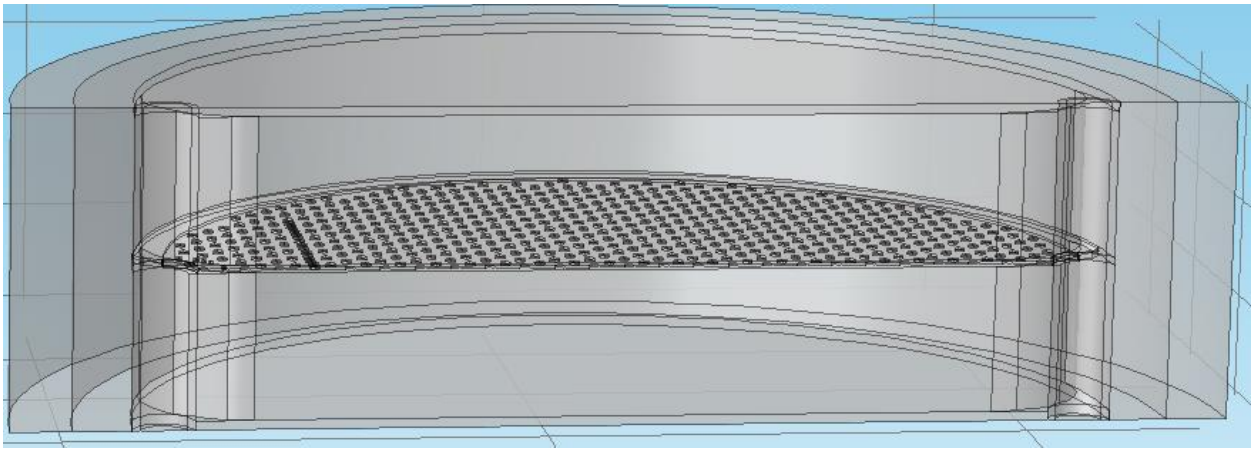

Figure 65: Representation of full cell geometry used in first stage of Phase III modeling effort.

The LiveLink between COMSOL and SolidWorks was identified as the optimal software configuration that will facilitated parametric studies as well as geometry updates such as the conduction enhancement aluminum pin array.

Configuration of the LiveLink between COMSOL and SolidWorks has been challenging because of the several boundary condition incorporated in the model. After the software update and following the geometry import to COMSOL via the LiveLink license, the model has six small additional physical domains. These new extra domains were virtual artifacts not intended as part of the first principal model. The new domains created several misleading error codes during meshing of the geometry, introducing discontinuity between nodes, and altered the specified boundary conditions. While

several traditional methodologies have been unsuccessful in solving this problem, a new approach using a virtual union operation on COMSOL has been tested and appears to be an appropriated strategy to avoid the automatic generation of additional domains. The implementation of this strategy to eliminate the additional domains in the model is currently being completed.

Key Findings: *Key findings from Task 3.6 include:*

- *Simulation helped select a prototype bed thickness of 1.5 cm*

- *When used with Phase 2 data, our simulation took was able to match experimental data with less than a 5% error.*

- *The LiveLink between COMSOL and SolidWorks turned out to be a significant problem and we have had to spend a significant amount of time addressing this issue. As of September 30th 2015, we believe this issue has been solved and we are proceeding with code validation.*

6.0 CONCLUSIONS: This section presents conclusions based on OSU's overall involvement in the Hydrogen Storage Engineering Center of Excellence. Given that the focus of our involvement was on the application of microchannel technology to hydrogen storage, this will be the main focus of our conclusions.

- **When We Are Addressing a Diffusion Limited Process Microchannel Technology Can Have a Dramatic Impact** – The microchannel combustor/heat exchanger is a classic application of microchannel technology because the performance of this device is limited by diffusion of mass and heat. Using microchannel dimensions can significantly improve the performance of this class of device. The OSU microchannel combustor/heat exchanger was a small fraction of the size of a state of the art conventional combustor/heat exchanger developed by Sandia National Laboratory. Clearly whenever a hydrogen storage system needs a device which is limited by diffusion, microchannel technology should be considered.

- **The MATI Highlights Other Advantages of Microchannel Technology** – Heating and cooling the media is a diffusion limited process due to the low thermal conductivity of many storage materials but the use of microchannels only improves the performance of a the cooling device and does not address the primary resistance to heat transfer which is the media itself. However the use of microchannels in the form of the MATI has other advantages including maximizing the fraction of the tank volume which is media and the use of a second fluid for heating and cooling. This is particularly important for the heating case where the MATI allows the use of fuel cell waste heat rather then electricity.

- **The MATI is Technically Feasible and Has the Potential For Low Cost** – Design, testing and simulation at OSU did not identify any issues related to the

feasibility of the concept and extensive manufacturing and cost studies confirmed that the MATI could be fabricated in high volumes using standard industrial practices and at an attractive cost.

- **Meeting Cost and Weight Goals Depends on Aluminum Being an Acceptable Material of Construction for Both the Combustor and MATI** – The cost and weight of both the combustor and the MATI are significantly improved if we can use aluminum as the material of construction. Fabrication studies conducted as part of this project demonstrated that stamping and laser welding can be used for patterning and bonding aluminum cooling plates. This is a significant development and may lead to the use of aluminum in other microchannel applications.

- **Microengineering the Densified Media Pucks Offers a Solution to Low Conductivity Materials** – The use of microengineered conduction enhancements in the densified media pucks appear to offer an attractive option for improving heat transfer in a low conductivity densified media. Simulation and preliminary experimental results suggest this approach is attractive but more detailed experimental investigations are required to optimize the conduction enhancements

7.0 PATENTS: Due to the lack of a near term market, OSU has not patented the MATI concept.

8.0 PUBLICATIONS / PRESENTATIONS: The publications and presentations resulting from OSU's involvement in the Hydrogen Storage Engineering Center of Excellence are listed below.

- M. Ghazvini, V. Narayanan, "Design of A Microscale Combustor- Heat Exchanger for Low Temperature Applications", *ASME 2013 Summer Conference* (HT2013), July 14-19, 2013, Minneapolis, Minnesota.
- M. Ghazvini, V. Narayanan, "A microscale combustor recuperator and oil heat exchanger – design and thermofluidic characterization", *International Journal of Heat and Mass Transfer,* Vol. 64, pp. 988-1002, 2013.
- M. Ghazvini, "Compact integrated microchannel combustor, recuperator and heat exchanger for hydrogen storage applications", PhD Dissertation, Oregon State University, September 23rd, 2013.
- Rasouli, E., and Narayanan, V., 2014, "Single-phase Cryogenic Flows Through Microchannel Heat Sinks," FEDSM2014-21275, Proceedings of the ASME 2014 4th US-European Fluids Engineering Division Summer Meeting and the 12th International Conference on Nanochannels, Microchannels, and Minichannels, August 3-7 2014, Chicago, IL, USA.
- Truong, E.D., Rasouli, E., and Narayanan, V., 2013, "Cryogenic Single-phase Heat Transfer in a Microscale Pin Fin Heat Sink," Paper HT2013-17660 (13 pages), Proceedings of the ASME 2013 Summer Heat Transfer Conference, Minneapolis, MN, July 2013.

- L. Steigleder, "A Microchannel-Based Thermal Management System for Hydrogen Storage Adsorbent Beds," MS Thesis, June 2012.
- S. Pawar, "Fabrication of Precipitation-Hardened Aluminum Microchannel Cooling Plates for Adsorption-Based Hydrogen Storage Systems," MS Thesis, March 2013.
- Truong, E. D., Rasouli, E., and Narayanan, V., 201, "Cryogenic single-phase heat transfer in a microscale pin fin heat sink," HT2013-17660, Proceedings of the ASME 2013 Summer Heat Transfer Conference, Minneapolis, MN, July 14-19 2013, accepted.
- A. Truszkowska, C. Loeb, R. Chahine, B. Hardy, G. Jovanovic, "*Temperature Distribution in Activated Carbon Bed During Adsorption of Nitrogen*", International Congress on Energy (ICE), 2011, American Institute of Chemical Engineers, Minneapolis, MN, (paper) Oct 18, 2011
- A. Truszkowska, C. Loeb, G.N. Jovanovic, "*Adsorption Based Hydrogen Storage System; Multiscale Approach and Mathematical Model*", International Congress on Energy (ICE), 2012 AIChE Annual Meeting, Pittsburgh, PA, (paper 347c) Oct. 30, 2012
- Loeb, C., Truszkowska, A.,Hardy, B., Chahine, R., Jovanovic, G., 2012, "*Removal of heat from a hydrogen storage media by a novel microscale-based heat exchanger*", International Congress on Energy (ICE) 2011. AIChE Annual Meeting, Minneapolis, MN, (paper 378d) Oct. 18, 2011
- Loeb, C., Truszkowska, A., Jovanovic, G.N., 2012, "*Removal of heat from a hydrogen storage media by a novel microscale-based heat exchanger*", World Hydrogen Energy Conference, Toronto, ON, Canada (2012)
- Loeb, C., Jovanovic, G, 2013 "*Cryogenic Hydrogen Adsorption On MOF-5 With Novel Microchannel Thermal Management System - Experiment and Simulation*", American Institute of Chemical Engineers, San Francisco, CA, USA
- Loeb, C., "*Enhancement and Modeling of Cryogenic Solid-State Hydrogen Storage Systems with a Novel Microchannel Thermal Management Device,*" PhD Thesis Oregon State University, Corvallis, OR, June 2013 (http://hdl.handle.net/1957/39687)
- Loeb, C., Jovanovic, G., 2014 "*Improved storage capacity of a MOF-5 hydrogen storage system using a novel microchannel heat exchange device,"* 23rd International Symposium on Chemical Reaction Engineering & 7th Asia-Pacific Chemical Reaction Engineering Symposium, Bangkok, Thailand
- Loeb, C., Truszkowska, A., Jovanovic, G., "Increasing hydrogen storage in compressed MOF-5 system using a microchannel thermal management device: experiment and simulation," Advances in Chemical Engineering and Science, 2014 (in review)

[i] AWS C3.3:2002 - Recommended Practices for the Design, Manufacture, and Examination of Critical Brazed Components, American Welding Society, 2002.